UNIVERSITÀ DEGLI STUDI DI TRIESTE

XXXI CICLO DEL DOTTORATO
DI RICERCA IN
FISICA

INTENSITY AND FLUCTUATION DYNAMICS IN PUMP-PROBE EXPERIMENTS IN COMPLEX MATERIALS

Settore scientifico-disciplinare: FIS/03

DOTTORANDA
Francesca Giusti

COORDINATORE
prof. Livio Lanceri

SUPERVISORE DI TESI
prof. Daniele Fausti

ANNO ACCADEMICO 2017/2018

Summary

The work presented in this thesis is focused on out-of-equilibrium experiments on strongly correlated systems, both with “standard” pump-probe spectroscopy and time resolved single pulse statistics. We applied these techniques mainly on a High Temperature Superconductor, an optimally doped $Bi_2Sr_2Y_{0.08}Ca_{0.92}Cu_2O_{(8+\delta)}$ (Y-Bi2212). These materials show intriguing and still unexplained properties, such as the presence of the pseudogap phase.

The aim of the first part of the thesis is to analyze the phase transition between superconducting and pseudogap phases, through the combination of time resolved techniques, suitable for the study of strongly correlated systems, and electronic Raman spectroscopy, which allows to detect anisotropic behaviors in the reciprocal space. The experimental result was a map of the de-excitation dynamics as a function of temperature across T_c. The excitation was provided by mid-infrared pulses at two photon energies ($E > 2\Delta$ and $E < 2\Delta$, where Δ is the superconducting gap) and different polarizations. The results show that a low photon energy pump polarized along the Cu-Cu direction causes a larger dynamical superconducting response with respect to the Cu-O polarized excitation, both below and above the critical temperature. The results are supported by an effective theoretical model based on BCS theory for a superconductor with an anisotropic d-wave gap typical of cuprates. The model reveals a dynamical enhancement of the superconducting order parameter for a Cu-Cu polarized pump, which is due to the increase of phase coherence of the pair operator, whereas the density of Cooper pairs seems not to be strongly affected by the excitation.

In the second part of the thesis we wanted to move a step forward and to study the statistical distribution of the probe pulses. The intrinsic noise of the photon number distribution reveals a completely distinct behavior in the various phases of the sample: it follows the mean photon number dynamics in the metallic states, whereas it has a different time resolved signal (and in particular the noise has a longer time decay) in the superconducting state. A simple quantum model, which describes the dissipative processes of the set-up as perfect beam splitters, has been developed to simulate the observed peculiar results. From the model it turns out that the non-selected polarization contributes to the final noise signal, giving rise to a completely different dynamics for high and low temperatures. This interpretation shows how, whereas it is always possible to select photons with certain features (such as polarization) in “standard” intensity measurements, footprints of every interaction are kept in the noise.

Contents

1 Introduction 1

I Intensity Dynamics in Complex Materials 5

2 Cuprates 9
- 2.1 Features of conventional superconductivity . . . 9
- 2.2 Non-conventional superconductors . . . 12
  - 2.2.1 Structure . . . 13
  - 2.2.2 Doping . . . 13
  - 2.2.3 Phase Diagram . . . 13
  - 2.2.4 Pseudogap . . . 14
  - 2.2.5 Superconducting Gap . . . 18
- 2.3 BSCCO . . . 20

3 Experimental techniques 23
- 3.1 Raman spectroscopy . . . 24
  - 3.1.1 Band structure contribution . . . 25
  - 3.1.2 Crystal structure contribution . . . 30
- 3.2 Time resolved spectroscopy . . . 36
  - 3.2.1 Pump-probe experiments . . . 36
  - 3.2.2 Time resolved spectroscopy on Cuprates . . . 38
- 3.3 Measurements . . . 43
- 3.4 Summary . . . 45

4 Preparatory measurements on Y-Bi2212 47
- 4.1 Probe linearity . . . 48
- 4.2 Probe polarization . . . 50
- 4.3 Fluence dependence of the Raman modes dynamics . . . 51
- 4.4 Excitation photon energy . . . 52
- 4.5 Temperature map . . . 55
  - 4.5.1 Probe photon energy . . . 56
  - 4.5.2 Pump photon energy . . . 60
- 4.6 Conclusions . . . 63

5 Signatures of enhanced superconducting phase coherence 65
5.1 Motivation . . . 65
5.2 Measurements . . . 66
5.2.1 Phase diagram and pump-probe measurements . . . 66
5.2.2 Pump photon energy dependence . . . 67
5.2.3 Linear fit . . . 69
5.2.4 High fluence measurements . . . 71
5.3 d-wave BCS model . . . 72
5.3.1 Quantities and methodologies . . . 73
5.3.2 Results: $T < T_c$ . . . 75
5.3.3 Results: $T > T_c$ . . . 77
5.3.4 Real Space representation . . . 79
5.4 Symmetry of the electronic excitation . . . 81
5.4.1 Birefringence measurements . . . 81
5.4.2 Results . . . 84
5.5 Conclusion . . . 88

II Fluctuation Dynamics in Pump-Probe Measurements 89

6 Noise in time domain measurements: a quantum model 95
6.1 Model concept . . . 95
6.2 Differential Acquisition . . . 97
6.3 Beam Splitter . . . 98
6.4 Shot noise . . . 103
6.5 Beam attenuation . . . 105
6.6 Additional dissipation effects . . . 111
6.7 Summary and observations . . . 114

7 Noise in time domain measurements: an effective description 119
7.1 Measurement and samples . . . 120
7.2 *Reversing* of the variance dynamics . . . 122
7.3 Minimum noise . . . 126
7.3.1 Oscillation amplitude dependence . . . 126
7.3.2 Double frequency amplitude . . . 128
7.3.3 Double frequency decay . . . 130
7.4 Two pumps measurements . . . 131
7.4.1 Bismuth: measurement concept . . . 133
7.4.2 Quartz: two phonon contributions . . . 135
7.5 Summary and conclusions . . . 142

8 Noise detection in Bi2212 measurements 145
8.1 Measurements and results . . . 146

8.2 Model comparison 147
8.3 Polarization selection 148
8.4 Temperature and fluence dependence 152
8.5 Conclusions 153

9 Conclusion **155**

A Short summary of BCS theory **159**
A.1 Hamiltonian 160
A.2 Eigenvualues 161
A.3 Eigenstates 161
A.4 Gap equation 162

B Irreducible representation **165**

C Acquisition system in noise measurements **167**
C.1 Detection system 167
C.2 Integration process 169

Bibliography **171**

1 Introduction

In ***complex materials*** unexpected and intriguing properties can arise from the intricate (and not completely understood) interplay between several degrees of freedom, such as electrons, spins, lattice etc. Among these interesting features, we stress their rich phase diagram, in which a small variation of external (such as temperature) or internal (e.g. chemical doping) parameters can modify completely the phase of the material, moving from superconductors to insulators, from Fermi liquid metals to "strange" ones and so on.

This abundance of phases leads not only to a revision of the description of the interaction between all the material degrees of freedom, but also to possible technological applications, exploiting the possibility of triggering phase transitions on short time scales. For instance, a metal-insulator transition may be adopted in fast switches.

The excitement in this field is intertwined with the difficulties in the comprehension of the origin of many of the properties of complex materials. As a matter of fact, the entanglement between the different degrees of freedom does not allow to identify their contribution separately in the creation of the described properties. The advent of ultrafast lasers[1] and the related time resolved spectroscopies partially answered to this need by providing a new technique able to separate the response of different degrees of freedom, even though for a very short time.

The base concept of this approach is to excite the sample with a very short perturbation and to measure its response to a certain stimulus as a function of the time passed from the excitation. Different degrees of freedom are supposed to show different de-excitation processes (for example, different recovery times), favoring the separation of their contributions to the total response. In particular, in ***pump-probe experiments*** the sample is excited by an ultrashort laser pulse (*pump*), and the variation of its optical properties (for example reflectivity or transmittance) is investigated by a second ultrashort pulse (*probe*), reflected or transmitted by the sample after a controlled time delay. The variation of this delay, controlled by changing the probe optical path, provides the complete dynamics of the sample de-excitation.

[1] The relevance of ultrafast systems was acknowledged by the Nobel Committee for Physics in 2018. The prize was awarded *for groundbreaking inventions in the field of laser physics*, with one half jointly to Gérard Mourou and Donna Strickland *for their method of generating high-intensity, ultra-short optical pulses*.

Ultrafast techniques have also the technological advantage to study and characterize variation of the optical behavior on very short time scales, which could be of interest in the modern need of speed up fast digital circuits. Furthermore, the non-equilibrium approach and especially it opens the possibility to trigger phase transitions and even discover new transient phases of the material.

Although the described technique is very powerful, we suppose that the light pulses used in the experiment can actually convey much more information. As a matter of fact, in a pump-probe experiment, we measure the mean light ***intensity*** transmitted or reflected by the sample; this average is performed on thousands of laser pulses and provides the mean response of the sample in time. But, on the other hand, light is not characterized only by its intensity: many other quantum properties are hidden in the detection of a light pulse. In this thesis we will focus on just one, that is the particle nature of light.

Considering each pulse as made up of a defined number of photons leads to the study of the distribution of the photon number (detecting each pulse separately) and especially the ***fluctuations*** on this quantity. The passage from intensity to photon number is not a simple generalization of the classical concept: let us think the *shot noise* experiment, for instance. If a single laser beam is split in two by a 50:50 beam splitter, the two output beams are expected to have the same intensity. In contrast, a single pulse measurement shows that the initial number of photons is not perfectly divided in two and the output photon number varies from pulse to pulse, giving rise to a noise due only to the particle nature of light. This simple example demonstrates that the study of the noise of the photon number provides information about the quantum nature of light. The open question is whether and, eventually, how the quantum properties of light can be affected by the interaction with the sample and the study of the fluctuations of the photon number can give additional information on the de-excitation process.

The choice of the use of a time resolved photon number distribution technique has been triggered by the observation that quantum fluctuations in materials, and especially fluctuations of the atomic positions are the origin of material properties such as quantum paraelectricity [27], high temperature superconduction and quantum phase transitions in general [82, 81], which are some of the features of the complex materials described above. The final goal of this work is to understand whether the quantum fluctuations of the sample can be mapped in the light ones and, consequently, to which extent the information encoded in the fluctuations of the probe photon number can be used to infer the nature of the quantum fluctuations in materials.

My thesis work is organized in two parts, one concerning the intensity measurements and a second about the fluctuation detection.

The first part starts with the introduction of high-temperature superconductivity and, specifically, of the copper oxides family, which is the subject of our experiments (***Chapter 2***). In the chapter the main features of conventional and non conventional superconductors are presented, in order to compare the two kinds of materials and to highlight the impact of strong correlations on the physical properties of cuprates. Finally, the properties of the material used in the pump-probe experiments, i.e. an optimally doped Yttrium substituted Bi2212 ($Bi_2Sr_2Y_xCa_{1-x}Cu_2O_{8+\delta}$), is presented.

The experimental technique is introduced in ***Chapter 3***, where the advantages of electronic Raman scattering and time resolved spectroscopy are shown, in relation to the measurement of strongly correlated systems and, in particular, superconductors. The chapter highlights that electronic Raman scattering is sensitive to the anisotropies in the reciprocal space, a peculiar feature of high temperature superconductivity in cuprates, whose electronic dispersion is characterized by nodes (*d-wave gap*), whereas time resolved spectroscopy detects the contributions of the different degrees of freedom, eventually producing metastable states which are not accessible through thermodynamics. The combination of the two complementary techniques provides a more complete characterization of the sample and of its dynamics.
At the end of the chapter we show and give more details on our experimental set-up.

In ***Chapter 4*** the first time resolved measurements on Y-Bi2212 are presented. The aim of the chapter is the introduction of the characteristic time resolved response in certain experimental conditions and its variation obtained by tuning some parameters. In particular, we analyzed the effects of pump and probe fluence and photon energy as a function of the temperature. The measurements allow us to characterize the dynamics associated to a specific phase (superconducting, pseudogap or metallic one) or to the transition between two phases, depending on the excitation and probing features.

Chapter 5 shows the effects on the same sample of a low photon energy excitation with defined polarization requirements. We focused our attention on the phase transition between superconducting and the so-called pseudogap phase, in order to understand if the dynamics in this temperature range can be affected by the pump photon energy and, in particular, if the energy is lower than the one required to break a Cooper pair, the electron couple whose presence is at the base of superconductivity. Measurements are sustained by an effective model, which qualitative describes the most peculiar time resolved results.

The second part of my PhD work concerns the fluctuation measurements described above. After a brief introduction of the concept, ***Chapter 6*** introduces the quantum description of the Beam Splitter formalism, in order to represent a general dissipative process present in the experimental set-up. The treatment is adopted to describe the whole fluctuation measurement, providing the relation between the mean number of photons the related variance and a way to interpret the results of the detection.

Chapter 7 compares the Beam Splitter model introduced in the previous chapter with the experimental results on three benchmark samples, characterized by coherent Raman active modes: two transparent ones (quartz and strontium titanate), in which the phonon oscillation is directly excited by the radiation and an absorbing one (bismuth), in which we expect an electron mediation between the impinging light and the vibrational mode.

Finally, in ***Chapter 8***, the fluctuation measurement is applied to our original sample, Y-Bi2212, in its different phases, in order to understand if the photon number fluctuations are somehow correlated to the phase properties of the material.

Part I

Intensity Dynamics in Complex Materials

107 years have passed since H. K. Onnes discovered that mercury is characterized by a negligible resistivity at very low temperatures ($T < 4.2\,\mathrm{K}$) [67]. It was subsequently found that the observed collapse of resistivity was common to a relatively wide class of elements when cooled at the liquid helium temperature: from this property these materials took the name of "superconductors". The implications of these samples are immediately clear if you consider the possibility of having no resistance at all: from transmission lines without dissipation, to the improvement (and dimensional reduction) of motors and generators, to the modern need of speed up computers performances and in general to use fast digital circuits.

But the resistence drop was just one of the characteristics of superconductivity. In 1933 W. Meissner and R. Ochsenfeld noticed that below the transition temperature these materials behave as perfect diamagnets, that is, in presence of an external magnetic field, they show no internal magnetism. It is the so-called *Meissner effect*, whose most spectacular consequence is the superconducting levitation [63].
This second feature of superconductivity widened the list of technological applications: from maglev trains (which uses magnetic levitation to reduce the friction between the rails and the train itself, making earth means of transport competing with airplanes), to the detection of very low magnetic fiels, with implication in geology (like mineral exploration and earthquake prediction), medical sciences (neuron activity and magnetic resonance), oil prospecting and research (for example in the study of gravitational waves).

Unfortunately the application of these materials had two strong limitations: on one hand the absence of a theoretical model able to describe the phenomenon and, on the other hand, the high costs of the cooling system (and especially of helium) needed to reach the superconducting phase.
The solution to the first point arrived in 1957 when J. Bardeen, L. N. Cooper and J. R. Schrieffer developed the first microscopic theory (then called *BCS theory*) able to describe the behaviors of this class of materials [5].
A great improvement regarding the second problem was reached in 1986, when J. G. Bednorz and K. A. Müller found that a new class of materials (mainly ceramics belonging to the cuprate family) enters the superconducting phase at relatively high temperature ($T \approx 40\,\mathrm{K}$) [7]. The turning point was the discovery of compounds whose transition temperatures exceed the nitrogen boiling one, thus making superconductivity achievable in a much cheaper way. On the other hand there was a price to be paid: the new samples showed completely different properties with respect to "conventional superconductors", which cannot even be explained by the BCS model (see Chapter 2).

Despite the evolution of non-equilibrium spectroscopies of the last two decades, have increased our understanding of the physics of strongly correlated materials

[39] (see chapter 3), after more than 30 years from its discovery *High Temperature Superconductivity* is still discussed and, while different samples are synthesized every year (Figure I1), a clear and unanimous explanation of the origin of the phenomenon is still lacking. In this framework the measurements of Chapters 4 and 5 find their motivation.

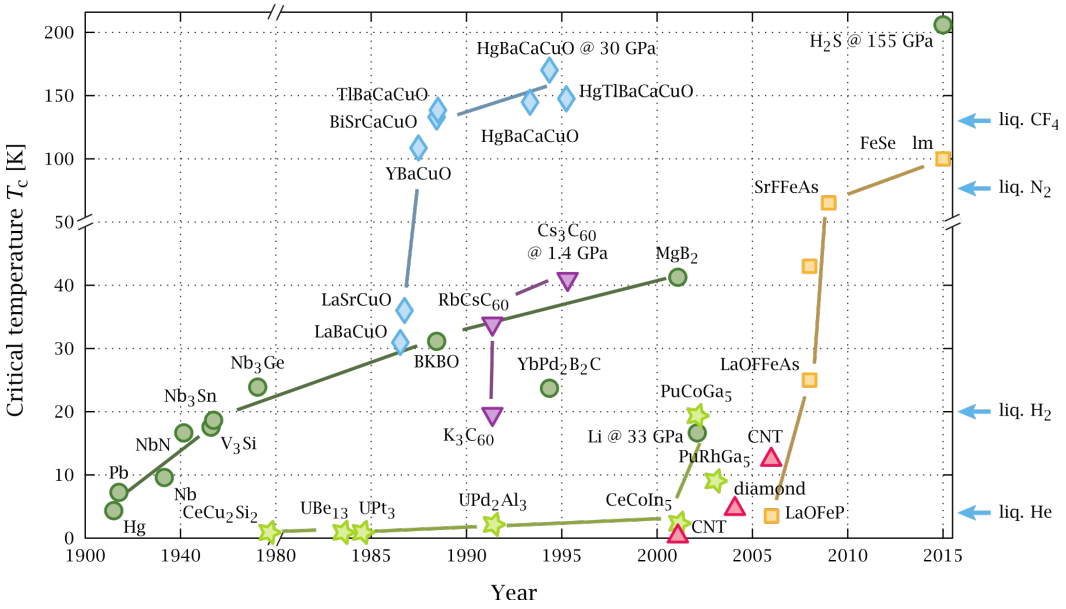

Fig. I1.: Timeline of Superconductivity. Several superconducting compounds as a function of the year of discovery and their transition temperature. BCS superconductors are displayed as green circles, cuprates as blue diamonds, iron-based superconductors as yellow squares, fullerenes with purple triangle and carbon nanotubes with red triangles [1].

2 Cuprates

In the present chapter I will introduce the system we studied during my PhD project, a Bi2212 ($Bi_2Sr_2Y_xCa_{1-x}Cu_2O_{8+\delta}$) with a hole doping, δ, close to that necessary to attain the highest critical temperature (δ=0.16, Tc=97 K). It is a cuprate and a High Critical Temperature Superconductor.
Starting from the main features of BCS (conventional) superconductivity, we will move to the intriguing properties of High Critical Temperature Superconductors and especially to their rich phase diagram. The last part is dedicated to our specific sample.

2.1 Features of conventional superconductivity

Superconductivity has been observed in several elements below a certain critical temperature T_c and eventually under particular pressure conditions (see Figure 2.1).

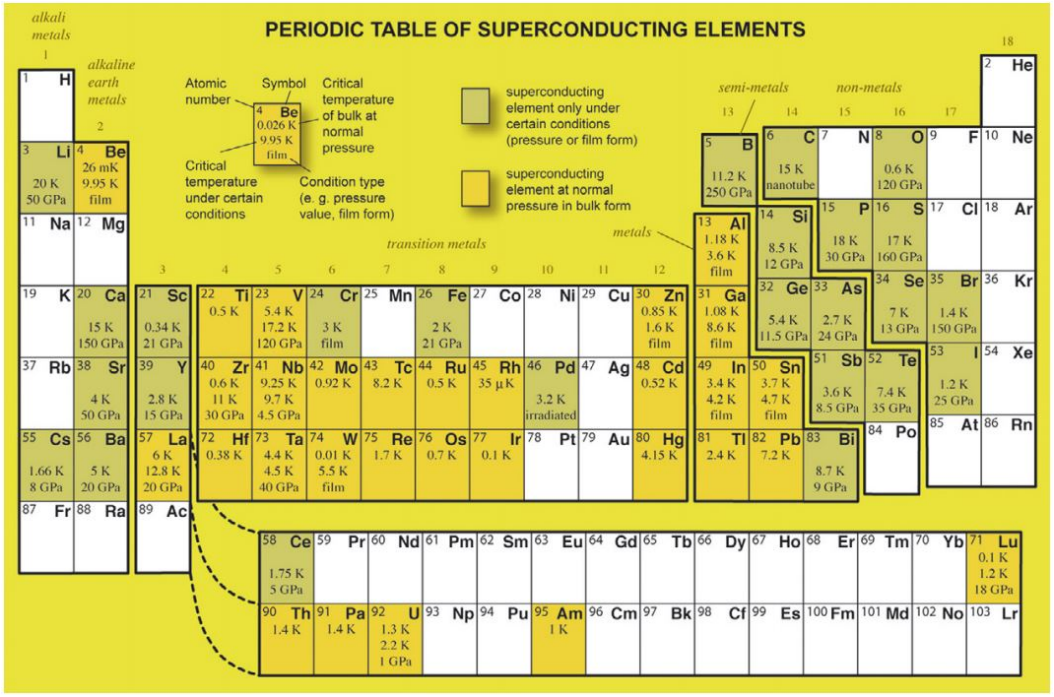

Fig. 2.1.: Periodic table of Superconductivity. [10]

The experimental evidences of a novel phase below T_c has been observed through different measurements and techniques [3]

1. RESISTIVITY: In a superconductor no DC electrical resistivity can be measured below the critical temperature.

2. GAP: Superconductors usually behave as if there were an energy gap 2Δ centered at the Fermi energy: an electron can be excited in a superconductor only if its energy exceeds the Fermi one by the gap value. It has been observed that the value of the gap at zero temperature and T_c are proportional in most of the cases. A peculiar manifestation of this property is the absence of "acoustic attenuation": when a sound propagates through a metal, the microscopic fields due to the displacements of the ions can give energy to the electrons close to the Fermi level, removing it from the wave. Usually the energy carried by a sound wave is smaller than the gap and so the energy cannot be transferred to the electrons, resulting in a reduction of the sound attenuation.

3. THERMAL PROPERTIES: Superconductors are poor thermal conductors (contrarily to normal metals) and the electric current is not accompanied by the thermal one.

4. SPECIFIC HEAT: In a normal metal the specific heat c_v fulfills the relation $c_v = AT + BT^3$, where the linear terms comes from the electronic excitations and the cubic one is due to lattice vibrations. In a superconductor the specific heat jumps at higher values at T_c and then decreases, with an exponential electronic contribution.

5. MAGNETIC PROPERTIES: A magnetic field (provided it is not too strong) is not able to penetrate into the interior of a superconductor. This perfect diamagnetism is called *Meissner effect* and is due to the formation of electrical surface currents which create an additional field that precisely cancels the applied one. Above a certain threshold, called critical field, the application of the magnetic field destroy the superconductive phase. The value of the critical field depend on the temperature.

Notice that the superconducting phase can be suppressed through
i. the application of a sufficiently intense magnetic field
ii. the application of an intense DC current
iii. the application of an AC current, whose frequency exceeds the value $\frac{\Delta}{\hbar}$ [3]

Conventional superconductivity is explained by the BCS theory (so called from the name of the physicists who developed it: J. Bardeen, L. N. Cooper e J. R. Schrieffer),

which is based on the hypothesis that a weak attractive potential between electrons can favour the formation of Cooper pairs, i.e. new bosonic particles with total momentum and spin equal to zero [5]. A possible origin for the attractive potential is provided by electron-phonon coupling. In order to understand the phononic contribution, the following intuitive argument can be used.
Let us consider an electron hopping throughout a crystal: its electric field would cause a retarded attraction of the positive ion of the lattice (the retardation is due to the mass difference between electrons and ions). A second electron would feel the attraction due to the increase of the positive charge density in the region where the first electron passed through, giving rise to an effective electron-electron attraction [5, 77].

The main effect of this ***pairing*** mechanism is the transformation of two fermionic particles of opposite spin and momentum into a single bosonic one (called Cooper pair), which obeys to the Bose-Einstein statistical distribution, allowing, for instance, the occupation of one state by an infinite number of particles.

The superconducting phase occurs below a ***critical temperature*** T_c and is characterized by an energy gain and by the opening of an ***energy gap*** in the band, which is conventionally called Δ and it is of the order of few tenths of meV. $E = 2\Delta$ is the minimum energy required to excite the system, that is to break a Cooper pair producing two quasiparticles [20].
The superconducting gap in a BCS system depends on the temperature (and, in particular, it is maximum for $T \to 0$ and it vanishes for $T \to T_c$), but it is isotropic in the reciprocal space (i.e. it is $\mathbf{k}-$independent), showing an *s-wave symmetry* [20].

The coherence length, that is the approximate spatial extent of a Cooper pair, is of the order of hundreds of nanometer, so that pairs average over pertubations at the atomic level, making the real space description usually irrelevant [85].

In the normal state ($T > T_c$) conventional superconductors are ***good metals*** that can be described as Fermi liquids. For further details on the BCS model see appendix A.

The brief introduction of this section, as well appendix A, has the double purpose of allowing the comparison between conventional and non-conventional superconductivity (that you will find in the following sections of this chapter) and to introduce the BCS model. As a matter of fact, despite this theory is not adequate to completely describe the properties of high temperature superconductors, sometimes models explaining conventional superconductivity can be used to describe non conventional compounds and especially their de-excitation dynamics, at least qualitatively. This is the case of the gap equation A.17 and of the Rothwarf-Taylor phenomenological

model (see section 3.21), which predicts a divergence of the decay in a time resolved measurement as the temperature approaches T_c, actually observed in pump-probe experiments.
This relation will be exploited in chapter 5, where we use a BCS model to describe the dynamical response of a high temperature superconductor.

2.2 Non-conventional superconductors

The term "high critical temperature superconductor" (HTSC) refers to unconventional superconductors which are able to sustain superconductivity at unexpected high temperatures. This phenomenon is of particular interest for its applications, since in most cases the critical temperature is higher than the nitrogen boiling temperature, making the "extended" use of these materials feasible and cheap.
However there exist BCS superconductors with relatively high T_c (for example MgB_2, with $T_c = 40\,\mathrm{K}$ [11]. In the last months even the evidence of BCS superconductivity at room temperature was claimed [93].) and HTSC with relatively low critical temperatures (see the cuprate $LaBaCuO$, with $T_c = 35\,K$ [7] or the iron based superconductor $LaOFeP$, with $T_c = 4\,K$ [48]). So, lately the term "high critical temperature superconductor" has been used to identify the unconventional physics which determines the origin and the properties of superconductivity in these compounds, which definitely goes beyond the simple T_c value.
Different families of non-conventional superconductors have been discovered, such as:

- *cuprates*: layered copper oxygen compounds. The first discovered HTSC (in 1986) belonged to this class;
- *pnictides* and *calchogenides*: iron-based superconductors, discovered in 2006;
- *fullerenes*: allotropes of carbon in the form of a hollow sphere, ellipsoid or tube (like nanotubes and Buckminsterfullerene, a type of fullerene with the formula C_{60});
- *heavy fermion systems*;
- *organic superconductors*.

Within this thesis work we will consider a copper oxides, therefore the terms *HTSC* and *cuprate* will be used as synonyms.

2.2.1 Structure

Copper Oxides based HTSC are a class of ceramic compounds with a perovskite-like structure. They are characterized by Copper-Oxygen (Cu-O) planes separated by spacer layers, which act as charge reservoirs.
The Cu-O planes determines most of the superconducting properties and, in particular, the number of Cu-O planes per unit cell seems to be related to the maximum value of the critical temperature (in general the higher the number of Cu-O planes, the higher the critical temperature).

2.2.2 Doping

Another key parameter is the doping: as a matter of fact cuprates are insulators in the absence of holes (we will refer to this condition as *parent compound*). Conventional band theory predicts such compounds to be metals, but, because of the effect of the strong electron-electron correlations, they turn out to be Mott insulators, as many transition metal oxides [18], with a gap of the order of 2 eV. Doping allows to fill the gap with states and, once a doping threshold is reached, to transform the material in a bad metal (at room temperature) and a superconductor below the critical temperature [15]. Doping refers to the chemical substitution of elements in the spacer layers or of oxygen atoms: in both cases the result is that electrons are pulled away from the Cu-O planes creating holes.

2.2.3 Phase Diagram

Up to now we cited two fundamental parameters to control the macroscopic phase of the material: temperature and doping. Therefore, the most natural phase diagram to describe these materials has the hole doping p on the x-axis and the temperature on the y-axis. A sketch of the typical phase diagram is shown in Figure 2.2.

Below the doping value $p = 0.05\,(5\%)$ the compound is an antiferromagnetic insulator; increasing the doping level a superconducting state arises at low temperatures. The critical temperature becomes larger with the doping, as far as it reaches its maximum value at $p_c \approx 0.16$: this condition is called *optimal doping*. For higher values of p (*overdoped* region) the critical temperature starts decreasing up to $p \approx 0.25$, when it falls to zero. The area enclosed by $T_c(p)$ is called superconducting dome. In the whole underdoped region ($p < p_c$) and sometimes also at optimally doping, a new phase (called *pseudogap phase*) arises from T_c to a second doping dependent temperature T^*, responsible for the transition to the bad metallic phase.

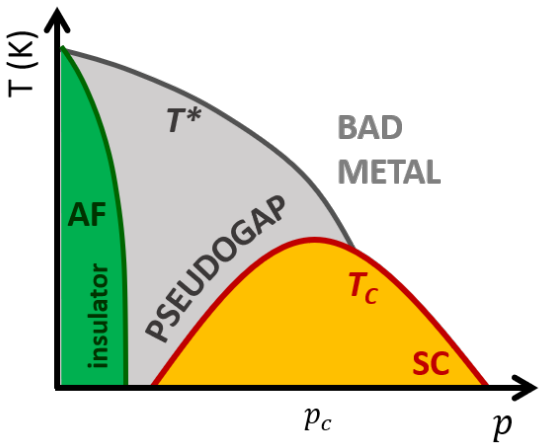

Fig. 2.2.: Cuprate phase diagram. Sketch of the temperature versus doping phase diagram for HTSC. At low doping (green area) the material is Mott insulator. Increasing the doping the sample enters in a bad metallic phase at high temperatures and in pseudogap phase (gray area) for $T < T^*$. The superconducting condition is reached in the interval of doping values about from 0.05 to 0.25 and for $T < T_c$ (orange area). Both T_c and T^* are doping dependent; the maximum value of the critical temperatures occurs at optimal doping $p = p_c$.

2.2.4 Pseudogap

The presence of the *pseudogap phase* is one of the most intriguing and still discussed properties of HTSC, which definitely differentiate them from the standard BCS superconductors.

Pseudogap measurements

The pseudogap phase can be recognized from several manifestations, which are typical neither of the superconducting phase nor of the metallic one.
In the following I will briefly describe the unusual results of some static measurements in the pseudogap phase and the comparison with the same properties as measured in superconducting and metallic phases.

- RESISTIVITY - The drop of the resistivity below T_c is probably the most characteristic feature of superconductivity, from which the name itself derives. In conventional superconductors for $T > T_c$ the resistivity is expected to be linear in T and to collapse at the critical temperature. In HTSC there is a temperature region in which the resistivity deviates from both behaviors [91], as shown in Figure 2.3.

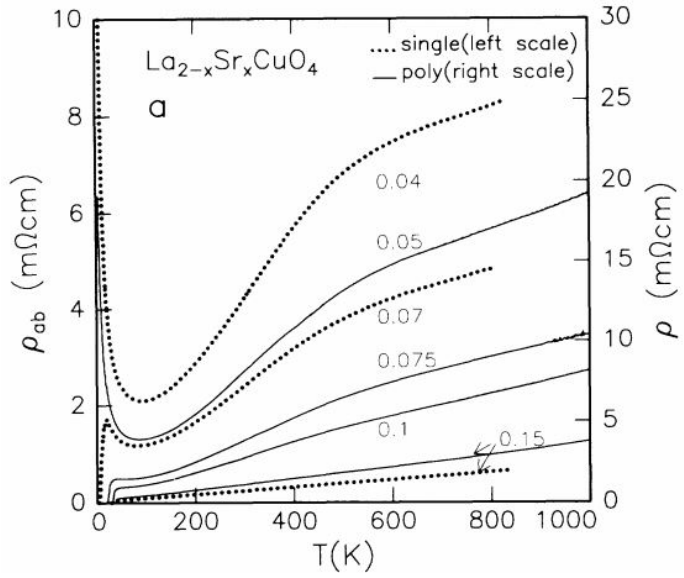

Fig. 2.3.: Resistivity in pseudagap phase. Temperature dependence of the longitudinal resistivity in underdoped and optimally doped $La_{2-x}Sr_xCuO_4$. Notice that at optimal doping ($p = 0.15$) the resistivity has a linear behavior for high temperatures and drops at T_c. In the underdoped case a region in between arises, in correspondence of the pseudogap phase [91].

- ENERGY GAP - NMR, ARPES measurements and c-axis tunneling revealed the suppression of the low energy single particle spectral wave, suggesting the presence of a gap (and so of some form of local superconducting pairing), usually associated to superconducting phase, even above the critical temperature, where the macroscopic superconducting properties vanish [13, 76]. Some results are plotted in Figure 2.4.

- SPECIFIC HEAT - In conventional superconductors for $T > T_c$ the specific heat is expected to be linear in the temperature, while it diverges from this behavior in the pseudogap phase [59], as highlighted from Figure 2.5.

- INFRARED CONDUCTIVITY - In overdoped materials a motion of the infrared spectral weight at low energies is observed just below the critical temperature, whereas in underdoped samples it survives at higher temperatures [73], as pointed out by Figure 2.6

- SPIN STRUCTURE - Inelastic neutron scattering revealed changes in the dynamic spin structure factor: magnetic correlations and “resonant peaks”, typical of the temperature region close to T_c in overdoped materials, are found to be considerably above the critical temperature in underdoped ones [24]. The intensity of the resonant peaks as a function of doping is plotted in Figure 2.7.

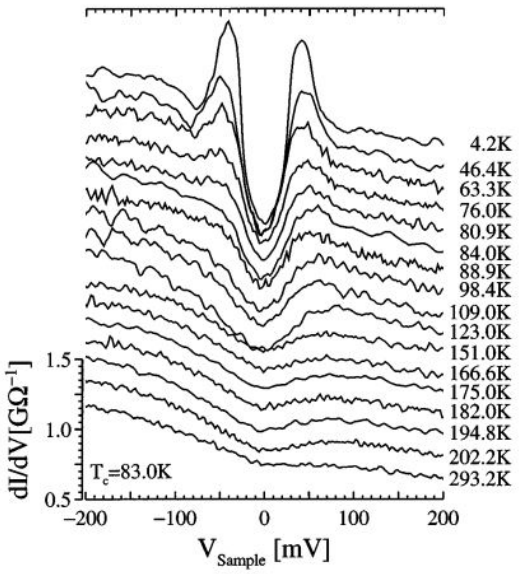

Fig. 2.4.: **Gap in pseudogap phase.** Tunneling spectra measured as a function of temperature on underdoped Bi2212 ($T_c = 83\,\mathrm{K}$). Notice that the gap does not close at T_c, while the amplitude of the "coherence peaks" vanishes at T_c [76].

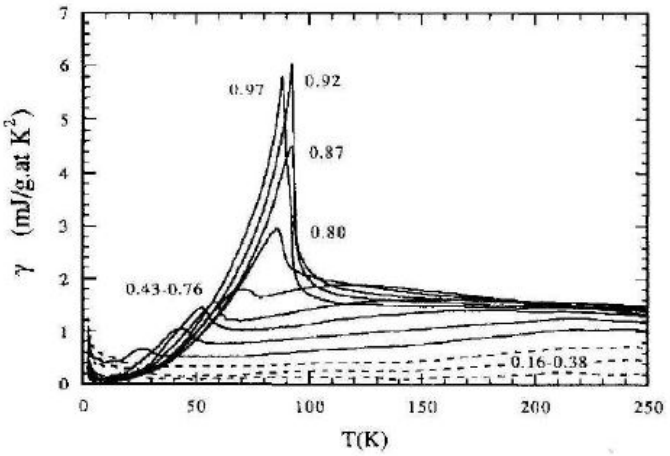

Fig. 2.5.: **Specific Heat in pseudogap phase.** Temperature dependence of the electronic specific heat resistivity in underdoped and optimally doped $YBa_2Cu_3O_{6+\delta}$. The plotted quantity is $\gamma = \frac{C_V}{T}$, which underlines the temperature regions in which the dipendence diverges from the linear one, represented by the horizontal lines [59].

Interpretation of pseudogap phenomena

Up to now there is no clear explanation for the origin of the pseudogap phase. It is suggested that in this phase two elements coexist: a superconducting order and a second element which is able to suppress the superconducting macroscopic properties. On the nature of this second elements two classes of models have been theoretically developed, in order to interpret the pseudogap phenomena [18, 13]:

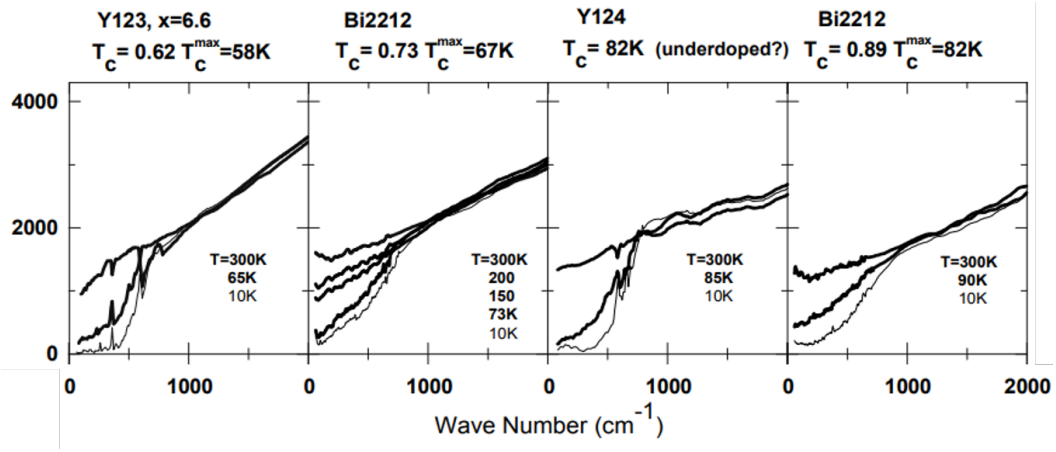

Fig. 2.6.: Infrared conductivity in pseudogap phase. Frequency dependent scattering rate for a series of underdoperd cuprate superconductors in superconducting, pseudogap and metallic phase. You can observe that the behavior in pseudogap phase is always different with respect to the metallic one (and actually it is more similar to the superconducting one) [73].

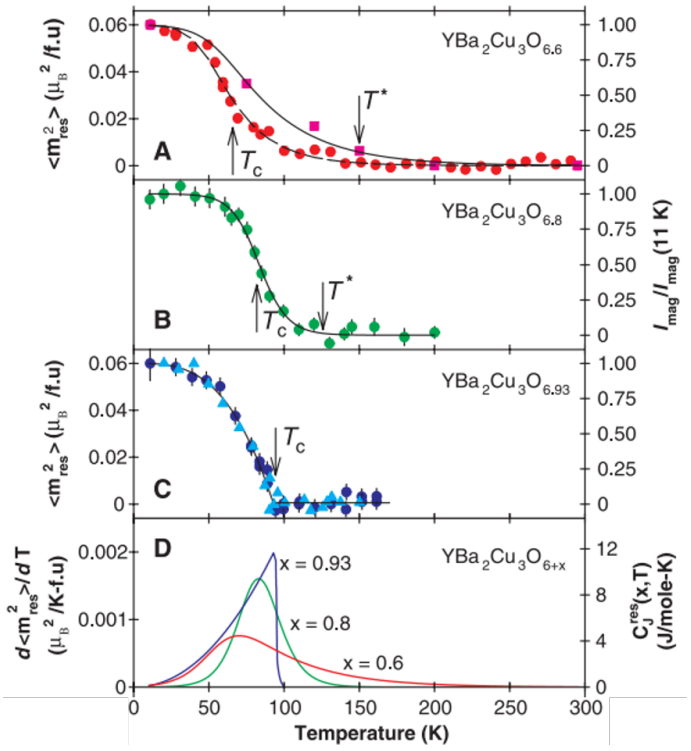

Fig. 2.7.: Inelastic neutron scattering in pseudogap phase. Temperature dependence of the so called resonant peak observed in neutron scattering in $YBa_2Cu_3O_{6+x}$ for three doping values. While at higher doping level the transition is quite sharp at T_c, at lower values it is much more smooth and in particular it affects a larger temperature range (from T_c to T^*), as highlighted from panel **D**, where the derivatives of the previous signals are plotted [24].

1. COMPETING ORDER. In these models the pseudogap is considered as a phase with its own order (current loops, stripe and antiferromagnetic order, density wave etc...), which breaks the symmetry of the system. Therefore in this model

the pseudogap phase is *in competition* with superconductivity.
The transition between the metallic phase and the pseudogap one it at $T = T^*$ (which is doping dependent), that exist even above optimal doping, although it enters in the superconducting dome [13].

2. NON-COMPETING ORDER. These models take into account the concept of fluctuation and in particular the possibility that, under suitable conditions, they produce a local order which can be extended in a disordered phase. In this case fluctuations can enhance some superconducting-like behaviors even above T_c.
An example of possible fluctuations is related to the phase coherence of Cooper pairs [32]: in this hypothesis pairing is still present above T_c, but phase fluctuations destroy their long range order, despite keeping some non-metallic macroscopic features.
Another discussed scenario proposes a spin (fermionic) - charge (bosonic) separation [55]: in this hypothesis the pseudogap is due to the "spin phase", whereas the system enters in the superconducting state when the charges undergo Bose-Einstein condensation at T_c. Notice that it is not necessary that a single type of fluctuations dominates the entire range of temperatures.

2.2.5 Superconducting Gap

Another fundamental difference between BCS and a unconventional superconductors is the strong anisotropy of the electronic properties of the latter. As a matter of fact, whereas conventional superconductors are characterized by an isotropic superconducting gap in the reciprocal space (*s-wave*), the cuprate gap shows a strong dependence of the gap on the **k** vector (*d-wave gap*) and in particular has a maximum value in the $\Gamma\mathrm{M}$ direction of the first Brillouin Zone (*antinode*) and it is zero in the $\Gamma\mathrm{X}$ direction (*node*). A sketch of a d-wave gap is plotted in Figure 2.8 c.

The main effect of the gap anisotropy is that the energy required for the creation of two quasiparticles from a Cooper pair depends on the direction of its momentum. In particular at the node single electronic states can be excited with negligible energy even at $T = 0\,\mathrm{K}$, resulting in long-living particle excitations. This feature of the electronic dispersion has implications on the electronic and thermodynamical properties of these systems, such as specific heat, thermal conductivity and transport [85], since in thermal equilibrium the population of quasiparticles is dominated by the low energy nodal contribution [36].

In order to study the sample (and especially the interaction of the antinodal quasiparticles at low temperatures), the creation of non-thermal populations by external

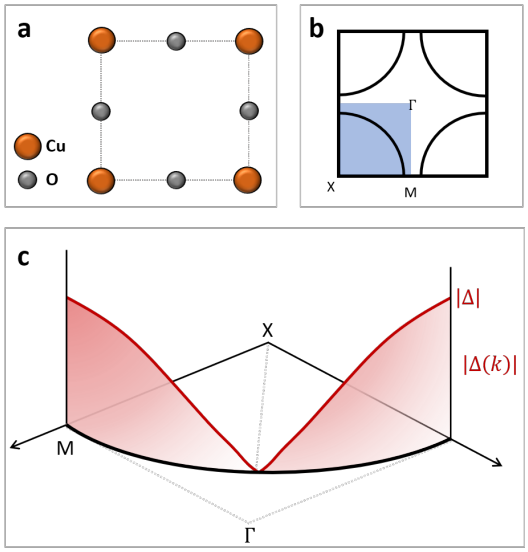

Fig. 2.8.: **d-wave gap**. **a** Copper-Oxygen layer of cuprates, from which the main superconducting properties derive. **b** scheme of the first Brillouin Zone ; the black curved lines represent the Fermi surface. **c** Sketch of the modulus of a d-wave gap (red line) in one fourth of the first Brillouin Zone, as highlighted by the blue area in **b**.

excitations can completely change the paradigm. In this respect time resolved techniques are ideal, since they are supposed to create a non-equilibrium density of quasiparticles and to measure the subsequent relaxation [39] (see Chapter 3).

The differences between the electronic dispersion of BCS and high temperature superconductors lead to the hypothesis that the pairing mechanism in the two classes of materials has a different origin. As already introduced, in standard superconductivity, pairing comes entirely from electron-phonon interactions, whose strength determines the critical temperature. On the contrary the origin of cuprate pairing is still unknown, despite many hypotheses of different electron-boson interactions (phonon [23, 54, 86] , spin [83, 2] or both) have been proposed. The large use of time resolved techniques on these materials is also justified by the possibility of disentangle the different interacting contributions through the study of their "return-to-equilibrium" after a system excitation (see section 3.2.1).

2.3 BSCCO

The Bismuth-Strontium-Calcium-Copper-Oxide family ($Bi_2Sr_2Ca_{m-1}Cu_mO_{2m+4+\delta}$), often abbreviated with BSCCO, contains some of the most studied cuprates superconductors. In the formula m represents the number of Copper-Oxygen planes in a unit cell (which is related to the critical temperature, as we already pointed out n section 2.2.1) and δ indicates the Oxygen concentration.

BSCCO can be synthesized in more than twenty phases, but only three of them show HTSC properties: they differ for the number of the Cu-O planes m and are indicated as

1. Bi2201 ($m = 1$ and $T_{c_{MAX}} = 20\,\mathrm{K}$);
2. Bi2212 ($m = 2$ and $T_{c_{MAX}} = 90\,\mathrm{K}$);
3. Bi2223 ($m = 3$ and $T_{c_{MAX}} = 110\,\mathrm{K}$).

Among them the most studied sample is Bi2212: its main quality is that it is an easily cleavable compound (in which the cleaving plane is parallel to the Cu-O layers) and therefore it facilitates experiments requiring very clean surfaces (such as photoelectron spectroscopy or STM). The wide literature on this system made it a benchmark for all subsequent measurements (e. g. optical time resolved spectroscopy).

Bi2212 has a perovskite-like crystal structure with dimensions $a = b = 5.4\,\text{Å}$ and $c = 30.6\,\text{Å}$ [17], where a and b are in the Cu-O plane and c is the perpendicular axis (see Figure 2.9).

Its phase diagram follows the main features of HTSC: the parent compound ($\delta = 0$) is an antiferromagnetic insulator, whereas for $\delta > 0$ it becomes a bad metal at room temperature. For $0.05 < \delta < 0.26$ the system undergoes a superconducting transition when cooled and the optimal doping is reached for $\delta_c = 0.16$. A pseudogap phase is detected in the underdoped and optimally doped region.
The T_c dependence on the doping for this sample can be found through the the following phenomenological relation [72]

$$T_c(\delta) = T_{c_{MAX}} \left[1 - 82.6\,(\delta - \delta_c)^2\right]. \tag{2.1}$$

In Bi2212 the maximum value of T_c can be modified by acting on the Sr or Ca disorder.

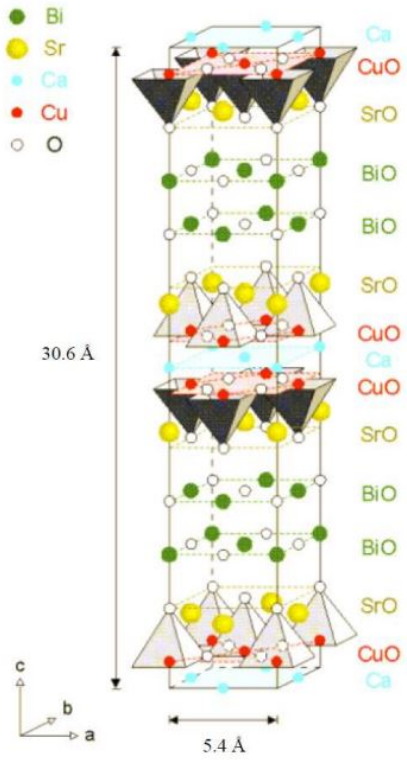

Fig. 2.9.: Bi2212 crystal structure. Unit cell of a Bi2212 crystal [18]

Good results have been obtained by substituting the Ca cation with *Yttrium*, creating the new compound $Bi_2Sr_2Y_xCa_{1-x}Cu_2O_{8+\delta}$. The maximum value $T_c(\delta_c) = 97\,\mathrm{K}$ is reached at $x = 0.08$. Moreover Yttrium substitution stabilizes the crystal structure, keeping electronic properties similar to the ones of the more known Bi2212 [18].

The measurements presented in the following chapters have been performed on an optimally doped Yttrium substituted Bi2212, which will be usually indicated as Y-Bi2212 or simply Bi2212.

3 Experimental techniques

In this chapter we introduce the experimental technique used in the study of our Y-Bi2212 sample and the reasons why it is particularly suitable for measurements on cuprates. The technique is called “pump-probe” and combines electronic Raman scattering to time-resolved spectroscopy; in the following we will consider the advantage of the two approaches and discusses how they can be combined.

Experimental techniques like ARPES or STM have been applied extensively to study correlated electronic systems [31]. Their contribution is related to single electron properties: for example, ARPES allows to measure the spectral function, a sort of “weight” to be applied to the Fermi distribution in order to switch from a free particle description to an interaction one. In particular, it takes into account both the interaction with the crystal lattice (which determines the band structure) and all other couplings of the system (electron-phonon, electron-electron Coulomb repulsion etc.). The net effect is a renormalization of the band structure due to the interactions and a finite lifetime of the particles.

The main disadvantage of single particle methods is that they do not give information on how the electrons may transport heat, current, energy etc. and on collective modes in general. To reach this aim one needs two particle correlation functions, which can be measured through optical and thermal conductivity, resistivity, nuclear magnetic resonance and electron-spin resonance [31]. These experiments have revealed basic properties of strongly correlated systems and characterized complex behaviors of high-T_c cuprates.

On the other hand two particle quantities are less sensitive to anisotropies, since they measure variables integrated in the reciprocal space. Electronic Raman spectroscopy is complementary to all these techniques, since it provides information about the electronic behavior in different regions of the Brillouin Zone, thanks to polarization selection rules [31].

Last but not least “equilibrium spectroscopies” (like ARPES, but also Raman scattering) can measure only overall sample responses, without discriminating the contributions of the different degrees of freedom of the sample (electrons, phonons, magnetization etc.), thus preventing a complete comprehension of the phenomena.

This limitation can be overcome through time resolved techniques, which in this thesis work have been combined with electronic Raman scattering.

In this chapter both the techniques will be presented, paying particular attention on the implications on cuprate samples, and finally the experimental set-up will be introduced.

3.1 Raman spectroscopy

Raman scattering is the elastic scattering of the electromagnetic radiation (photons) creating or annihilating an elementary excitation in the solid, like phonons, plasmons, excitons and spin fluctuations [94]. The scattered photons are detected and their frequency shifts, as well as polarization rotations, are analyzed in order to get information on the elementary excitation.

In general Raman spectroscopy is very advantageous for its experimental versatility and because it is a non-destructive experiment that allows to study even small samples under the effect of external parameters (like temperature, electric and magnetic fields, excitations energy and pressure).

This technique produces different effects depending on the band structure of the material: if the photon energy causes an electronic transition (this is the case of absorbing materials, for example) the elementary excitation is mediated by the electronic one (electronic Raman scattering); on the contrary if the electronic gap is too large, there is no electronic mediation and the elemental excitation is excited "directly" [31].

The electronic Raman scattering process can be described by the three steps shown in Figure 3.1:

1. The external electromagnetic field couples with the electronic system of the solid sample; the absorption of incident light gives rise to en electron-hole pair (virtual intermediate level).

2. The transition of the electron-hole pair to another state is responsible of an elementary excitation.

3. The final scattered photon is produced by the recombination of the electron-hole pair. Its energy and polarization are used to characterize the elemental excitation [12].

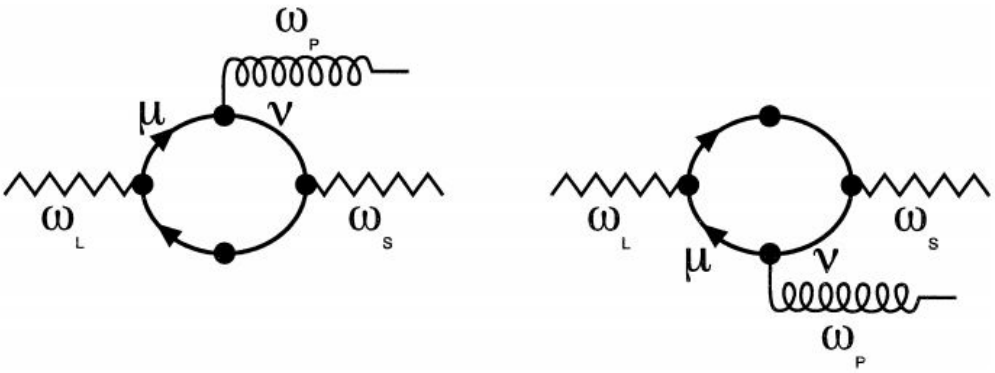

Fig. 3.1.: Description of the Raman process through Feynman diagrams. The initial photonic laser state, with frequency ω_L excites a virtual intermediate electronic state μ, which decays in a photon of energy $\hbar\omega_P$ and a second virtual electronic state ν. Finally the recombination of the electron-hole pair produces the scattered photon of frequency ω_S. The second diagram represents the hole phonon interaction [12].

In each step the interaction between the electrons and the photons or the phonons is fundamental and determines the effectiveness (or ineffectiveness) of the measurement. These couplings strictly depend on the material band structure (because of the electronic mediation) and on its atomic structure (which determines the allowed phonon modes). In the next subsections the contribution of these two material features is discussed.

3.1.1 Band structure contribution

The electronic contribution to the interaction between the photons and phonons, typical of the electronic Raman scattering, is strictly related to the material band structure. Although it is a specific characteristic of the sample, different classes of materials can be defined, which share the main electron band features.

In the following, three classes of materials are considered (metals, semiconductors/insulators and superconductors), in order to qualitatively discuss the expected results of a static Raman measurement. We will especially focus on the effects on superconductors, which are the subject of the first part of the thesis. Anyway the treatment of the other two classes will be useful in the second half of the work (and in particular in Chapter 7), where impulsive stimulated Raman scattering results on bismuth (metal) and quartz (semiconductor) will be shown.

Metals

In metals the Raman cross section is small because of two main reasons: it is a second order process (see section 3.1.2), intrinsically weaker than the dipole absorption, and in conductors the electromagnetic radiation penetrates only a few hundreds of

nanometers, making the interaction volume small [12].
In normal metals there are two kinds of electronic excitations: interband and intraband ones. Let us focus on the latter, since the former require higher photon energies.

In the *clean metal* approximation (which means in absence of surface effects, doping and impurities, phonons etc.)[1] low frequency excitations cannot be produced by optical techniques, because of their small transfer vector $\mathbf{k}$. In particular in the Stokes case, optical photons can provide a transfer energy and momentum

$$\begin{cases} E_T = E_L - E_S = \hbar c\,|\mathbf{k}_L| - \hbar c\,|\mathbf{k}_S| \\ \mathbf{k}_T = \mathbf{k}_L - \mathbf{k}_S \end{cases} \tag{3.1}$$

(where the label T stands for "transfer", L for "laser", and so refers to the incoming beam, and S for "scattered"), whereas an electronic transition in a metal in free electron approximation requires the following set of equations

$$\begin{cases} E_T = \frac{\hbar^2}{2m}\mathbf{k}_F^2 - \frac{\hbar^2}{2m}\mathbf{k}_I^2 \\ \mathbf{k}_T = \mathbf{k}_F - \mathbf{k}_I \end{cases} \tag{3.2}$$

(where I and F are the initial and final state respectively). The two equation systems cannot be simultaneously fulfilled for optical photons (see sketch of Figure 3.2a). In

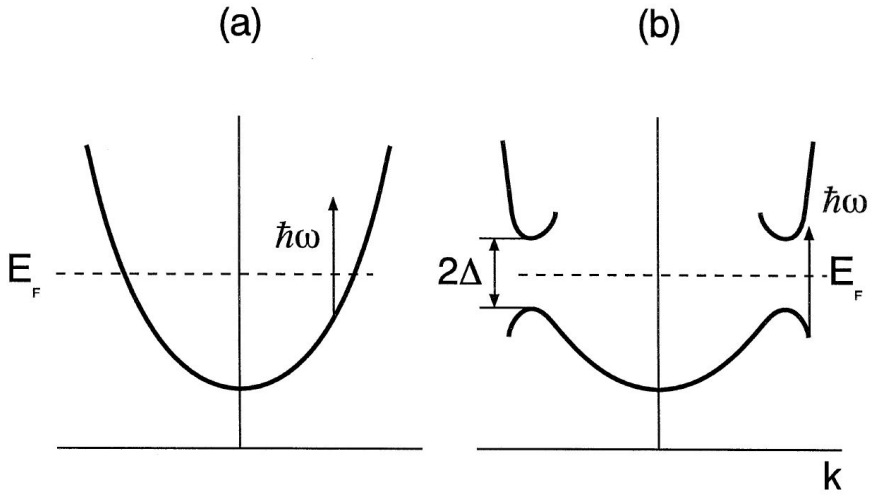

Fig. 3.2.: **Electronic dispersion and optical transitions. a** 1-D sketch of electronic dispersion of a clean metal (parabola) and of the optical transition (vertical arrow): the optical momentum is too small to fullfill the momentum conservation, so the transition is optically forbidden in the electric dipole approximation. E_F is the Fermi energy. **b** Corresponding dispersion for the superconducting state [12].

the *dirty limit* defects produce a shorter electron mean free path l, which results in a

[1] The clean limit can never be reached: even in the best cases, scattering by acoustic phonons and many body electron-electron interactions cannot be avoided.

smearing of the scattering $\mathbf{k}$ vector by an amount $\frac{1}{l}$. If l is sufficiently short Raman scattering can induce intraband electronic excitations [12].

Semiconductors and insulators

Semiconductors and insulators need high excitation energies to excite states across the gap: this kind of samples is more advisable to study "direct" phonon excitations since, if the photon energy is lower than the band gap, phonon modes can be excited without the electronic mediation (see as an example coherent phonons excited on quartz [80]). In this case the technique is called *Impulsive Stimulated Raman Scattering* and it is a third order process, caused by the broad content of the excitation pulse: the sample de-excitation is then studied by a probe pulse (see section 7.1). For this reason in semiconductors and insulators it is usually difficult to investigate the low energy electron dynamics.

On the contrary, a study of low energy electrons is recommended for systems where many-body interactions are essential: this is why electronic Raman scattering is considered a good technique for the investigation of low energy elementary excitations in high temperature superconductors and for their characterization [12].

Superconductors

In Raman measurements a key role is played by the coupling of elementary excitations to electron-hole pairs, which is also related to the phenomenon of high temperature superconductivity [12]. Moreover Raman scattering allows the measurements of the superconducting gap, thus giving information on the symmetry of the order parameter and on the coupling mechanism. In addition these measurements can characterize the sample with respect to the oxygen content (a different concentration can modify the Raman modes), the orientation, because of the sensibility to angle between the light polarization and crystallographic axes, and the different phases [94].

In conventional superconductors, excitations across the gap are Raman active: these transitions break Cooper pairs preserving the momentum (the two quasiparticles have momenta $\mathbf{k}$ and $-\mathbf{k}$), highlighting a clear peak at 2Δ (see Figure 3.3). As a matter of fact in BCS theory the electronic dispersion is $\Delta E_{\mathbf{k}} = 2\sqrt{|\Delta|^2 + \epsilon_{\mathbf{k}}}$ (see appendix A), so the minimum energy required to beak a Cooper pair is 2Δ. This excitation is feasible even at $\mathbf{k_P} \approx 0$, (with $\mathbf{k_P}$ the phonon wavevector), whereas it is not possible in the metallic phase, at least in the clean limit (Figure 3.2).

In cuprates the Raman spectrum is dominated by phonons which are superimposed to an energy independent continuum. Contrarily to BCS superconductors they have no clear onset at 2Δ. In Figure 3.4 the high temperature Raman spectrum of a

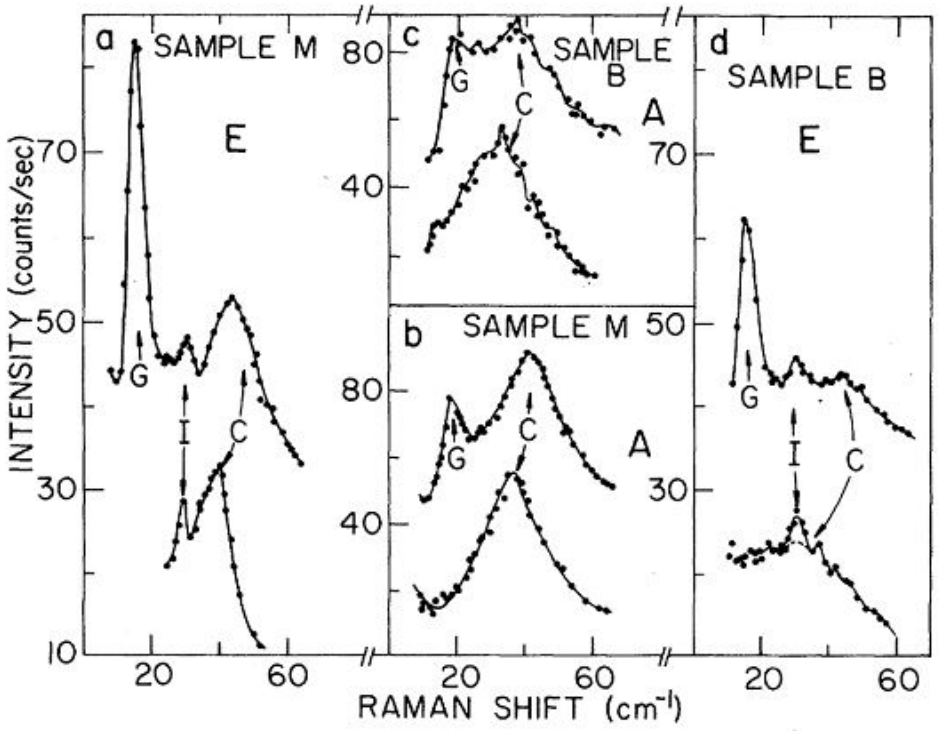

Fig. 3.3.: Raman measurements on BCS superconductors. Raman peaks on $2H-NbSe_2$: the peak at 2Δ, indicated with **G** is very strong in the superconducting state (the top ones in the graphs) and completely absent at higher temperatures. The energy shift of peak *C* between superconducting and metallic phase is always visible.[90].

$YBa_2Cu_3O_{7-\delta}$ is subtracted from the superconducting one (open circles) [12]. We notice a continuous increase of the signal until $2\Delta = 350\,\mathrm{cm}^{-1}$. The absence of a net step at 2Δ demonstrates the anisotropic character of cuprates gap: as a matter of fact, the nodes of the gap allow electronic transitions even for very low photon energies (that is for $h\omega < 2\Delta$).

In the approximation in which the lattice properties do not change significantly, the study of $\mathbf{k_P} = 0$ Raman scattering leads to the value of the superconducting gap and to the main characteristics of its symmetry. More in details, the presence of a superconducting gap determines the following effects on the Raman spectra [94]:

1. MODIFICATION OF THE PHONON LIFETIME: the phonon lifetime depends on the decay channels. For $T > T_c$ the only available decay channel is the normal state carriers, whereas in the superconducting state the interaction with Cooper pairs must also be taken in account. In particular:

   - if $\hbar\omega_{ph} > 2\Delta$ (where the label "ph" stands for "phonon"), the phonon can break Cooper pairs activating a second channel with respect to the metallic phase, so the phonon lifetime becomes shorter and the Raman

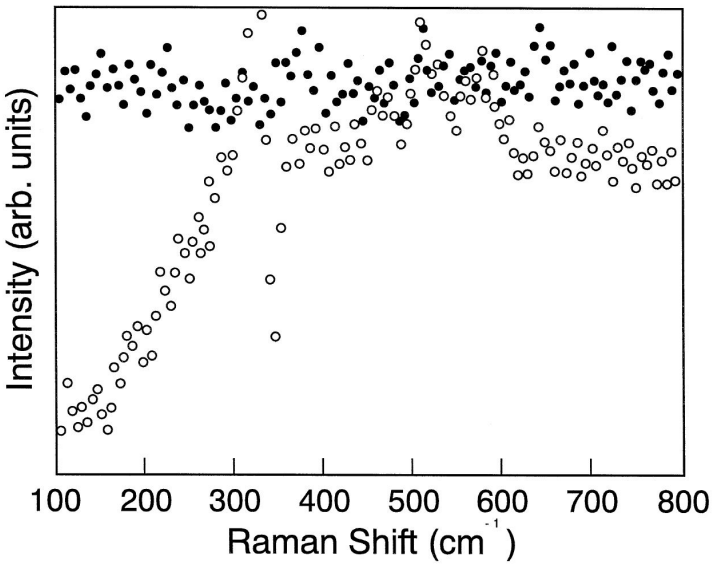

Fig. 3.4.: Raman measurements on High-T_c superconductors. Electronic Raman scattering of a $YBa_2Cu_3O_{7-\delta}$. for two temperatures: 4K (open circles) and 89 K (solid circles). In both measurement the spectrum at $T = 100\,\mathrm{K}$ has been subtracted is order to cancel the strongest phonon peaks and to highlight the gap one.[12].

peaks broaden ($\gamma_{ph}\tau_{ph} = C$, where γ_{ph} is the full width at half maximum of the Raman peak, τ_{ph} is the phonon lifetime and C is a constant.)

- if $\hbar\omega_{ph} < 2\Delta$ the phonon cannot break a Cooper pair, so the only decay channel is the normal state carriers: the peak sharpens with respect to the previous case.

2. ENERGY SHIFT: in perturbation theory at first order the energy shift is

$$\Delta E_n = \sum_m \frac{|\langle n|\, V\, |m\rangle|^2}{E_n - E_m}, \tag{3.3}$$

where n is the phononic state and m are the electronic ones. So, below T_c:

- if $\hbar\omega_{ph} = E_n > 2\Delta \Rightarrow \Delta E_n > 0$ and the phonon peaks shift up in energy.

- if $\hbar\omega_{ph} = E_n < 2\Delta \Rightarrow \Delta E_n < 0$, because the relevant terms of the sum are negative and the energy of the phonon peak decreases with respect to the metallic state. [94]

Both the effects are visible in Figure 3.3 for $\hbar\omega_{ph} > 2\Delta$.

3.1.2 Crystal structure contribution

The measurment of Figure 3.4 already introduced the concept of anisotropy of the superconducting gap in the first Brillouin Zone in cuprates, an interesting feature which distinguish them from standard superconductors. Anyway the presented measurement does not exhaust the possibilities provided by this technique, which allows to select different phonon modes by tuning the photon polarization directions. These selection rules are related to the crystal structure of the material.

In order to understand this relation, a systematic description of the process is needed. The approach is completely general and its application to cuprates is straightforward (it will be discussed in section 3.1.2).

Description of the process

The process of electronic Raman scattering can be modelled both in semi-classical and quantum framework: in the following a summary of the two treatments are provided. More details can be found in [31, 99].

Semi-classical treatment

The Raman scattering of phonons in solids is due to a linear coupling of the electromagnetic field with the electronic system of the target, whose crystal responds with a change of susceptibility (and consequently in the induced polarization). The semi-classical model is based on the assumption that the vibrational ionic motion is much slower that the electronic one (responsible for the susceptibility tensor $\chi(\omega)$ change): this allows to consider the lattice as static at each time, with instantaneous electron position determined by the lattice vibration.
The incoming electric field is

$$\mathbf{E}_L(\mathbf{r},t) = \mathbf{E}_L e^{i(\mathbf{k}_L\cdot\mathbf{r}-\omega_L t)} + c.c., \tag{3.4}$$

where $\mathbf{E}_L$ is the amplitude in the polarization direction, ω_L is the frequency and $\mathbf{k}$ the wavevector of the incident beam. The induced polarization can be expressed as

$$\mathbf{P}(\mathbf{r},t) = \epsilon_0 \chi(\mathbf{r},t)\,\mathbf{E}_L(\mathbf{r},t), \tag{3.5}$$

where ϵ_0 is the dielectric constant in vacuum.
Let us consider a small excitation of the generalized coordinate $\mathbf{Q}(\mathbf{r},t)$: the susceptibility can be expressed in Taylor series as

$$\chi(\mathbf{r},t) = \chi_0 + \sum_i \frac{\partial\chi(\mathbf{r},t)}{\partial Q_i(\mathbf{r},t)} Q_i(\mathbf{r},t)\cdot\hat{i} + ..., \tag{3.6}$$

where $Q_i(\mathbf{r},t)$ is the i^{th} component of the vector $\mathbf{Q}(\mathbf{r},t)$ and $\hat{i}$ is the unitary vector in the i^{th} direction. Putting the expansion of χ (up to the first order) in the polarization equation 3.5 and considering a lattice vibrational excitation with frequency ω $Q = Q_0 e^{-i\omega t} + c.c.$, one ends up with a term of order zero, which corresponds to elastic Rayleigh scattering, and the linear term

$$\mathbf{P^{(1)}}(\mathbf{r},\mathbf{t}) = \sum_i \left[\frac{\partial\chi(\mathbf{r},t)}{\partial Q_i(\mathbf{r},t)}\right] Q_{0i}\cdot\hat{i}\cdot\mathbf{E}_L\left(e^{i[(\mathbf{k}_L-\mathbf{k})\cdot\mathbf{r}-(\omega_L-\omega)t]} + e^{i[(\mathbf{k}_L+\mathbf{k})\cdot\mathbf{r}-(\omega_L+\omega)t]} + c.c.\right). \tag{3.7}$$

Notice that

- the frequency of the scattered photon can be $\omega_S = \omega_i - \omega$ (Stokes process) or $\omega_S = \omega_i + \omega$ (Antistokes process): in the former case an elementary excitation of energy $\hbar\omega$ is created, in the latter it is annihilated.

- the term $\sum_i \left[\frac{\partial\chi(\mathbf{r},t)}{\partial Q_i(\mathbf{r},t)}\right] Q_{0i}(\mathbf{r},t)\cdot\hat{i}$ is responsible for the polarization direction of the scattered electric field and its product with E_L determines the selection rules of the experiment. In the semi-classical approximation it is the so-called *Raman tensor*.

Quantum treatment
Let us consider an Hamiltonian for N electrons coupled to an electromagnetic field:

$$H = \sum_{i=1}^{N} \frac{\left[\hat{\mathbf{p}}_i + \frac{e}{c}\hat{\mathbf{A}}(\mathbf{r}_i)\right]^2}{2m} + H_C + H_F \tag{3.8}$$

where $\hat{\mathbf{p}} = -i\hbar\nabla$, e is the absolute value of the elementary charge, m is the electron mass, c is the speed of light and $\hat{\mathbf{A}}$ is the electromagnetic vector potential, which in its second quantization form can be expanded in the Fourier modes as

$$\hat{\mathbf{A}}(\mathbf{r}_i) = \sum_{\mathbf{q}} e^{i\mathbf{q}\cdot\mathbf{r}_i}\sqrt{\frac{hc^2}{\omega_{\mathbf{q}}V}}\left[\hat{e}_{\mathbf{q}}\hat{a}_{-\mathbf{q}} + \hat{e}^*_{\mathbf{q}}\hat{a}^\dagger_{-\mathbf{q}}\right], \tag{3.9}$$

with V the volume, $\hat{a}_{\mathbf{q}}$ the annihilation operator of transverse photons with $E = \hbar\omega_{\mathbf{q}}$ and $\hat{e}_{\mathbf{q}}$ the polarization unit vector. H_C represents the Coulomb interaction and H_F the free electromagnetic part.

We can rewrite the Hamiltonian as

$$H = H' + \underbrace{\frac{e}{2mc}\sum_i \left[\hat{\mathbf{p}}_i \cdot \hat{\mathbf{A}}\left(\mathbf{r}_i\right) + \hat{\mathbf{A}}\left(\mathbf{r}_i\right) \cdot \hat{\mathbf{p}}_i\right] + \frac{e^2}{2mc^2}\sum_i \hat{\mathbf{A}}\left(\mathbf{r}_i\right)\hat{\mathbf{A}}\left(\mathbf{r}_i\right)}_{M}, \tag{3.10}$$

where $H' = \frac{1}{2m}\sum_i \hat{\mathbf{p}}^2 + H_C + H_F$.

The electronic Raman scattering measures the total cross section for scattering from all the electrons illuminated by the incident light, which is determined by the probability that an incident photon with frequency ω_I is scattered into a solid angle interval between Γ and $\Gamma + \delta\Gamma$ with a frequency between ω_S and $\omega_S + \delta\omega_S$. This probability can be evaluated using time dependent perturbation theory to the second order, so

$$\frac{\partial^2\sigma}{\partial\Gamma\partial\omega_S} \propto \frac{1}{Z}\sum_{I,F} e^{-\frac{E_I}{k_B T}} M_{FI} \cdot \delta\left(E_F - E_I - \hbar\Omega\right). \tag{3.11}$$

Here k_B is the Boltzmann coefficient, $Z = \sum_j e^{-\frac{E_j}{k_B T}}$ is the partition function ($\frac{1}{Z}e^{-\frac{E_j}{k_B T}}$ is the probability that the system occupies the microstate j), I and F represent the initial and final state respectively, $\Omega = \omega_S - \omega_I$ and M_{FI} is the time dependent perturbation theory matrix element up to the second order[2]. A key role in this expression is attributed to the Dirac delta, which ensures the energy conservation, and to the matrix element M_{FI}, which is responsible for the polarization selection rules.

Using second quantization for electronic states[3] and the long wavelength approximation ($\mathbf{k}\cdot\mathbf{r} << 1$ and so $e^{i\mathbf{k}\cdot\mathbf{r}} \approx 1$) one gets

$$\begin{aligned} M_{FI} =& \hat{e}_I \cdot \hat{e}_S \sum_{ab} \rho_{ab}(\mathbf{q}) \left\langle F \left| c_a^\dagger c_b \right| I \right\rangle + \\ &+ \frac{1}{m}\sum_\nu \sum_{\substack{a_1,b_1\\a_2,b_2}} \left\langle a_2 \left| \sum_j \hat{\mathbf{p}}\cdot\hat{e}_S \right| b_2 \right\rangle \left\langle a_1 \left| \sum_j \hat{\mathbf{p}}\cdot\hat{e}_I \right| b_1 \right\rangle \cdot \\ &\cdot \left(\frac{\left\langle F \left| a_2^\dagger b_2 \right| \nu \right\rangle \left\langle \nu \left| a_1^\dagger b_1 \right| I \right\rangle}{E_I + \hbar\omega_I - E_\nu} + \frac{\left\langle F \left| a_1^\dagger b_1 \right| \nu \right\rangle \left\langle \nu \left| a_2^\dagger b_2 \right| I \right\rangle}{E_I + \hbar\omega_S - E_\nu} \right). \end{aligned} \tag{3.12}$$

The first term of equation 3.12 comes from the $\mathbf{A}^2$ term of the Hamiltonian and refers to a non resonant Raman scattering where the photon energy is transferred to

[2] The matrix elements up to the second order are $V_{FI}^{(1)} = |\langle F|V|I\rangle|^2$ and $V_{FI}^{(2)} = \left|\sum_{K\neq I}\left[\frac{\langle I|V|K\rangle\langle K|V|F\rangle}{E_K - E_I - \hbar\omega_I}\right]\right|^2$

[3] In the second quantization treatment we can rewrite the exponential as $\sum_i e^{i\mathbf{q}\mathbf{r}} = \sum_{ab}\rho_{ab}(\mathbf{q})c_a^\dagger c_b$, where $\rho_{ab}(\mathbf{q}) = \sum_i \left\langle a \left| e^{i\mathbf{q}\cdot\mathbf{r}} \right| b \right\rangle$ and $c_a^\dagger$ and c_b are the creation and annihilation operators for the H_0 electronic eigenstates $|a\rangle$ and $|b\rangle$.

an electron-hole pair and than re-emitted with a scattered photon. The remaining contributions are derived from second order time dependent perturbation theory of $\hat{\mathbf{p}} \cdot \mathbf{A}$: a virtual intermediate state $|\nu\rangle$ is created from the absorption of the incident photon, which finally decays to the final state with the emission of a second photon: since resonances occurs when the incident photon energy matches the difference between the initial state and the intermediate state resonance Raman scattering provides information on the electronic structure of the system.

One of the advantages of Raman scattering is that selection rules can be easily derived from the Raman tensor R:

$$M_{FI} = \langle F | R | I \rangle , \tag{3.13}$$

where the matrix elements $R_{\mu\nu}$ is expressed as a function of the polarization of the incident μ and scattered ν beam. The Raman tensor can be decomposed in the basis of the irreducible representation of the symmetry group of the crystal as

$$R = \sum_n a_n R_{\Gamma_n}, \tag{3.14}$$

where Γ_n is a representation of the symmetry group [99]. The Mulliken symbols, that is, the symbols used to identify the irreducible representation of symmetry groups, are listed in Appendix B.

Selection rules for cuprates

The symmetry of the crystal is fundamental to determine the vibrational modes allowed in particular scattering configurations, as shown in Eq. 3.14.
Most cuprates can be described by a D_{4h} tetragonal point group and have inversion centers, so vibrations can be classified as even or odd (if the wavevector does or does not change sign upon inversion). Odd vibration ("u", *ungerade*) are infrared (IR) active modes, while even ("g", *gerade*) are Raman modes [94] (the complete character table for D_{4h} is reported in appendix B). So, for parity reasons, the only Raman active modes of the group are A_{1g}, A_{2g}, B_{1g}, B_{2g} and E_g.

From Eq. 3.14 we can decompose the Raman tensor as

$$\begin{aligned} R = \frac{1}{2}\Big[& O^{(1)}_{A1g}\,(e^x_I \cdot e^x_S + e^y_I \cdot e^y_S) \\ & + O^{(2)}_{A1g}\,(e^z_I \cdot e^z_S) \\ & + O_{B1g}\,(e^x_I \cdot e^x_S - e^y_I \cdot e^y_S) \\ & + O_{B2g}\,(e^x_I \cdot e^y_S + e^y_I \cdot e^x_S) \\ & + O_{A2g}\,(e^x_I \cdot e^y_S - e^y_I \cdot e^x_S) \\ & + O^{(1)}_{Eg}\,(e^x_I \cdot e^z_S + e^z_I \cdot e^x_S) \\ & + O^{(2)}_{Eg}\,(e^y_I \cdot e^z_S + e^z_I \cdot e^y_S)\Big], \end{aligned} \tag{3.15}$$

where O_j are the projection on the different configurations, while e^X_Y are the polarization vectors, where X represents the direction with respect to the Cu-O crystal axis (z is perpendicular to the Cu-O plane)[4] and $Y = I, S$ indicate the incoming and scattered beam. Finally the polarization product $J \cdot K$ (where J and K are two polarization unit vectors) is defined as

$$J \cdot K = \begin{bmatrix} J^{(1)} \\ J^{(2)} \\ J^{(3)} \end{bmatrix} \begin{bmatrix} K^{(1)} & K^{(2)} & K^{(3)} \end{bmatrix} = \begin{bmatrix} J^{(1)}K^{(1)} & J^{(1)}K^{(2)} & J^{(1)}K^{(3)} \\ J^{(2)}K^{(1)} & J^{(2)}K^{(2)} & J^{(2)}K^{(3)} \\ J^{(3)}K^{(1)} & J^{(3)}K^{(2)} & J^{(3)}K^{(3)}. \end{bmatrix} \tag{3.16}$$

So, for example, the B_{1g} contribution to the Raman tensor is

$$\begin{aligned} R_{B1g} =& \frac{1}{2} O_{B1g} \left\{ \begin{bmatrix} 1 \\ 0 \\ 0 \end{bmatrix} \begin{bmatrix} 1 & 0 & 0 \end{bmatrix} - \begin{bmatrix} 0 \\ 1 \\ 0 \end{bmatrix} \begin{bmatrix} 0 & 1 & 0 \end{bmatrix} \right\} \\ =& \frac{1}{2} O_{B1g} \left\{ \begin{bmatrix} 1 & 0 & 0 \\ 0 & 0 & 0 \\ 0 & 0 & 0 \end{bmatrix} - \begin{bmatrix} 0 & 0 & 0 \\ 0 & 1 & 0 \\ 0 & 0 & 0 \end{bmatrix} \right\} \\ =& \frac{1}{2} O_{B1g} \begin{bmatrix} 1 & 0 & 0 \\ 0 & -1 & 0 \\ 0 & 0 & 0 \end{bmatrix}. \end{aligned} \tag{3.17}$$

The polarization vectors define the polarization selection rules needed to measure a defined mode. For example the B_{1g} signal can be selected with an incoming field polarized along x or y and selecting after the same polarization. On the other hand the same configuration would select also the A_{1g} mode. The following table [31] summarizes all the selection rules for the D_{4h} group.

[4] A sketch of the crystal structure is plotted in Figure 2.9, whereas the Cu-O layer is displayed in Figure 2.8 **a**.

e_I	e_S	R
$\hat{x}, \hat{y}$	$\hat{x}, \hat{y}$	$R_{A1g^{(1)}} + R_{B1g}$
$\frac{1}{\sqrt{2}}(\hat{x}+\hat{y})$	$\frac{1}{\sqrt{2}}(\hat{x}+\hat{y})$	$R_{A1g^{(1)}} + R_{B1g}$
$\frac{1}{\sqrt{2}}(\hat{x}+\hat{y})$	$\frac{1}{\sqrt{2}}(\hat{x}-\hat{y})$	$R_{B1g} + R_{A2g}$
$\hat{x}$	$\hat{y}$	$R_{B2g} + R_{A2g}$
$\frac{1}{\sqrt{2}}(\hat{x}+i\hat{y})$	$\frac{1}{\sqrt{2}}(\hat{x}+i\hat{y})$	$R_{B1g} + R_{B2g}$
$\frac{1}{\sqrt{2}}(\hat{x}+i\hat{y})$	$\frac{1}{\sqrt{2}}(\hat{x}-i\hat{y})$	$R_{A1g^{(1)}} + R_{A2g}$
$\hat{x}$	$\hat{z}$	R_{E1g}
$\hat{y}$	$\hat{z}$	R_{E1g}
$\hat{z}$	$\hat{z}$	$R_{A1g^{(2)}}$

In our experimental configuration, with the incoming beam propagating along the $\hat{z}$ axis, (perpendicular to the Cu-O plane), the A_{2g} mode does not contribute [97] and the Raman tensor is reduced to the 2 x 2 matrix

$$\begin{aligned} R_{B_{2212}} =& \frac{1}{2}\left\{ O_{A1g}\begin{bmatrix}1 & 0\\ 0 & 1\end{bmatrix} + O_{B1g}\begin{bmatrix}1 & 0\\ 0 & -1\end{bmatrix} + O_{B2g}\begin{bmatrix}0 & 1\\ 1 & 0\end{bmatrix}\right\} \\ =& \frac{1}{2}\begin{bmatrix} O_{A1g}+O_{B1g} & O_{B2g} \\ O_{B2g} & O_{A1g}-O_{B1g}\end{bmatrix}. \end{aligned} \tag{3.18}$$

It is easy to note that in this experimental configuration the B_{2g} symmetry can be obtained with incident and scattered beam polarized along the two orthogonal Cu-O axis. The B_{1g} mode can be measured through a beam polarized along the Cu-Cu direction and selecting the orthogonal polarization: to prove it , it is sufficient to select the polarization beams as follows:

$$\begin{aligned} \langle e_I | R_{B_{2212}} | e_S \rangle =& \frac{1}{2}\begin{bmatrix}1 & 1\end{bmatrix}\begin{bmatrix} O_{A1g}+O_{B1g} & O_{B2g} \\ O_{B2g} & O_{A1g}-O_{B1g}\end{bmatrix}\begin{bmatrix}1\\ -1\end{bmatrix} \\ =& \frac{1}{2}\left(O_{A1g}+O_{B1g}-O_{B2g}+O_{B2g}-O_{A1g}+O_{B1g}\right) \\ =& O_{B1g}. \end{aligned} \tag{3.19}$$

On the other hand the A_g mode cannot be completely separated from the other symmetries. Further details on Raman modes selection rules are given in section 5.4

3.2 Time resolved spectroscopy

Although the so-called “static measurements” are actually perturbative of the sample equilibrium state, both the weakness of the stimuli and their relatively long application time (with respect to the system degrees of freedom) allow to study a steady regime, which may or may not correspond to the real ground state, that can be treated with standard statistical approaches. The advent of ultrafast laser sources changes the perspective completely: in this case the perturbation should not be avoided, but it becomes a fundamental ingredient of the measurements, whose effect can be studied in time through ultrashort light pulses (hundreds of femtoseconds or less) [39].

In complex systems all the degrees of freedom are strictly intertwined and equilibrium measurements are not able to distinguish their inner properties. On the contrary time resolved measurements can discriminate between the contributions of the different interactions to the total de-excitation process of a previously perturbed sample. A key role is played by the duration of the excitation and of the sampling, which must be faster than the energy exchange between the electronic, vibrational, magnetic etc. degrees of freedom of the system.

High critical temperature superconductors (HTSC) belong to the wide class of strongly correlated materials and in the last decades their unusual and intriguing properties have been tested through time resolved experiments, both in the low perturbation limit, to study the quasiparticle relaxation, and in the strong one, to analyze the order parameter dynamics and eventually the photo-induced phase transitions [50].

3.2.1 Pump-probe experiments

Pump probe spectroscopy is a time resolved technique, in which the sample is excited by a relatively intense ultrashort light pulse called *pump*, which produces an (electronic) Raman excitation, and the de-excitation process is explored by a second weak, but still ultrashort, light pulse called *probe*. The probe is transmitted or reflected by the sample, in order to measure the optical properties of the system at a definite time delay after the excitation; a tunable probe optical path allows to scan a wide interval of time delays, leading to the measurement of the whole de-excitation dynamics. A sketch of the typical set-up is shown in Figure 3.5. For sake of simplicity, form now on we will consider only a reflective configuration, as the one shown in the sketch of Figure 3.5 **a**.

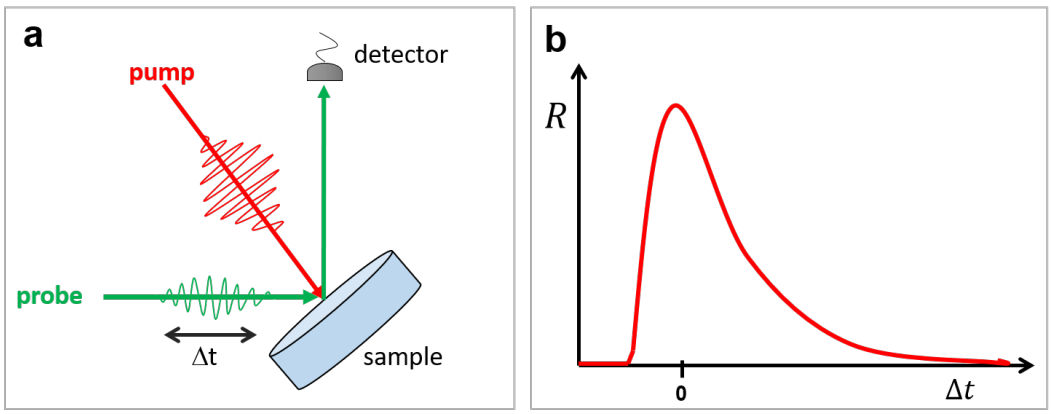

Fig. 3.5.: Sketch of a pump-probe experiment. **a** The pump pulse excites the sample at time $t = 0$ and, after a time delay Δt, the probe pulse is reflected by the sample. Finally the reflected probe intensity is measured by a photodiode. **b** Measurement result: the transient reflectivity of the sample during its de-excitation is plotted as a function of the time delay Δt between the pump and the probe, which can be tuned changing the probe light path, for example through a micrometer translation stage.

The measured quantity is the transient reflectivity, i.e.

$$\frac{\Delta R(\Delta t)}{R} = \frac{R_{EX}(\Delta t) - R_{EQ}}{R_{EQ}}, \tag{3.20}$$

where $R_{EX}(\Delta t)$ and R_{EQ} are the pumped and equilibrium reflectivity respectively. $R_{EX}(\Delta t)$ contains all the contributions to the de-excitation, which can differ for "starting" time delay, lifetime and intensity: these differences allow to separate and study the decay channels, in order to get information on the internal correlations of the sample.

In general the signal $\frac{\Delta R(\Delta t)}{R}$ is characterized by a magnitude, a sign and a decay time: all these features are fingerprints of the sample phase. For example, a parameter like temperature affects most of the sample degrees of freedom (electrons, crystal structure...), which are responsible of the sample de-excitation, so, different temperatures correspond to different signals. The same argument can be valid for pressure, doping and so on [18]. This feature is particularly interesting across phase transition, as we will see in Chapter 5. Moreover, set-up parameters like the pump wavelength and fluence or the probe wavelength can modify the signal, leading to a complete characterization of the sample phase dynamics.

Time resolved measurements can be performed in two different regimes, as a function of the pump intensity:

1. QUASI-EQUILIBRIUM: the system is weakly perturbed and the matter is driven into an excited state which eventually relaxes toward the equilibrium ground

state. The process is driven by electronic, vibrational and magnetic excitations and de-excitations. We refer to the interval of pump fluences used in this kind of experiments as *linear regime*, since the transient reflectivity is linear in the pump intensity. The results of a quasi-equilibrium experiment are shown in Figure 3.6, where a typical transient reflectivity is plotted and the different de-excitation contributions are highlighted.

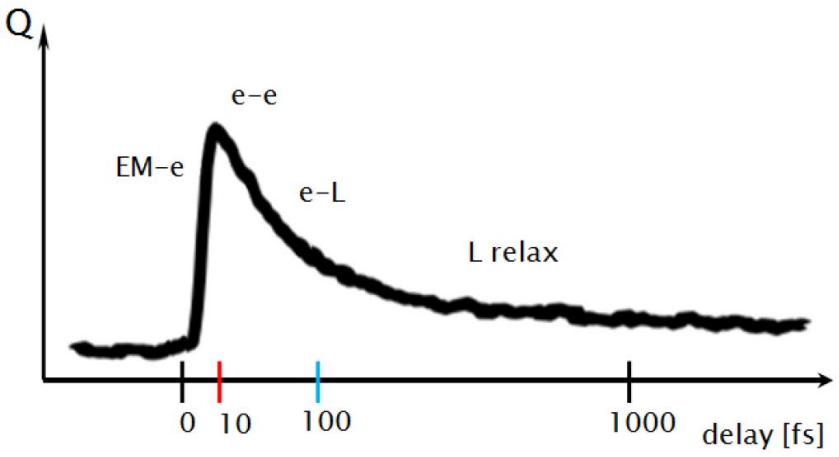

Fig. 3.6.: Transient reflectivity in a quasi-equilibrium measurement in a strongly correlated system. Several contributions to the dynamics are highlighted, such as the interaction of the electromagnetic field with the electronic system (EM-e), the electronic interaction (e-e), electron-lattice one (e-L) and the final lattice relaxation (L_{relax}) [66].

2. NON-EQUILIBRIUM: high pump fluences belonging to the non-linear regime, that is where the sample response is completely non-linear in the pump fluence, can produce metastable states which are not accessible through thermodynamics [66]. These dynamical phase transitions can have two different origins: either the pump destroys the equilibrium order (for example it can melt a charge density wave order parameter [84, 101, 43, 78] or break the superconducting pairing [28, 40, 87]) or it can dynamically induce a long range order (for light induced superconductivity see [34, 62, 64]).

3.2.2 Time resolved spectroscopy on Cuprates

The unexpected and still unexplained main properties of cuprate HTSC, such as their rich phase diagram and especially the presence of the pseudogap, are correlated to the inherent strong short-range electronic interactions between two elecrtons occupying the same Cu-3d orbital. For this reason time resolved techniques have been widely used to study these materials and to complete the information derived from equilibrium measurements.

Since in strongly correlated materials the low and high-energy scales are intrinsically entangled [38], high photon energy excitations of the system (in the optical range, for example) can produce variations of the low energy response (e.g. with a THz probe [46, 4]). Conversely it is possible to excite a mid-infrared perturbation and probe the reflectivity dynamics with optical pulses. It is known [97, 61] that the optical properties of the sample change as the phase of matter changes. In particular in the superconducting phase an optical pump $h\nu > 2\Delta$ (where Δ is the superconducting gap) perturbation consists in the breakdown of Cooper pairs (of whatever $\mathbf{k}$-vector) in two electrons, which are brought in a non-equilibrium high energy state. In this case the probe detects the recombination of photoexcited carriers into a superconducting state [89]. But then, what happens if the pump photon energy decreases below the gap amplitude? In the de-excitation process still detectable by a high energy probe? We tried to add some clues in this respect with the experiment described in chapter 5, where two pump photon energies ($h\nu > 2\Delta$ and $h\nu \approx 2\Delta$) have been used in order to study the superconducting-pseudogap phase transition.

In order to describe the correspondence between the phase of the sample and the pump-probe transient response. I will here briefly present the typical results and expectations of the main processes for the superconducting ($T < T_c$) and metallic ($T > T^*$) response at fixed doping. If not indicated explicitly, we will always consider the quasi-equilibrium regime.

$\mathbf{T < T_c}$: Rothwarf-Taylor model

The pump-probe response of a conventional superconducting sample was firstly described by A. Rothwarf and B. N. Taylor in 1967 [79] with a phenomenological model, which describes the superconducting recovery in a BCS system. The main assumptions of the model are
i. the presence of the superconducting gap Δ below the critical temperature
ii. the relevance of the quasiparticle-phonon interaction.
The process can be divided in three steps:

1. The pump pulse breaks some Cooper pairs, creating quasiparticles at higher energies.

2. The quasiparticles tend to recombine loosing an amount of energy 2Δ (binding energy of the Cooper pair) through a phononic excitation.

3. The phonon energy (2Δ) is large enough to break another Cooper pair into two particles and so on.

The phonon lifetime determines the superconducting recovery dynamics: for instance a slow decay of the phonons means a higher probability of breaking Cooper pairs. This slowdown of the dynamics can reach a limiting behavior due to the equilibium between phonon and quasiparticle creation, which is called *bottleneck*. The process is shown in Figure 3.7.

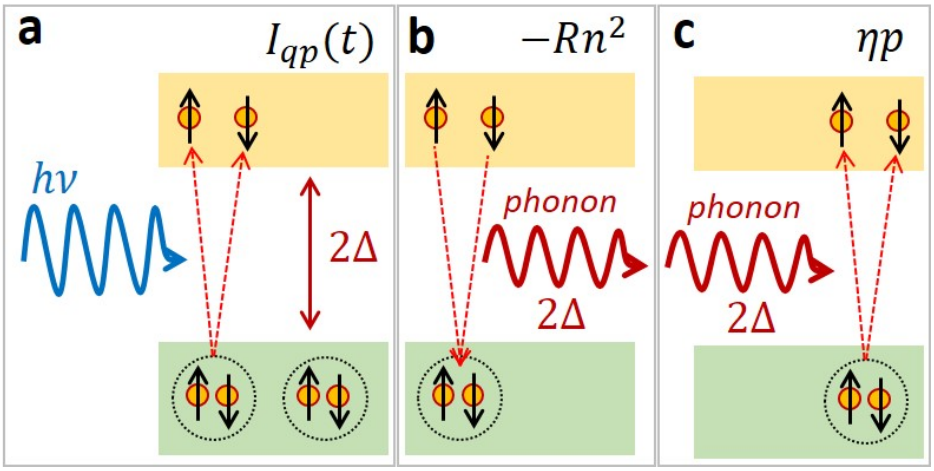

Fig. 3.7.: Process of time resolved measurements at $\mathrm{T} < \mathrm{T_c}$**. a** creation of two quasiparticles due to the interaction with the pump pulse. **b** quasiparticle recombination in a Cooper pair, with the emission of a photon of energy 2Δ. **c** the phonon excite another Cooper pair.

The process can be described by the following system of coupled equations:

$$\begin{cases} \frac{dn}{dt} = I_{qp}(T) + \eta p - Rn^2 \\ \frac{dp}{dt} = I_p(T) - \eta\frac{p}{2} + \frac{Rn^2}{2} - \gamma\left(p - p_T\right), \end{cases} \tag{3.21}$$

where n and p represent the quasiparticle and phonon total number respectively. The phonon has always energy $h\nu \geq 2\Delta$.
$I_{qp}(T)$ and $I_p(T)$ are the external sources of quasiparticles and phonons respectively; $I_p(T)$ can usually be neglected, because the main effect of the pump is not the injection of phonons but the Cooper pair breaking, whereas $I_{qp}(T)$ has the profile of the pump pulse.
Rn is the rate of recombination of quasiarticle (and so of production of high energy phonons), whereas η is the transition probability for pair breaking due to phonon absorption.

In the second equation γ is the rate at which the phonons decay by a process other than pair excitation (for example anharmonic decay to an energy smaller that 2Δ or diffusion of phonons into the thermal bath) and p_T is the number of phonons in

thermal equilibrium at a temperature T. The factor $\frac{1}{2}$ is due to the production of two quasiparticle from a single phonon and vice versa. To sum up, the first equation of the system 3.21 means that the number of quasiparticles is increased by the pump excitation and from the destruction of Cooper pairs, due to phononic excitations, and it is limited by the recombination process. The second equation points out that the phonon number dynamics is enhanced by the recombination process $\frac{Rn^2}{2}$ (and eventually by the less probable direct excitation of phonons due to the pump $I_P(T)$), whereas it is decreased by Cooper pair breaking ($\frac{\eta p}{2}$) and by the anharmonic thermal decay $\gamma(p - p_T)$.

The dynamics of the superconducting recombination is determined by the parameter R, η, γ.
A particularly interesting limiting case is $\gamma << \eta$, that represents the condition for which the most likely decay channel for a high energy phonon is the creation of two quasiparticles (rather than thermalization). In the $I_P \approx 0$ approximation, the phonon population increases ($\frac{dp}{dt} > 0$) as far as $\eta p = Rn^2$, that is when the rate of recombination equals the quasiparticle creation one. When the condition $\gamma << \eta$ is fulfilled, the two populations are strongly coupled and their dynamics is characterized by the common parameter γ, which is small by hypothesis. This is the already mentioned *bottleneck* limit. Notice that no bottleneck regime can be reached for $\gamma >> \eta$).

$\mathbf{T \to T_c}$: limit of the Rothwarf-Taylor model

Although the Rothwarf-Taylor model has been developed for BCS superconductors, it has been applied also for the qualitative description of HTSC dynamics, even if in the latter case the de-excitation process could be driven by different interactions and the presence of a bottleneck regime is still not proved.
Approaching the critical temperature the superconducting gap decreases, allowing an increasing number of phonons to break Cooper pairs. In terms of the equations 3.21, this means an enhancement of the rates η and Rn with respect to γ: a quasi-equilibrium between quasiparticles and phonons establishes, which slows down the recombination dynamics. This phenomenon produces an increase of the decay time, which is easily recognizable in HTSC time resolved measurements across T_c.

Low Temperature non-equilibrium measurements
At higher pump fluences we enter the so called non linear regime, in which dynamical phase transitions can be excited (see section 3.2.1).
Let us consider an intense pump excitation in the superconducting phase: in this case the long range order can be perturbed by the pump pulse, provoking a dynamical

destruction of the macroscopic phase coherence of the superconducting phase [9]. In the sample we measured (Y-Bi2212) this phenomenon causes a fast response immediately after the excitation, followed by relatively slow dynamics (with respect to the quasi-equilibrium one) [74].
In the work of I. Madan et al. [61] the possibility of destroying the superconducting phase is used to study the pairing above T_c: a three pulse experiment[5] allows to separate the superconducting contribution from the pseudogap one, assuming the presence of superconducting properties (like pairing) even above the critical temperature.

$\mathbf{T > T^*}$

For high temperature no gap characterizes the metallic phase, so there is no particular requirement on photon and phonon energies. However the system is still strongly correlated and a single decay channel is not sufficient to describe its de-excitation [25].
This aspect is visible in room temperature time resolved measurements, in which a unique exponential decay cannot fit the experimental data [74]. In order to find a better fitting function, it is useful to consider two exponentials (representing two decay channels of the primary excitation), convoluted with a gaussian, which takes into account the pump and probe pulse duration.

The final function is

$$f(t) = \sum_{i=1,2} \left(\sigma_i \sqrt{\frac{\pi}{2}} e^{-\frac{\sigma_i^2}{2\tau_i^2}} e^{-\frac{t}{\tau_i}} \left[\mathrm{erf}\left(\frac{t}{\sqrt{2}\sigma_i} - \frac{\sigma_i}{\sqrt{2}\tau_i} \right) + 1 \right] \right), \tag{3.22}$$

where τ_i is the life time of the i^{th} decay channel, $\mathrm{erf}(x)$ is the error function (that is the derivative of a gaussian function), and σ is the pulse length.

An analysis of the time resolved response to different excitation energies showed that the longest decay time (τ_2) is independent of the photon frequency, whereas the shortest one (τ_1) decreases if the photon energy increases [74]. This is probably due to the fact that the primary excitation does not have enough energy to relax emitting quasiparticles.

[5] In the experiment they propose, the first pulse melts the superconducting phase, the others are used like in a standard pump-probe measurement

3.3 Measurements

To sum up, time resolved electronic Raman scattering is a good technique to study correlated systems and cuprates in particular. It combines the anisotropy k-resolved measurements provided by the electronic Raman scattering (just by changing the polarization of the impinging electromagnetic fields and selecting the output one) with the discrimination of the different contributions to the total de-excitation process offered by pump-probe measurements. An additional contribution is given by the possibility of tuning the pump wavelength.

Set-up

Our experiment consists of a mid-infrared pump-optical probe temperature resolved spectroscopy on Y-Bi2212. A sketch of the set-up is shown in Figure 3.8.

The **Laser system** is made up of a Non-Collinear Parametric Amplifier (*Orpheus-N* by *Light Conversion*) and a Twin Optical Parametric Amplifier (*Orpheus TWIN* by *Light Conversion*), both pumped on the *Light Conversion Pharos Laser*, producing 400 μJ pulses with 1.2 eV photon energy at 50 KHz repetition rate.
The optical probe (generated by the NOPA system) is a ~ 25 fs wavelength pulse, tunable in the visible and near-infrared (from about 1.27 to 2 eV). The carrier envelope phase stable mid-infrared pump pulses are produced by Difference Frequency Generation (DFG), mixing the signal outputs of the twin OPA seeded with the same white light. The final range of pump photon energies varies from 70 to 300 meV.

As shown in Figure 3.8, the mid-infrared pulses are sent to the sample (the focal spot has about $150\,\mu\mathrm{m}$ diameter). The NOPA beam is divided in two by a beam splitter, in order to have a reference to minimize the external noise contribution, while the other branch is reflected by the sample and collected by a differential detector. The measured output is the intensity difference between the reference and the probe reflected by the excited sample.

In most of the measurements, data have been amplified by a **Lock-in system**, but in some of them the signal has been digitized by a **fast digitizer** (*Spectrum M214964-exp*, see appendix C.1). In both cases the pump beam have been chopped, but whereas in lock-in measurement the chopping frequency was an input parameter of the amplification system, which can extract the desired data even from very noisy signals, in the second case it was used directly to compare pumped and non-pumped measurements: the subtraction between the two pulses improved the signal, reducing significantly the acquisition time.

A closed cycle cryostat (DE 204 by *Advanced research systems*) allows to cool the sample up to about 12 K (well below the critical temperature for our sample), avoiding vibrations, which could strongly affect our measurements, especially in the fluctuation case (see chapters 7 and 8).

The **sample** is a large and high-quality optimally doped Y-substituted Bi2212 single crystals ($Bi_2Sr_2Y_{0.08}Ca_{0.92}Cu_2O_{8+\delta}$), grown in an image furnace by the traveling-solvent floating-zone technique with a non-zero Yttrium content. The critical temperature is $T_c = 97$ K and the transition temperature is $T^* \sim 135$ K.

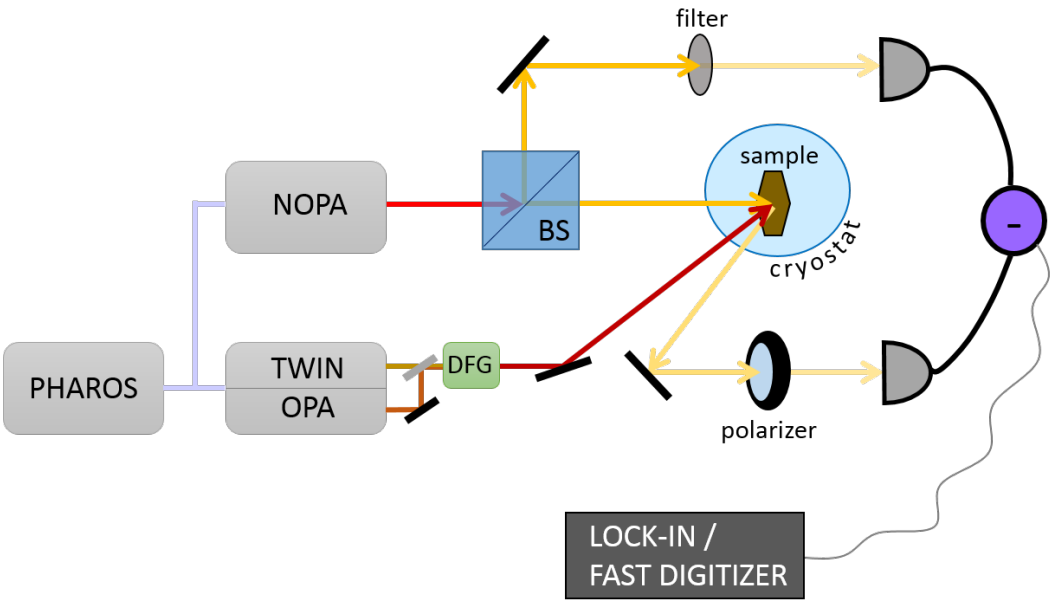

Fig. 3.8.: **Set-up scheme.** The Laser and the DFG system generates ultrashort optical pulses (probe) form the NOPA and mid-infrared pulses (pump) from the TWIN OPA plus DFG system. The tunable time delay between the pump and the probe is obtained by changing the optical path of the probe through a μm-translation stage. The final measured signal is the difference between the probe intensity reflected by the sample (excited by the mid-infrared pump) and a reference signal originated by the same optical pulse. The time resolved signal is acquired through a Lock-in amplifier or a fast digitizer. The sample temperature can be tuned through a closed cycle cryostat and the variation of pump and probe wavelength and intensity allows a complete characterization of the time resolved response in the different phases.

3.4 Summary

In the present chapter we explained the reasons for the choice of the experimental technique for the study of an HTSC sample: we listed the advantages coming from the use of electronic Raman scattering and pump-probe spectroscopy in relation to some cuprate features.

Electronic Raman scattering gives information about the superconducting gap and in particular:

1. reveals the existence and the value of the gap of BCS superconductors, by showing a peak at 2Δ;

2. detects the presence of nodes in the gap of HTSC

3. allows to study anisotropies of the gap in the reciprocal space and to detects specific symmetry modes, though polarization selection rules.

The choice of a ***time resolved techniques*** is due to the strongly correlated nature of cuprates: pump-probe spectroscopies allow to disentangle the degrees of freedom of the sample by studying their response to an external excitation (an ultrashort mid-infrared pump, in our measurements).

Finally we introduced our experimental set-up in which different parameters of the light pulses and of the sample can be tuned:

1. **pump wavelength and fluence**. These parameters changes the entity of the excitation: in particular, in chapter 5 we will focus on the difference between excitation above and below the gap energy 2Δ, both in the linear regime (low pump fluence) and in the non linear one (hogh fluence).

2. **probe wavelength and fluence**. Different probe photon energies can be used to sample the material de-excitation in several spectral regions. The choice of the probe fluence (provided it is not too large (see section 4.1) is only related to the quality of the measurement (in terms of signal to noise ratio)

3. **sample temperature**. A close cycle cryostat is used to lower the sample temperature and scan all possible phases at fixed doping (in our case, at optimally doping, the possible phases are metallic, pseudogap and superconducting)

The effects of the tuning of the set-up parameter are shown in Chapter 4.

4 Preparatory measurements on Y-Bi2212

In this chapter the preliminary time resolved measurements on Y-substituted optimally doped BSCCO, $Bi_2Sr_2Y_{0.08}Ca_{0.92}Cu_2O_{8+\delta}$ (Y-Bi2212), are presented.
The aim of the present section is first of all to characterize the dependence of the pump-probe signal of the sample as a function of excitation and detection energy, selection of Raman modes and phase of the material. This characterization allows to study the "standard" time resolved response of the sample to a defined excitation, before moving to unusual experimental conditions, as the one described in chapter 5.
Moreover the following preliminary analyses define some limitations and thresholds which ensures the validity of the experiment itself (see section 4.1) and some quantities for the measurements of tricky properties, such as the direction of the crystallographic axes of the sample (see section 4.2).
Finally they provide a useful comparison with literature and with the theoretical expectations (see for example the divergence of the time decay predicted by the Rotwarf-Taylor equations and the temperature resolved data of section 4.5).

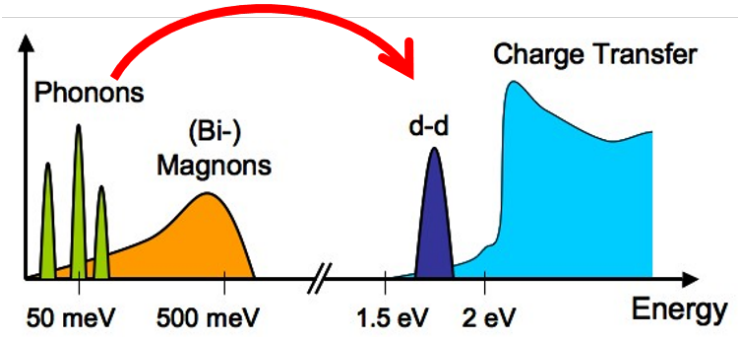

Fig. 4.1.: Photon energies. Sketch of the different possible excitations of the sample at the related energies. The red arrow connects the excitation energy with the detected one.

Our set-up has already been described in section 3.3: a mid-infrared pump pulse excites the cuprate and the transient reflectivity is measured through an optical/near-infrared probe pulse. So in our experiment the sample is excited with a quite low photon energy, whereas we observe the response at much higher energies (from 6 to 20 times larger, see Figure 4.1). The entanglement between high and low

energies is ensured by the strong electronic correlation which characterizes the cuprate systems.

The characterization of the sample response has been obtained by tuning several experimental parameters, such as

1. the fluence of the probe (see section 4.1 and 4.3) and pump (see section 4.3) pulses;

2. the probe beam polarization (section 4.2)

3. the probe and pump photon energy (section 4.4 and 4.5)

4. the sample temperature (section 4.5), in order to measure different phases of the sample (superconducting phase if $T < T_c = 97\,\mathrm{K}$, pseudogap phase if $T_c < T < T^* \approx 135\,\mathrm{K}$, strange metallic phase at larger temperatures; see chapter 2).

4.1 Probe linearity

In pump-probe measurements, as well as for equilibrium ones, the probe should provide the lowest perturbation possible on the sample.

The strength of the probe perturbation is mainly due to its fluence, which must be much lower than the pump one. We expect that small variations in the probe fluence do not change the de-excitation dynamics, except for a moltiplicative constant proportional to the impinging pulse intensity and independent of the material. In order to find out an intensity threshold, we performed time resolved measurements at 80 K with different probe powers in the quasi-equilibrium regime (see section 3.2.1).

The results are plotted in Figure 4.2**a**, where four pump-probe measurements at different probe fluences are plotted (the data have been rescaled by the value of the probe power). It is clear from the plot that the lower intensity measurements are linear, whereas the higher intensity one differ from the others. In order to study the fluence dependence of the signal, we show in Figure 4.2**b** the peak value of the dynamics (that is the maximum value in Figure 4.2**a**) versus the probe fluence. We observe a linear dependence on the probe fluence for low values ($f \leq 1.25\,\mu\mathrm{J}\cdot\mathrm{cm}^{-2}$) and a competely different behavior for higher probe intensities.

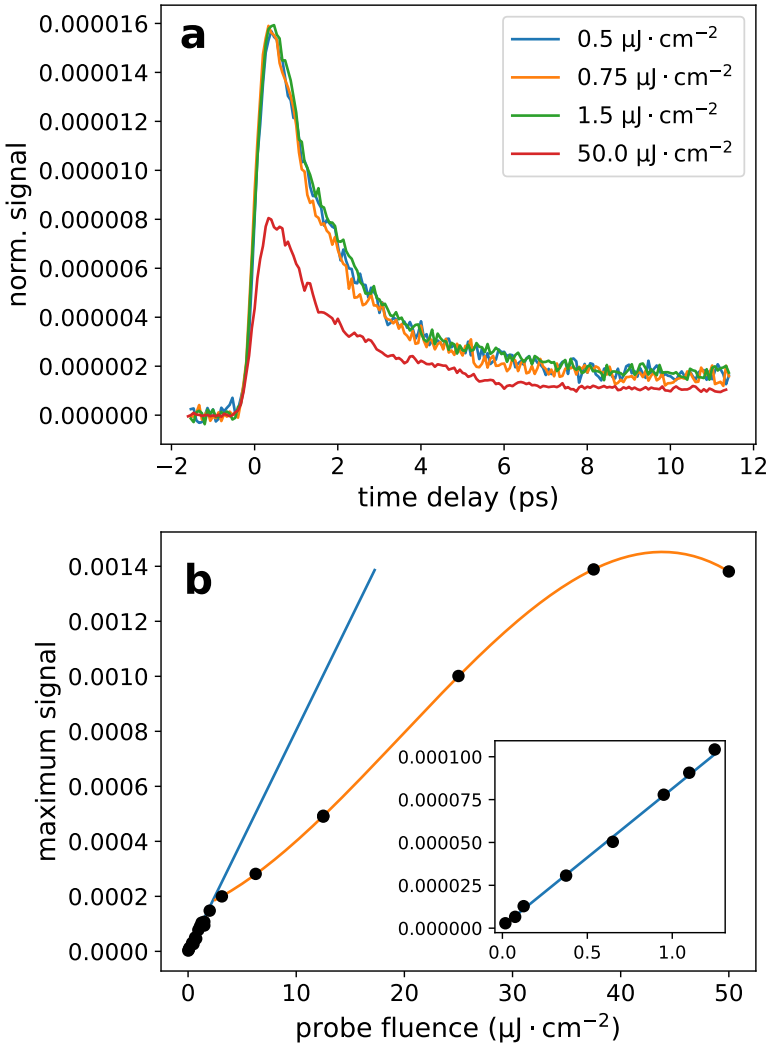

Fig. 4.2.: **Probe linearity. a** Time-resolved signals at different probe fluences, rescaled by the probe power: the lower fluence signals are very similar in the plot (and so proportional), contrarily to the high intensity one. **b** Peak of the time resolved signal at 80 K integrated in polarization, versus probe fluence. The pump and probe photon energies are respectively 170 meV and 1.63 eV. A linear behavior is obtained for $f \leq 1.25\,\mu\mathrm{J}\cdot\mathrm{cm}^{-2}$ (blue line), whereas for higher intensities a different dependence is shown (orange line). The inset is a zoom on low fluence results.

This preliminary measurement allows to understand the maximum fluence value for which the dynamics can be described by the pump probe approximation and also confirms that differences in the probe fluence below this limit should not affect the results, apart from a scaling factor. For this reason the choice of a probe fluence just below the threshold is very convenient, since it increases the signal to noise ratio while keeping the same dynamical features.

4.2 Probe polarization

The second measurement deals with the angle between the probe polarization and the sample crystallographic axes in the Copper Oxygen plane.
We already know that the probe input and output polarization directions are essential to select the desired Raman mode. In this measurements we rotated the sample with respect to the pump and probe polarization directions and we did not select the polarization of the output beam (that is to say that the signal is integrated in polarization).

We noticed that the time resolved signal in the superconducting phase has always the same dynamics, that is, the transient reflectivity obtained at different angles[1] differs for a multiplicative constant (see Figure 4.3**a**), whose angle dependence is approximately sinusoidal (Figure 4.3**a**).

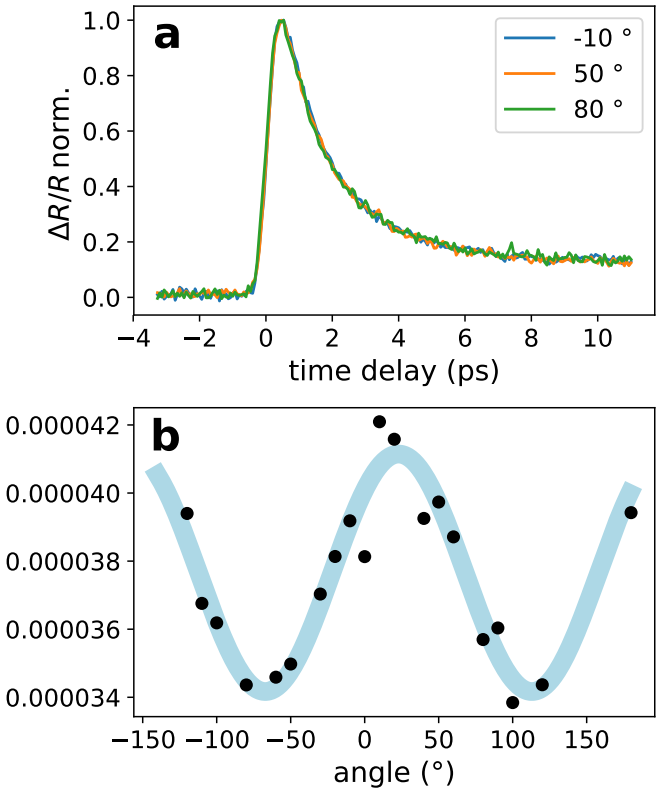

Fig. 4.3.: Reflectivity versus pump-probe polarization angle. **a** Transient reflectivity of superconducting Y-Bi2212 at different polarization angles between pump and probe. They have been normalized for their maximum value in order to check the linear relation. **b** Peak value of the signals in **a** as a function of the polarization angle. The light blue sinusoidal line is a guide for the eye.

[1] In the present section the "angles" refers to the rotation of the probe polarization with respect to the pump, which is fixed with respect to the crystal. The measurements revealed that the pump polarization direction (and so the zero angle) is parallel to the Cu-O axis, as described in the following.

The dynamics of the sample de-excitation has been studied by Y. Toda et al. in [97], where, although the completely different choices for pump and probe photon energies, they obtained a similar polarization dependence in the superconducting phase. They observed that the maximum (and the minimum) of the signal are associated to a polarization close to the Cu-O axis direction. Because of this feature the described measurements can be used to check the sample orientation: in this configuration we observe that the Cu-O axis is approximately vertical (0° angle) and parallel to the pump polarization direction.

4.3 Fluence dependence of the Raman modes dynamics

As shown in section 3.1.2 different polarizations of the pulses with respect to the crystal axes can select different Raman active modes of the sample. In our experimental configuration both the pump and the probe propagate in the direction perpendicular to the Cu-O layers of the system (z-axis). Rotating the polarization of the probe and of the final analyzer (see Figure 3.8) in the x-y plane it is possible to select only the B_{1g} and B_{2g} modes. The A_g symmetry can never be selected with linear polarizations, but since its response is much more intense than the others, from now on we will call "A_g" signal the one with the analyzer parallel to the probe polarization.

In section 3.2.1 we discussed the difference between quasi-equilibrium and non-equilibrium measurements, depending on the strength of the excitation. We remind here that in the former case the pump intensity is low and the de-excitation dynamics is almost linear for small variations of the pump fluence; in the latter the excitation is much more perturbative and the time resolved signal is non-linear in the pump power and, in principle, dynamical phase transitions may take place.

In order to characterize the sample response in the superconducting phase, we performed time resolved measurements in three polarization configurations (with the analyzer parallel to the probe polarization and in the orthogonal polarization both along the Cu-Cu and Cu-O axes)[2] and three pump fluences. The results are plotted in Figure 4.4.

The lowest fluence measurements are related to the linear regime and the de-excitation dynamics is very similar for the three selected modes. The other two measurements belong to the non-equilibrium regime: the non-linearity between two

[2]The described polarization configurations are the ones used for the detection of the three mentioned active modes in a Raman (static) measurement

results within the same experimental symmetry is quite evident for all the modes. Moreover the dynamics of the modes are much more peculiar in the high fluence range.

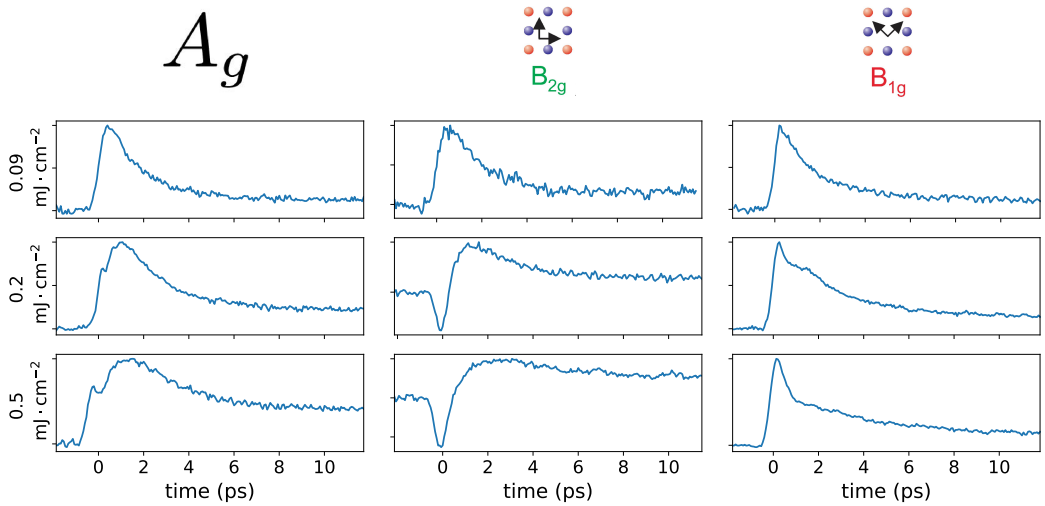

Fig. 4.4.: Different modes dynamics in superconducting phase. Optical ($h\nu = 1.63\,\mathrm{eV}$) time resolved response to a mid-infrared excitation ($h\nu = 170\,\mathrm{meV}$) at several pump fluences (rows) and input-output polarization configurations (columns), indicated by the black arrows in the first line. The first fluence ($0.09\,\mathrm{mJ}\cdot\mathrm{cm}^{-2}$) belongs to the linear regime, whereas the others are non-equilibrium measurements.

4.4 Excitation photon energy

Broadly speaking, the excitation pathways depends on two characteristics of the pump beam: its fluence, which can cause different kinds of excitations (as already pointed out many times) and its photon energy, which determines the allowed electronic transitions.
As described in section 2.2.5, because of the peculiar anisotropy of the d-wave gap, electronic transitions are always feasible, even at very low temperatures. Anyway the 2Δ value is a crucial parameter of the cuprate systems, so we wanted to study the excitation of the sample around this characteristic value ($2\Delta \approx 75\,\mathrm{meV}$).
Our twin OPAs system, associated with the Difference Frequency Generation is able to produce pulses with tunable photon energy in the range ($70 - 275\,\mathrm{meV}$).

In order to test the photon energy dependence we firstly performed measurements in the superconducting phase at different pump photon energies (275, 170, 85 and 70 meV) and several fluences (see Figure 4.5). We notice that at fixed temperatures the main features in the fluence dependence are the same: a quasi-linear behavior is characteristic of low excitation intensities, while a dip appears at about $0.5\,\mathrm{ps}$. This

effect is associated to the incipient melting of the superconducting phase, due to the high pump fluence [61, 53, 92]: this is one of the dynamical phase transitin expected for the non-equilibrium regimes.

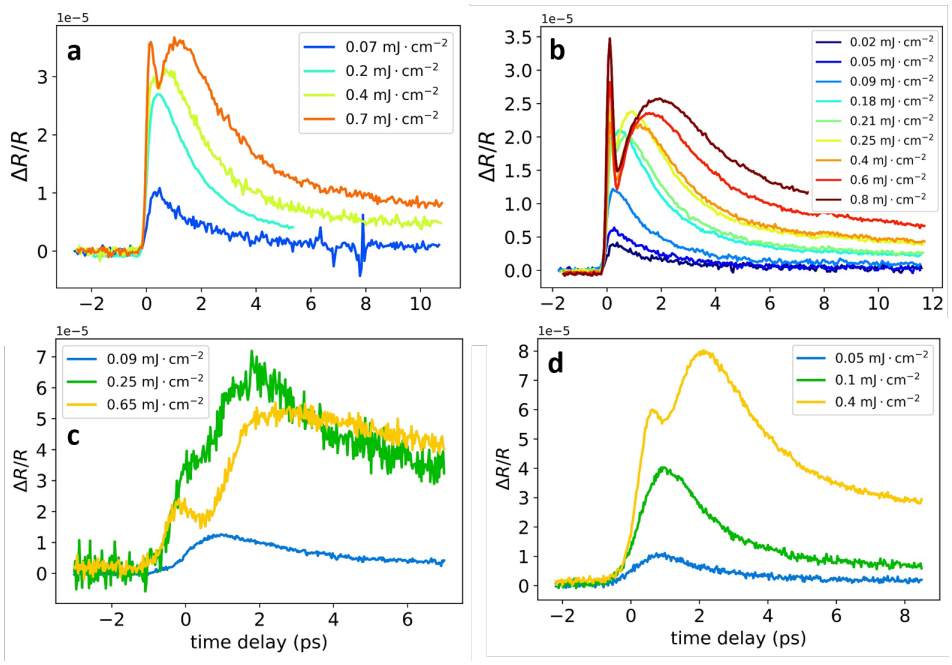

Fig. 4.5.: Pump photon energy and fluence dependence at 80 K. Time resolved reflectivity of the sample in superconducting phase at different pump photon energies: **a** 275 meV, **b** 170 meV, **c** 85 meV and **d** 70 meV. The probe photon energy has been fixed at 1.88 eV.

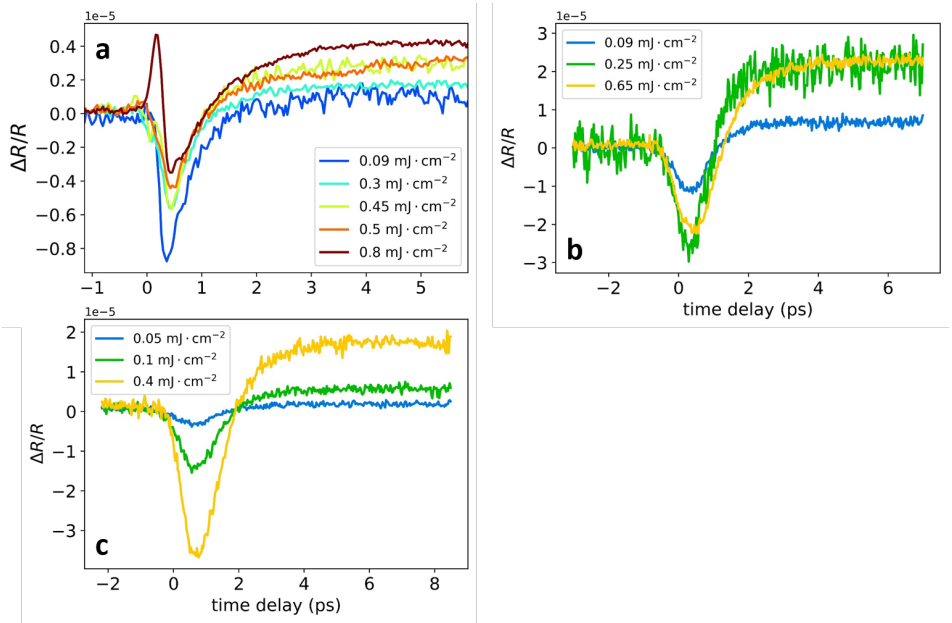

Fig. 4.6.: Pump photon energy and fluence dependence at 110 K. Time resolved reflectivity in pseudogap phase at different pump photon energies: **a** 170 meV, **b** 85 meV and **c** 70 meV. The probe photon energy has been fixed at 1.88 eV.

The same analysis can be performed in different phases of the sample. In particular, we studied the pseudogap response at several photon energy excitations as a function of the fluence.
Up to $f \approx 0.7\,\mathrm{mJ}\cdot\mathrm{cm}^{-2}$ the pump-probe signal has always the same dynamics: an initial decrease of the reflectivity followed by an enhancement and finally a slow (quasi-constant in our time interval) time decay. Although the transient reflectivity signals are similar, also in this case they are not proportional. Moreover, if we reach higher fluences ($0.8\,\mathrm{mJ}\cdot\mathrm{cm}^{-2}$), the behavior completely changes, as we observe in Figure 4.6**a**.

A direct comparison of the pump photon energy effects can be obtained by fixing the pump fluence (in our case in the quasi-equilibrium regime) and measuring the different phases (see Figures 4.7 from **a** to **c**). Notice that the longer decay typical

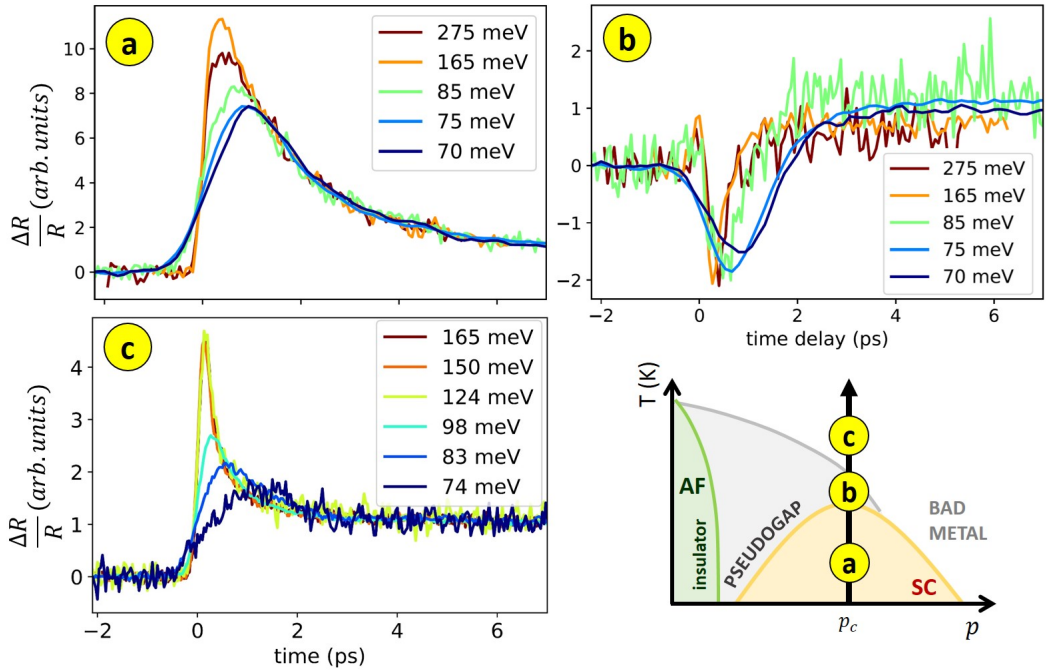

Fig. 4.7.: Pump photon energy dependence. Transient reflectivity in **a** the superconducting (T=86 K), **b** pseudogap (T=110 K) and **c** metallic (T=295 K) phase as a function of the excitation photon energy. All the signals has been normalized on the long time scale, in order to facilitate the comparison. On the bottom right corner the sketch of the phase diagram with the reference to the measured phases is shown.

of smaller photon energies is not due to the sample response, but to the pump pulse duration, which increases as the wavelength increases. This difference in the cross-correlation is evident in the rise time dependence on the pump wavelength of Figures 4.7 **a** - **c**.

4.5 Temperature map

The measurements of the previous section allowed to characterize the single phase response, but, on the other hand, reveal that no significant difference is visible at a defined phase, even at low photon energies ($h\nu \approx 2\Delta = 75\,\mathrm{meV}$). But what happens at the transition between two phases?
In order to study the complete dynamics of the phase transition, we performed temperature resolved pump-probe measurements, whose typical result is the map of Figure 4.8. Here the x-axis shows the time delay between the pump and the probe,

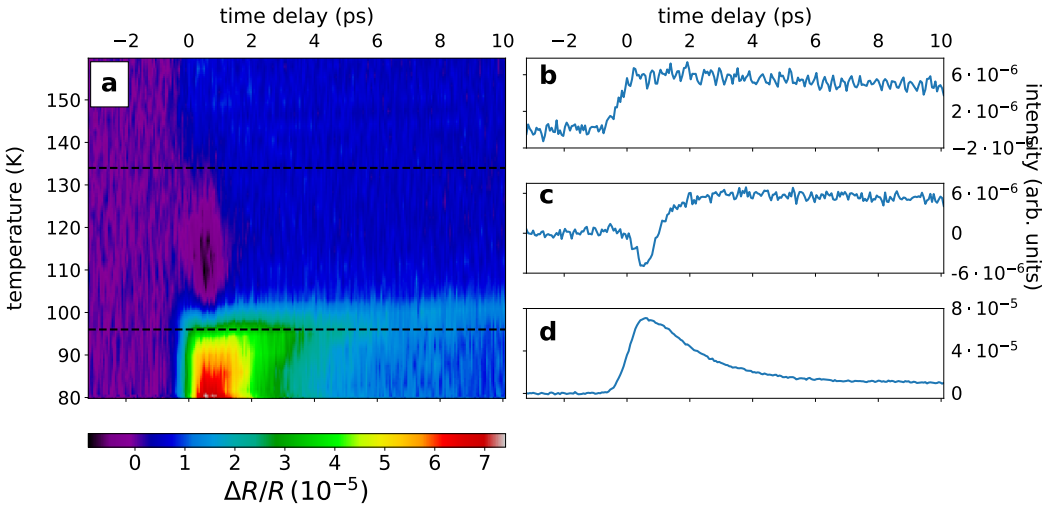

Fig. 4.8.: **Temperature map.** **a** Pump-probe measurement in temperature on Y-Bi2212, with high pump photon energy ($h\nu = 170$ meV). Horizontal black lines represent the transition temperatures. **b**, **c** and **d** represent the transient reflectivity of the three phases (metallic, pseudogap and superconductive ones respectively). See also [19]

the y-axis is the temperature and the color scale represents the transient reflectivity, so each horizontal line represents the reflectivity dynamics at a fixed temperature, as the one plotted in Figure 4.8 **b**, **c** and **d**. As expected (see section 3.2.2), there is a divergence of the time decay when approaching the critical temperature. This increase of the lifetime can be used as a measurement of the "dynamical critical temperature".

4.5.1 Probe photon energy

In the first set of temperature measurements the tuned parameter is the probe photon energy, in order to completely characterize the sample response to the same excitation (photon energy $h\nu = 170\,\mathrm{meV}$, fluence $f \approx 0.1\,\mathrm{mJ}\cdot\mathrm{cm}^{-2}$) at several energies. The results for $h\nu_{probe} = 1.88,\ 1.63,\ 1.44\,\mathrm{eV}$ are plotted in Figure 4.9**a**, **b** and **c** respectively, whereas Figures 4.9**d**, **e** and **f** show the characteristic dynamics of the sample phases (superconducting, pseudogap and metallic) for the same probe energies.

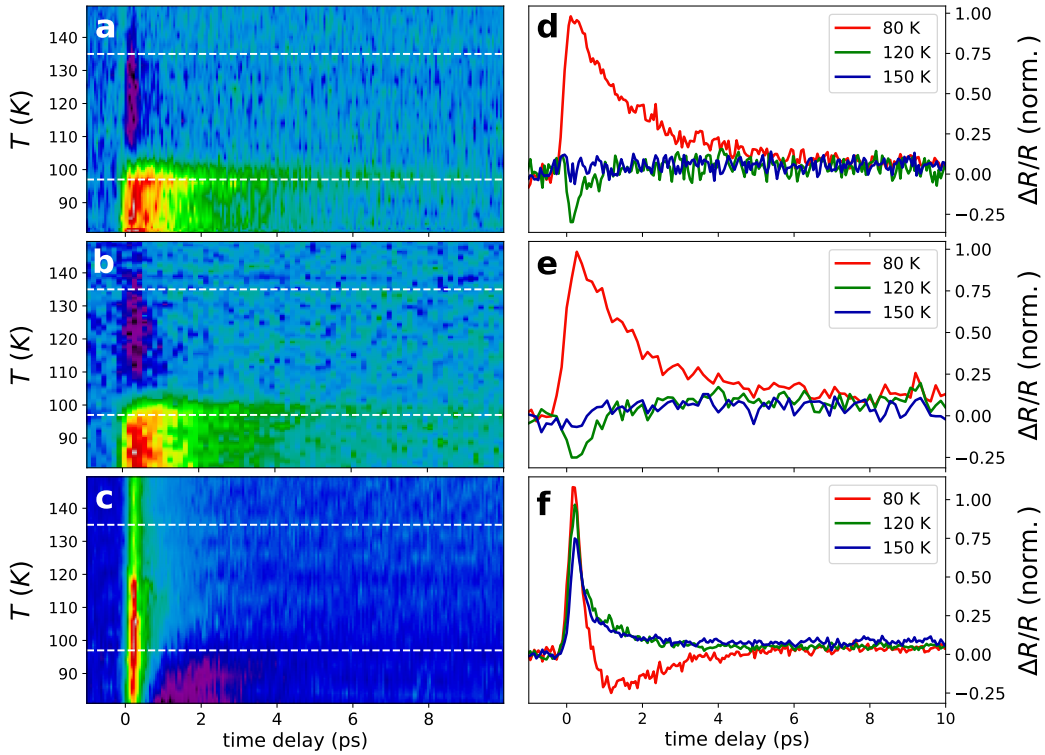

Fig. 4.9.: Probe photon energy dependence. On the left column, temperature maps of the pump-probe dynamics due to a low intensity excitation ($f = 0.1\,\mathrm{mJ}\cdot\mathrm{cm}^{-2}$) with photon energy $170\,\mathrm{meV}$. The measurements plotted in **a**, **b** and **c** have been performed with a probe photon energy of 1.88, 1.63 and $1.44\,\mathrm{eV}$ respectively. The white dashed lines mark the transition temperatures T_c and T^*. On the right column, horizontal "cuts"of the corresponding maps at fixed temperatures, in different phase domains. All the signals have been normalized to the maximum value at $80\,\mathrm{K}$, in order to favor the comparison.
Comparable results are shown in [38].

The different phases usually show a typical behavior, although it is strongly energy dependent.
The 1.88 and 1.63 eV detections in the linear regime produced similar results, with a positive signal appearing at $t > 0$ in the superconducting phase (red line in Figure 4.9 **d** and **e**) and a dip in the pseudogap one (green line in the same plot). The similarity of the two maps is confirmed by their subtractions, plotted in Figure 4.10 **a**.

The differential map show a a quasi-constant behavior, except for the small structures at short time delays, probably related to small difference in the pulse duration due to the energy change. The effect is particularly evident when the dynamics has a sharp variation, as highlighted in yellow and orange in graphs 4.10 **b** and **c**, where th original signals for the two energies and their subtraction are plotted in pseudogap and superconducting phase respectively.

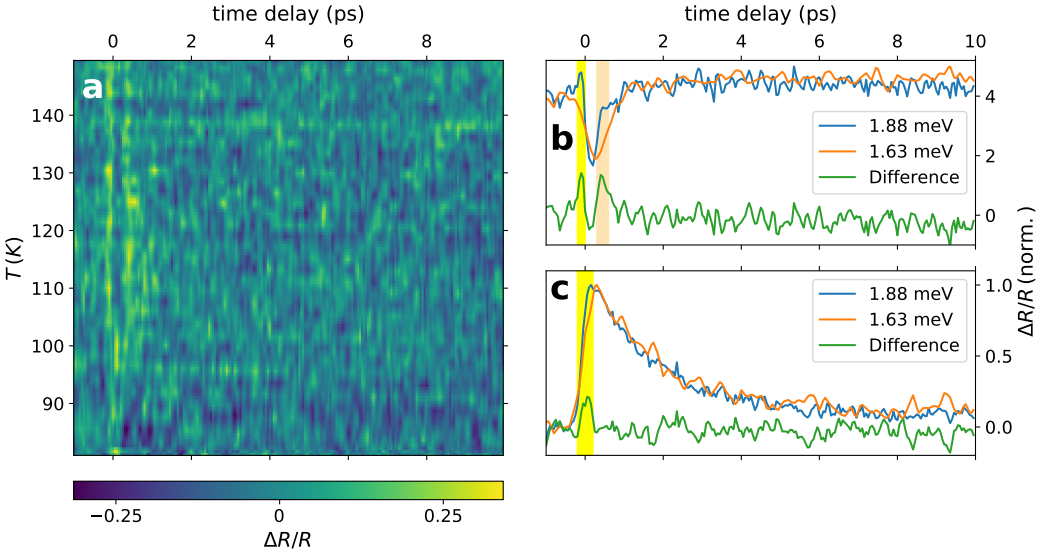

Fig. 4.10.: High photon energy probes comparison. **a** Map of the subtraction between Figures 4.9 **a** and **b**. The map is quasi-zero everywhere, apart for small positive contributions between -500 and 500 fs. In **b** and **c** the dynamics at the two photon energies are compared: in blue the original signal at $h\nu_{probe} = 1.88\,\mathrm{eV}$, in orange the $1.63\,\mathrm{eV}$ one and in green the difference between the two, that is, the corresponding horizontal cut of map **a**, both in the superconducting (**c**) and pseudogap **d** phase. The results point out that the non-zero contributions of map **a** refers to the maximum derivative of the signal (yellow and orange area), suggesting that the reason for the non-zero difference is related to the pulse duration.

Notice that the similarity between these two measurements is confined to the low fluence excitation regime. For higher fluences (see Figure 4.11**b**)the dip associated to the melting of the superconducting phase is much more visible in the larger photon energy case.

As anticipated at the beginning of the section, the described temperature maps can be used to study the phase transitions of the sample and their modification, if any, due to the variation on the experimental conditions.

In order to extract the value of the transition temperatures, we analyzed the temperature dependence of the transient reflectivity at a fixed time delay after the excitation (that is a vertical cut in the maps of Figure 4.9).

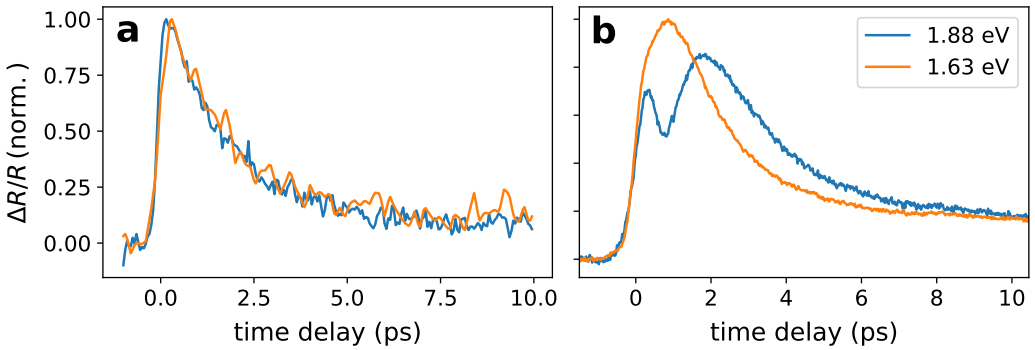

Fig. 4.11.: High photon energy probes comparison: non-equilibrium. Superconducting (T=80 K) dynamics at $h\nu_{probe} = 1.88$ and 1.63 eV, for low (**a**) and high low (**b**) excitation intensities.

For "higher" photon energy detection (1.88 and 1.63 eV)[3], the analysis of the temperature signal immediately after the excitation ($t = 0.3\,\mathrm{ps}$) shows that both transitions are characterized by a sudden variation of the reflectivity trend (Figure 4.12 **a**), which is revealed by a rapid enhancement (or even a divergence) of the signal derivative in temperature (Figure 4.12 **b**).
The same analysis can be performed at longer time delays ($t > 4\,\mathrm{ps}$), where we expect a divergence of the time decay and so a maximum in the reflectivity. This behavior is observed for both transition temperatures (Figure 4.12 **c**), although it is much more evident for T_c, and is confirmed by the derivative graph 4.12 **d**, in which the transition is associated to the zero value (revealing a stationary point) and neagtive slope (related to a concave function).

The same analysis can be performed for the low probe photon energy measurements ($h\nu = 1.44\,\mathrm{eV}$), which are characterized by a completely different dynamics and temperature dependence, as shown in Figure 4.9 **c** and **f**. In this configuration the pump-probe signals at all temperatures are characterized by a an initial enhancement of the reflectivity ($T \approx 0 - 3\,\mathrm{ps}$), followed by an exponential decay. The peculiarity of the superconducting phase is the presence of a negative dynamics from about 0.5 to 4 ps.

The study of the temperature dependence of the reflectivity highlights a the opposite trend with respect to the high photon energy one, Here the critical temperature T_c os associated to the maximum of the signal (and so to a zero value of the derivative) immediately after the excitation (Figure 4.13 **a** and **b**), whereas the long time signal has the maximum slope (that is the maximum of the derivative) ate the critical temperature (Figure 4.13 **c** and **d**). Notice that with this probe photon energy it is hard to detect the transition between the psedogap and the metallic phase.

[3] Since the response of the sample at these energies is very similar in the linear regime, we will consider just one of these frequencies.

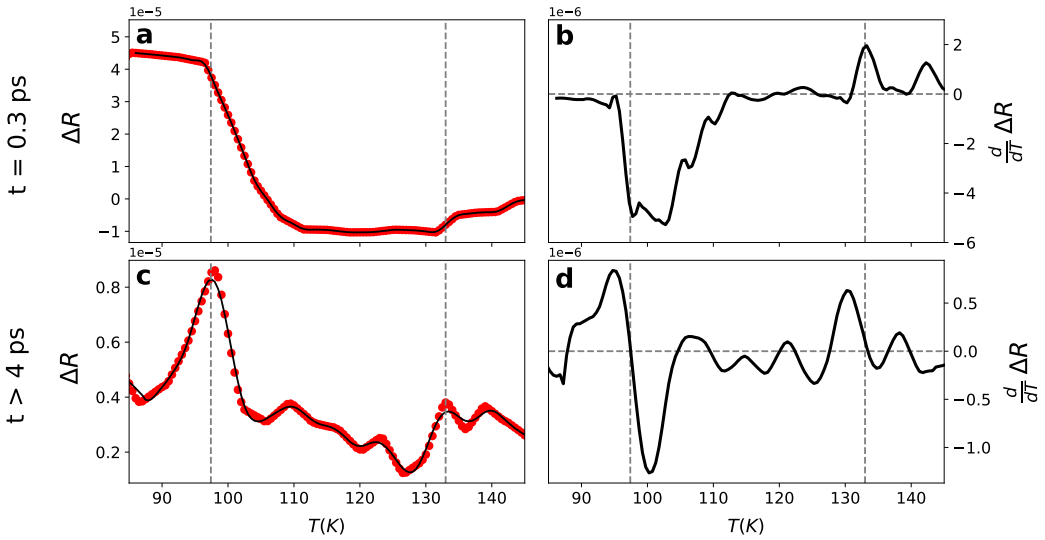

Fig. 4.12.: **Transition temperature at $h\nu_{probe} = 1.88\,\mathrm{eV}$.** Vertical cut of map 4.9**a** at 0.3 ps (**a**) and more then 4 ps (**c**) after the arrival of the pump. The red dots are the (interpolated) data, whereas the black line is a smoothing used for the calculation of the derivative in temperature plotted in **b** and **d**. The vertical dashed lines represent the transition temperatures T_c and T^*, whereas the horizontal one in the derivative graph is put at zero, in order to highlight the stationary points.

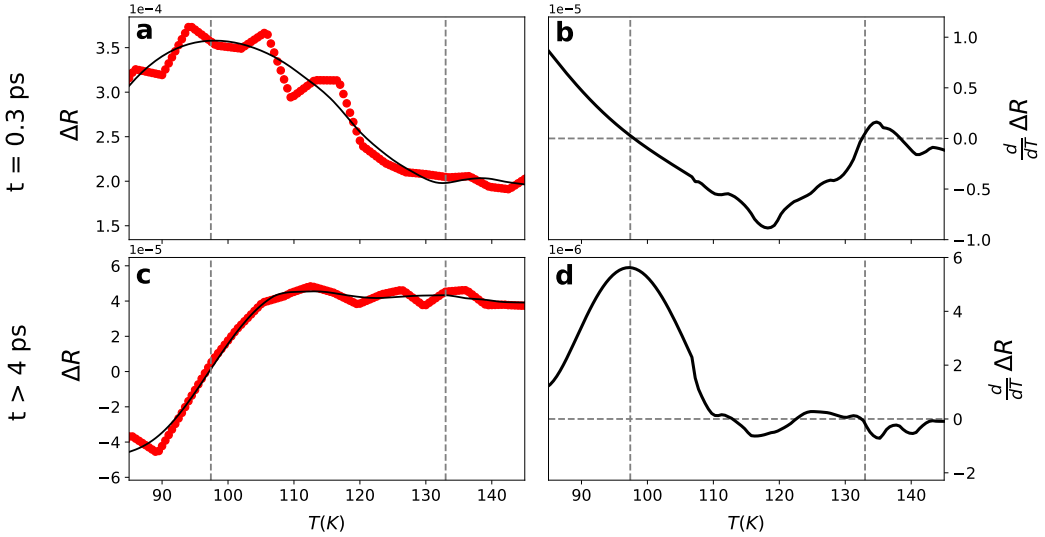

Fig. 4.13.: **Transition temperature at $h\nu_{probe} = 1.88\,\mathrm{eV}$.** Vertical cut of map 4.9**a** at 0.3 ps (**a**) and more then 4 ps (**c**) after the arrival of the pump. The red dots are the (interpolated) data, whereas the black line is a smoothing used for the calculation of the derivative in temperature plotted in **b** and **d**. The vertical dashed lines represent the transition temperatures T_c and T^*, whereas the horizontal one in the derivative graph is put at zero, in order to highlight the stationary points.

For its more accurate representation of the critical temperature only the high photon energy detection will be discussed from now on.

4.5.2 Pump photon energy

Similar measurements have been performed in two different pump fluence regimes (linear and non-linear, which are plotted in the two columns of Figure 4.14) and several excitation photon energies (275, 165, 85 and 70 meV, see the rows of Figure 4.14).
Apart for the expected broadening due to the increase of the pulse duration with the wavelength, no significant difference is visible between maps of the same "excitation regime" (so within the same column), even about the transition temperatures T_c and T^*.

On the other hand different pump fluences (at the same photon energy) show different responses close to the superconducting-pseudogap phase transition, not only for the presence of the dip related to the melting of the superconducting phase at higher fluences, but also small variations of T_c can be extracted from the time decays. For instance maps 4.14 **d** and **e** highlight a slightly different temperature for the divergence of the time decay, depending on the pump intensity, even at the same excitation frequency. This effect is pointed out by figure 4.15, where the temperature profile at long time delays is shown.
As described in the previous section, at this probe photon energy we expect a maximum in the reflectivity at the critical temperature, leading to the detection of the dynamical T_c from the time resolved data. In Figure 4.15**a** the temperature dependence after several photon energy excitations is shown: it is clear that in this experimental configuration[4] the dynamical T_c is energy independent, since it occur exactly at the same temperature $T = T_c = 97\,\mathrm{K}$.

In Figure 4.15**b** the same analysis at fixed photon energy is shown for the two fluence regimes. In this case we notice that a stronger excitation causes a small decrease of the dynamical T_c. This phenomenon is related again to the melting of the superconducting phase (see section 3.2.2): high fluences can destroy the pairing at lower temperatures with respect to the equilibrium case, thus decreasing the effective dynamical critical temperature.

The observation emphasizes the importance of performing measurements exactly at the same fluence (that is at the same ratio between the incident intensity and the area of the beam spot on the sample). This condition is not easy to be fulfilled for at least two reasons:

[4]The experimental geometry is the one measured in section 4.2: the pump and probe polarization directions are both parallel to the Copper-Oxygen axis of the Y-Bi2212. We will see in chapter 5 how the rotation of the sample can provide differences at the transition temperature.

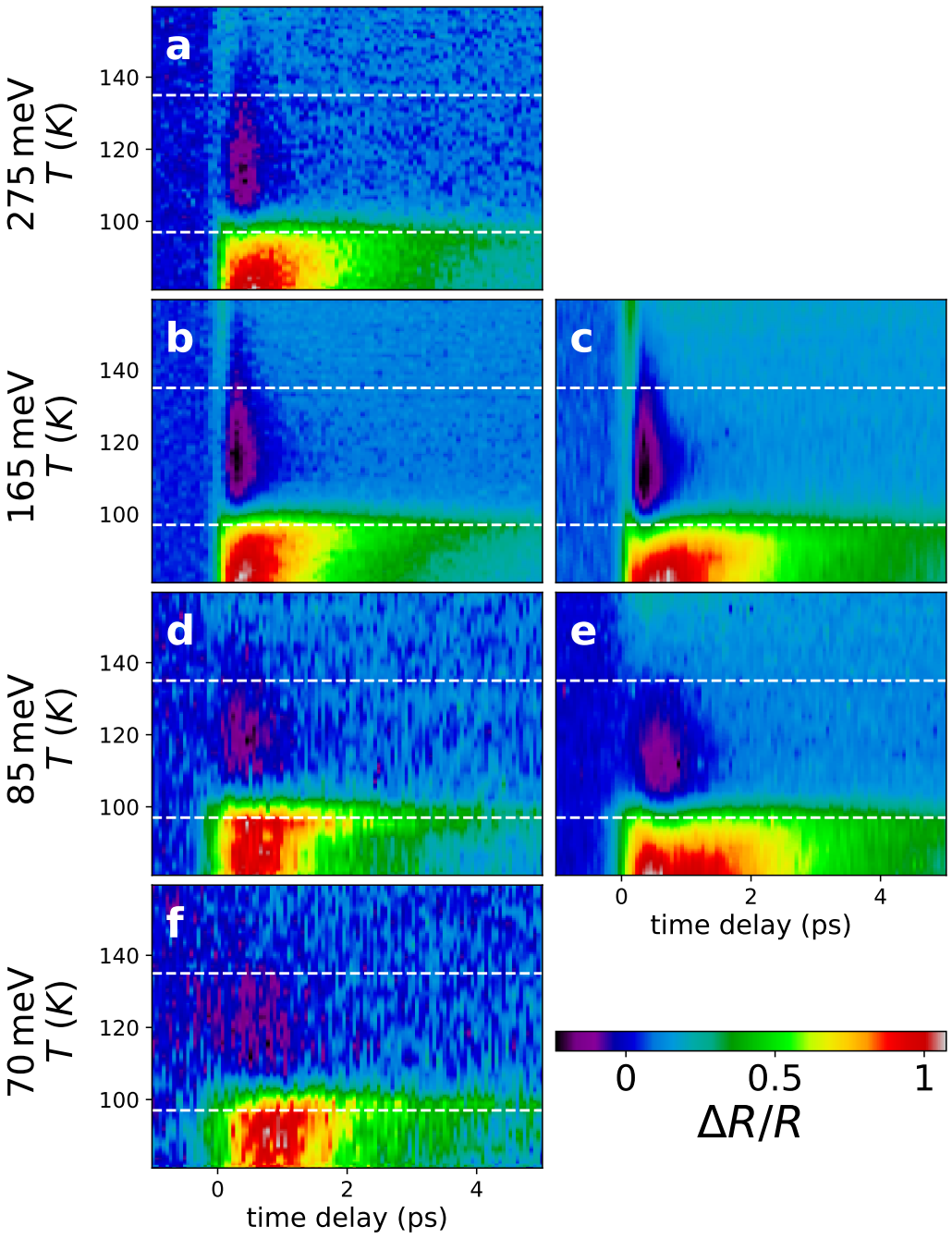

Fig. 4.14.: Temperature maps as a function of pump frequency and fluence. Pump-probe temperature resolved measurements at different excitation photon energies (the value is reported in the left of each row and it is expressed in *meV*) and for different pump fluence regimes: linear (in the left column) and non-linear (right column). The color scale has been normalized to the maximum value of the superconducting signal for each map.

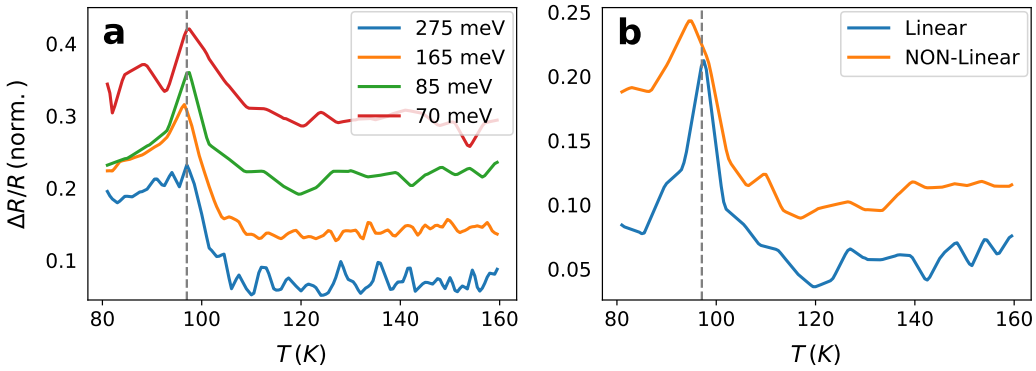

Fig. 4.15.: Temperature maps as a function of pump frequency and fluence. Reflectivity temperature dependence measured at "long time" after the pump excitation ($t > 4\,\mathrm{ps}$). The maximum of the signal occurs at he critical temperature for $h\nu_{probe} = 1.88\mathrm{eV}$. **a** Comparison between measurements at different excitation energies. **b** comparison between measurements with different excitation fluences ($f_{Linear} = 0.1\,\mathrm{mJ}\cdot\mathrm{cm}^{-2}$ and $f_{Non-Linear} = 0.5\,\mathrm{mJ}\cdot\mathrm{cm}^{-2}$) at the same photon energy ($h\nu_{pump} = 85\,\mathrm{meV}$).

- the focal length of a lens depends on the photon energy, so the position of the pump focus on the sample can move along the propagation direction, changing the dimension of the light spot on the sample and so the fluence of the excitation beam.

- some optical elements (such as the ZnSe lens used to focus the pump beam on the sample) have different absorption at different wavelength. For this reason, provided the same efficiency of the mid-infrared pulses generation for all photon energy, the intensity of the impinging beam is frequency dependent.

In order to check this condition for different photon energies we tuned the pump power in order to have the same dynamical response on the sample at a definite temperature (possibly far from the transition), apart from the differences due to the intrinsic increase of the pulse duration with the photon energy. Within this conditions it is possible to compare the phase transition dynamics of different excitations, as shown in chapter 5.
Concerning the second point, notice that actually the difference frequency generation has not the same efficiency for all wavelength and that also the OPAs provide different intensities for different wavelength. So, at the time when the measurements of Figure 4.14 have been performed we were not able to reach high fluences for 275 and 70 meV (notice that in the first case a key role was played also by the ZnSe absorption). Subsequent improvements on the set-up allowed to reach the non-linear regime even at these photon energies.

4.6 Conclusions

The measurements presented in this chapter allowed to characterize both the sample and the set-up in order to understand and interpret the results of the next chapters. In particular we noticed that:

1. There is an upper limit for the probe fluence ($f \leq 1.25\,\mu\mathrm{J}\cdot\mathrm{cm}^{-2}$) above which the sample is too strongly perturbed by the probe pulse.

2. The sample orientation can be checked by measuring the reflectivity at a defined time after the excitation for different probe polarization. The maximum (or minimum) signal identifies that the probe polarization is parallel to the Cu-O axis.

3. The probe photon energy significantly affects the dynamics, probably because of intraband transitions. The comparison between several probe photon energies made us opt for higher detection energies. As a matter of fact its time and temperature dependence is more evidently affected by the phase of the sample leading to a more accurate analysis of the data.

4. Different pump photon energies show similar time resolved signals at fixed temperatures. Interesting features may arise from the comparison of pump-probe experiments across the phase transition with different pump wavelength, especially from the measurement of the "dynamical T_c".
   Since these measurements are strongly affected by the pump intensity, which is responsible for the dynamical vaporization of the superconducting phase, it is fundamental to compare data with the same absorbed energy density.

5 Signatures of enhanced superconducting phase coherence

MID-IR EXCITATION IN OPTIMALLY DOPED Y-BI2212

In this chapter, pump-probe measurements on Y-Bi2212 as a function of temperature are presented, started from the observations of the previous one. We are especially interested in the transition between superconducting and pseudogap phase, which has been analyzed with respect to the photon energy and polarization of the pump pulse. In the second part of the chapter an effective theoretical model is introduced in order to justify the experimental results. Finally further experimental configurations are taken into account in order to reinforce the obtained results.

5.1 Motivation

Many of the ingredients required for superconductivity in cuprates survive well beyond the region of the phase diagram where the actual macroscopic superconducting phase resides. An example of this hindered superconductivity is represented by the behavior of underdoped cuprates just above the critical temperature (T_c), where some hints indicate that pairing occurs, but the presence of the superconducting phase is inhibited either by a competing charge order or by the local nature of the pair incoherence (global phase incoherence), blocking the formation of a mesoscopic superconducting state [96, 16, 26, 56, 49]. Signatures of an incipient superconductivity at temperatures larger than T_c have been revealed also in optimally doped samples, where the superconducting fluctuations survive tens of Kelvin above the actual T_c [70, 22, 61, 9, 52].
The relative fragility of the superconducting phase, together with the underlying presence of its ingredients on large portions of the phase diagram, enables the possibility of controlling superconductivity through ultra-short light pulses.
While there is ample evidence that photo-excitation with ultrashort high photon energy pulses melts the superconducting phase under some specific conditions [70, 9, 88, 39, 61], it has been shown that the formation of a superconducting phase

can be triggered by mid-infrared (MIR) excitations in regions of the phase diagram that are not superconducting at equilibrium [34, 47, 44, 14, 64]. The possibility of triggering the onset of quantum coherence through MIR excitations could open up new avenues to control quantum states of matter through light.

5.2 Measurements

5.2.1 Phase diagram and pump-probe measurements

We performed pump probe measurements on Yttrium substituted Bi2212, (Y-Bi2212), at optimal doping presents a superconducting phase below $T_c = 97$ K, a pseudogap phase between T_c and $T^* \approx 135$ K and an unusual "strange-metal" phase for higher temperatures (see chapter 4). The intensity map shown in Figure 5.1a represents

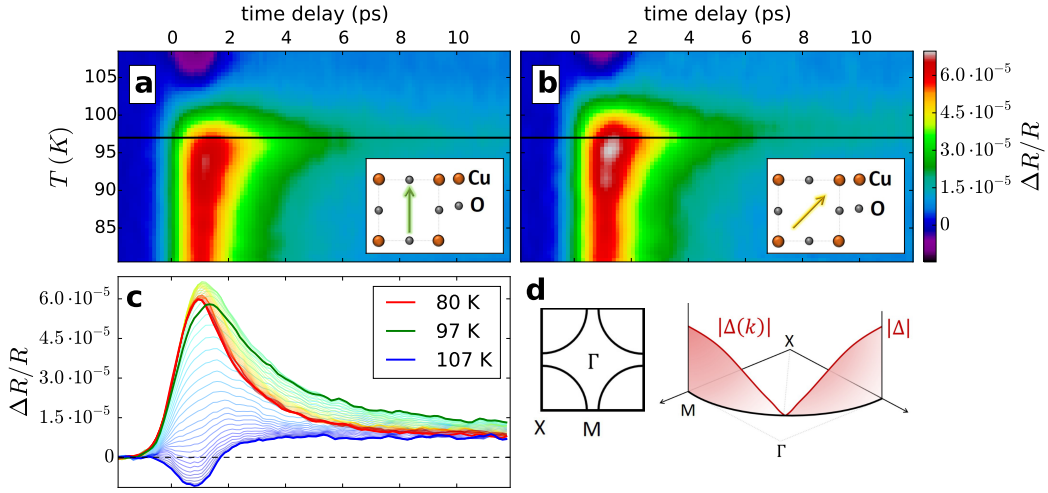

Fig. 5.1.: MIR pump, optical probe measurements. a) and b) Reflectivity variation due to an impulsive excitation at time delay 0 by a MIR pulse ($h\nu \approx 70$ meV) as a function of the temperature of the sample (vertical axis). The two maps differ for the polarization of the impinging pump, as highlighted by the two insets, representing the direction of the polarization (green and orange arrow) in the Cu-O plane. c) Time resolved signal at fixed temperatures for Bi2212: the brown line represents the characteristic superconductive signal, while the blue one refers to the pseudogap phase. The transition between the two phases is marked with the black line and is related to the divergence of the time decay. Light colored lines represent intermediate temperatures. d) Sketch of the first Brillouin zone and of the superconducting d-wave gap amplitude $|\Delta(\mathbf{k})|$ in the reciprocal space. The black curved lines represent the Fermi surface.

the relative variation of the reflectivity upon the pump excitation as a function of the time delay between the pump and the probe pulses (horizontal axis) and of the temperature of the sample (vertical axis).

Notice that in time resolved measurement as a function of temperature all the phase contributions are visible and have a characteristic dynamics. In particular a “positive” dynamics is associated to the superconducting state, while a “dip” at about 1 ps is related to the pseudogap.

From the experimental point of view our contribution is related to the excitation photon energy, which is close to the characteristic energy of the system (that is, for our sample, $2\,|\Delta| \approx 75\mathrm{meV}$. The de-excitation is then probed by an optical pulse ($h\nu = 1.62\mathrm{eV}$). This is possible since in cuprates the onset of the superconducting phase is followed by a change of spectral weight at an energy scale orders of magnitude larger than the superconducting gap. In particular, in Bi2212, the opening of a superconducting gap at about $\Delta = 35 - 40\mathrm{meV}$ results in spectral weight redistribution at frequency as high as several eV [65, 6, 8]. This is visible in time domain studies where, upon a sudden perturbation of the superconducting gap, the reflectivity in the visible range changes consistently [30, 35, 46, 53, 37, 28, 4]. Here we leverage this characteristic and work under the assumption that the spectral response in the visible-near infrared region is intimately related to the dynamics.

5.2.2 Pump photon energy dependence

We focused our investigation on a temperature range across the superconducting-pseudogap transition (from 80 to 110 K). For $T < T_c$, the reflectivity increases for about 1 ps after the arrival of the pump (at 0 ps) and then it starts decreasing through an exponential decay (red line in Figure 5.1c). The characteristic time of the decay increases with temperature, it is maximum at $T = 97$ K (green line) and drops for higher temperatures. The observed divergence of the time decay is an indicator of the phase transition [29, 39]. For higher temperatures, the sample enters the so-called pseudogap phase, whose time domain response is shown by the blue line in Figure 5.1c.

The anisotropy of the gap of d-wave superconductors (Figure 5.1 d) suggests a detailed analysis of the effects of excitations with different pump polarizations [31]. Figure 5.1a and 5.1b show the measured transient reflectivity for two different pulse polarizations: along the Cu-O axis (Figure 5.1a) and the Cu-Cu direction (Figure 5.1b). We measured the transient reflectivity in both polarizations, using a pump photon energy around the characteristic energy of the system in the superconducting phase, that is $2|\Delta| \approx 75$ meV [57]. A convenient way to visualize the polarization dependence of our measurements is to subtract the two maps in Figure 5.1a and 5.1b, as displayed in the differential map of Figure 5.2a. The difference map reveals a sizable signal around T_c, for time delays from 0 to 2 ps, corresponding to the maximum response in the superconducting phase (red region at about 1 ps in Figure

5.2a).

The result is confirmed by the visual inspection of the temperature response at a

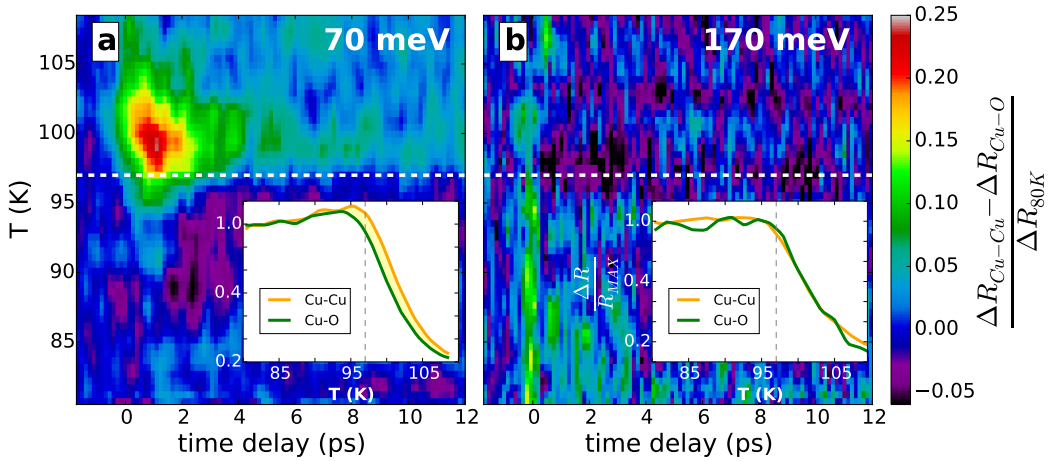

Fig. 5.2.: **Wavelength dependent anisotropy.** Difference between the transient reflectivities due to Cu-Cu and Cu-O polarized pump in time (x-axis) and temperature (y-axis), induced by excitations with a) 70 meV and b) 170 meV pump photon energies. The dashed lines highlight the critical temperature $T_c = 97$ K. The insets represent the response as a function of temperature at 1 ps time delay for Cu-Cu (orange line) and Cu-O (green line) polarized pump excitations for low and high pump photon energies (a and b, respectively). The gray dashed lines mark T_c. Both in the maps and in the insets the values of the reflectivity have been normalized to the maximum value at 80 K (ΔR_{80K}).

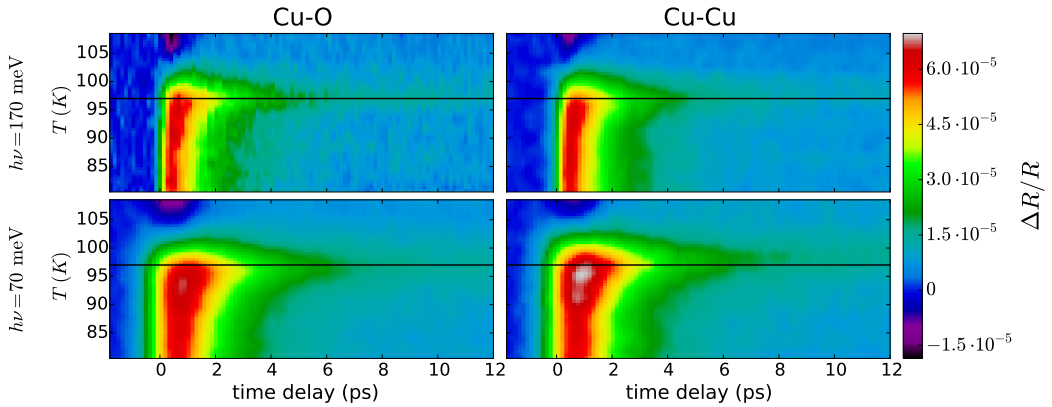

Fig. 5.3.: **Complete dataset for wavelength dependent anisotropy.** Time resolved measurements in a smaller temperature range, in order to focus on the supercoductive-pseudogap phase transition. Measurements have been performed at different pump photon energies (170 and 70 meV, first and second row respectively), but same fluence, at two different pump polarizations.

fixed time delay (1 ps) for different polarizations of the pump, as shown in the inset of Figure 5.2a.

We observe an increase of response the associated to the onset of the superconductivity when the pump is polarized along the Cu-Cu direction both above and below $T_c = 97$ K. We stress that this is an anisotropic response strongly dependent on the

photoexcitation wavelength: in Figure 5.2b we display the differential map retrieved for higher pump photon energy ($h\nu \approx 170$ meV), which reveals no anisotropy at any temperature. In Figure 5.3 representative measurements at different pump photon energies and polarizations are reported. These data have been used to obtain the map difference in Figure 5.2. The difference in the decay times between measurements at different photon energies is accounted for the duration of the pulse itself, which is different at different pump wavelengths. For low excitation energies the divergence of the decay time marks the critical temperature.

5.2.3 Linear fit

In order to observe the temperature evolution of the transient reflectivity in the different polarization and photon energy configurations, we performed an analysis on the contributions of the "pure" superconducting and pseudogap signal on the total reflectivity. We implemented a fit of the signal at each temperature using the function

$$f_{FIT}(T) = A(T) \cdot S_{80K} + B(T) \cdot S_{110K}, \tag{5.1}$$

where S_{80K} is the typical superconducting dynamics (at $T = 80$K in in this case) and S_{110K} represents the pseudogap one.

The advantage of this simple function is that the parameters $A(T)$ and $B(T)$ in this approximation are indicators of the superconducting and pseudogap contributions respectively and their tempperature dependence can be a further confirmation of the observed increase of the superconducting signal.

First of all we can check that the function is representative of the phase transitions, at least in first approximation, since the data in every configuration can be fitted, as shown in Figures 5.4 and 5.5.

The analysis of the parameters A and B as a function of the temperature (Figure 5.6) shows some common features: both A and B are maximum around T_c (dashed line in Figure 5.6) and both for high and low energy photoexcitations the Cu-Cu pseudogap contribution evolves more "slowly" in temperature with respect to the other polarization. Notice that the parameter B (Figure 5.6 **b** and **d**) seems to be energy independent, whereas A has a strong dependence on the pump photon energy. As a matter of fact, while for high photon energies (Figure 5.6 **a**) a Cu-O polarized pump has a higher superconducting contribution, for low photon energy excitations the most relevant superconducting contribution is provided by the Cu-Cu polarized pump. Moreover in this configuration the high values of A are preserved also above T_c.

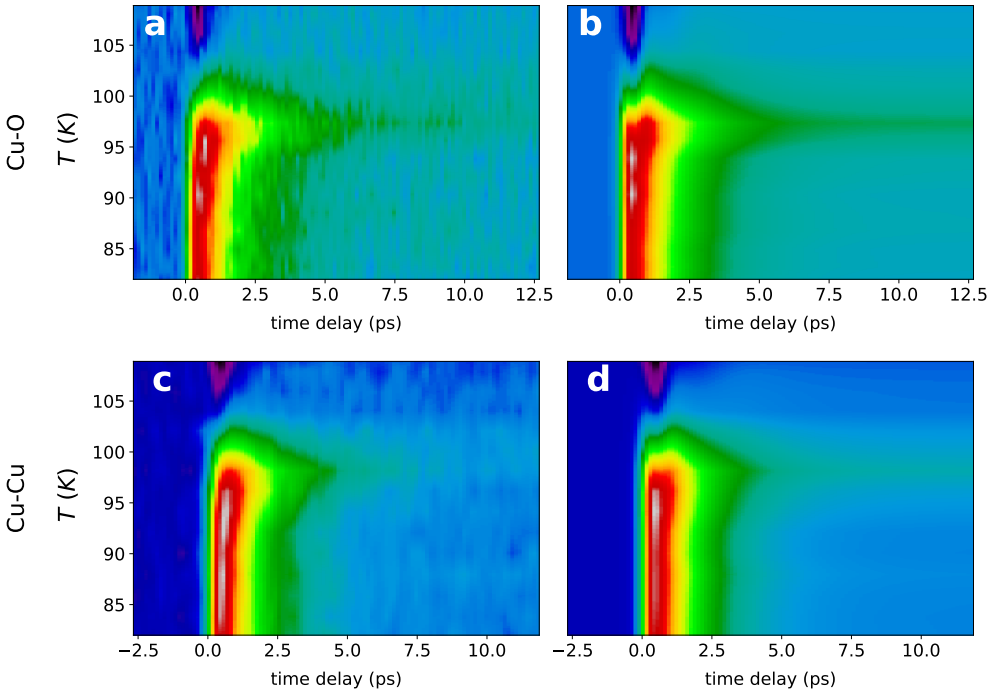

Fig. 5.4.: High photon energy fit. **a** and **c** Pump-probe measurement in temperature on Y-Bi2212, with high pump photon energy ($h\nu = 170$ meV) for pump pulses polarized along the Cu-O and Cu-Cu axis respectively. In **b** and **d** the related fits (based on the function 5.1) are shown.

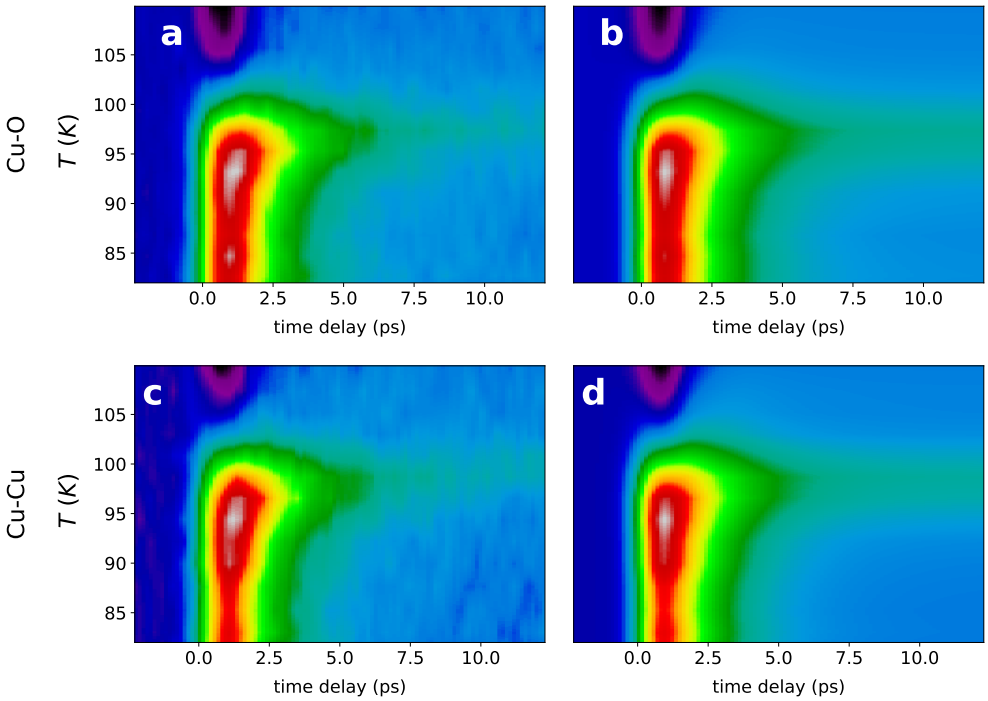

Fig. 5.5.: Low photon energy fit. **a** and **c** Pump-probe measurement in temperature on Y-Bi2212, with high pump photon energy ($h\nu = 170$ meV) for pump pulses polarized along the Cu-O and Cu-Cu axis respectively. In **b** and **d** the related fits

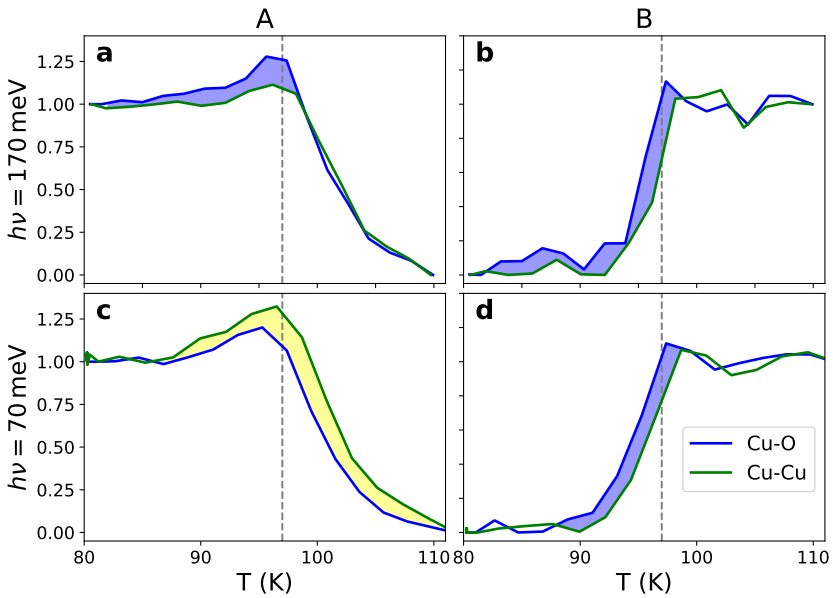

Fig. 5.6.: Temperature evolution of the fit parameters. In **a** and **b** temperature evolution of the fit parameters A (which represents the superconducting contribution) and B (pseudogap contribuion) respectively for Cu-Cu and Cu-O polarized pump at high photon energy. In **c** and **d** the same quantities are calculated for low energy potoexcitations.

The inversion of the A parameter behavior represents the increase of the superconducting signal: whereas for high photon energy excitations the two contributions are "concordant" (that is, a change in the polarization produce an increase or a decrease of both A and B at a certain temperature), this is not the case for low energy excitations.

So, rotating the pump polarization from the Cu-O to the Cu-Cu direction the superconducting contribution is increased and the pseudogap one in decreased, thus resulting in an overall enhancement of the superconducting response.

5.2.4 High fluence measurements

The time resolved measurements shown in the previous section (Figure 5.3) have been performed with low pump fluence ($f = 0.09\,\mathrm{mJ}\cdot\mathrm{cm}^{-2}$). In order to consolidate the physical picture emerging, i.e. that low photon energy excitations can trigger an increase of the superconducting signal above the equilibrium critical temperature, we have performed experiments at higher excitation density ($f = 0.39\,\mathrm{mJ}\cdot\mathrm{cm}^{-2}$). The results for high excitation density are plotted in Figure 5.7 for different photon energies, with pump and probe polarized along the Cu-Cu direction. In optical pump and probe experiments based on high probe photon energy ($1.5\,\mathrm{eV}$), photo-excitation with excitation density above critical value results in an addi-

tional pronounced response at longer times [39]. This response was interpreted as non-thermal superconducting-to-normal state phase transition where the superconducting condensate is vaporized before the closing of the gap, leading to a transient inhomogeneous superconducting state.

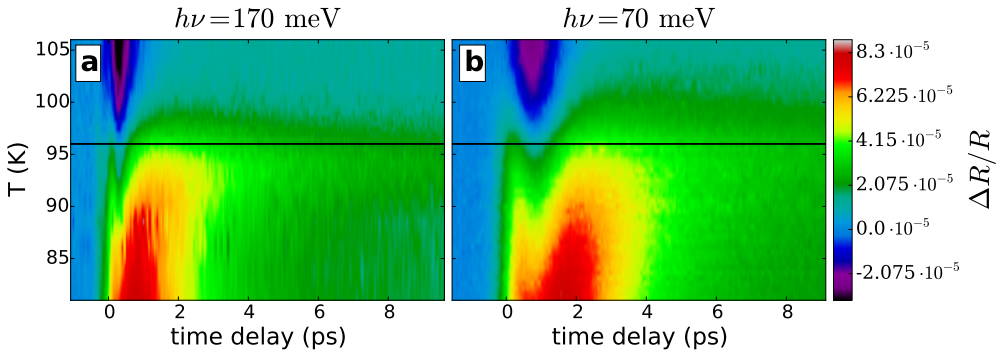

Fig. 5.7.: High fluence regime. Time resolved measurements with intense pump pulses (fluence $f = 0.39\,\mathrm{mJ}\cdot\mathrm{cm}^{-2}$) for two pump photon energies, polarized along the Cu-Cu direction. The black line represents the critical temperature $T_c = 97\,\mathrm{K}$

.

Our measurements based on long wavelength photons reveal an overall similar response. On the other hand, from a comparison between the temperature dependence of the transient reflectivity (Figure 5.7) for photon energy comparable to 2Δ (Figure 5.7b) or much larger ($h\nu > 2\Delta$, Figure 5.7a) it is evident that the positive $\frac{\Delta R}{R}$, which characterizes the superconducting phase, extends to significantly larger temperature for longer wavelengths. We stress that the two measurements were performed with similar absorbed fluence.

5.3 d-wave BCS model

In order to draw a picture of the physical scenario emerging from the anisotropic response to low photon energy ultra-short pulses, we implemented a microscopic description based on a generalized BCS Hamiltonian allowing for a *k*-dependent *d*-wave gap. While it is well known that a simple BCS formalism, disregarding first and foremost the presence of electronic correlations, cannot explain the whole cuprate phenomenology, we will argue here that it accounts well for the non-equilibrium response of the low-energy superconducting gap, at least at a qualitative level.
From the described Hamiltonian, it is possible, through density matrix formalism, to calculate the time evolution of several meaningful quantities (such as the superconducting gap amplitude $|\Delta|$).

The following sections describe:
i. the details of the model and in particular the Hamiltonian and the relevant

quantities related to the pump-probe measurement (5.3.1),
ii. the results of the calculations for the superconducting phase (5.3.2), and in pseudogap (5.3.3),
iii. the interpretation of the results in real space (5.3.4).

5.3.1 Quantities and methodologies

The generalized BCS Hamiltonian[1] has the following expression

$$H = \sum_{\mathbf{k}} \varepsilon \left(\mathbf{k} - \frac{e}{\hbar} A(t) \boldsymbol{\epsilon} \right) \hat{n}(\mathbf{k}) + \sum_{\mathbf{k}} \left(\Delta^*(\mathbf{k}) \hat{\Psi}(\mathbf{k}) + \Delta(\mathbf{k}) \hat{\Psi}^\dagger(\mathbf{k}) \right), \tag{5.2}$$

where $\varepsilon(\mathbf{k}) = -2t\left(\cos k_x + \cos k_y\right) - \mu$ is the two-dimensional tight-binding electronic dispersion with a nearest-neighbor hopping integral $t = 250$ meV and μ is the chemical potential, which has been fixed self-consistently in order to have a filling of $n = 0.9$ and $\hat{\Psi}(\mathbf{k}) = c_\uparrow(\mathbf{k}) c_\downarrow(-\mathbf{k})$ is the so-called pair operator.

The homogenous time-dependent vector potential of the pump pulse has the following expression

$$\mathbf{A}\left(t\right) = A\left(t\right) \boldsymbol{\epsilon} = A_0 \exp\left(- \left(\frac{2\sqrt{\ln 2}\left(t - t_0\right)}{\tau} \right)^2 \right) \cos\left(\omega_0 \left(t - t_0\right)\right) \boldsymbol{\epsilon} \tag{5.3}$$

where A_0 is the intensity, which has been fixed to $1000\ \frac{\text{meV}\cdot\text{fs}}{\text{nm}}$ unless stated otherwise, $\tau = 200$ fs is the FWHM, ω_0 is the frequency, $\boldsymbol{\epsilon}$ is the in-plane polarization, which has been varied between the Cu-Cu $\frac{1}{\sqrt{2}}\left(1,1\right)$ and Cu-O $\left(1,0\right)$ direction, and t_0 has been chosen such that $A\left(t = 0\right) = 10^{-4} A_0$, so that one can use $A\left(t < 0\right) = 0$ without incurring in any significant step-like change.

$\hat{n}(\mathbf{k}) = \sum_\sigma \hat{n}_\sigma(\mathbf{k})$, where $\hat{n}_\sigma(\mathbf{k}) = c_\sigma^\dagger(\mathbf{k}) c_\sigma(\mathbf{k})$ is the number operator for spin σ of the Wannier electronic state with momentum $\mathbf{k}$, whose annihilation operator is $c_\sigma(\mathbf{k})$. $\Delta(\mathbf{k}) = \zeta(\mathbf{k}) \left|\Delta\right| e^{\mathrm{i}\theta}$ is the gap function, where $\zeta(\mathbf{k}) = \frac{1}{2}\left(\cos k_x - \cos k_y\right)$ parametrizes the d-wave momentum dependence of the gap function, $|\Delta|$ is the amplitude of the gap parameter, θ is its phase. The amplitude of the gap parameter at $T = 0$ K has been set to $\left|\Delta\left(T = 0\,K\right)\right| = 25$ meV, while the phase of the gap parameter has been set to zero ($\theta = 0$ rad) at the equilibrium ($t < 0$ fs), for the sake of simplicity and without losing generality. The critical temperature is $T_c = 139.7$ K and the ratio between the zero-temperature gap parameter and the critical temperature gives $\frac{\left|\Delta(T=0\,K)\right|}{k_\text{B} T_c} = 2.08$, which is the typical d-wave BCS value. The temperature used is $T = 120$ K and the corresponding value of the gap at equilibrium is $\left|\Delta\left(T = 120\,K\right)\right| = 14.8315\,\text{meV}$.

[1] for further information see Appendix A

A relevant parameter is the pair operator $\hat{\Psi}(\mathbf{k})$ and it is related to the gap function through the equation

$$\Delta(\mathbf{k}) = G\zeta(\mathbf{k}) \sum_{\mathbf{k}'} \zeta(\mathbf{k}') \Lambda(\mathbf{k}'), \tag{5.4}$$

where G is the attractive BCS coupling constant and $\Lambda(\mathbf{k}) = \left\langle \hat{\Psi}(\mathbf{k}) \right\rangle = |\Lambda(\mathbf{k})| \, \mathrm{e}^{\mathrm{i}\phi(\mathbf{k})}$ is the complex expectation value of the pair operator.

The Hamiltonian 5.2 is used to compute the time evolution of relevant quantities of the system (such as the superconducting gap amplitude $|\Delta|$) through density matrix formalism.
In particular we start considering the expectation values:

1. $\langle \hat{n}_{\uparrow}(\mathbf{k}) \rangle = \langle \hat{n}_{\uparrow}(\mathbf{k}) \rangle \equiv \left\langle \hat{\bar{n}} \right\rangle = \bar{n}$

2. $\left\langle \hat{\Psi}(\mathbf{k}) \right\rangle = \Lambda(\mathbf{k}) = |\Lambda(\mathbf{k})| \, e^{i\phi(\mathbf{k})}$.

The time evolution is obtained through the commutation between the desired operators and the Hamiltonian:

1. $\left\langle i\hbar \frac{\partial \hat{\bar{n}}(\mathbf{k})}{\partial t} \right\rangle = \left\langle \left[H, \hat{\bar{n}}(\mathbf{k}) \right] \right\rangle$

2. $\left\langle i\hbar \frac{\partial \hat{\Psi}(\mathbf{k})}{\partial t} \right\rangle = \left\langle \left[H, \hat{\Psi}(\mathbf{k}) \right] \right\rangle$.

Let us separate the Hamiltonian as $H = H_K + H_{INT}$, where $H_K = \sum_{\mathbf{k}} \varepsilon \left(\mathbf{k} - \frac{e}{\hbar} A(t) \boldsymbol{\epsilon} \right) \hat{n}(\mathbf{k})$ is the kinetic part and contains just the interaction with the pump pulse, whereas the Cooper attraction is completely stored in $H_{INT} = \sum_{\mathbf{k}} \left(\Delta^*(\mathbf{k}) \hat{\Psi}(\mathbf{k}) + \Delta(\mathbf{k}) \hat{\Psi}^{\dagger}(\mathbf{k}) \right)$.
Keeping in mind the fermionic anticommutation relations of the annihilation operator $\hat{c}$[2] and that $\hat{n}(\mathbf{k}) = \hat{n}_{\uparrow}(\mathbf{k}) + \hat{n}_{\downarrow}(\mathbf{k})$, one gets $\left[H_K, \hat{\bar{n}} \right] = 0$ and $\left\langle \left[H_{INT}, \hat{\bar{n}} \right] \right\rangle = \Delta\Lambda^*(\mathbf{k}) - \Delta^*\Lambda(\mathbf{k})$.
The same kind of calculations can be performed for $\Psi(\mathbf{k})$ and the result is

$$\langle [H, \Psi(\mathbf{k})] \rangle = \left[\varepsilon \left(\mathbf{k} - \frac{e}{\hbar} A(t) \boldsymbol{\epsilon} \right) + \varepsilon \left(\mathbf{k} + \frac{e}{\hbar} A(t) \boldsymbol{\epsilon} \right) \right] \left\langle \hat{\Psi}(\mathbf{k}) \right\rangle + \Delta(\mathbf{k}) (1 - 2\bar{n}(\mathbf{k})) \tag{5.5}$$

[2] $\left\{ c_{\sigma}^{\dagger}(\mathbf{k}), c_{\sigma'}(\mathbf{k}') \right\} = \delta_{\sigma\sigma'} \delta k k'$, $\left\{ c_{\sigma}^{\dagger}(\mathbf{k}), c_{\sigma'}^{\dagger}(\mathbf{k}') \right\} = \{ c_{\sigma}(\mathbf{k}), c_{\sigma'}(\mathbf{k}') \} = 0$

Finally, keeping in mind the definition of the pair operator $\hat{\Psi}(\mathbf{k}) c_{\uparrow}(\mathbf{k}) c_{\downarrow}(-\mathbf{k})$ and of its expectation value $\Lambda(\mathbf{k}) = \left\langle \hat{\Psi}(\mathbf{k}) \right\rangle$, one gets the following set of relevant equations:

$$i\hbar \frac{\partial}{\partial t} \bar{n}(\mathbf{k}) = \Delta(\mathbf{k}) \Lambda^*(\mathbf{k}) - \Delta^*(\mathbf{k}) \Lambda(\mathbf{k}) \tag{5.6}$$

$$i\hbar \frac{\partial}{\partial t} \Lambda(\mathbf{k}) = \left[\varepsilon\left(\mathbf{k} - \frac{e}{\hbar}\mathbf{A}(t)\right) + \varepsilon\left(\mathbf{k} + \frac{e}{\hbar}\mathbf{A}(t)\right) \right] \Lambda(\mathbf{k}) + \Delta(\mathbf{k}) \left[1 - 2\bar{n}(\mathbf{k})\right] \tag{5.7}$$

with variables $\bar{n}(\mathbf{k})$ and $\Lambda(\mathbf{k})$[3]. They are used to calculate the dynamics of the $\mathbf{k}$-dependent gap amplitude $|\Delta|$ and of the modulus and phase of the expectation value of the pair operator ($|\Lambda(\mathbf{k})|$ and $\phi(\mathbf{k})$ respectively).

5.3.2 Results: $T < T_c$

The model predicts different behaviors depending on the frequency and the polarization of the pump pulse. In particular, Figure 5.8a shows that low photon energy

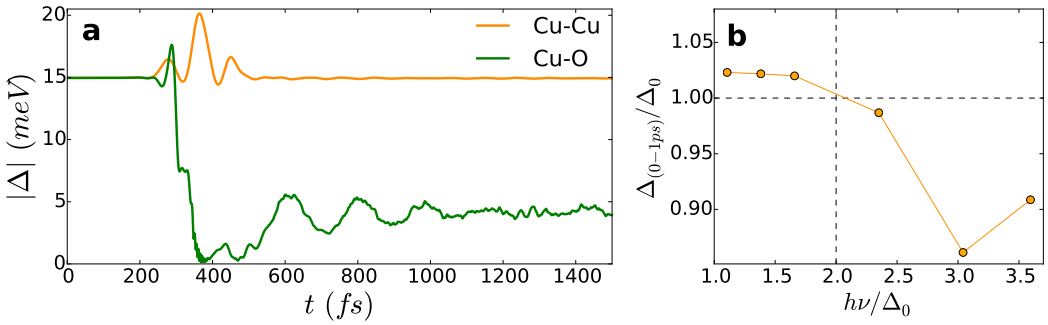

Fig. 5.8.: d-wave BCS microscopic model. Results of the microscopic model: **a** Time evolution of the modulus of the superconducting gap ($|\Delta|$) in both Cu-Cu (orange line) and Cu-O (green line) excitation case. The maximum of the pump electric field is reached at about 350 fs. **b** Normalized integral of $|\Delta|$ in the time interval from 0 to 1 ps as a function of the pump photon energy ($\Delta_0 = |\Delta(t=0)|$) for Cu-Cu polarized pump excitations.

excitations with polarization parallel to the Cu-Cu direction are predicted to drive an instantaneous enhancement of the superconducting gap, while a pump polarization rotated $45°$ induces a dynamical quench of the gap. These results qualitatively rationalize the experimentally observed enhancement of the positive signal associated to the superconducting response, triggered by photoexcitation polarized along the Cu-Cu direction for pump photon energy $h\nu \approx 2|\Delta|$. On the other hand, the collapse of the superconducting signal in the Cu-Cu polarization configuration is predicted for higher pump photon energies, as shown in Fig. 5.8b, where we display the transient decreases of $|\Delta|$ as a function of the pump photon energy.

[3]The other quantities in the equations are $\mathbf{A}(t)$, whose value and direction are set depending on the experimental configuration, and the superconducting gap, which depends only on $\Lambda(\mathbf{k})$, since $\Delta(\mathbf{k}) = G\zeta(\mathbf{k}) \sum_{\mathbf{k}'} \zeta(\mathbf{k}') \Lambda(\mathbf{k}')$ and G and $\zeta(\mathbf{k})$ are fixed

The complete gap amplitude dependence on the pump photon energy in shown in

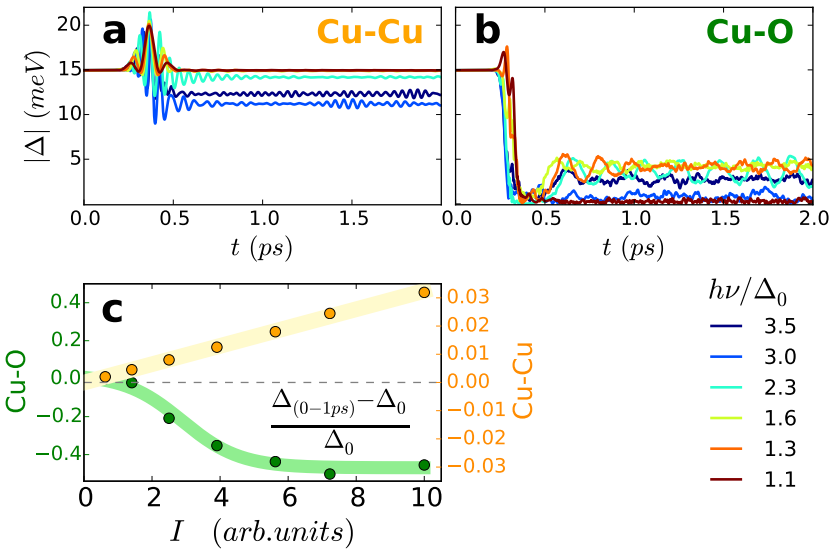

Fig. 5.9.: Photon energy and fluence dependence. a) and b) Time dependence of the maximum amplitude of the superconducting gap for different photon energies and polarizations of the pump. c) Integration of the gap amplitude in time (from 0 to 1 ps) as a function of the intensity of the applied fields (for photon energies $h\nu < 2\Delta$). Yellow and light green areas guide the eye.

Figure 5.9 The graphs represent the time dependence of the maximum values of the gap amplitude due to the pump excitation, both in Cu-Cu and Cu-O polarization configuration, for several pump photon energies. The difference between the time response of the superconducting signal in experiments and calculations related to the time decay (the increase of the superconducting signal lasts for some picoseconds in the measurements, while the enhancement of Δ is instantaneous in the calculations) is due to the absence of dissipation effects in the microscopic model.
Figure 5.9c shows the fluence dependence of the superconducting gap, for Cu-Cu (orange dots) and Cu-O (green ones) polarized pump excitations. Notice that while the Cu-Cu excitations leads to a linear increase of the gap with respect to the fluence, the decrease induced by an Cu-O excitation is not linear at all and seems to saturate to a minimum value for high pump fluences.

In order to grasp the physical picture that emerges from this microscopic model, we calculated the expectation value of the pair operator $\hat{\Psi}(\mathbf{k})$.

Figure 5.10 displays the modulus and the phase of the pair amplitude $\Lambda\,(\mathbf{k})$ (in the first Brillouin zone) calculated in three different cases: at equilibrium and during a Cu-Cu and Cu-O low photon energy excitation ($h\nu \approx 2\Delta$). We observe that the value of $\left|\left\langle \hat{\Psi}(\mathbf{k})\right\rangle\right|$ around the Fermi surface is nearly unperturbed (and actually slightly enhanced) in both excitation schemes (Figure 5.10b and 5.10c), i.e., that

pairing is still present in both cases[4]. On the other hand, the phase reveals a strong anisotropic response (Figure 5.10e and 5.10f): the model shows that Cu-O polarized excitations drive intense phase fluctuations, which are responsible for the collapse of $|\Delta|$ shown in Figure 5.8a. The reason is clear if we observe equation 5.4: strong oscillations od $\phi(\mathbf{k})$ can cancel the sum on $\mathbf{k}$ and suppress $|\Delta(\mathbf{k})|$. Cu-Cu polarized low-photon-energy excitations preserve instead phase coherence and enable an enhanced superconducting dynamical response.

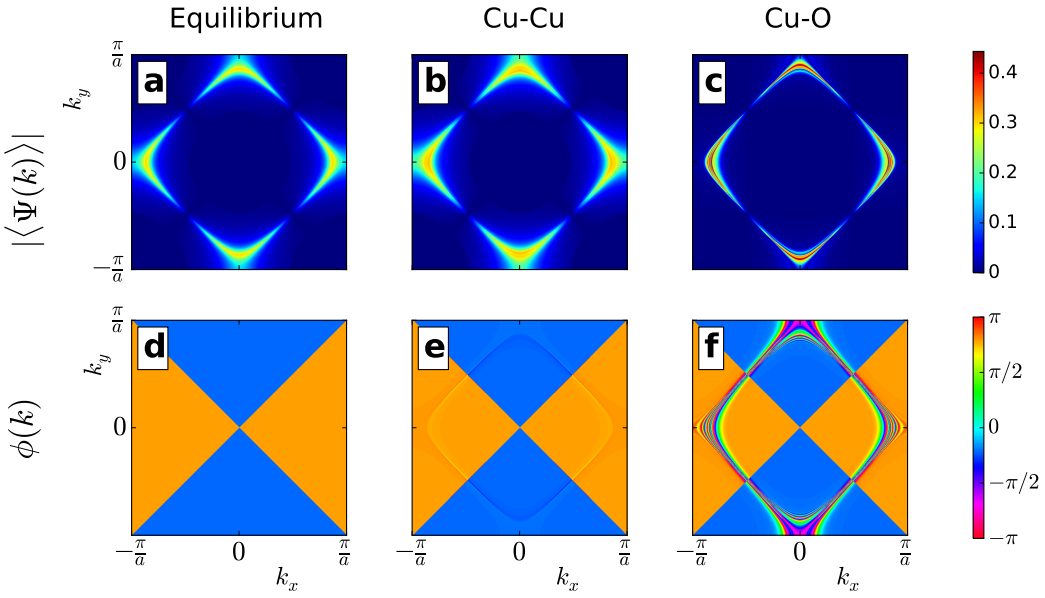

Fig. 5.10.: Time dependent pair operator representation. a-c) Modulus of the expectation value of the pair operator $\hat{\Psi}(\mathbf{k})$ in the reciprocal space in three different situations: a) no excitation ("Equilibrium"), b) during a pump excitation polarized along the Cu-Cu and c) Cu-O direction. Analogously, pictures from d to f show the phase $\phi(\mathbf{k})$ of $\left\langle\hat{\Psi}(\mathbf{k})\right\rangle$, in the same three conditions.

5.3.3 Results: $T > T_c$

We stress that all previous calculations were performed at a temperature $T < T_c$, where the amplitude of the superconducting gap $|\Delta|$ has a non-zero equilibrium value. This is an intrinsic limitation of the microscopic BCS model, which does not allow superconducting pairing at temperatures higher than the critical value (T_c). The data instead report a well visible enhancement of the superconducting behavior at temperatures larger than the equilibrium critical temperature T_c (inset of Figure 5.2a).

In order to extend this effective description to higher temperatures, we propose to run calculations from a modified equilibrium state (whose features are justified in the following) maintaining the BCS framework. Different from standard BCS

[4]Notice that $|\Lambda(\mathbf{k})|$ is not exactly the number of Cooper pairs, but the two quantities are related, since $\langle\hat{n}_c\rangle = \left\langle\Psi^{\dagger}(\mathbf{k})\,\Psi(\mathbf{k})\right\rangle$, while $|\Lambda(\mathbf{k})| = \sqrt{\langle\Psi^{\dagger}(\mathbf{k})\rangle\,\langle\Psi(\mathbf{k})\rangle}$

superconductors, cuprates exhibit signatures of strong superconducting fluctuations at temperatures larger than T_c [22]. In particular, in optimally-doped Bi2212, both equilibrium and time-domain techniques revealed superconducting fluctuations up to tens of Kelvin above the critical temperature [61, 9, 70, 52, 98, 58]. This anomalous feature is commonly taken to imply the presence of Cooper pairs losing phase coherence; i.e. while the mesoscopic coherence vanishes above the transition temperature, pairing remains, together with phase correlations, which are local in space and time [22, 100, 68, 71, 69]. Transport and magnetization studies suggest that the local correlations lead to a universal superconducting percolative regime above T_c; a local gap distribution was able to explain [68] the presence of an effective average gap above T_c in photoemission experiments [75].

In order to explore these effects within the generalized BCS model, we employ the following simple procedure. We proposed a new equilibrium state artificially built by adding a random noise to the phase of the original state pair amplitude $\phi(\mathbf{k})$, while retaining its modulus $\left(\left|\left\langle\hat{\Psi}(\mathbf{k})\right\rangle\right|\right)$. The phase noise introduced in the model leads to a reduction of the gap, as shown in Figure 5.11a, in which the dependence of the gap amplitude on the maximum value for the phase fluctuations $(\delta\phi)$ is plotted. Calculations of the dynamic response, starting from this inhomogeneous (in momentum space) equilibrium state, reveal that Cu-Cu low-photon-energy excitations induce not only an increase of the gap amplitude (Figure 5.12), but also a significant enhancement of phase coherence (and negligible variation in the amplitude) of the pair operator, as highlighted in Figure 5.11b, which depicts a histogram of the phase distribution before (blue line) and during (red line) the photo-excitation (350 fs), for an initial fluctuation of $\delta\phi = \pi/8$ (value chosen for sake of clarity). The plot reveals that the phase distribution, which becomes narrower after the excitation, leads to an enhanced superconducting response. We argue that this scenario rationalizes, at

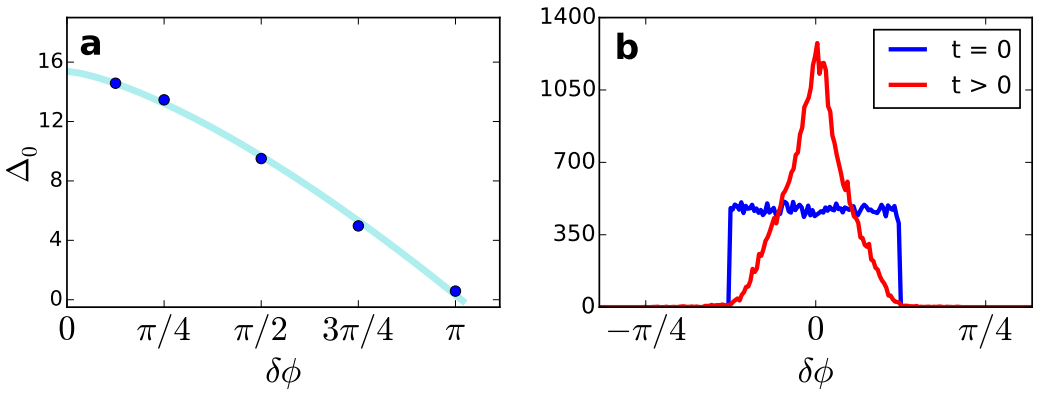

Fig. 5.11.: Extension of the d-wave BCS model to larger temperatures. a) Values of the superconducting gap at equilibrium ($\Delta_0 = |\Delta|\,(t = 0)$) as a function of the amplitude of the phase noise. b) Distribution of the phase values at equilibrium (blue line) and during the excitation polarized along the Cu-Cu direction (red line) for an initial noise amplitude of $\delta\phi = \pi/8$.

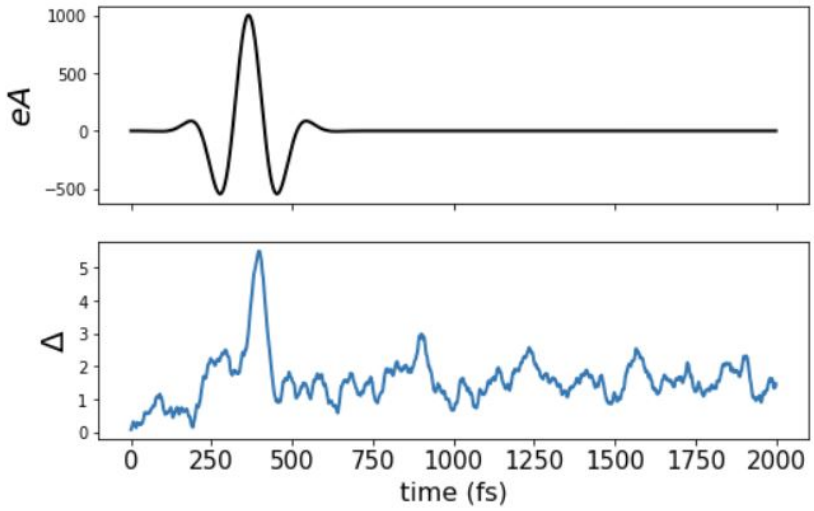

Fig. 5.12.: **Gap amplitude evolution at $T > T_c$.** **a** Time dependence of the vector potential of the pump pulse. **b** Gap amplitude dynamics for a low energy photoexcitation ($h\nu < 2|\Delta(T=0)|$) polarized along the Cu-Cu axis for an initial "pseudogap" state. The noise (with amplitude $\delta\phi = \pi$) added in the phase of the initial state causes the initial negligible value of the gap amplitude, which increases when the pump intensity reaches its maximum, because of the increase of phase coherence (see Figure 5.11).

qualitative level, the enhancement of an out-of-equilibrium superconducting behavior above T_c, which could therefore be associated to a light-driven boost of phase coherence.

5.3.4 Real Space representation

In this section we want to briefly discuss the effect of the enhanced superconducting coherence in real space.
Real and reciprocal space are conected through Fourier Transform, so let us consider the inverse Fourier Transform of the pair operator expectation value $\Lambda(\mathbf{k})$

$$\Lambda(r,r') = \langle c_\uparrow(\mathbf{r})\, c_\downarrow(\mathbf{r}')\rangle \quad = \frac{1}{N}\sum_{\mathbf{k}\mathbf{k}'} c_\uparrow(\mathbf{k})\, c_\downarrow(\mathbf{k}')\, e^{i(\mathbf{k}\mathbf{r}\cdot\mathbf{k}'\mathbf{r}')}. \tag{5.8}$$

In a BCS system the electrons in a Cooper pair are connected by the value of $\mathbf{k}$ ($\hat{\Psi}(\mathbf{k}) = c_\uparrow(\mathbf{k})\, c_\downarrow(-\mathbf{k})$), so the second sum of equation 5.8 disappears since $\mathbf{k}' = -\mathbf{k}$, and one gets

$$\Lambda(r,r') = \frac{1}{N}\sum_{\mathbf{k}} c_\uparrow(\mathbf{k})\, c_\downarrow(-\mathbf{k}')\, e^{i(\mathbf{k}\cdot(\mathbf{r}-\mathbf{r}'))} = \Lambda(r-r'). \tag{5.9}$$

The quantity $\Lambda(r-r')$ allows to get the coherence length of Cooper pairs in the system: typical results are plotted in Figure 5.13 **a** and **b**. The axes represent

$x - x'$ and $y - y'$ (where $\mathbf{r} = (x, y)$) and the interesting information is related to the spot eventually present around (0,0). The width of the central area (in which $\Lambda(r - r') \neq 0$) gives us an idea of the coherence length in real space. In the BCS

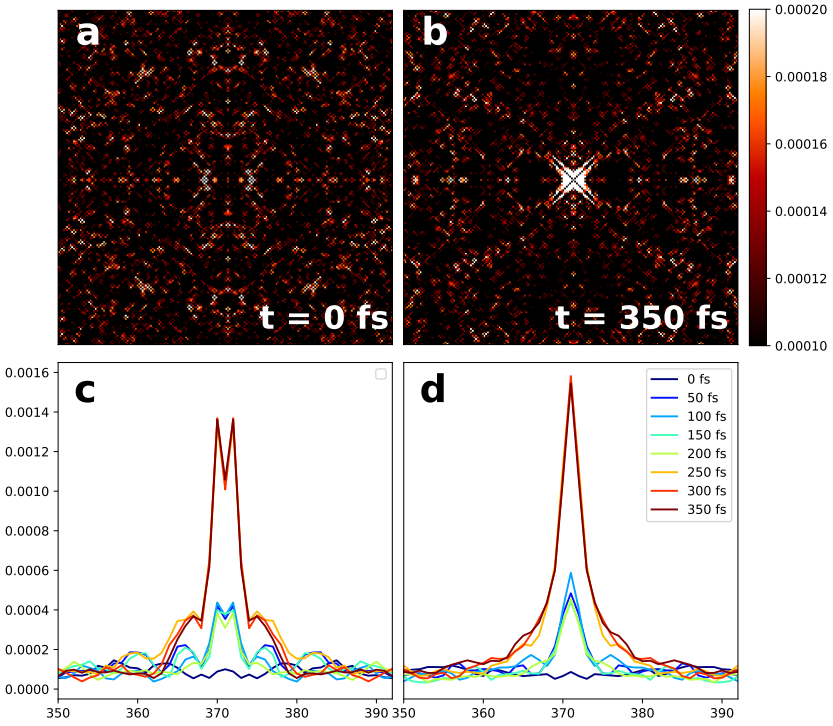

Fig. 5.13.: **Coherence length.** $\Lambda(r - r')$ at equilibrium **a** and during the excitation **b**. Horizontal **c** and diagonal **d** cuts of $\Lambda(r - r')$ maps for several time delays between pump and probe.

effective model the pair operator evolves as a result of the Hamiltonian 5.2: the inverse Fourier transform at different time delays allows us to study the dynamics of the coherence length. We apply this calculation to the initial "noisy" state described in section 5.3.3, with phase fluctuation $\delta\phi = \pi$. In particular, in Figure 5.13 **a** and **b** the modulus of the inverse Fourier Transform of $\Lambda(\mathbf{k})$ for the equilibrium situation and at $t = 350\text{fs}$ (delay at which the pump intensity reaches its maximum value) are plotted. Whereas at $t = 0$ (equilibrium case) the map is almost zero for any value of $\mathbf{r} - \mathbf{r}'$, during the excitation a positive area appears in the center of the map, indicating an increase of the coherence length due to the low photon energy excitation. To highlight the time evolution of the coherence length, in Figure5.13 **c** and **d** $\Lambda(\mathbf{r} - \mathbf{r}')$ is plotted for $\mathbf{r} = (x, 0)$ and $\mathbf{r} = \left(\frac{x}{\sqrt{2}}, \frac{x}{\sqrt{2}}\right)$. The result confirms the increase of the coherence length due to the low photon energy Cu-Cu polarized pump.

5.4 Symmetry of the electronic excitation

In the measurements presented in this chapter no polarization selection has been performed *after* the interaction with the sample. The geometry of the sample allows to activate three Raman modes: A_g, B_{1g} and B_{2g} (see chapter 4. The A_g signal is the most intense, and in reflectivity measurements integrated in polarization all other contributions are negligible.
B_{1g} and B_{2g} modes can be selected by acquiring the signal with orthogonal polarization with respect to the probe one. This requirement and the relatively high intensity of the A_g signal make these measurements experimentally complicated, especially for temperature scans.

In order to acquire temperature and time resolved maps for these Raman modes, we performed birefringence measurements in suitable configurations.

5.4.1 Birefringence measurements

The aim of a birefringence measurement is to quantify the variation of a beam polarization due to the interaction with a sample. This kind of measurement is performed acquiring two orthogonal components of the probe pulses reflected or transmitted by the sample. In time resolved spectroscopy we are interested in the time dependent variation of polarization after the excitation of the sample. In order to study this parameter we performed a "standard" pump probe experiment, in which the output beam is split by a Wollaston prism. The final signal is the subtraction of the two projections of the probe beam, performed by a differential detector. The set-up is shown in Figure 5.14. In our configuration the prism was always oriented such that the measured signals have the same intensity (and so the subtraction is negligible in average) before the excitation.

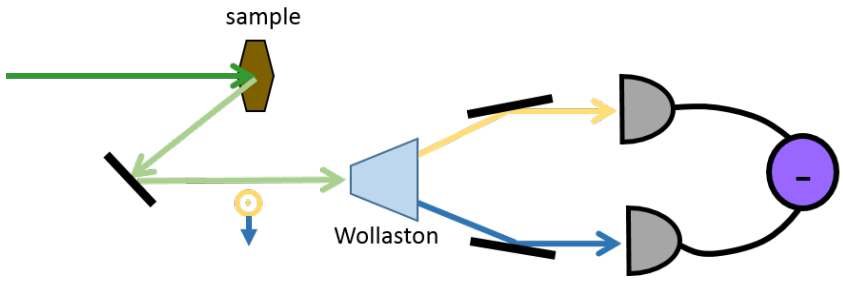

Fig. 5.14.: Birefringence acquisition set-up: the probe pulse is reflected by the sample and sent to a Wollaston prism, which separates the vertical and horizontal polarization component of the reflected signal.

Angle dependence of the transient reflectivity

In order to study the polarization dependence of a "standard" pump-probe signal after the interaction with the sample, the transient reflectivity can be described as a Raman-like process [97]. At the first order the transient reflectivity can be expressed as $\Delta R(\theta) = \frac{\partial R}{\partial \epsilon} \cdot \Delta\epsilon$, where $\Delta\epsilon = \frac{\partial \epsilon}{\partial f(\mathbf{q})} \cdot \Delta f(\mathbf{q})$, $\Re^{\mathbf{q}} = \frac{\partial \epsilon}{\partial f(\mathbf{q})}$ is a Raman-like tensor and $\Delta f(\mathbf{q})$ is the pump-induced change of the occupation around the Fermi surface. For our sample (D_{4h} symmetry) and our experimental configuration (the pump direction is orthogonal to the Cu-O plane of Bi2212) the photoinduced changes of the dielectric tensor can be decomposed as

$$\Delta\epsilon = \begin{bmatrix} a & 0 \\ 0 & a \end{bmatrix} + \begin{bmatrix} c & 0 \\ 0 & -c \end{bmatrix} + \begin{bmatrix} 0 & d \\ d & 0 \end{bmatrix}, \tag{5.10}$$

where $a = \Delta\epsilon^{A_{1g}}$, $c = \Delta\epsilon^{B_{1g}}$, $d = \Delta\epsilon^{B_{2g}}$.
Applying on both sides of the matrix an electric field like $\vec{E} = E_0 \binom{\cos\theta}{\sin\theta}$ one ends up with the relation

$$\Delta R(\theta) \propto \left(\Delta R_{A_{1g}} + \Delta R_{B_{1g}} \cos 2\theta + \Delta R_{B_{2g}} \sin 2\theta\right), \tag{5.11}$$

where θ represents the probe polarization rotation with respect to the the Cu-Cu axis of the crystal. Notice that, in general, ΔR_i is time-dependent.
In order to consider the polarization rotation induced by the sample at a certain pump-probe time delay, we introduce another angle α, which represents the polarization of the output beam (in an experimental set-up we can consider θ as the angle of the polarizer before the sample and α the angle of the polarizer, or analyzer, after the sample). In this case the matrix element is calculated on two different states (or electric fields), $\vec{E}_0 = \propto \binom{\cos\theta}{\sin\theta}$ and $\vec{E}_1 \propto \binom{\cos\alpha}{\sin\alpha}$ and the resulting transient reflectivity is

$$\Delta R(\theta, \alpha) \propto \left(\Delta R_{A_{1g}} \cos(\alpha - \theta) + \Delta R_{B_{1g}} \cos(\alpha + \theta) + \Delta R_{B_{2g}} \sin(\alpha + \theta)\right). \tag{5.12}$$

From equation 5.12 one can derive the most suitable configurations to select the desired Raman mode (A_{1g}, B_{1g} or B_{2g}). In particular if $\theta = \alpha$ it is not possible to isolate a single symmetry. In particular for some significant angles we get:

$\theta = \alpha$	ΔR
$0°$	$\Delta R_{A_{1g}} + \Delta R_{B_{1g}}$
$45°$	$\Delta R_{A_{1g}} + \Delta R_{B_{2g}}$
$90°$	$\Delta R_{A_{1g}} - \Delta R_{B_{1g}}$

On the other hand, crossed polarizations allow to select B_{1g} or B_{2g} modes, as shown in the following table

θ	α	ΔR
$0°$	$90°$	$\Delta R_{B_{2g}}$
$90°$	$0°$	$\Delta R_{B_{2g}}$
$45°$	$-45°$	$\Delta R_{B_{1g}}$
$-45°$	$45°$	$\Delta R_{B_{1g}}$

while the total symmetric A_{1g} mode can never be selected, although its relative high intensity makes all other contributions negligible in a parallel polarization measurements ($\theta = \alpha$).

Birefringent measurement can be treated with the same formalism, just by considering two orthogonal α angles and subtracting the two signals. In particular for $\theta = 0°$ and $\alpha_{1,2} = \pm 45°$ one gets

$$\Delta R_{1,2}(\theta) \propto \left(\frac{1}{\sqrt{2}} \Delta R_{A_{1g}} + \frac{1}{\sqrt{2}} \Delta R_{B_{1g}} \pm \frac{1}{\sqrt{2}} \Delta R_{B_{2g}} \right), \tag{5.13}$$

so $\Delta R_1 - \Delta R_2 \propto \Delta R_{B_{2g}}$.
Performing the same calculation for $\theta = 45°$ and $\alpha = 0°$ and $90°$, one gets $\Delta R_1 - \Delta R_2 \propto \Delta R_{B_{1g}}$.
The previous calculations shows that birefringent measurements (choosing suitable

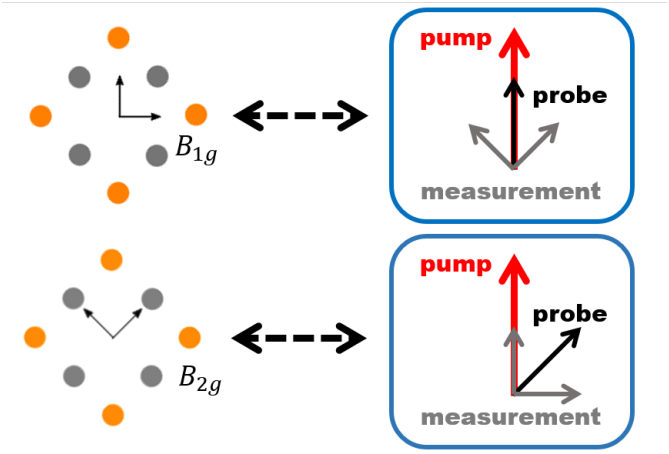

Fig. 5.15.: Measurement correspondence. Correspondence between "standard" pump-probe measurements (on the left) and birefringence measurements (on the right).

angles) can be an alternative way to acquire B_{1g} and B_{2g} signals. This trick is particularly convenient since the cross polarization measurements needed to select B_{1g} and B_{2g} signals can be disturbed by A_{1g} contributions, often present because

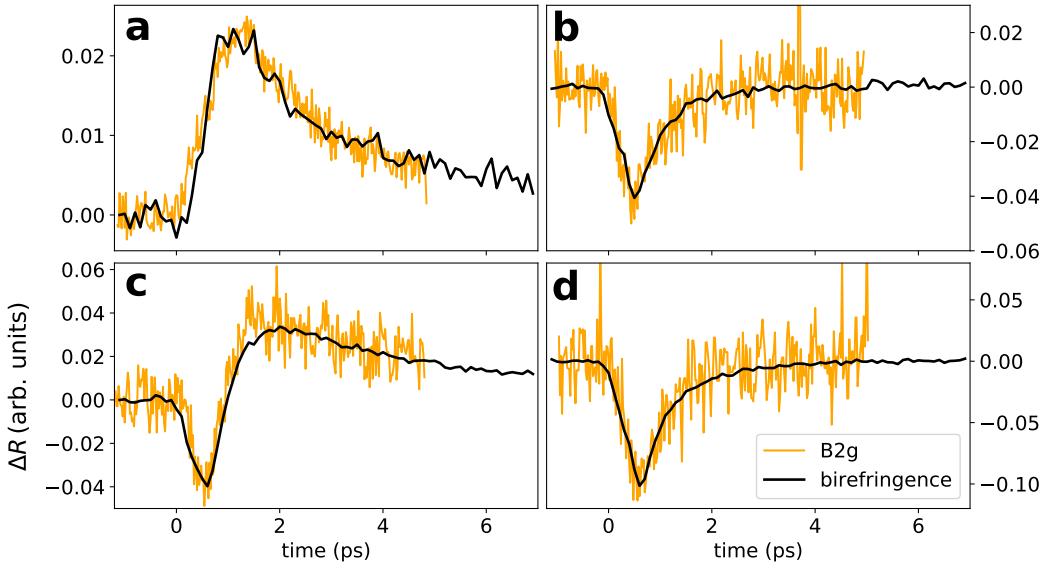

Fig. 5.16.: Measurement comparison. Comparison between a pump probe measurement performed in B_{2g} configuration (orange line) and a birefringence measurement (black line, obtained by subtracting the polarization components along the Cu-Cu axes), both in superconducting phase (**a** and **c**) and in pseudogap (**b** and **d**). The measurements have been performed in two different pump fluence regimes (about $0.2\,\mathrm{mJ/cm^2}$ in **a** and **b** and $1.3\,\mathrm{mJ/cm^2}$ in **c** and **d**). The signals have been rescaled in order to verify the proportionality between the two measurements.

of the high intensity of this symmetry signal with respect to the others (about 20 times more in the superconducting phase). As a matter of fact in a birefringence measurement the A_{1g} component is split in two contributions, which are equal if the polarization angles selected by the Wollaston prism ($\alpha_{1,2}$) are symmetric with respect to the probe polarization (θ). The final subtraction cancels completely the total symmetric contribution.
The summary of the correspondence between cross-polarization and birefringence measurements is summarized in Figure 5.15.

5.4.2 Results

B2g symmetry

In order to verify if the linear approximation we have considered in the previous section is consistent with our experimental results, we compare a "standard" B_{2g} measurement [74] (that is, a pump-probe measurement in which the probe polarization is along the Cu-O axis and the analyzer selects the orthogonal component) with a birefringence one, in which the signal polarization components along the Cu-Cu axis are subtracted. The results are shown in Figure 5.16: both in superconducting phase (Figure 5.16 **a** and **c**) and in pseudogap (figure 5.16 **b** and **d**) the signals

obtained by the two measurements are proportional, confirming the results derived from equation 5.13. Notice that the results are confirmed both for low and high pump fluence.

Using the birefringence set-up we were able to collect pump-probe signals at different temperatures, in order to focus on the phase transition between superconducting and pseudogap phases in this symmetries. We measured the effects of different pump fluences and wavelength, while the pump polarization was fixed in the Cu-Cu direction.

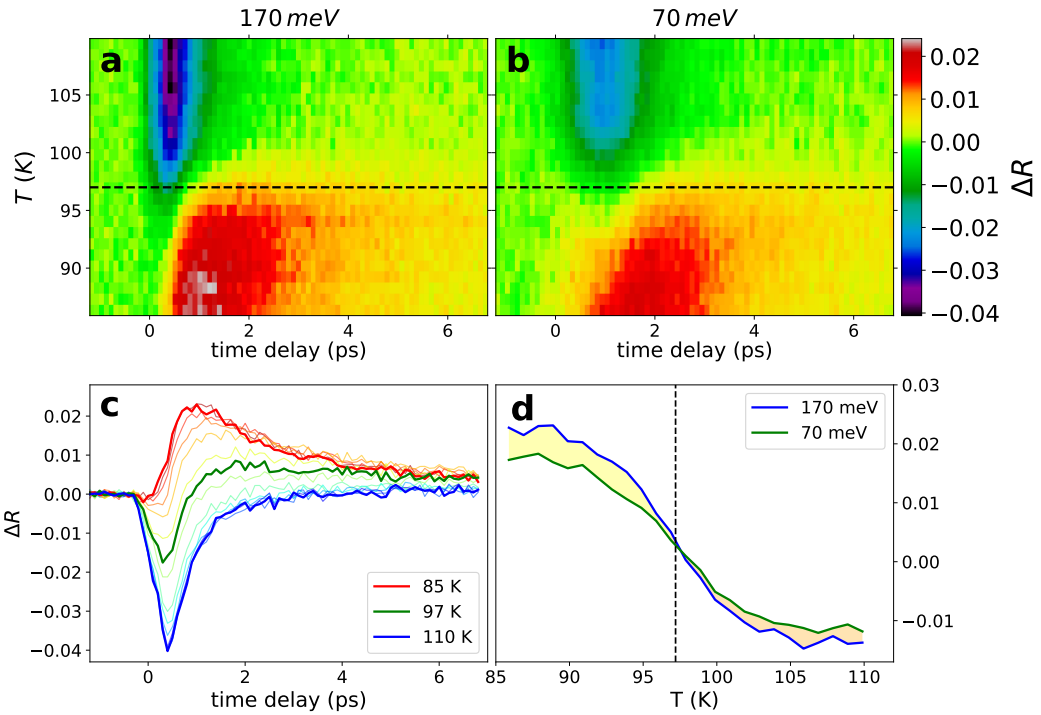

Fig. 5.17.: B_{2g} **temperature measurement - low pump fluence.** Comparison between temperature pump probe birefringence measurements, subtracting the polarization contributons along the Cu-Cu axes. **a** and **b** represent the temperature time resolved maps for two different photon energies (170 and 70 meV respectively). In **c** the transient reflectivity for different temperatures is plotted; marked lines represent the characteristic superconducting signal (red), the pseudogap one (blue), and the reflectivity measured at $T_c = 97\,K$ (green). The pump fluence is within the linear regime (about $0.2\,\mathrm{mJ/cm^2}$). In **d** two temperature dependencies at a fixed time delay are compared.

Figure 5.17 **a** and **b** shows the results of the temperature measurements for low pump fluence ($0.09\,mJ/cm^2$) at 170 meV ($h\nu > 2\Delta$) and 70 meV ($h\nu < 2\Delta$) pump photon energies. The details of the dynamics for each temperatures are shown in Figure 5.17 **c** for the high photon energy case. The results show a behavior similar to the one observed in the integrated polarization measurements: after a photon excitation of 70 meV, the sample dynamics is characterized by a higher signal (associated to a superconducting de-excitation, as shown by the red line in Figure 5.17 **c**), while the typical dip of the pseudogap transient reflectivity becomes visible

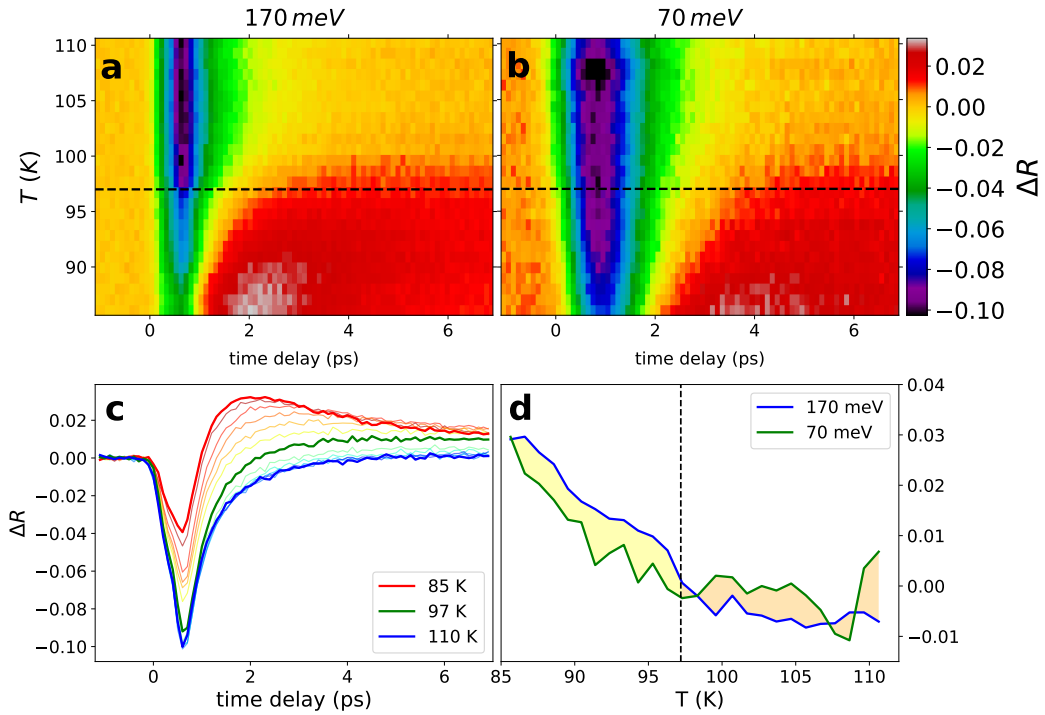

Fig. 5.18.: B_{2g} **temperature measurement - high pump fluence.** Maps **a** and **b** show the temperature time-resolved maps for the usual photon energies ($h\nu > 2\Delta$ and $h\nu < 2\Delta$ respectively). In **c** several horizontal cuts of map **a** are plotted; marked lines represent the characteristic superconducting signal (red), the pseudogap one (blue), and the reflectivity measured at $T_c = 97\,K$ (green). The pump fluence is within the non-linear regime (about $1.3\,\mathrm{mJ/cm^2}$). In **d** two temperature dependencies at a fixed time delay (white line in maps **a** and **b**) are compared. Because of the slowdown of the dynamics in the low energy case (due to the higher pump duration), in order to compare the two reflectivities, we chose the time delay in which the maximum signal at 80 K is reached.

only at higher temperatures. This behavior is highlighted by Figure 5.17 **d**, where the temperature response at a fixed time delay between pump and probe is shown (the plotted one refers to the minimum of the pseudogap signal). We observe an increase of the low photon energy signal around and above the critical temperature T_c, marked by the yellow area.

Similar results have been obtained through high fluence measurements (Figure 5.18).

B1g symmetry

Analogous measurements have been performed by rotating the probe and analyzer polarization of $45°$, in order to select the B_{1g} symmetry through the usual birefringence measurements. In this case the results seems to be even more affected by the photon energy, since the transient reflectivity after a high and low photon energy excitation shows quite a different behavior at each temperature, both in low and high fluence regimes. In particular low photon energy de-excitations are characterized by bigger time decays with respect to high photon energies one.

This effect is clearly visible in Figure 5.19 and 5.20 **c** and **d**, where the transient reflectivity at several temperatures is plotted. In particular the pseudogap and $T = T_c$ responses show an evident divergence of the time decay for low photon energy excitation, which is not visible for high photon energy excitations. This discrepancy seems not to be due just to different pump duration (always relevant when the pump wavelength is modified), since we observe qualitatively different responses for the two excitation photon energies. The effect is even more evident at short time delays, were 170 meV excitation generate a positive instantaneous pseudogap response, while $h\nu < 2\Delta$ seems to be responsible of a negative pseudogap transient reflectivity around t=0.

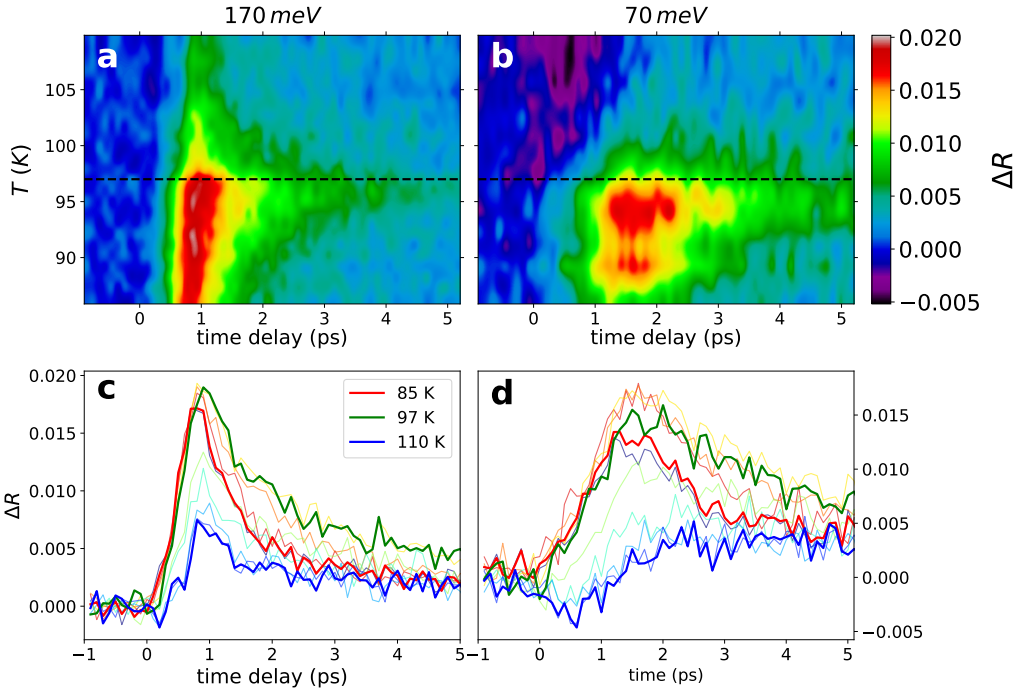

Fig. 5.19.: B_{1g} **temperature measurement - low pump fluence.** Maps **a** and **b** show the temperature time-resolved maps for $h\nu > 2\Delta$ and $h\nu < 2\Delta$ respectively. In **c** and **d** several horizontal cuts of map **a** and **b** are plotted; marked lines represent the characteristic superconducting signal (red), the pseudogap one (blue), and the reflectivity measured at $T_c = 97\,K$ (green). The pump fluence is within the linear regime (about $0.2\,\mathrm{mJ/cm^2}$).

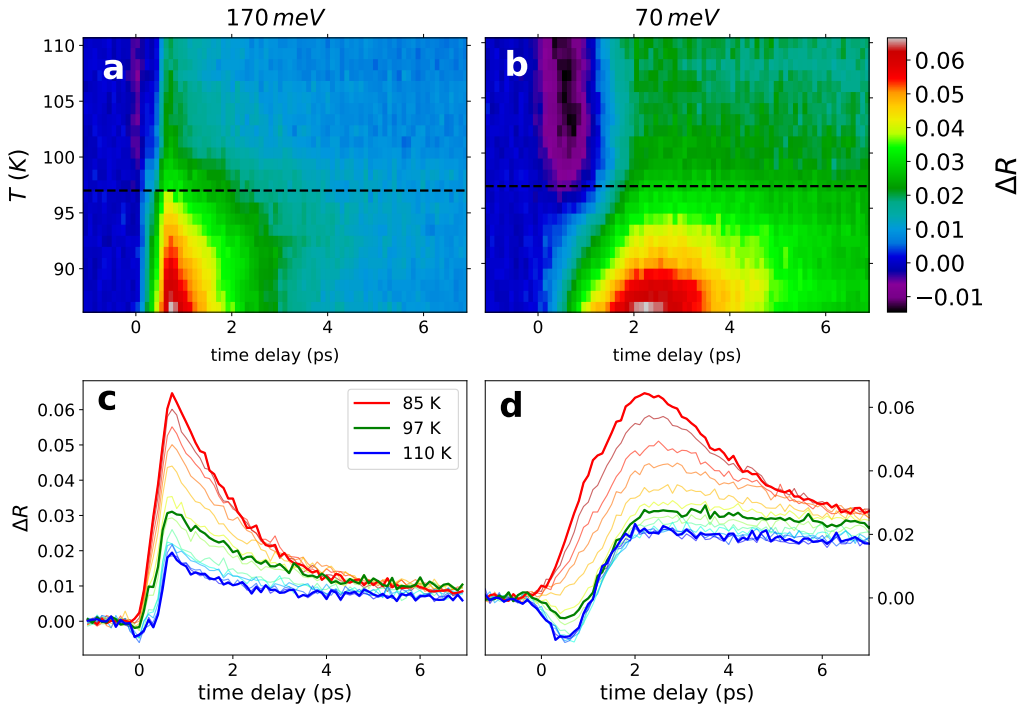

Fig. 5.20.: B_{1g} **temperature measurement - high pump fluence.** Maps **a** and **b** show the temperature time-resolved maps for $h\nu > 2\Delta$ and $h\nu < 2\Delta$ respectively. In **c** and **d** several horizontal cuts of map **a** and **b** are plotted; marked lines represent the characteristic superconducting signal (red), the pseudogap one (blue), and the reflectivity measured at $T_c = 97\,K$ (green). The pump fluence is within the non-linear regime (about $1.3\,\mathrm{mJ/cm^2}$).

5.5 Conclusion

The scenario that emerges from our pump-probe experiments (for both polarization integrated measurement and selected Raman modes) reveals the capability to enhance the transient response associated with superconducting fluctuations in cuprates by means of photo-excitations with low-energy photons polarized in the Cu-Cu direction. The effective *d*-wave BCS description of the interaction of the superconductor and pulsed electromagnetic radiation is in qualitative agreement with the experimental results. Moreover it allows us to ascribe the observed dynamical increase of the superconductive response to a light-driven enhancement of phase coherence below and above T_c, where thermodynamic constraints make the superconducting equilibrium state unattainable. The revealed field-driven increase of phase coherence highlights the possibility of driving the onsets of quantum coherence in complex oxides.

Part II

Fluctuation Dynamics in Pump-Probe Measurements

The word “noise” in experimental physics (but even in everyday life) has always conveyed a negative connotation and been associated to a useless phenomenon which overcomes the interesting information, or, at least, compromises its comprehension. In this work we would like to overturn completely the point of view: if we cannot avoid the presence of noise (at least of some kinds of noise), why don’t we exploit it in order to get more information on the system under study?
The following chapters describe this new approach to time resolved measurements and the kind of information that can be extracted from it.

“Standard” time resolved techniques detect the transient reflectivity or transmittance of a sample after a certain excitation. In other words, the pump-probe technique measures the variation of the *mean* number of photons transmitted or reflected by the sample after the excitation (see chapter 3). The *mean* is a powerful tool, which allows to study the average behavior of a certain quantity. On the other hand, the mean (or expected) value is not enough to completely define a statistics: even the common and simple gaussian distribution requires another parameter: the *variance* (or its square root, named standard deviation). More complicated distributions are characterized by higher order moments (the variance is the second order one and represents the width of the distribution, so it is related to the concept of *noise*). The purpose of the second part of my PhD project is to go beyond the mean value pump-probe measurements and to study the variation of the distribution (and in particular the noise on the photon number) of the probe signal, produced by the interaction with the excited sample.

In standard experiments the probe intensity is measured by integrating the signal in the time domain (typically on hundreds of milliseconds) using, for instance, a lock-in amplifier. The system provides very clean measurements, in which the noise is considerably reduced by the average on hundreds of pulses. The limit of this detection system is that the reduction of the noise affects not only the environmental one but also the intrinsic fluctuations of the detected signal, which could be induced by intrinsic properties of the sample, such as quantum fluctuations. The capability to detect these quantum effects, although indirectly, is quite sought, since it is clear now that their consequences could affect condensed matter even at “high temperatures” [21]: for example, fluctuations of the atomic positions are the origin of material properties such as quantum paraelectricity [27], high temperature superconductivity and quantum phase transitions in general [82, 81].

Therefore, the perspective and the aims of a time resolved measurement can change completely by implementing a single pulse acquisition, in which the number of photons of each probe pulse, after the interaction with the sample, can be observed. This detection technique provides the whole statistical distribution of the probe photon number as a function of time. The aim is to understand if, and eventually

how, the photon distribution (and in particular photon number fluctuation) dynamics can carry additional information on the sample with respect to the mean photon number.

Measurements

The measurements presented in the next chapters combine time resolved spectroscopy with photon number distribution, resulting in the detection of the photon number statistics for each time delay between the excitation and the probe pulse.
A sketch of the measurement concept is shown in Figure II1: in **a** a mean photon

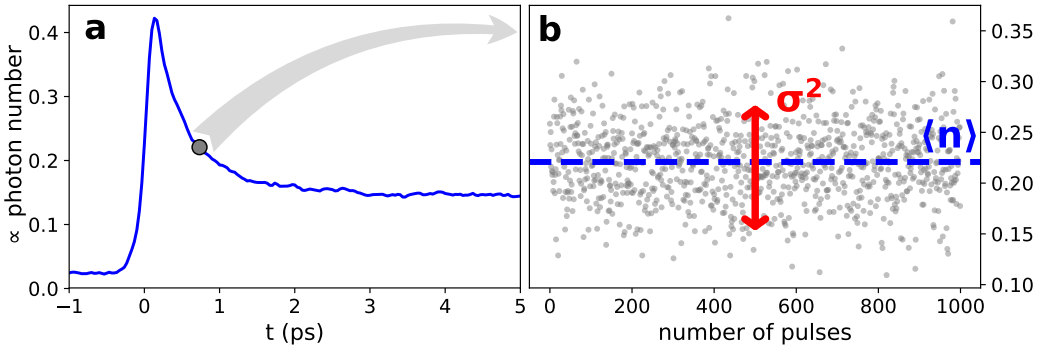

Fig. II1.: **Concept of a distribution measurement.** **a** Example of time resolved mean photon number measurement. **b** Measurement of pulse intensities for a fixed time delay between the excitation and the probe pulse (grey point in **a**). The mean value of the pulse intensities $\langle \hat{n} \rangle$ is marked by a blue dashed line, while the noise σ is indicated by the red arrow.

number measurement is shown in which a certain time delay is selected (grey point); Figure II1**b** shows the single pulse measurement for the chosen time delay. Both the mean value $\langle \hat{n} \rangle$ (blue dashed line) and the noise amplitude σ (red arrow) are highlighted.
These quantities can be trivially calculated for each time delay through the relations $\langle \hat{n} \rangle \propto \frac{1}{N} \sum_i I_i$ and $\sigma \propto \sqrt{\frac{1}{N-1} \sum_i (I_i - \bar{I})^2}$ (where I_i is the intensity of the i^{th} pulse and N is the number of pulses) and then, if needed, averaged on tens of scans, in order to improve the quality of the measurement.

The general result of this time dependent photon distribution is shown in Figure II2 **a**, where the x-axis represents the time delay between the pump and the probe, the y-axis is the photon intensity (which is proportional to the photon number) and the colors refers to the number of pulses with a certain intensity. Therefore, each vertical line in the measurement is the histogram of the photon number distribution at a fixed time delay. The response of the typical pump-probe measurement is plotted in Figure II2**b** and can be obtained just by calculating the intensity mean value $\langle \hat{n} \rangle$ for

the N measured pulses of every time delay. Notice that a similar result could have been obtained through a lock-in amplification system.

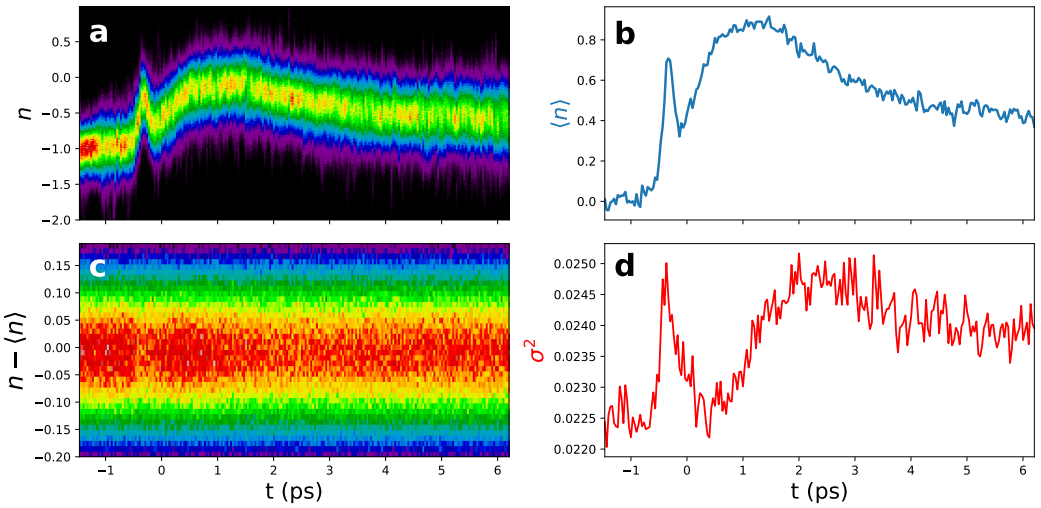

Fig. II2.: **Typical result of a distribution measurement.** **a** Histograms of the photon number distribution as a function of the time delay between pump and probe: the x-axis represent the time delay, the y-axis the intensity associated to the photon distribution, while the color scale represents the number of pulses of a certain intensity. **b** Transient reflectivity (intensity) in a pump probe experiment. **c** Histograms rescaled by the mean intensity value as a function of time. **d** Time dependent variance (related to the broadening of the histograms plotted in **c**).

The variation of the photon distribution can be highlighted by subtracting the mean value $\langle \hat{n} \rangle$ to the original intensity data, as displayed in Figure II2**c**. This representation allows to draw the attention to the evolution of higher statistical moments. In particular, from now on, we will focus only on the second moment, or variance $\sigma^2 = \frac{1}{N-1} \sum_i \left(I_i - \bar{I} \right)^2$, which is related to the width of the distribution and so to the amplitude of the noise.

6 Noise in time domain measurements: a quantum model

In this chapter the theoretical bases for the interpretation of a statistical differential measurement are given.
The experimental set-up used to get the fluctuation results is described by a theoretical quantum model. The main point of the model is the treatment of each dissipative process of the experiment as a *Beam Splitter*, a device which transmits a certain percentage of the incoming beam (signal) and reflects the remaining part (dissipation[1]). We will start from the effect of a single Beam Splitter on the input beam (with particular attention to the so-called *Shot-Noise measurement*) and we will increase progressively the complexity by adding more and more dissipators, such as filters, polarizers and the sample itself.

6.1 Model concept

In this section we present a quantum model to describe the dissipation processes of the optical experimental set-up of Figure 3.8. The model is based on the assumption that any dissipative process (absorption of the sample, transmission through a filter etc.) can be described as a Beam Splitter which splits the beam in two, with a defined intensity percentage: for instance, the transmitted beam can serve as the selected beam and the reflected beam is dissipated. For example, to describe a polarizer, the beam transmitted from the beam splitter represents the selected polarization, while the reflected one is the orthogonal polarized one.

In order to understand the effects of the dissipation processes of each component of the experiment, we will start from very simple modeled set-ups and then increase the complexity by adding optical elements (and correspondingly Beam Splitters in the model).

In particular, the following measurements and set-ups will be described:

[1] In the following we will call *dissipation* the beam which is not selected in the experiment. It can refer to the reflected beam is we use a certain optical element in transmission (or vice versa), the absorbed or scattered radiation and so on

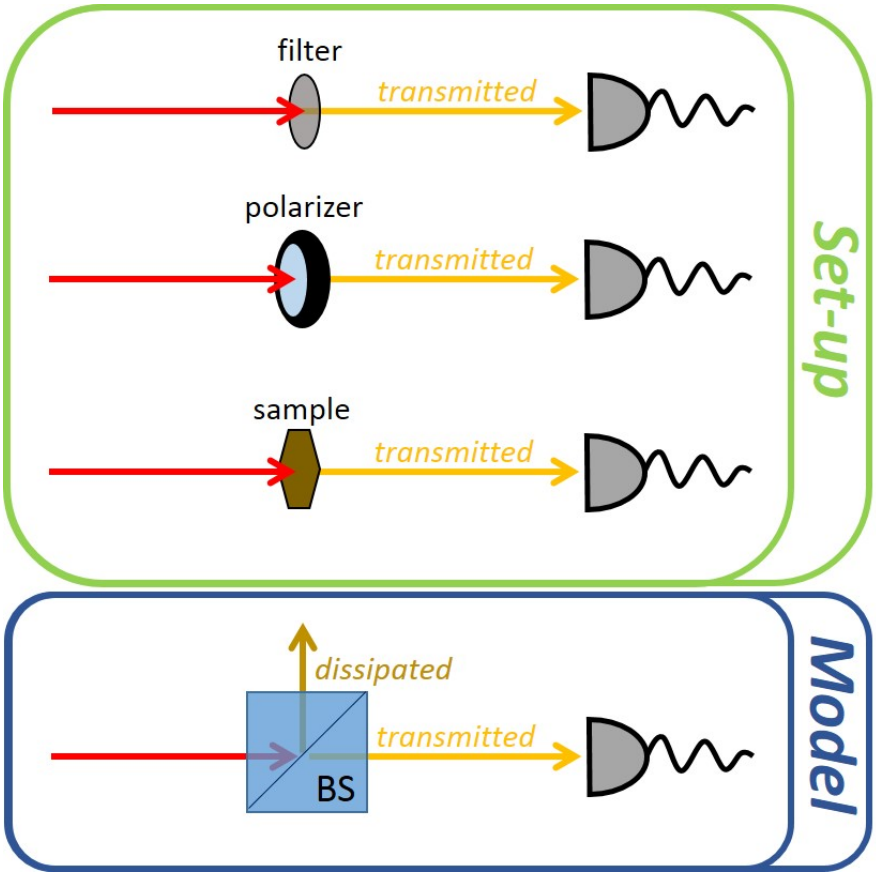

Fig. 6.1.: Description of dissipative effects. Example of simple experimental set-ups which describes a dissipation process: transmission of a light beam through a filter, a polarizer, a sample and detection of the final beam. All these optical elements can be described as a Beam Splitter, which transmit a certain percentage of the original beam. The remaining part represent the dissipated radiation and is not detected.

1. differential acquisition with no dissipation on the beams and its role in the reduction of the environmental noise;

2. single Beam Splitter: mean and variance of the split beams;

3. Shot-Noise measurements: differential detection of the photons coming from a single Beam Splitter;

4. intensity attenuation (filtering) after beam splitting and its effects on the final noise.

6.2 Differential Acquisition

In the first section we consider a very simple set-up: a differential single pulse acquisition with no dissipation, like the one sketched in Figure 6.2.
In first approximation we can describe the acquisition system as made up of two

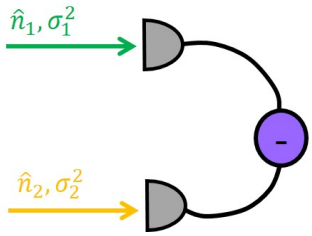

Fig. 6.2.: Differential acquisition set-up Sketch of the differential acquisition set-up for two non-correlated pulses with photon number $\hat{n}_1$ and $\hat{n}_2$ and variance σ_1^2 and σ_2^2.

photodiodes, which measure the light intensity of any incoming pulse, and the electronic part, which performs the difference between the intensities of pulses 1 and 2 and then amplifies the differential signal. No constraint on the input pulses is taken into account now, exception made for the absence of correlation between the light states 1 and 2, which will be identified through their number operators $\hat{n}_1$ and $\hat{n}_2$ and to the variance of the photon number σ_1^2 and σ_2^2 respectively.

The mean differential intensity measured in this experiment is proportional to the differential photon number

$$\langle \hat{n}_1 - \hat{n}_2 \rangle = \langle \hat{n}_2 \rangle - \langle \hat{n}_1 \rangle, \tag{6.1}$$

whereas the variance of the photon number is

$$\sigma_{1-2}^2 = (\langle \hat{n}_1 - \hat{n}_2 \rangle)^2 - \langle (\hat{n}_1 - \hat{n}_2)^2 \rangle = \sigma_1^2 + \sigma_2^2. \tag{6.2}$$

Equation 6.2 shows that, if the input states are not correlated, the noise of the differential number of photons is the sum of the noise of the single pulses.
Notice that in our set-up the two pulses are always correlated, since they come from the same laser source (see Figure 3.8). Anyway this hypothesis highlights that if some non correlated constant noise impinges on one diode, the effect on the detection is just a rigid shift of both mean and variance, which in principle should not affect the dynamics of a time domain response.

Of course in this configuration the differential acquisition has no practical advantage with the respect to the measurement of the single signals separately (on the contrary it increases the noise of the measurement - Equation 6.2). A real improvement is

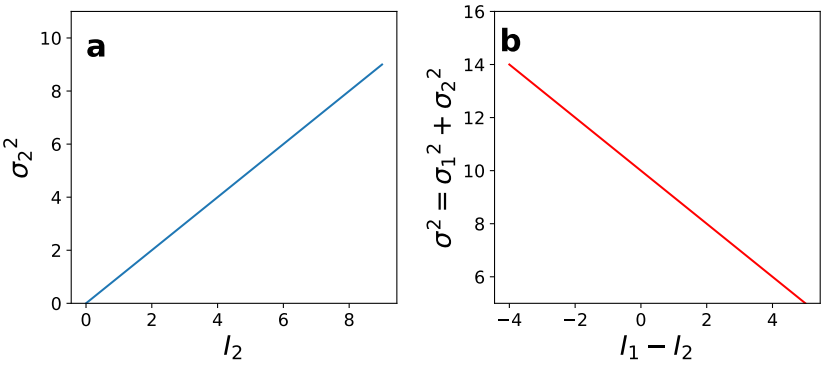

Fig. 6.3.: Variance for a photon poissonian distribution. **a** Variance *vs* mean photon number graph for a Poissonian distribution. **b** Simulated variance of the differential signal as a function of the intensity signal itself for a Poissonian distribution of the number of photons. Pulses 1 and 2 are supposed not to be correlated. In the plot just the pulse 2 has been tuned.

obtained when a systematic environmental signal $\hat{n}_3$ is detected by both the diodes: in this case the $\hat{n}_3$ contribution is cancelled both in the mean value and in the variance, because of the differential acquisition.

Notice that in the particular case of a Poissonian distribution of the photon number (in which $\sigma^2 = \langle \hat{n} \rangle$) for both pulses, the variance of the differential photon number is linear with respect to the differential intensity, as shown in Figure 6.3.

6.3 Beam Splitter

In this section we describe the Beam Splitter (BS), a dielectric medium able to split a beam into two with a certain proportion. This optical element is the core of the model, since the treatment [60] not only describes a real BS, but also whatever dissipator or adsorber.

A representation of a lossless BS is shown in Figure 6.4, in which two beams, that we will indicate with their annihilation operators $\hat{a}_1$ and $\hat{a}_2$, are impinging on it and two other beams ($\hat{a}_3$ and $\hat{a}_4$) are emerging from it. We can write the relation between output and input states as

$$\hat{a}_3 = R\hat{a}_1 + T\hat{a}_2 \tag{6.3}$$

and

$$\hat{a}_4 = T\hat{a}_1 + R\hat{a}_2, \tag{6.4}$$

where R and T represent the Fresnel reflection and transmission coefficients of the BS.

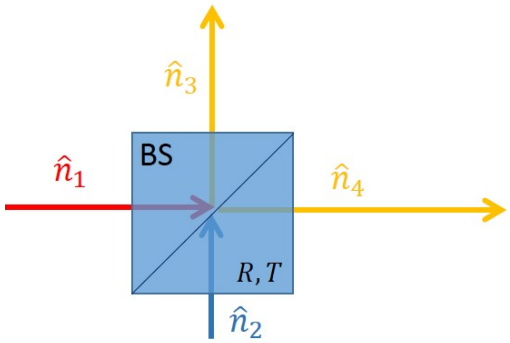

Fig. 6.4.: Representation of a lossless Beam Splitter. The incoming beams $\hat{n}_1$ and $\hat{n}_2$ are combined through the Beam Splitter in the output beams $\hat{n}_3$ and $\hat{n}_4$. In a quantum treatment $\hat{n}_2$must always be present, although no laser beam enters the BS on that side: in this case $\hat{n}_2$ is described by the vacuum state $|0\rangle$.

The output photon number operators are related to the input annihilation and creation operators by the relations

$$\begin{aligned}\hat{n}_3 &= \hat{a}_3^\dagger \hat{a}_3 \\ &= |R|^2\, \hat{a}_1^\dagger \hat{a}_1 + R^* T \hat{a}_1^\dagger \hat{a}_2 + T^* R \hat{a}_2^\dagger \hat{a}_1 + |T|^2\, \hat{a}_2^\dagger \hat{a}_2\end{aligned} \tag{6.5}$$

$$\begin{aligned}\hat{n}_4 &= \hat{a}_4^\dagger \hat{a}_4 \\ &= |T|^2\, \hat{a}_1^\dagger \hat{a}_1 + T^* R \hat{a}_1^\dagger \hat{a}_2 + R^* T \hat{a}_2^\dagger \hat{a}_1 + |R|^2\, \hat{a}_2^\dagger \hat{a}_2.\end{aligned} \tag{6.6}$$

Since we are considering a lossless BS, we expect that the total number of photon is conserved, that is $\hat{n}_3 + \hat{n}_4 = \hat{n}_1 + \hat{n}_2$; from the previous relation and equations 6.5 and 6.6 one can obtain the fundamental BS equations

$$|T|^2 + |R|^2 = 1 \tag{6.7}$$

$$RT^* + TR^* = 0, \tag{6.8}$$

which allow to demonstrate that, if the input states are independent and fulfill the boson commutation relations $\left[\hat{a}_1, \hat{a}_1^\dagger\right] = \left[\hat{a}_2, \hat{a}_2^\dagger\right] = 1$ and $\left[\hat{a}_1, \hat{a}_2^\dagger\right] = \left[\hat{a}_2, \hat{a}_1^\dagger\right] = 0$, also the output state are described by the same commutation relations. Moreover, just separating modulus and phase in equation 6.8, one get the phase relation between $R = |R|\, e^{\phi_R}$ and $T = |T|\, e^{\phi_T}$, which is $\phi_R - \phi_T = \pm\frac{\pi}{2}$.

From equations 6.3-6.6, we can compute the mean number of photons and the related variance for each output beam. The expressions for the mean photon number are:

$$\langle \hat{n}_3 \rangle = |R|^2 \langle \hat{n}_1 \rangle + |T|^2 \langle \hat{n}_2 \rangle \tag{6.9}$$

$$\langle \hat{n}_4 \rangle = |T|^2 \langle \hat{n}_1 \rangle + |R|^2 \langle \hat{n}_2 \rangle. \tag{6.10}$$

The same calculation can be done for the related variances. From now on we will only consider the particular case in which the state $\hat{n}_2$ is a vacuum state (that means that just one laser beam $\hat{n}_1$ impinges on the BS), so we report the expression of the variances in this simplified case:

$$\sigma_3^2 = |R|^4 \sigma_1^2 + |T|^2 |R|^2 \langle \hat{n}_1 \rangle \tag{6.11}$$

$$\sigma_4^2 = |T|^4 \sigma_1^2 + |T|^2 |R|^2 \langle \hat{n}_1 \rangle. \tag{6.12}$$

Both expressions of the variance contains two terms: the first one is due to the input noise σ_1^2 (*Classical* noise), while the second is caused by the random division of the input photon stream in the two outputs with probabilities $|R|^2$ and $|T|^2$ (*Partition* noise).

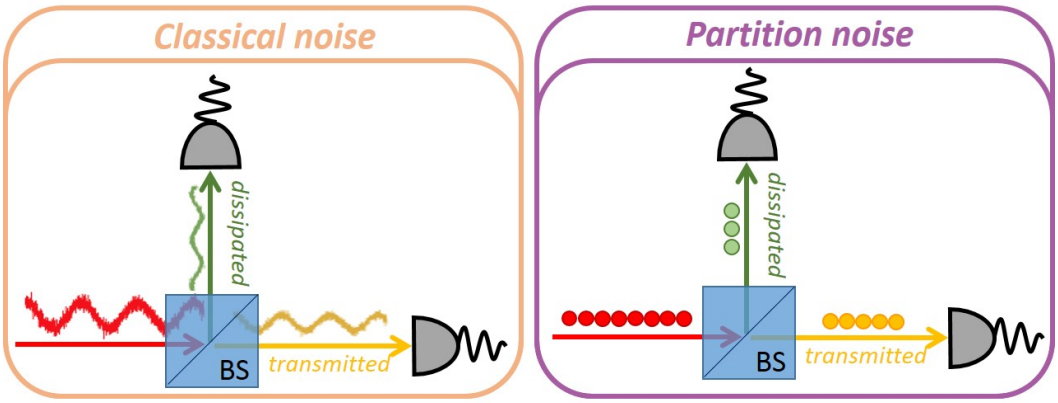

Fig. 6.5.: Classical *vs* Partition noise. Pictorial representation of the two noise components of equations 6.11 and 6.12. The *classical* noise is related to the intensity of the transmitted or reflected beam, whereas the 6.5 one is due to the particle nature of light: although the mean value of $\hat{n}_3$ and $\hat{n}_4$ are equal, single measurements are characterized by fluctuations of the number of transmitted or reflected photons.

Single beam

The next step is the study of the measurements of just one of the outputs of the Beam Splitter, detecting both its mean photon number and the related variance, as shown in Figure 6.6. In this case the Beam Splitter can have whatever value of $|T|^2$ (provided that it is less than one), thus representing a general attenuator or absorber, like a filter, a combination of half-wave plate and polarizer or a sample. The reflected number of photons, which depends on the parameter $|R|^2 = 1 - |T|^2$, serves as the dissipated portion of the initial beam and therefore is not detected by the photodiode.

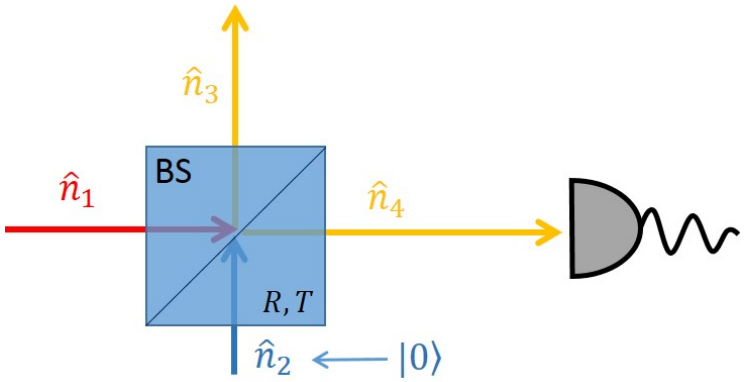

Fig. 6.6.: One beam Splitter output. Set-up for the differential measurement of one output of the Beam Splitter. Beam 1 is the "real" laser input, whereas Beam 2 represents a vacuum state.

From the results 6.1, 6.2, one easily gets that the measured mean value is

$$\langle \hat{n}_4 \rangle = |T|^2 \langle \hat{n}_1 \rangle, \tag{6.13}$$

while the variance is

$$\sigma_4^2 = |T|^4 \sigma_1^2 + |T|^2 |R|^2 \langle \hat{n}_1 \rangle. \tag{6.14}$$

As an example notice that a Poissonian distribution of the input photon number ($\langle \hat{n}_1 \rangle = \sigma_1^2$ in Figure 6.6) generates still a linear dependence of the variance on the measured mean photon number ($\sigma_4^2 = \langle \hat{n}_4 \rangle$, which means $\sigma_4^2 \propto |T|^2$, if the input mean photon number $\langle \hat{n}_1 \rangle$ remains constant).

On the other hand, if we move to a more general case, in which $\hat{n}_1 \neq \sigma_1^2$, the expression for the variance becomes

$$\sigma_4^2 = \frac{\sigma_1^2 - \langle \hat{n}_1 \rangle}{\langle \hat{n}_1 \rangle} X^2 + X, \tag{6.15}$$

where $X = \langle \hat{n}_4 \rangle$ is the detected mean value.
So, the dependence of the variance on the measured average is quadratic (a poissonian distribution is a limit case) and the concavity is determined by the ratio between the variance and the mean number of photons of the original state $|1\rangle$. The most common case is the superpoissonian distribution, for which $\sigma_1^2 > \langle \hat{n}_1 \rangle$ and the coefficient $\frac{\sigma_1^2 - \langle \hat{n}_1 \rangle}{\langle \hat{n}_1 \rangle} > 0$, such that $\sigma_4^2(X)$ is a parabola with positive concavity (for subpoissonian distributions the concavity is opposite). In particular the point of minimum variance is at $X_0 = -\frac{\langle \hat{n}_1 \rangle}{2\left(\sigma_1^2 - \langle \hat{n}_1 \rangle\right)}$, which tends to zero if the variance is much higher than the mean number or vice versa.

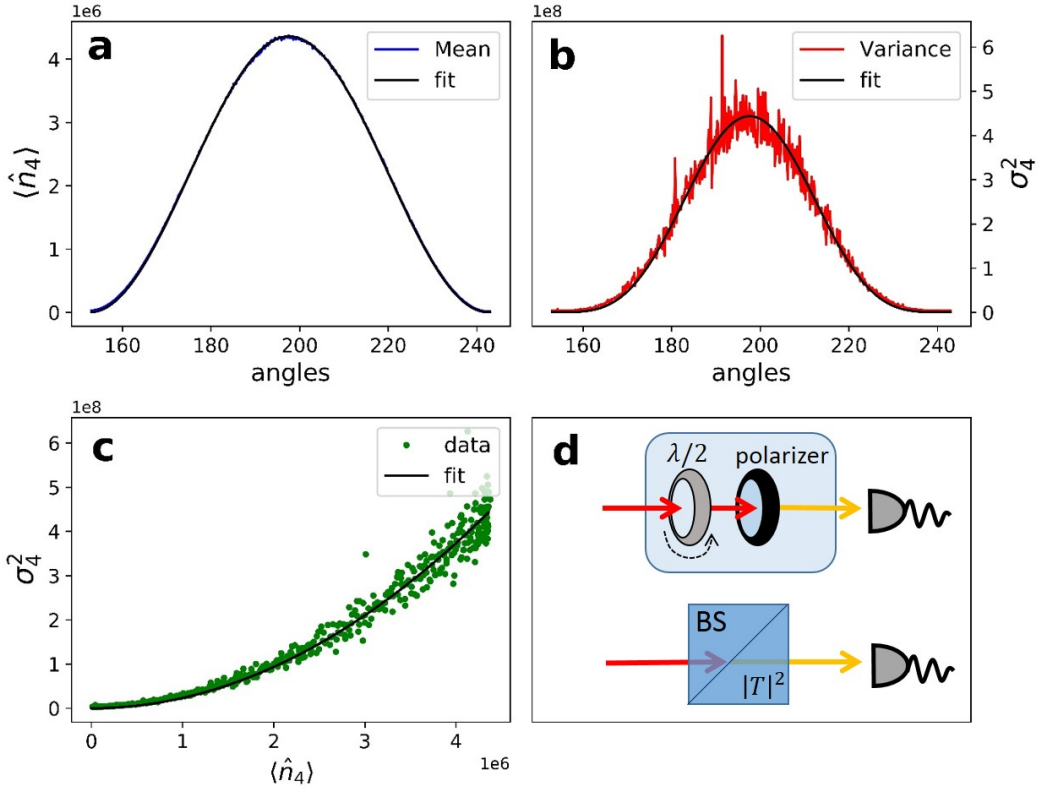

Fig. 6.7.: Mean and variance measurements as a function of the beam attenuation. In our experimental set-up the changes in $|T|^2$ are due to the combination of half-wave plate and polarizer, so variations of the intensity are related to the rotation of the half-wave plate with respect to the polarizer axis. In **a** and **b** the blue and red lines represent the detected intensity and variance respectively as a function of the angle of the half-wave plate. In **c** the detected variance is plotted as a function of the measured intensity (green points). The black line is the result of the fit with the function 6.15. **d** shows the set-up used for the measurement and its BS model representation.

In Figure 6.7 the results of the described measurements are shown, together with the fit obtained from equation 6.15. The mean value can be modified by changing the initial number of photons or the BS transmittance. We chose the second option, since it allows to keep the same input conditions ($\langle \hat{n}_1 \rangle$ and σ_1^2) and to study the variance behavior as a function of one parameter.
In order to tune the transmission $|T|^2$ of the effective BS, we used a combination of a half wave plate $\lambda/2$ (which rotates the polarization of the beam) and a polarizer (which instead selects a defined polarization). In Figure 6.7 **a** and **b** the x-axis represents the angle of rotation of the half wave plate, while the y-axis is the mean (blue line) and the variance (red line) of the number of photons and the fits (black lines) with the *Malus Law*[2] for polarizers and Equation 6.14 respectively. Figure 6.7 **c** displays the relation between variance and mean, which shows the expected

[2]The *Malus Law* states that if a light beam of intensity I_0 impinges on a perfect polarizer, the intesity of the transmitted beam is $I = I_0 \cdot \cos^2 \theta$, where θ is the angle between the polarization direction of the incoming beam and the polarization selected by the polarizer itself.

parabolic behavior. The fit (black line) has been obtained through the function 6.15. From now on we will refere to the variance dependence on the measured mean value ($\sigma^2(\hat{n}_1)$) as *characterization function*, since it allows to characterize the systematic noise related to a certain signal intensity.

6.4 Shot noise

The concept of *Shot noise* is related to the intrinsic fluctuations of the photon number, due to the particle nature of light and is strictly related to the *Partition noise* introduced in section 6.3 and to Figure 6.5. It is the minimum noise level that you can measure, since it comes from *intrinsic* fluctuations of the number of photons.

The experimental set-up used to measure the shot noise level combines the differential acquisition and the BS treatments we have introduced in the previous sections. A sketch of the set-up is shown in Figure 6.8, where $\hat{n}_1$ is the beam coming from the laser and $\hat{n}_2$ is a vacuum state. Starting form equations 6.5 and 6.6 we can compute

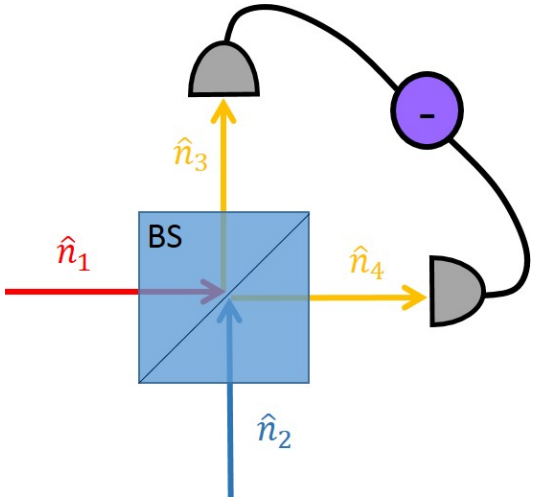

Fig. 6.8.: Sketch of the Shot Noise set-up. A laser beam $\hat{n}_1$ is split in two beams $\hat{n}_3$ and $\hat{n}_4$ and then the noise on the intensity difference $\hat{n}_3 - \hat{n}_4$ is acquired. Notice that in a quantum mechanical description the second input beam $\hat{n}_2$ must be present and described as a vacuum state.

the measured **mean value**, that is

$$\langle \hat{n}_{3-4} \rangle = \langle \hat{n}_3 - \hat{n}_4 \rangle = \left(|R|^2 - |T|^2 \right) \langle n_1 \rangle , \tag{6.16}$$

where $|R|^2$ and $|T|^2$ are the reflectance and transmittance of the beam splitter. For a perfect 50:50 beam splitter $|R| = |T| = \frac{1}{\sqrt{2}}$, so we get

$$\langle \hat{n}_3 - \hat{n}_4 \rangle = 0, \tag{6.17}$$

as expected even at the classical level.

The measured **variance** is

$$\sigma^2_{3-4} = \left\langle (\hat{n}_3 - \hat{n}_4)^2 \right\rangle - \left(\langle \hat{n}_3 - \hat{n}_4 \rangle \right)^2 = \left(|R|^2 - |T|^2 \right)^2 \sigma_1^2 + 4 |R|^2 |T|^2 \langle n_1 \rangle . \quad (6.18)$$

For a perfect 50:50 beam splitter we have $|R| = |T| = \frac{1}{\sqrt{2}}$ and a phase difference $\phi_R - \phi_T = \frac{\pi}{2}$ [60], so we get the Shot Noise relation

$$\sigma^2_{3-4} = \langle n_1 \rangle . \quad (6.19)$$

The Shot Noise test has been performed on our set-up in order to characterize the acquisition system. The measurement has been executed by acquiring the variance of the differential signal as a funcion of the intensity of the original beam $\hat{n}_1$. The result is plotted in Figure 6.9. The linear dependence of the variance as a function of the incoming mean number of photons $\langle \hat{n}_1 \rangle$ is directly due to the shot noise, while the positive background represents the electronic noise, which is just related to the detection process and is independent of $\langle \hat{n}_1 \rangle$. In this configuration the shot noise is the minimum reachable noise level for a certain intensity of the input beam $\hat{n}_1$.
As a matter of fact, if we rewrite equation 6.18 as a function of the mean value $X = \langle \hat{n}_{3-4} \rangle = \left(|R|^2 - |T|^2 \right) \langle \hat{n}_1 \rangle = \left(1 - 2 |T|^2 \right) \langle \hat{n}_1 \rangle$, one gets

$$\sigma^2_{3-4} = \frac{\sigma_1^2 - \langle \hat{n}_1 \rangle}{\langle \hat{n}_1 \rangle^2} X^2 + \langle \hat{n}_1 \rangle , \quad (6.20)$$

which is a parabola centered in $X = 0$ (that means perfect balancing between the two branches, and so $|R|^2 = |T|^2 = \frac{1}{2}$).
For superpoissonian statistics ($\sigma_1^2 > \langle \hat{n}_1 \rangle$) the minimum noise is reached at $\sigma^2_{3-4}(X = 0) = \langle \hat{n}_1 \rangle$, which is the shot noise level[3], therefore any deviation from the perfect 50:50 splitting ($X \neq 0$) induces an increase of the measured variance. Notice that for a poissonian statistics ($\sigma_1^2 = \langle \hat{n}_1 \rangle$) the shot noise limit is always guaranteed, since σ^2_{3-4} does not depend on the unbalancing X.

The shot noise test for our detector is plotted in Figure 6.9

[3] $X = 0$ means $\langle \hat{n}_3 \rangle = \langle \hat{n}_4 \rangle$ or $|T|^2 = |R|^2 = \frac{1}{2}$

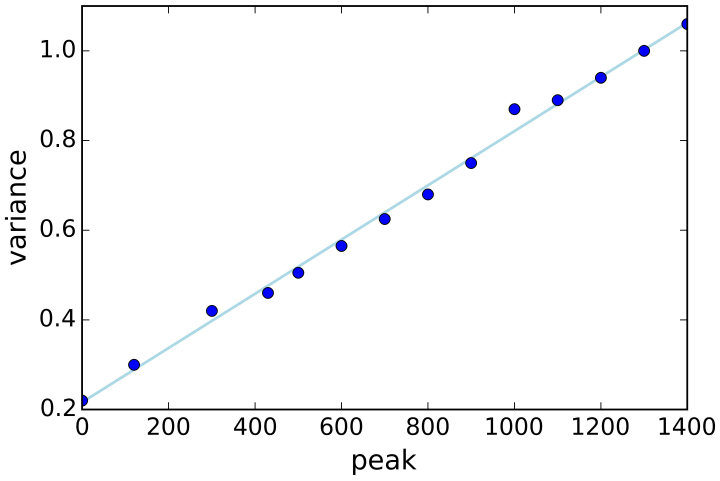

Fig. 6.9.: Shot noise test for our detection system. The blue dots represent the measurements of the variance as a function of the beam intensity, while the line is a linear fit. The positive background is due to the electronic noise and is detectable through a variance measurement with no light on the diodes. The axis (peak) represents the maximum value (in meV) provided by the shaper of the detection system using just one photodiode to measure the initial beam. The value is proportional to the light intensity.

6.5 Beam attenuation

We can increase the complexity of the model by adding two BSs, one on each branch, in order to consider the possible attenuation of the beams. The attenuation can be produced by filters, polarizers, couples $\lambda/2$-polarizer, mirrors etc...

Performing the same calculations of the previous sections, but starting from the initial states $\hat{n}_3$ (reference beam) and $\hat{n}_4$ (signal beam), one finds out that the measured **mean value** is

$$\langle \hat{n}_{5-6} \rangle = \langle \hat{n}_5 - \hat{n}_6 \rangle = |T_1|^2 |R|^2 \langle \hat{n_1} \rangle - |T_2|^2 |T|^2 \langle \hat{n_1} \rangle , \tag{6.21}$$

where $|T|^2$ and $|R|^2$ refers to the first Beam Splitter, whereas $|T_1|^2$ and $|T_2|^2$ represent the transmittance of the Beam Splitters on the branches 3 (reference beam) and 4 (probe beam) respectively. For a perfect 50:50 beam splitter, we obtain

$$\langle \hat{n}_5 - \hat{n}_6 \rangle = \frac{1}{2} |T_1|^2 \langle \hat{n}_1 \rangle - \frac{1}{2} |T_2|^2 \langle \hat{n}_1 \rangle . \tag{6.22}$$

Equation 6.22 is the expression of the unbalancing between the two branches. The measured **variance** is

$$\begin{aligned}\sigma^2_{5-6} &= \left\langle (\hat{n}_5 - \hat{n}_6)^2 \right\rangle - (\langle \hat{n}_5 - \hat{n}_6 \rangle)^2 \\ &= \left(|T_1|^2 |R|^2 - |T_2|^2 |T|^2 \right)^2 \sigma_1^2 + \\ &+ \left(|T_1|^4 |R|^2 |T|^2 + |T_1|^4 |R_1|^2 |R|^2 + |T_2|^4 |T|^2 |R|^2 \right. \\ &+ \left. |T_2|^4 |R_2|^2 |T|^2 + 2 |T_2|^2 |T_1|^2 |R|^2 |T|^2 \right) \langle \hat{n}_1 \rangle\end{aligned} \tag{6.23}$$

which reduces to

$$\begin{aligned}\sigma^2_{5-6} &= \frac{1}{4} \left(|T_1|^2 - |T_2|^2 \right)^2 \sigma_1^2 \\ &+ \left(\frac{|T_1|^4}{4} + \frac{|T_1|^4 |R_1|^2}{2} + \frac{|T_2|^4}{4} + \frac{|T_2|^4 |R_2|^2}{2} + \frac{|T_2|^2 |T_1|^2}{2} \right) \langle \hat{n}_1 \rangle .\end{aligned} \tag{6.24}$$

for a perfect 50:50 initial BS.

From Equations 6.23 and 6.24 the reader understands that the variance depends on the mean value 6.22, even in absence of a sample: the knowledge of this dependence is fundamental to distinguish the interesting contribution of the sample from the systematic effects of the set-up. To characterize the response of the system we measured the dependence of the variance on the unbalancing of the beams intensities ($\hat{n}_{5-6}$), obtained by tuning the intensity of the $\hat{n}_6$ beam (that is, the transmittance $|T_2|^2$ in the model).

The plot of the variance σ^2_{5-6} as a function of the measured mean value signal $\langle \hat{n}_{5-6} \rangle$ is plotted in Figure 6.11. The graph shows a quasi-quadratic dependence in which the minimum value of the noise does not occur at the perfect balancing ($|T_1|^2 = |T_2|^2$). The position of the minimum variance point x_{MIN} as a function of the initial variance and of the filter on the reference branch is studied in Figure 6.12. Notice that the value of x_{MIN} decreases as the input variance increases, although it remains always positive. This means that in this configuration the minimum noise limit can be reached only for $|T_1|^2 > |T_2|^2$, that is if the reference beam ($\hat{n}_5$) is less attenuated than the signal one ($\hat{n}_4$).

Contributions

In this subsection we focus on the several terms of the characterization function 6.24, in order to understand their contribution to the characteristic response of Figure 6.11. The following observations refer to the simplified case of a 50:50 first beam splitter; more general results will be briefly discussed in the next sections.

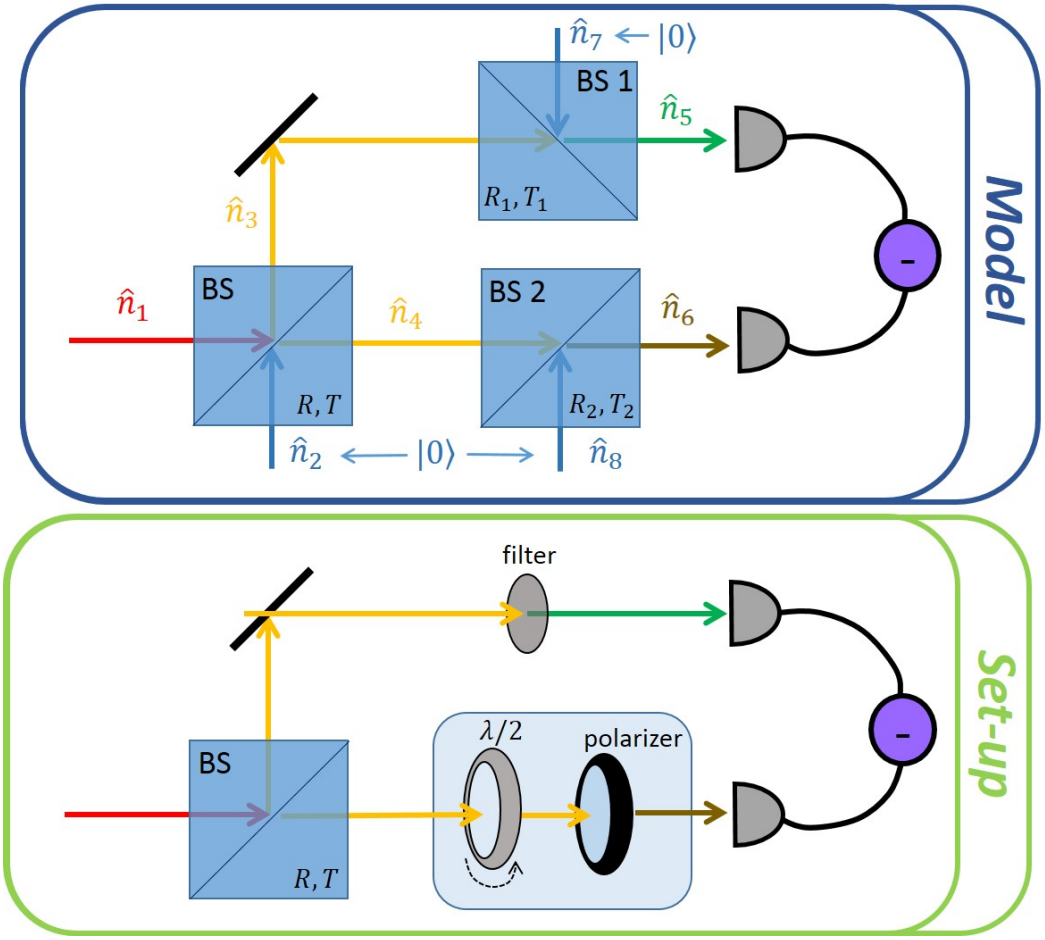

Fig. 6.10.: First approximation of the experimental set-up. The top picture shows a model set-up in which the first Beam Splitter represents real Beam Splitter, while BS1 and BS2 stand for dissipative optical elements of the set-up. $\hat{n}_2$, $\hat{n}_7$, $\hat{n}_8$ represent vacuum states. The bottom picture is an example of set-up which could be described by the model of the top picture.

We can rewrite equation 6.24 as

$$\begin{aligned}\sigma_{5-6}^2 = &\left[\frac{1}{2}\left(|T_1|^2 - |T_2|^2\right)\right]^2 \sigma_1^2 \\ &+ \left[\frac{1}{2}\left(|T_1|^2 + |T_2|^2\right)\right]^2 \langle \hat{n}_1 \rangle \\ &+ \frac{|T_2|^4 |R_2|^2}{2} \langle \hat{n}_1 \rangle \\ &+ \frac{|T_1|^4 |R_1|^2}{2} \langle \hat{n}_1 \rangle .\end{aligned} \tag{6.25}$$

Notice that during a measurement the acquired quantity is the difference $x = \langle \hat{n}_{5-6} \rangle = \frac{1}{2}\left(|T_1|^2 - |T_2|^2\right) \langle \hat{n}_1 \rangle$, whose only tunable parameter in this case is $|T_2|^2$ ($x \in \left[-\frac{1}{2}\langle \hat{n}_1 \rangle , \frac{1}{2}\langle \hat{n}_1 \rangle\right]$, since $|T_{1,2}|^2 \leq 1$). Therefore the last term of equation 6.25 is

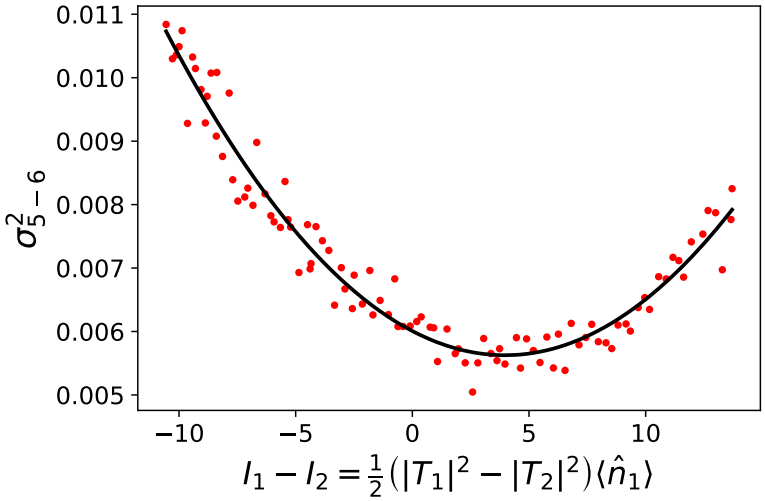

Fig. 6.11.: Characterization function. Measurement of the variance as a function of the mean value for the set-up dislplayed in Figure 6.10. The red dots represent a measurement of the variance dependence on the mean value in a set-up like the one sketched in figure 6.10, in which $|T_2|^2$ can be tuned. The black line is a fit of the data starting from equation 6.24 and free parameters $|T_1|^2$, $\hat{n}_1$ and σ_1. The number of photons and the related variance on the x and y axis are expressed as the voltage provided by the detector (which is proportional to the beam intensity).

constant with respect to x. On the contrary the other terms contribute to the shape of the detector response in the following way:

1. The first term can be rewritten as

$$y^{(1)} = \frac{\sigma_1^2}{\langle n_1 \rangle^2} x^2 \tag{6.26}$$

(where we have substituted $\langle \hat{n}_1 \rangle$ with $\frac{2x}{|T_1|^2 - |T_2|^2}$), which is a convex parabola centered in $x = 0$. Therefore the minimum value of this portion of variance is reached when the two measured beams have the same intensity. The strength of this contribution to the total shape depends on the features of the initial beam, and in particular on the ratio $\frac{\sigma_1}{\langle n_1 \rangle}$.

2. Since the intensity of the tunable beam $|T_2|^2 \langle \hat{n}_1 \rangle$ can be expressed as a function of the variable x through the relation

$$|T_2|^2 \langle \hat{n}_1 \rangle = \langle \hat{n}_1 \rangle |T_1|^2 - 2x, \tag{6.27}$$

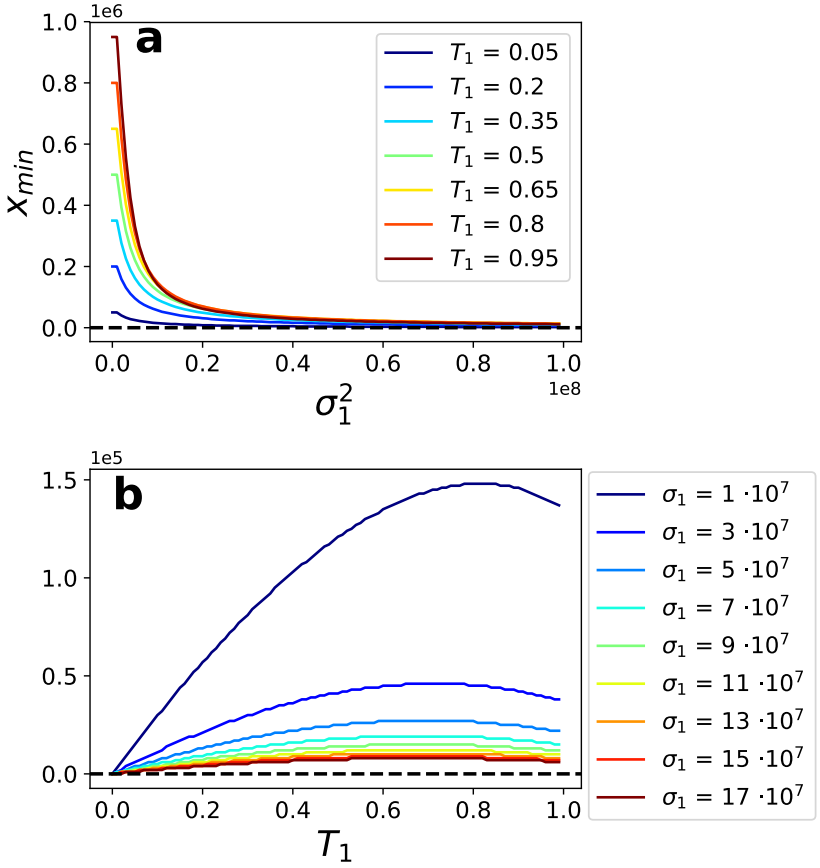

Fig. 6.12.: **Point of minimum of the variance.** Dependence of the differential intensity required to reach the minimum variance as a function of the input noise σ_1^2 and of the filtering on the reference beam T_1 (for a perfect 50:50 initial Beam Splitter).

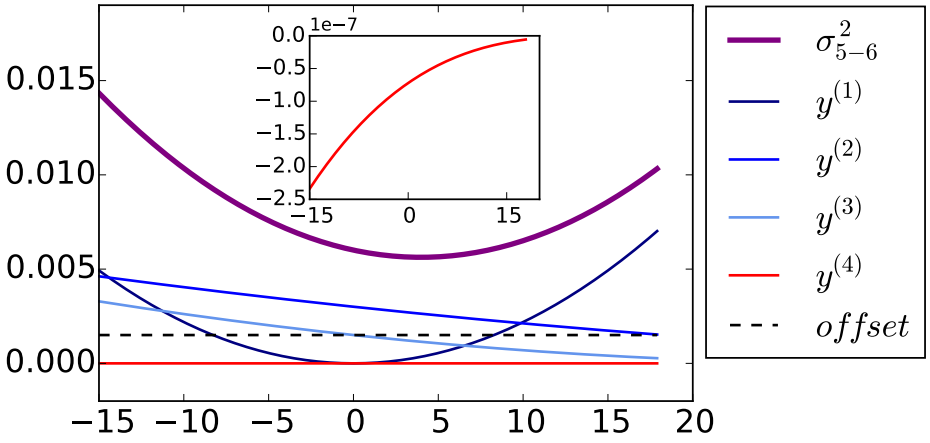

Fig. 6.13.: **Characterization function: contributions.** Contribution to the total variance σ_{5-6}^2 for an initial perfect 50:50 BS. The inset displays a zoom of the third order term $y^{(4)}$.

the second term becomes

$$\begin{aligned} y^{(2)} &= \frac{1}{\langle \hat{n}_1 \rangle} \left(x^2 - 2x \left| T_1 \right|^2 \langle \hat{n}_1 \rangle + \left| T_1 \right|^4 \langle \hat{n}_1 \rangle^2 \right) \\ &= \frac{1}{\langle \hat{n}_1 \rangle} \left(x - \left| T_1 \right|^2 \langle \hat{n}_1 \rangle \right)^2 \end{aligned} \tag{6.28}$$

that is again a convex parabola, whose minimum value (zero) occurs at $x = |T_1|^2 \langle \hat{n}_1 \rangle$, that is $|T_2|^2 = -|T_1|^2$, which is not experimentally reachable unless $|T_2|^2 = |T_1|^2 = 0$. Moreover the coefficient $\frac{1}{\langle \hat{n}_1 \rangle}$ associated to the second order term makes it almost negligible with respect to the linear one.

3. The third term contains also the reflectivity $|R_2|^2$, which makes us suppose that if Beam Splitter 2 is used to select a certain signal ($|T_2|^2 \langle \hat{n}_1 \rangle$), a print of the non-selected signal ($|R_2|^2 \langle \hat{n}_1 \rangle$) will be visible in the variance. This can be particularly interesting if T_2 and R_2 are time dependent.
   Using the relation $|R_1|^2 = 1 - |T_1|^2$, the last term can be separated in two contributions:

   - $$\begin{aligned} y^{(3)} &= \frac{1}{2} \langle \hat{n}_1 \rangle |T_2|^4 \\ &= \frac{1}{2 \langle \hat{n}_1 \rangle} \left(4x^2 - 4x \langle \hat{n}_1 \rangle |T_1|^2 + \langle \hat{n}_1 \rangle^2 |T_1|^4 \right) \\ &= \frac{1}{2 \langle \hat{n}_1 \rangle} \left(2x - \langle \hat{n}_1 \rangle |T_1|^2 \right)^2, \end{aligned} \tag{6.29}$$

     which represents again a second order polynomial.
     The total contribution of the obtained terms ($y^{(1)} + y^{(2)} + y^{(3)}$) is a convex parabola, centered in

     $$x_{MIN} = \frac{4 |T_1|^2 \langle \hat{n}_1 \rangle^2}{\sigma_1^2 + 3 \langle \hat{n}_1 \rangle}, \tag{6.30}$$

     which reduces to $|T_1|^2 \langle \hat{n}_1 \rangle$ if the input photon distribution s Poissonian. The minimum of the parabola approaches zero if $\sigma_1^2 >> \langle \hat{n}_1 \rangle$ or if $|T_1|^2 \to 0$.

   - The remaining term

     $$\begin{aligned} y^{(4)} &= -\frac{1}{2} \langle \hat{n}_1 \rangle |T_2|^6 \\ &= \frac{1}{2 \langle \hat{n}_1 \rangle^2} \left(8x^3 + \langle \hat{n}_1 \rangle^3 |T_1|^6 + 12x^2 \langle \hat{n}_1 \rangle |T_1|^2 - 6x \langle \hat{n}_1 \rangle^2 |T_1|^4 \right) \\ &= \frac{1}{2 \langle \hat{n}_1 \rangle^2} \left(2x - \langle \hat{n}_1 \rangle |T_1|^2 \right)^3, \end{aligned} \tag{6.31}$$

     is a third order polynomial, which is responsible for the light asymmetry of the variance response.

All contributions to the total variance σ_{5-6}^2 are displayed in Figure 6.13.

First BS dependence

Notice that a difference in the transmittance $|T|^2$ of the first Beam Splitter could change the response of the variance as a function of mean value. The results of the calculations are plotted in Figure 6.14: both the minimum variance and the related mean value x_{MIN} change as a function of T, although the general shape remains the same. Moreover the point of minimum variance x_{MIN} does not change sign for all possible values of $|T|^2$.

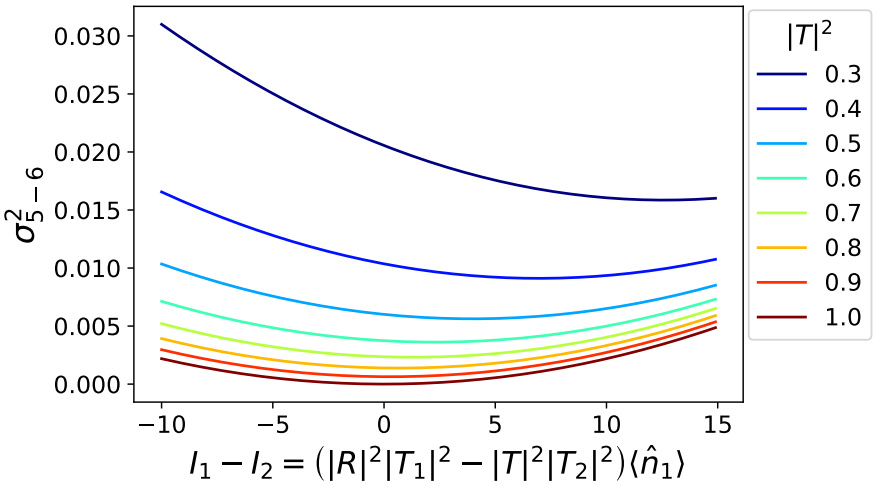

Fig. 6.14.: Variance for non-50:50 beam splitter. Simulated variance as a function of the integrated mean value for different values of transmittance of the first beam splitter. The input parameters of the function ($\langle\hat{n}_1\rangle$ and σ_1^2) comes from the fit plotted in figure 6.11

.

6.6 Additional dissipation effects

The described model provides a qualitative description of the set-up, but it cannot account for all the dissipative processes of the system. As an example consider that each mirror used in the set-up dissipates at least the 2% of the impinging radiation intensity. The introduction of such a number of Beam Splitters in the model would increase considerably the complexity of the calculations, so we work in the approximation in which a single Beam Splitter represents a sum of all the dissipative processes in a certain optical path. For instance, BS1 in Figure 6.10 stands for the sum of the contributions of filters and mirrors of the "upper" branch. As a consequence the parameter $|T_1|^2$, obtained by the characterization fit of Figure 6.11 underestimates the actual filter transmittance. Moreover, when performing this characterization, it could be worth to add another Beam Splitter on the second branch, in order to take into account all "non-tunable" dissipation effects.

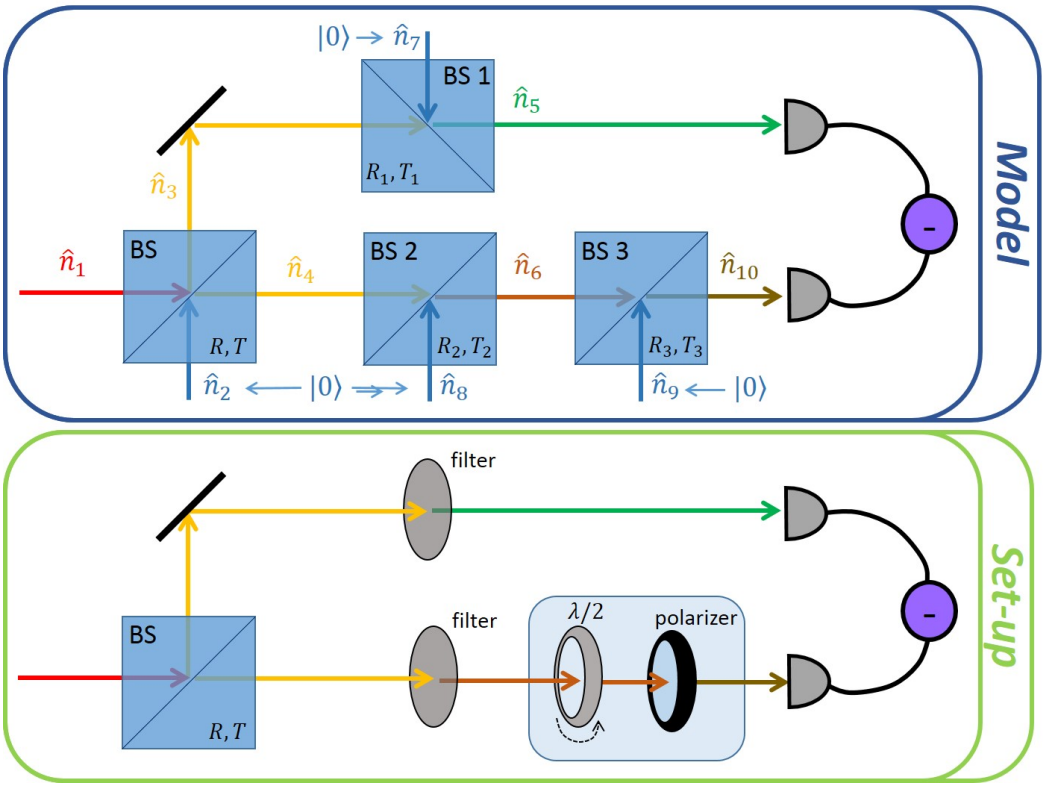

Fig. 6.15.: Additional dissipation: model set-up. Top: Model set-up for the characterization of the detected noise: BS1 and BS2 serves as the sum of all dissipation effects on the two branches, whereas BS3 is used to tune the unbalancing between them. **Bottom:** Example of experimental set-up, which can be described by the model shown in the **top** picture.

The new set-up is plotted in Figure 6.15: to sum up, the first Beam Splitter (BS) represents a real Beam Splitter, that splits the input light beam in two, BS1 and BS2 serve as the sum of dissipative or absorbing processes (mirrors, filters etc.) with *fixed transmittance*, whereas BS3 has the tunable transmittance that allows to characterize the variance response as a function of the unbalancing between the two beams impinging on the detector photodiodes.

The results of the calculations are

$$\langle \hat{n}_5 - \hat{n}_{10} \rangle = \left(|T_1|^2 |R|^2 - |T_3|^2 |T_2|^2 |T|^2 \right) \langle \hat{n}_1 \rangle \,, \tag{6.32}$$

$$\begin{aligned} \sigma^2_{5-10} &= \left\langle (\hat{n}_5 - \hat{n}_{10})^2 \right\rangle - (\langle \hat{n}_5 - \hat{n}_{10} \rangle)^2 \\ &= \left(|T_1|^2 |R|^2 - |T_3|^2 |T_2|^2 |T|^2 \right)^2 \sigma^2_{n1} + \\ &+ \Big(|T_3|^4 |T_2|^2 |R|^2 |T|^2 + |T_3|^4 |T_2|^2 |R_2|^2 |T|^2 + \\ &+ |T_3|^4 |R_3|^2 |T_2|^2 |T|^2 + |T_1|^4 |R|^2 |T|^2 + \\ &+ |T_1|^4 |R_1|^2 |T|^2 + 2 |T_3|^2 |T_2|^2 |T_1|^2 |R|^2 |T|^2 \Big) \langle \hat{n}_1 \rangle \,. \end{aligned} \tag{6.33}$$

The variance characterization is plotted in Figure 6.16 and 6.17.

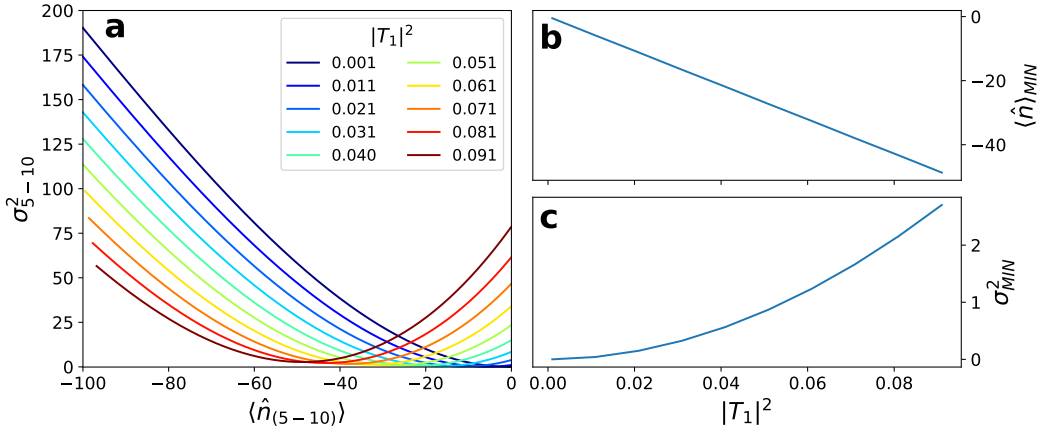

Fig. 6.16.: **Additional dissipation: effects of the filtering.** **a** Variance response to the unbalancing (Equations 6.32 and 6.33) as a function of the filtering of the reference branch (parameter $|T_1|^2$). **b** Differential mean value corresponding to the minimum noise level, as a function of $|T_1|^2$. **c** Minimum noise level, as a function of $|T_1|^2$.

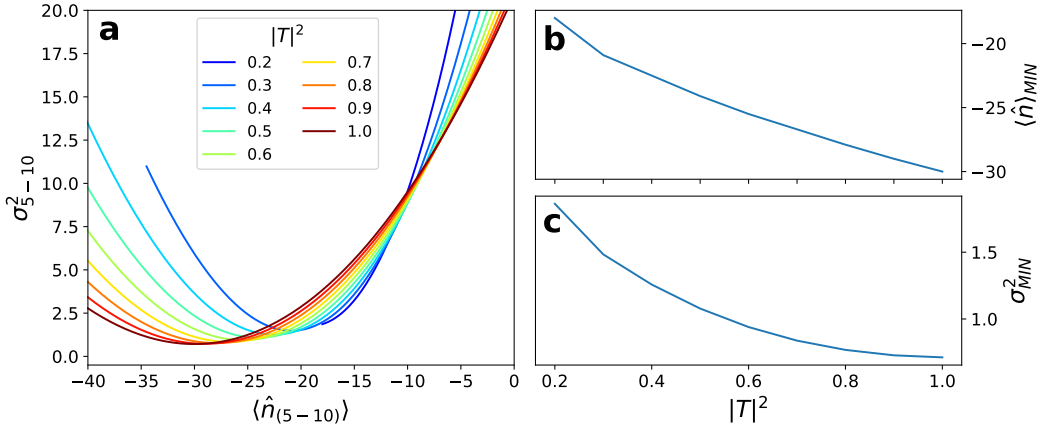

Fig. 6.17.: **Additional dissipation: effects of the splitting.** **a** Variance response to the unbalancing (Equations 6.32 and 6.33) as a function of the splitting ratio performed the first Beam Splitter (parameter $|T|^2$). **b** Differential mean value corresponding to the minimum noise level, as a function of $|T|^2$. **c** Minimum noise level, as a function of $|T|^2$.

Despite the variance maintains the same almost quadratic dependence in the unbalancing, important differences can be detected in its minimum value:

- first of all Figures 6.16 and 6.17 show that different values of the first Beam Splitter (the one which divides the initial beam) and of BS1 (representing the filter on the reference beam) affect the lower noise limit of the system. In particular the minimum level increases if the transmittance $|T_1|^2$ is increased

(Figure 6.16 **c**) or if a larger portion of the initial beam is sent to the reference branch (Figure 6.17 **c**).

- the unbalancing needed to reach the minimum noise level is affected by the transmittances $|T_1|^2$ (Figure 6.16 **b**) and $|T|^2$ (Figure 6.17 **b**). In both cases an increase of the transmittance requires a more and more negative unbalancing (which means an increase of $|T_3|^2$).

6.7 Summary and observations

In the present chapter we described the expected results of a differential optical measurements through a simple quantum model. The key assumption of this picture is the use of the quantum formalism for Beam Splittes to describe each optical element of the set-up, which is, by nature, a dissipator. The progressive increase of the number of Beam Splitters provides a better approximation of the system itself.

The calculations highlighted some curious behaviors of the noise of the detected number of photons and some critical points related to the measurements. The consequences of these features are summarized in the following.

Experimental issues in Shot Noise measurements

The topic of dissipation allows to open a short parenthesis about the validity of the shot noise measurement, that is the detection of the intrinsic noise due to the quantum nature of light. The optical element require to detet this quantum noise is a 50:50 Beam Splitter, which eliminates the classical contribution of the noise (proportional to the mean value) and keeps the partition one (see Equation 6.18 and 6.19).

Experimentally it is very hard to find a perfect 50:50 BS, so sometimes, in order to balance the outputs of the BS, one uses to filter the intensity on one branch. This small variation can be described by the set-up shown in Figure 6.10, where BS 1 and 2 are filters or couple $\lambda/2$-polarizer, while the first beam splitter has $|R|^2 = \frac{1}{2} \pm \delta$ and $|T|^2 = \frac{1}{2} \mp \delta$, with $\delta << \frac{1}{2}$. In the present section we want to briefly comment on the difference between this measurement and the shot noise one and whether the former could substitute the latter.

If we consider the set-up of Figure 6.10 and the two output beams are perfectly balanced, the first term of σ^2_{5-6} (equation 6.24) is zero and the variance is proportional

to the mean number of photons, as in the shot noise case. The result of the model for this measurement is plotted in Figure 6.18.

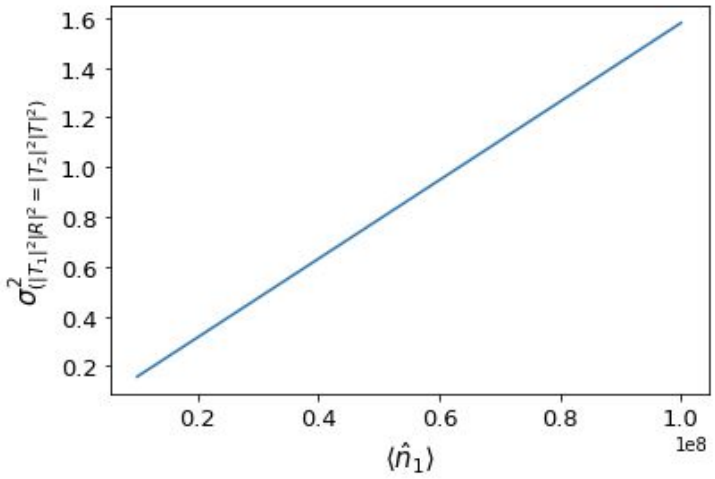

Fig. 6.18.: Shot noise test with non-50:50 BS. Calculation of the variance as a function of the original beam intensity for perfect balancing obtained through the use of filters (or other attenuators) on the two branches, after the Beam Splitter.

On the other hand Figure 6.14 and 6.12 point out that in this kind of set-up the minimum value of the variance is not reached at the perfect balancing, while this is not the case for the shot noise set-up, as demonstrated in section 6.4. So, a non-perfect 50:50 beam splitter does not allow to reach the shot noise level, compromising the measurement result, although the measured noise is still proportional to the initial intensity.

Characterization

The model points out also the necessity to characterize the system before each measurement: as a matter of fact the variation of a number of parameters can completely change the detected noise, even in absence of peculiar features of the sample.

Mean value dependence

As pointed out in section 6.5 and 6.6 the detected variance strictly depends on the number of photons. This effect is not surprising, since we intuitively expect an increase of the noise due to an increase of the signal (or better, to the increase of its modulus).
On the other hand calculations (as well as characterizations performed on our set-up) show that the minimum noise is rarely reached at the minimum of the signal (see

Figure 6.12, 6.16 and 6.17) and that this minimum point is strictly related to the presence of dissipators in the set-up, that can, in principle, change from measurement to measurement (consider the rotation of a $\lambda/2$, or the use of a different filter, for example).

Improvement of the signal-to-noise ratio

Most of the time the aim of the experimentalist is to enhance the signal-to-noise ratio, in order to get the most defined results possible. Even in statistical measurements this requirement is fundamental, since classical and external noise in general could overcame the inner quantum fluctuations of the probe pulse. On the other hand a reduction of the noise related to a certain differential mean value does not necessarily mean that the experimental conditions improved.

Consider for instance Figures 6.16 and 6.17, where the expected variance has been calculated for different filtering and splitting coefficients ($|T_1|^2$ and $|T|^2$ respectively). All plotted cases have the same initial conditions (number of photons and related variance) and no other noise contribution is taken into account. From the figures it is clear that for a fixed value of $\left\langle \hat{n}_{(5-10)} \right\rangle$ (for example zero, that is, perfect balancing between the two beams detected the photodiodes), the value of the noise could change just because of the " hotizontal shift" of the characterization function.

Nevertheless the distance of the mean values $\left\langle \hat{n}_{(5-10)} \right\rangle$ from the point of minimum variance x_{MIN} is a key parameter for understanding the noise effects. For this reason a complete characterization of the set-up (as the one plotted in Figure 6.11 - red points) must be taken into account before each measurement.

Effects on time resolved measurements

Up to now we have considered the effects of the set-up on the noise in *static* measurements: we chose a certain value of the differential current (proportional to the difference of the mean number of photons impinging on the detector) and calculate the expected variance.

However the consequences of the experimental choices become more and more evident and peculiar when associated to a pump-probe measurement. In the latter case, the mean value signal changes in time because of the sample excitation due to the pump pulse, so a time dependence is expected also for the variance. This dynamics can actually present very different features, depending on the position of the minimum variance point x_{MIN}.

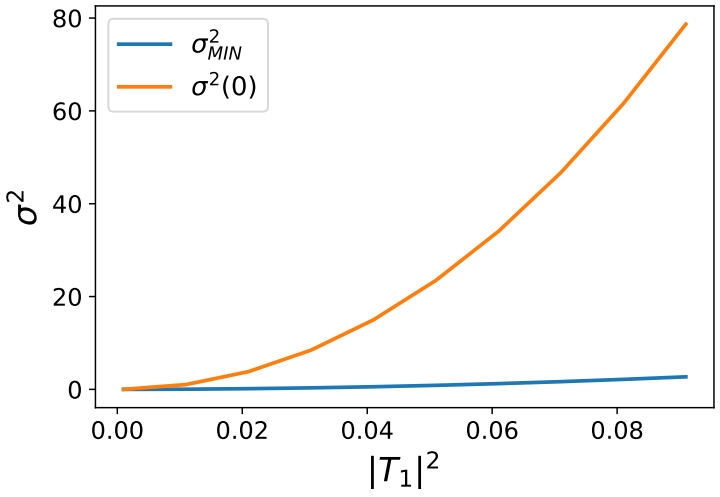

Fig. 6.19.: Signal-to-noise ratio: minimum noise. Minimum variance level (blue line) and variance at perfect balancing (orange line) as a function of the transmittance of the Beam Splitter on the reference beam (parameter: $|T_1|$). Notice that the increase of the noise is much quicker in the latter case.

In particular, if the mean value is always bigger than x_{MIN} in the whole considered time interval (see the green area of Figure 6.20), the characterization function $\sigma^2(\langle\hat{n}\rangle)$ (black line) is a monotonic increasing function. Therefore we expect to measure a variance dynamics qualitatively similar to the mean photon number one (that is, if the latter increases, also the former increases etc...)
If the mean value moves to the other side (orange area of Figure 6.20), $\sigma^2(\langle\hat{n}\rangle)$ is a decreasing function and we expect a "reversed" variance dynamics (if the mean value increases, the noise decreases). Moreover in both the cases the distance of the mean value from x_{MIN} determines the amplitude of the noise signal, because of the non-linear dependence of the characterization function (see the right graphs of Figure 6.20).

Finally if the mean value oscillates around x_{MIN} and if the amplitude of the signal is wide enough, strange dynamical effects could come out, since the function $\sigma^2(\langle\hat{n}\rangle)$ is not monotonic any more (yellow area in Figure 6.20).

The expected effects for a sample signal with different balancing are shown in Figure 6.20, whereas their measurement is the argument of the next chapter.

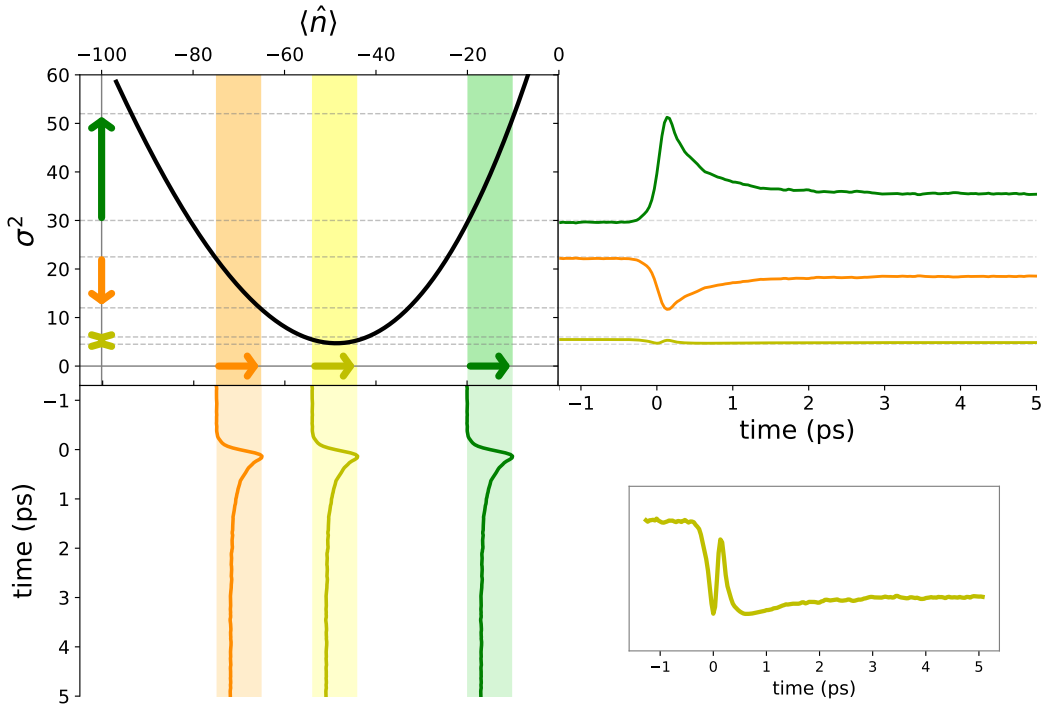

Fig. 6.20.: Systematic effects on the variance. In the top left panel a characterization function of the set-up is plotted (black line) and three different mean value regimes are highlighted. The arrows marks the (non-)monotonic dependence of the variance on the mean and so how the increase of the mean value is related to the increase/decrease of the variance. The graphs in the bottom panel show the time resolved mean value signal for different initial unbalancings between the probe and the reference. The right graphs represent the corresponding variance dynamics, calculated applying the characterization function to the mean value signals of the bottom plot. The variance graphs show the predicted "reversing", the difference in amplitude (green and orange curves) and the different time dependence expected for low noise measurements (yellow curve - the bottom inset is a zoom of the same signal).

7

Noise in time domain measurements: an effective description

The attempt to interpret the information carried by the noise of a pump-probe experiment revealed itself to be as intriguing as complex, since any detail must be taken into account. I will show here that many of the feature which are commonly observed in noise measurements can be described in the theoretical framework established in the previous chapter. Most importantly, I will show that unintuitive results can occur and a formal description of all overall measurements, not only the dynamical response of the sample, should be included in the description.

In the previous chapter we described the repercussions of the dissipation from the set-up optical elements on a pump-probe differential measurement. We were able to define a *characterization function* $\sigma^2\left(\langle\hat{n}\rangle\right)$, which determines the noise dependence on the signal intensity and in particular on the unbalancing between the probe beam and the reference one (see Figure 3.8). We have also analyzed the variation of this function due to the increasing number of set-up elements and to their dissipation rates (that is, their transmittance $|T|^2$). The treatment allowed to derive some important consequences for time resolved measurements, and revealed that the noise dynamics is determined by the whole experimental apparatus and not only by the photon number fluctuations associated to the sample response.

The purpose of the present chapter is to verify experimentally what we predicted with the Beam Splitter model described in Chapter 6 and in particular (see Figure 6.20):

1. the "reversing" of the variance dynamics [1] due to the relative change of intensity of the two optical beams (probe and reference) impinging on the differential detector;

[1] Of course the variance does not change sign. With the term *reversing* we mean a reversing of its derivative (so if in one case the variance increases in a certain time interval, in the second it decreases and analogously a maximum in the first case corresponds to a minimum in the second one and vice versa). The effect is clear in Figure 6.20 (green and orange lines).

2. the variance behavior around the minimum of the characterization function (in this case the qualitative difference between of the signal and the noise dynamics could be due to the non-monotonicity of the function itself, see section 6.7);

3. the effects of more than one phonon excitation.

In order to present an extensive study of this effect we performed measurements on different samples: Bismuth (Bi), Quartz (SiO_2) and Strontium Titanate ($SrTiO_3$); the choice of three samples allowed to check the generality of the model and of its effects in different experimental conditions. In particular we will show than the model can account for reflectivity and transmission measurements as well as measurements with samples with more than one phonon mode visible in time domain measurements.

The chapter is structured as follows: after a short and general introduction on the measurements and the samples (section 7.1), each section is dedicated to one of the three effects listed above. For each of the experiments discussed we will present both time dependent intensity and time dependent noise, complemented by a separate measurement of the apparatus characterization functions $\sigma^2\left(\langle\hat{n}\rangle\right)$.

7.1 Measurement and samples

The general idea of the measurement has already been introduced in section II: the aim is to measure the dynamics of the statistical distribution of the number of photons after the interaction with the sample. It is possible through the detection of hundreds of pulses for each time delay from the pump excitation.

In the measurements presented in this chapter, the pump and the probe pulses have the same photon energy ($h\nu = 1.55\,\mathrm{eV}$) and are obtained through a laser system made up of Ti:Sapphire oscillator (*Coherent Mira Seed*), pumped by a $Nd:YVO_4$ laser (*Coherent Verdi V-18*), and the amplifier *Coherent RegA*. The final outputs are ultrashort pulses ($\approx 150\,\mathrm{fs}$), with repetition rate of 250 kHz: the latter feature determines the time response of the detector, which must be lower than $4\,\mu\mathrm{s}$. Further details on the acquisition system are given in appendix C.

All samples considered in the present chapter show coherent phononic modes at few THz. In this case the oscillation frequency can be detected not only by Raman spectroscopy, but also by time resolved experiments: the pump pulse induces the phononic excitation, which results in an oscillating time dependence of the

dielectric function. The transmitted (or reflected) probe intensity is affected by the "instantaneous" sample dielectric function and therefore is modulated with the same frequency of the phonon.
Notice that the pump radiation is not resonant with the phonon energy, which is about one hundredth of the photon one. The excitation of the vibrational mode is anyway possible if the spectrum of the light pulse is broad enough: as a matter of fact, it can excite Raman active modes with frequency $\Omega = \nu_1 - \nu_2$, where ν_1 and ν_2 are both contained in the envelope of the pulse in frequency domain (see Figure 7.1).

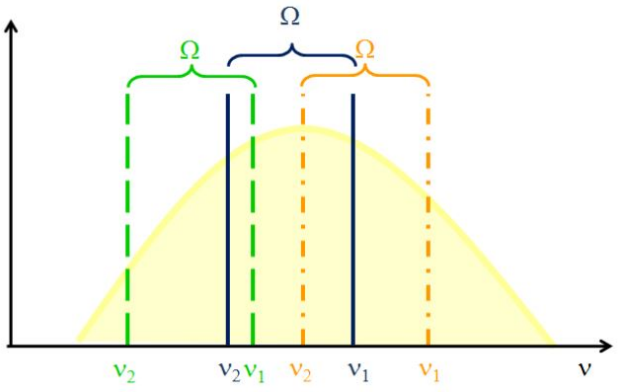

Fig. 7.1.: ISRS: frequency difference. Sketch of the spectral envelope of the pump pulse in frequency domain. Three different couples of frequencies (ν_1; ν_1) for which $\nu_1 - \nu_2 = \Omega$ are shown.

The described process is called *Impulsive Stimulated Raman Scattering* (ISRS) and is formally described by a third order process in which the i^{th} of the final Polarization is defined by the relation

$$P_i^{(3)}(z,\omega) \propto \sum_{jkl} \chi_{ijkl}^{(3)} E_{1,j}(z,\omega_1) E_{2,k}(z,\omega_2) E_{3,l}(z,\omega_3), \tag{7.1}$$

where $E_{2,k}(z,\omega_2)$ and $E_{3,l}(z,\omega_3)$ represent the two spectral components of the pump pulse, with propagation direction z, frequency $\omega_{2,3}$ and polarization in the k and l direction respectively, whereas $E_{1,j}(z,\omega_1)$ is the probe pulse electric field. $\chi_{ijkl}^{(3)}$ is the fourth order susceptibility tensor and is obtained through the sum $\chi_{ijkl}^{(3)} = \sum_{n=1}^{N} M_{ij}^{[n]} M_{kl}^{[n]}$ (where $M_{ij}^{[n]}$ is the susceptibility tensor related to the n^{th} Raman mode) and reflects the two step nature of ISRS: in the first one phonons are created from the pump photons, while in the second probe photons interact with the newly created phonons, producing the final scattered photons.
Equation 7.1 reveals also the importance of the polarization contributions (indices i, j, k, l) and suggests the presence of selection rules, as for static Raman measurements (see, for instance, section 3.1.2).

In particular, the results presented in this chapter concerns the the measurements of the Raman active modes of three different samples:

- **BISMUTH**: A_g mode, with frequency $\Omega = 2.8\,\mathrm{THz}$. Both beams propagates along the trigonal axis $[0001]$ and the mode detection does not require any polarization selection after the interaction with sample. The time resolved A_g signal is a very intense, while footprints of the E_g mode at $\Omega = 2\,\mathrm{THz}$ are rarely visible and just in the differential contribution $A_g - E_g$ [45]. Measurements have been performed at room temperature.

- **QUARTZ**: E_g mode, with frequency $\Omega = 3.8\,\mathrm{THz}$. This mode is obtained when the probe polarization direction is parallel to the a or b crystal axis, the pump polarization is rotated of $45°$ with respect to the probe one and the selected emitted field polarization is orthogonal to the probe. Because of the strength of the total symmetric mode at $\Omega = 6.2\,\mathrm{THz}$, sometimes it can be observed, despite the final polarization selection. Also in this case measurements have been performed at room temperature.

- **STRONTIUM TITANATE**: E_g mode, with frequency $\Omega = 0.4\,\mathrm{THz}$. The signal is obtained choosing a pump polarization rotated of $45°$ with respect to the [100] axis, while the probe polarization direction is parallel or perpendicular to the same axis [51]. Measurements have been performed at 10 K: for higher temperatures the phonon is expected to soften, to finally disappear at the structural transition temperature $T_c = 105\,\mathrm{K}$, which leads the sample from a tetragonal (D_{4h}) to a cubic perovskite structure (O_h) [51].

7.2 *Reversing* of the variance dynamics

The model predicts that the difference between the variance of the data (at a given pump and probe delay) with the equilibrium variance changes by different unbalancing of the detector. This can be measured with the rigid shift of the measured intensity above or below the point of minimum variance x_{MIN} changing the number of photons that impinges on the two photodiodes of the differential detector. We observed the effect for the first time in a pump-probe measurement on Bismuth.

A typical result of a pump probe measurement on a Bismuth single crystal is shown in Figure 7.2 **a**, where the transient reflectivity is plotted as a function of the time delay between the pump and the probe. As reported in many literature results [45, 42], the signal oscillations due to the phononic excitation are very intense and

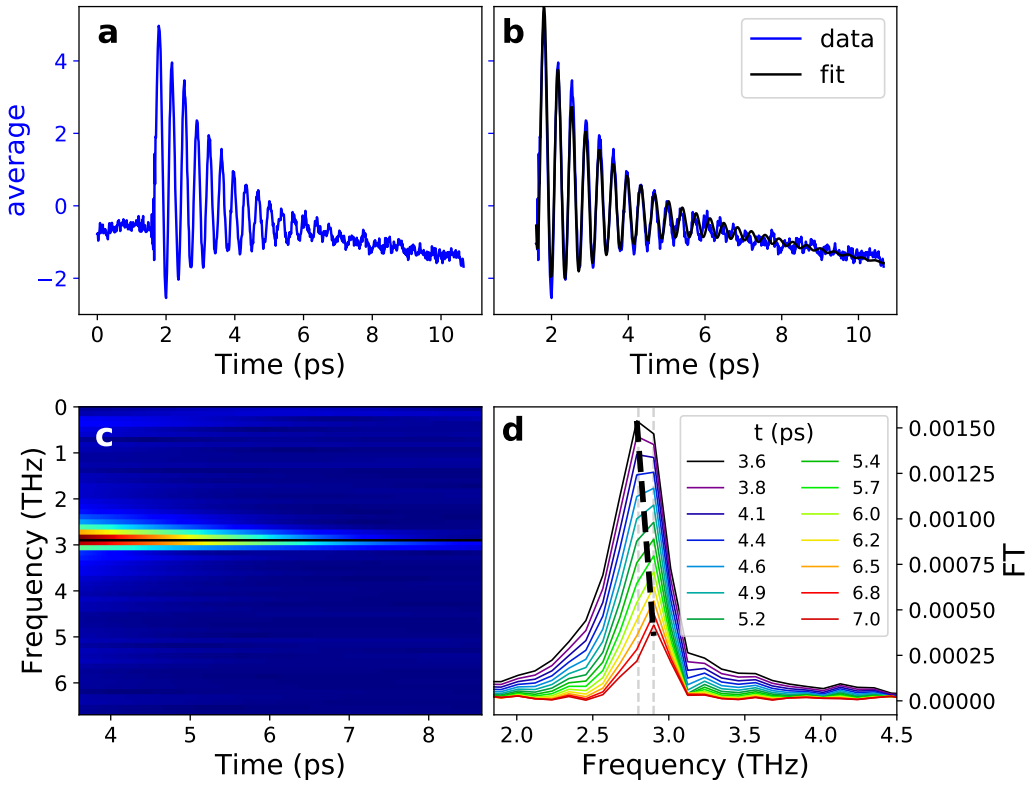

Fig. 7.2.: Bismuth time-resolved response. **a** Transient reflectivity of a bismuth sample as a function of the time delay between the pump and the probe. The probe signal after the pump excitation is modulated at the phonon frequency. **b** Comparison between the signal (blue) and a fit with fixed oscillation period. The analysis marks the time dependence of the phonon frequency. **c** Wavelet analysis of the measurement plotted in **a**. **d** Fourier transforms for different pump-probe delays (purple: $3.8\,\mathrm{ps}$, red: $8.5\,\mathrm{ps}$): the lines corresponds to vertical cuts of the map **c**.

allow, through a simple Fourier transform, to calculate the phonon frequency, which is about $2.8\,\mathrm{THz}$. On the other hand, a growth of the frequency value in time is expected for long time delays [42]. We checked this effect in Figure 7.2 **b**: the blue line represents the original signal, while the black one is a fit with a fixed oscillation frequency[2]. It is evident that after $5\,\mathrm{ps}$, the difference between the two curves is no more negligible, demonstrating the variation of the phonon frequency in time.

The effect can be checked with another tool, called *Wavelet Analysis*, which allows to study the time evolution of the frequency component of a signal. In order to perform this analysis, we multiplied the signal by a normalized gaussian function, centered on a certain time delay between pump and probe, and then perform the Fourier Transform of the new signal. This analysis allows to study a short time interval without reducing too much the frequency resolution. The tuning of the time position of the gaussian in the whole time interval, provides the complete frequency dynamics.

[2]The fitting function is the product of a sinusoidal function with $\nu = 2.8\,\mathrm{THz}$ and a negative exponential, which takes into account the oscillation damping. Another exponential decay is added in order to fit the electronic contribution.

The crucial parameter of this analysis is the width of the gaussian function: if is to large the frequency resolution improves, because of the increasing number of oscillation considered, but on the other hand, the time resolution worsens, since the frequency evolution cold be no more appreciable averaging on lots of periods.
The result for our measurement is plotted in map 7.2 **c**: the x-axis represent the time delay between the pump and the probe, whereas the y-axis is the frequency one. The decrease of the amplitude of the only Fourier peak during the de-excitation is clearly visible, while the frequency shift is hard to detect: in order to highlight it, we plotted the Fourier Transform at each time delay in Figure 7.2 **d**.

Once we have understood the main features of our "standard" pump-probe data we are ready to measure and interpret the noise dynamics, provided that we know the characterization function for our system.

In Figure 7.3 and 7.4 the same measurement for different unbalancings between the probe and the reference beams are shown.
Let us start from Figure 7.3. Figure 7.3 **a** shows the time dependence of the mean photon number (blue line) and the variance one (red curve). The vertical dashed lines highlights that mean value and variance are in phase.
The inset of the right panel of Figure 7.3 **b** shows the characterization function of the apparatus. The purple line represents the noise characteristic of the apparatus as a function of the detector unbalancing, which can be controlled by changing the intensity of the beams. The black line is obtained through a fit of the model used in the previous chapter to the experimental data (red curve). The fitting function is given by Equation 6.33, whereas the red points represent the mean and variance values of the time resolved measurement, that is, the data plotted in the left panel. The characterization plot reveals that the mean photon number data never reach the point of minimum noise and that the $\sigma^2(\langle\hat{n}\rangle)$ is monotonic in the considered region. In this case the model predicts that the main features of the mean and variance dynamics should be qualitatively similar (see Figure 6.20). This effect is checked in the right panel of Figure 7.3, where the detected variance (red curve) and the model variance are plotted. In order to obtain the variance dynamics, we inserted the mean value at a certain time delay in the characterization function and repeated the process for each time delay. The model variance (black curve) fits the data, especially concerning the oscillation, both in frequency and phase.

In order to test the validity of our model we performed an experiment decreasing the intensity of the reference beam. If the mean value $\langle\hat{n}\rangle$ is lower than the point of minimum noise x_{MIN} (Figure 7.4) the BS model predicts that the variance dynamics is "reversed" with respect to the mean photon number one (and so also to the variance in case of positive balancing). The effect is confirmed by the experimental data plotted in Figure 7.4 and highlighted by the vertical dashed lines: you can

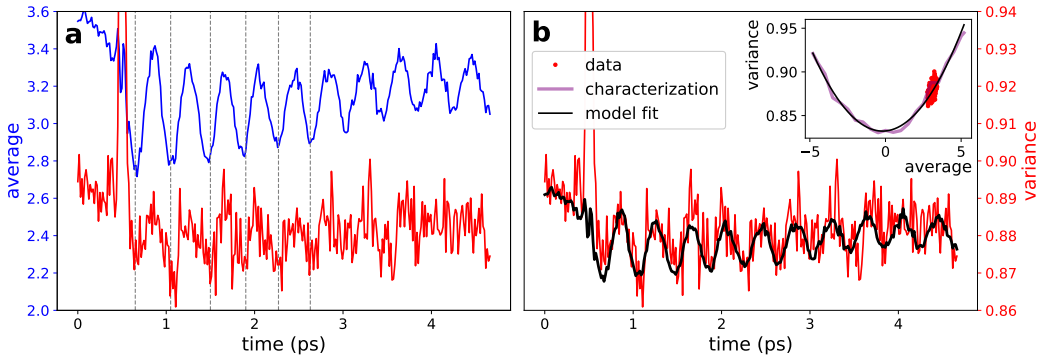

Fig. 7.3.: **Bismuth noise dynamics: positive balancing.** Mean photon number and variance time resolved measurement for values of the balancing higher than x_{MIN} (point of minimum variance). **Left panel**: transient reflectivity mean (blue curve) and variance (red curve). The vertical dashed lines facilitate the comparison between the two time resolved signals, revealing that their oscillations are *in phase*. **Right panel**: Comparison between the acquired variance (red curve) and the one predicted by the Beam Splitter model (black line). The **inset** shows the acquired characterization function (purple line), the fit with the characterization function predicted by the Beam Splitter model (black curve) and the relation between mean and variance obtained from the data plotted in the left panel (red dots). The described plot highlights the set-up contribution (fileting, splitting of the beam etc...) to the variance results, even in absence of the sample.

notice that the minima of the variance oscillation correspond to a the maxima of the mean one and vice versa. The final verification of the model validity (and of its reversing effect in particular) is given by the comparison between the acquired variance and the calculated one, plotted in the right panel of Figure 7.4.

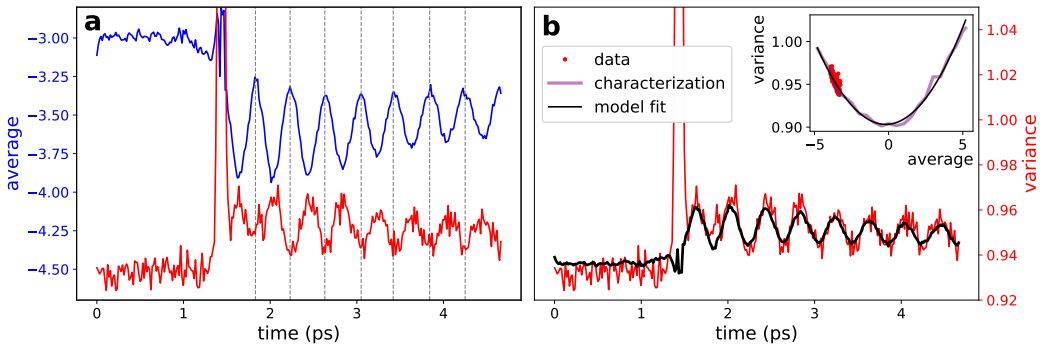

Fig. 7.4.: **Bismuth noise dynamics: negative balancing.** Mean photon number and variance time resolved measurement for a value of the balancing lower than x_{MIN} (see **Inset**. The plots have the same meaning of Figure 7.3. Notice that in the present case the mean value is below the minimum noise one (**inset**) and the variance oscillation is reversed with respect to the mean one (**left panel**). Also in this case the phenomenon can be explained by the Beam Splitter model (whose variance calculation is compared with the experimental data in the **right panel**

7.3 Minimum noise

Looking at the results described in section 7.2, a question immediately comes out: since the variance dynamics changes moving from one arm to the other of the characterization function $\sigma^2(\langle\hat{n}\rangle)$, what happens at the center, that is, when the differential mean photon number approaches the point of minimum variance? Different results are expected, depending on the range of the reflectivity variation in time.

7.3.1 Oscillation amplitude dependence

Let us consider, first of all, the same measurement of section 7.2, in which the probe and reference intensities have been tuned in order to obtain a differential intensity close to the minimum point of the characterization function. Notice that in this particular measurement the condition is really closed to the perfect balancing, but it is not necessarily the case, as shown in the previous chapter (see Figures 6.12, 6.14 and 6.19).
In this measurement ΔR is very low and the mean value moves in a small (quasi-flat) range of the characterization function (see inset of Figure 7.5). Therefore we expect a very small (if any) time dependence of the variance. The experimental data confirms the hypothesis: no variance dynamics is detected after the arrival of the pump (see Figure 7.5). Moreover the Fourier Transform (left inset of Figure 7.5) reveals that no oscillation is detected in the variance (red curve), despite the usual $2.8\,\mathrm{THz}$ one is recognizable in the modulation of the transient reflectivity (blue curve). The same evidence is observed in the calculated variance (black line of the right panel), which is almost time independent after 1 ps).

The results can change completely if the amplitude of the intensity signal is enhanced. You find an example in Figure 7.6 **a**, where the range of the transient reflectivity variation (blue line) is about 10 times larger than the one of Figure 7.5. The corresponding variance dynamics (red curve of Figure 7.6 **a**) is characterized by a second frequency contribution, whose value is twice the one detected in the mean signal (see the inset of Figure 7.6 **a** in which the Fourier Transform of the time resolved photon number and of its variance are plotted). This effect is due to the oscillation of the mean in time around the point the minimum variance. Since the characterization function around this point is almost quadratic, both an increase or a decrease of the intensity value with respect to x_{MIN} gives rise to an increase of the variance signal. The effect is pointed out in Figure 7.6 **a**, where the horizontal gray line represents the point of minimum variance x_{MIN}, which in this case is close to zero. The vertical dashed lines highlight the times delay in which the mean value

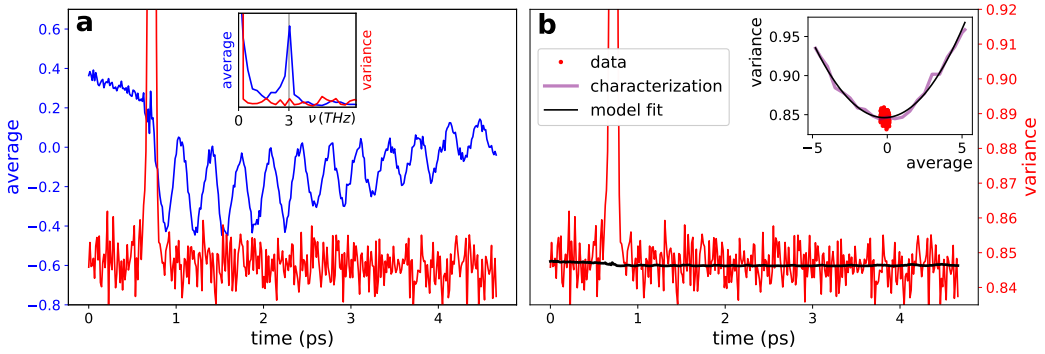

Fig. 7.5.: **Noise dynamics: minimum noise and low signal intensity.** Mean photon number and variance time resolved measurement for the minimum noise values. The plots have the same meaning of Figure 7.3 and 7.4. Noise oscillation are neither predicted by the model nor observed experimentally, as highlighted by the **left inset**, in which the Fourier transform of the mean (blue curve) and the variance (red curve) are plotted. Also in this configuration the model fits the general behavior of the variance dynamics (**right panel**)

time resolved signal (blue curve) crosses the x_{MIN} line, that is the points for which we expect a change of slope of the variance. The variance dynamics below (red line) confirms the hypothesis. Figure 7.6 **b** shows again the variance dynamics and the fit obtained with the Beam Slitter model (black line), whereas the characterization function (both data and fit) and the measurement variance (red dots) are plotted in the inset.

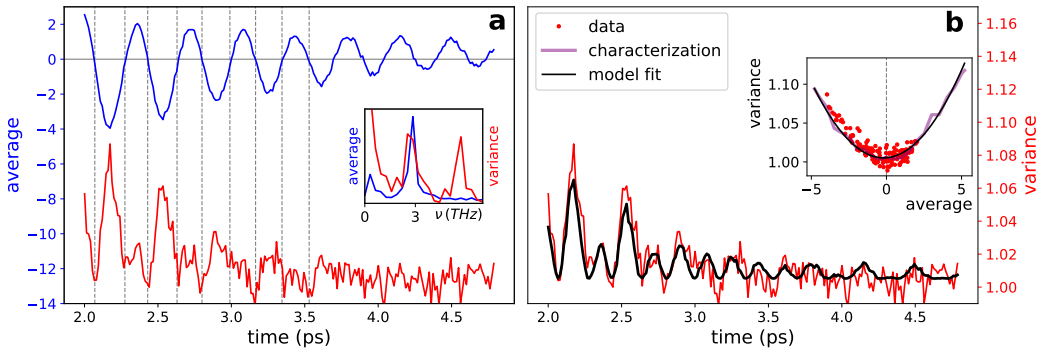

Fig. 7.6.: **Noise dynamics: minimum noise and higher signal intensity.** **a** Mean photon number (blue) and variance (red) time resolved measurement for the minimum noise values. The horizontal gray line represents the value of the mean where the minimum variance is reached (x_{MIN}), whereas the vertical dashed lines mark the time delays for which this value is reached. **Inset**: Fourier Transform of the same signals; the second peak of the variance is clearly visible. **b** Comparison between the acquired variance and the model fit, performed using the characterization function shown in the **inset** (the purple point are the characterization data, the black line is the model fit and the red dots represent the points of **a**, displayed in a variance versus mean graph).

7.3.2 Double frequency amplitude

In order to test the general validity of the model we performed experiments on different samples in transmission: quartz and strontium titanate. In particular notice that these materials are transparent to the pump and probe radiation, conversely to bismuth, so in this case, there is no electronic mediation between the radiation and the phonon excitation.

In order to study the second frequency oscillation of the variance, we performed three time resolved measurement on quartz in which the unbalancing between probe and reference have been slightly modified. In all cases the oscillations reach the point of minimum variance but, while in the first case (blue dots and line) the mean oscillations are almost centered in x_{MIN}, in the other cases they concern only the upper (or lower) part of the oscillation.

In Figure 7.7 the three variance measurements as a function of their unbalancing

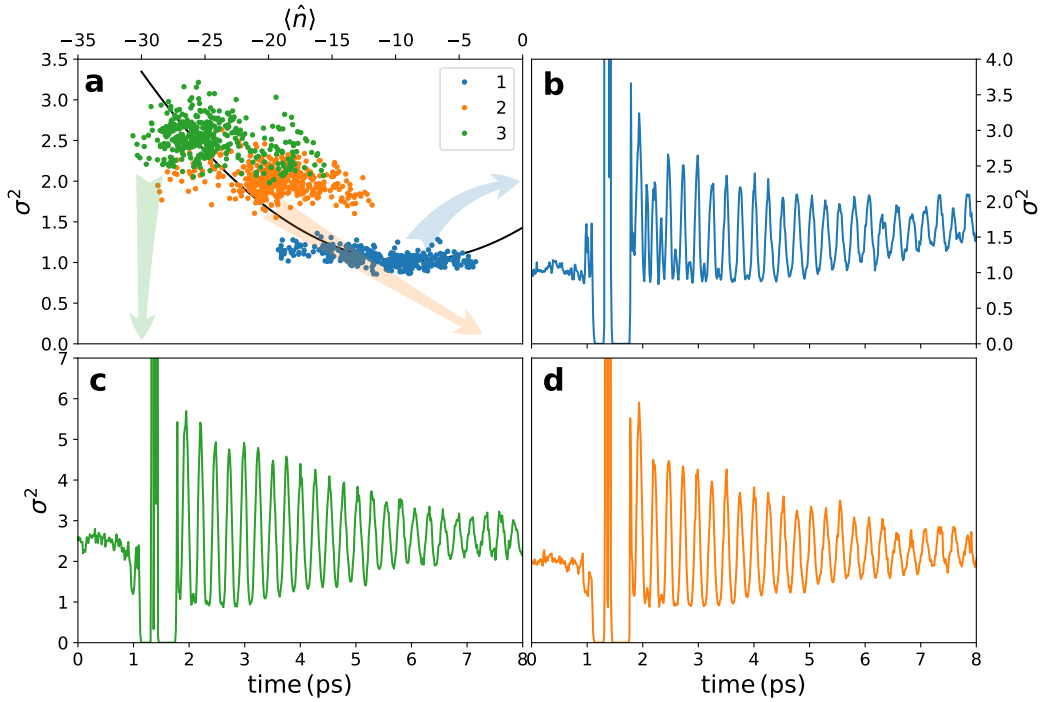

Fig. 7.7.: Noise dynamics: double frequency amplitude. Amplitude of the double frequency component for quartz in the variance dynamics as a function of the unbalancing. **a** Characterization function of the experiment (black lines) and balancing between the probe beam and the reference one before the excitation (colored dots). **b** Variance dynamics for balancing around x_{MIN} (blue dots in **a**): the second frequency contribution is clearly visible for about 2 ps after the excitation and its amplitude immediately after the pump arrival is comparable with the phonon frequency one. **c** and **d** Variance dynamics for balancing far from x_{MIN} (green and orange dots in **a**): the second frequency amplitude is smaller with respect to the phonon frequency one.

are shown. Figure 7.7 **a** displays the characterization function (black line) and three

possible values of the balancing (blue, orange and green dots), acquired without exciting the sample. Figure 7.7 **b** shows the variance dynamics related to the blue points: the double frequency is clear for about 2 ps, although its time decay is much faster than the phonon frequency one. On the other hand, in Figures 7.7 **c** and **d** the ratio between the amplitudes of the second and first oscillation is definitely decreased. The effect is even more visible by plotting the variance dynamics of the three measurements in the same graph (Figure 7.8 **a**). This representation highlights that the presence of the second Fourier component is actually more visible if the mean value oscillations are closed to the point of minimum variance. Moreover the plot shows that the amplitude of the variance changes with the unbalancing: this phenomenon is also predicted by the model, since the variance dynamics is related to the slope of the characterization function for a certain mean value (see Figure 6.20).

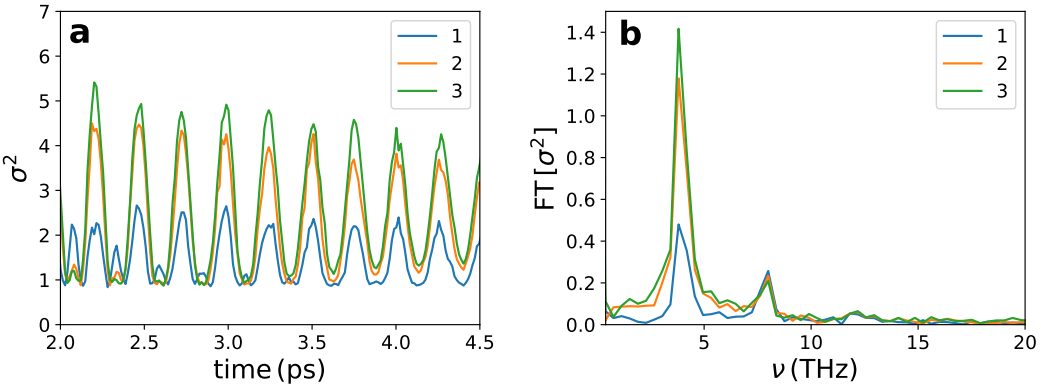

Fig. 7.8.: **Noise dynamics: variance comparison.** Comparison between the different variance dynamics displayed in Figure 7.7. **a** First 2 picoseconds after the excitation of the variance dynamics for the three signals. If the mean oscillates around the minimum variance point, the value of the variance is small, but the ratio between the amplitude of the two frequency contributions (Ω and 2Ω, where Ω is the phonon frequency) is relatively high (blue curve). On the other hand, far from x_{MIN} (orange and green lines), the amplitude of the Ω contribution is enhanced and the 2Ω one is reduced. **b** Corresponding Fourier Transform for the three signals.

In section 6.5 we observed that, although the characterization function is very similar to a *parabola*, it is characterized also by a small third order contribution, so we wonder whether this third order term can be observed in the acquired variance. We observed a small evidence of the described dependence in the measurement plotted in Figure 7.9 **a**. Again, the mean value oscillates around x_{MIN}, which is about -5 now[3], and correspondingly a double frequency signal is observed in the variance. Anyway another piece of information can be extracted from the Fourier Transform of the mean number of photons and variance signal, where a third peak appears

[3]In all the measurements the mean value and the variance are expressed in the units provided by the detection and acquisition system (V) and are proportional to the differential intensity and so to the differential number of photons impinging on the diodes.

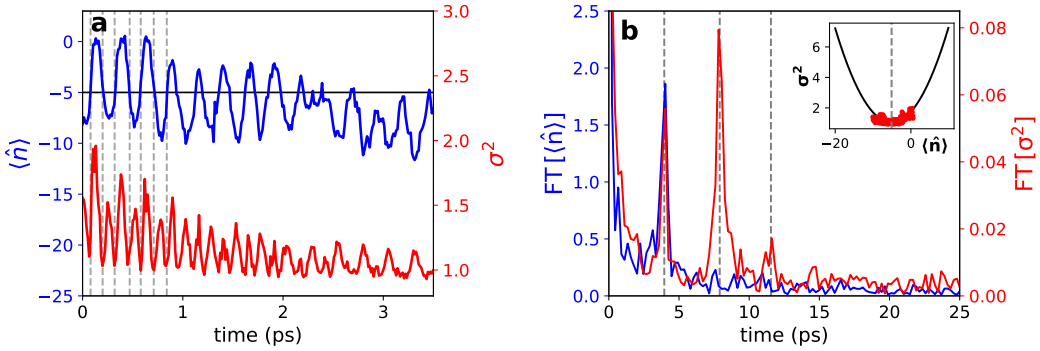

Fig. 7.9.: Noise dynamics: 3Ω component. **a** Mean (blue line) and variance (red line) dynamics for a quartz measurement. The horizontal line represents the point of minimum variance x_{MIN}, while the vertical dashed ones are the time delays in which we expect a change of the variance slope in time. **b** Fourier transforms of the average and variance signal. A small peak at $3\Omega \approx 11.5\,\mathrm{THz}$ is visible in the variance Fourier Transform. **Inset:** characterization function (black line) and variance *versus* mean points (red) for the measurement plotted in **a**.

(only in the noise Transform) at three times the phonon frequency. This is a quite strong evidence of a third order dependence of the variance on the mean value, and a possible further proof of the validity of the Beam Splitter model.

7.3.3 Double frequency decay

In the previous measurements the amplitude of the double frequency (2Ω) component has always a different time decay with respect to the Ω one. The aim of the present section is to understand how this difference is related to the Beam Splitter model and, in particular, to the characterization function.

The following measurements have been performed on strontium titanate ($SrTiO_3$) at about 10 K, selecting an E_g mode, with frequency $\Omega = 0.5\,\mathrm{THz}$. The measurement is shown in Figure 7.10, where both the mean and the variance dynamics are plotted, together with the characterization function of the system.
The 2Ω component is not clearly visible from the measurement, so we moved to a Fourier analysis. In particular, since we are interested in the duration of a certain frequency component, we opted for the wavelet analysis described in section 7.2, which is plotted in Figure 7.11 **c**.

The $\Omega \approx 0.5\,\mathrm{THz}$ is quite intense and visible (red and yellow area) in the variance wavelet analysis. The second contribution ($2\Omega \approx 1\,\mathrm{THz}$) is also present for about 2 ps (light blue area in the map). In order to understand the reason of this fast decay, we plotted the mean dynamics in Figure 7.11 **a**: the blue line is the signal, the horizontal line marks the value of x_{MIN} and the vertical line highlights the last time delay in which the signal crosses x_{MIN}, that is, the last time delay for which

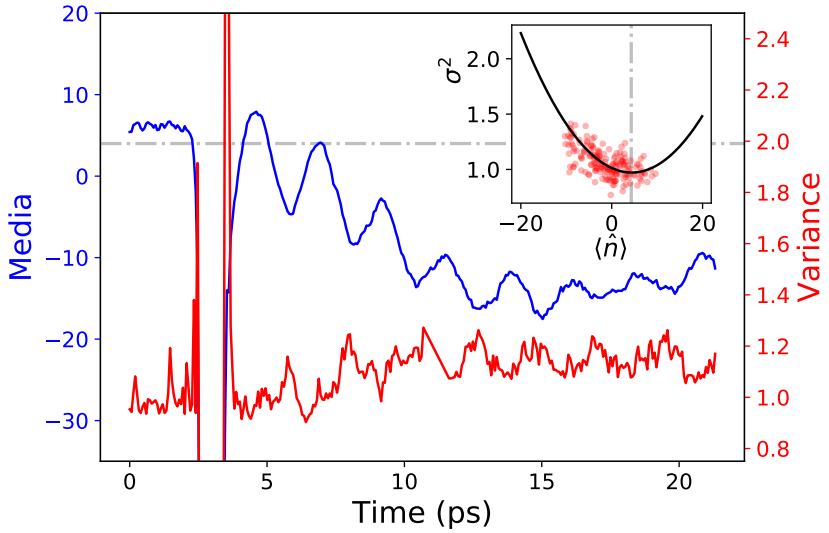

Fig. 7.10.: **$SrTiO_3$ measurement.** Mean (blue line) and variance (red line) dynamics for a $SrTiO_3$ measurement. The horizontal line represents the point of minimum variance x_{MIN}. **Inset:** characterization function (black line) and variance *versus* mean points (red) for the considered measurement.

we expect a double frequency contribution, according to the model. The same time delay is marked by the continuous vertical straight line in the map **c**: notice that the main contribution of the double frequency signal decays before this time delay. The small broadening until the time marked by the dashed line is due to the width of the gaussian function used in the wavelet analysis (for example, if the gaussian is centered at 7.5 ps and its σ is 1 ps, we could still observe a small contribution of the frequency content at 6.5 ps). Therefore, the analysis points out that the reason for the different time decays between the first and second frequency components is simply the crossing between the average signal and the point of minimum variance. Another proof of the double frequency dependence on the balancing between probe and reference beam is given by the absence of the 2Ω component in case of no crossing between the signal and x_{MIN} (Figure 7.12).

7.4 Two pumps measurements

In the present section we are presenting time resolved measurements in which two pumps impinges on the sample and the probe beam measures the variation in the reflectivity or transmission. In particular the pulses are set in order to create the phonon excitation with the first pump and destroy it with the second. The aim was to understand the effect of this exciting-destroying couple on the noise dynamics.

In the following we consider two samples: the results on Bismuth allows to understand the measurement concept and the main consequences of the presence of

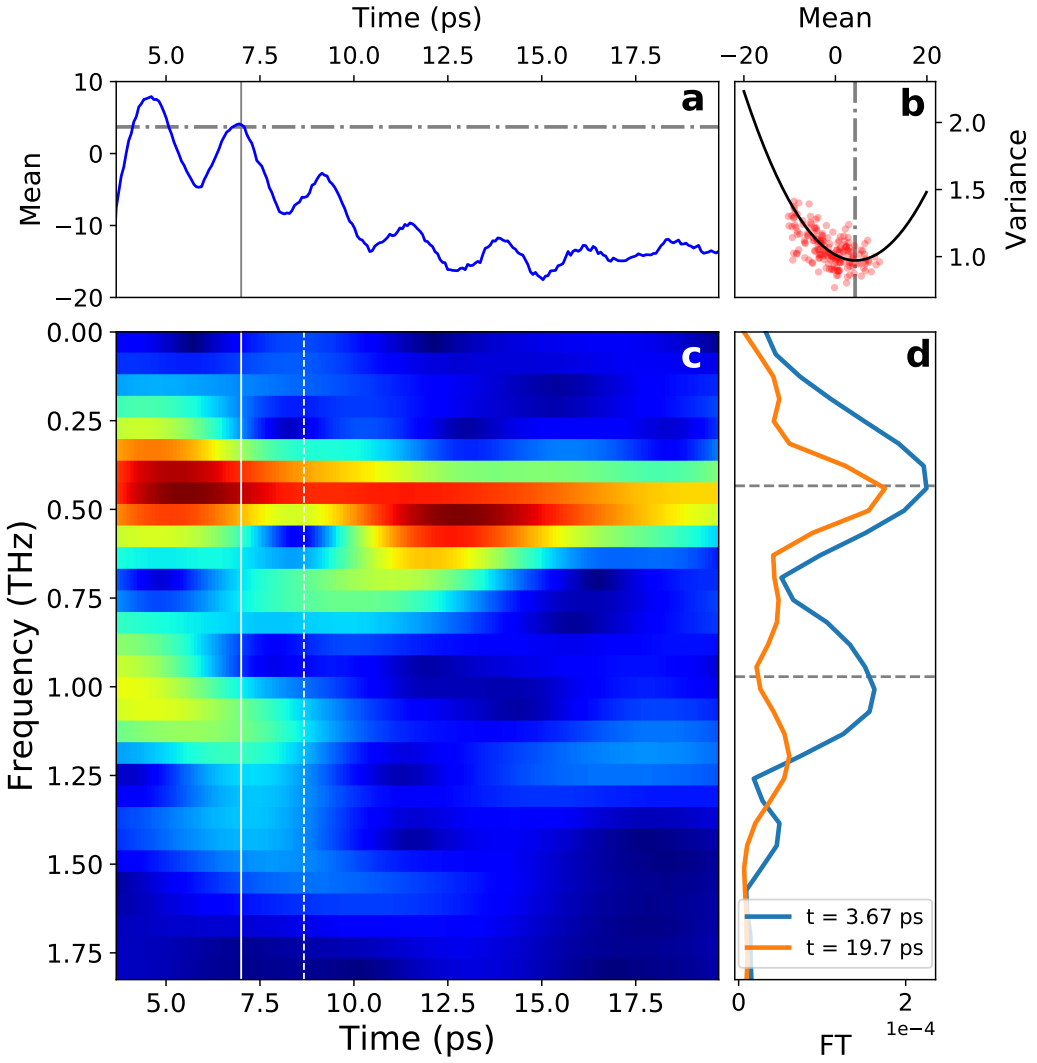

Fig. 7.11.: 2Ω component: wavelet analysis. **a** Mean value time dependent signal (blue line) for a $SrTiO_3$ measurement after the pump excitation. The oscillation has the frequency of the E_g phonon mode at $\Omega \approx 0.5\,\mathrm{THz}$. The horizontal line represents the point of minimum variance x_{MIN}, while the vertical one marks the last time delay in which the signal crosses x_{MIN} **b** characterization function (black line) and variance *versus* mean points (red) for the considered measurement. **c** Wavelet analysis for the ***variance*** dynamics after the excitation: the x-axis represents the time delay between the pump and the probe, and the y-axis the frequencies. The Ω component is present (and intense) for all time delays, whereas the 2Ω one has a faster time decay. The vertical continuous line highlights the relation between the 2Ω decay and the last crossing between signal and the point of minimum variance. The time difference between the two vertical lines in the map represents the width of the gaussian function used for the analysis. Therefore the dashed line highlights the time delay until which we still expect a small contribution of the 2Ω component. **d** Fourier Transform at two fixed time delays (they are obtained as vertical cuts of the map **c**. We observe that the 2Ω component, visible immediately after the excitation (blue line), completely disappears at longer time delays (orange line).

the second pump on the mean photon number and the variance dynamics. The same approach on a quartz sample leads to the unexpected measurement of more

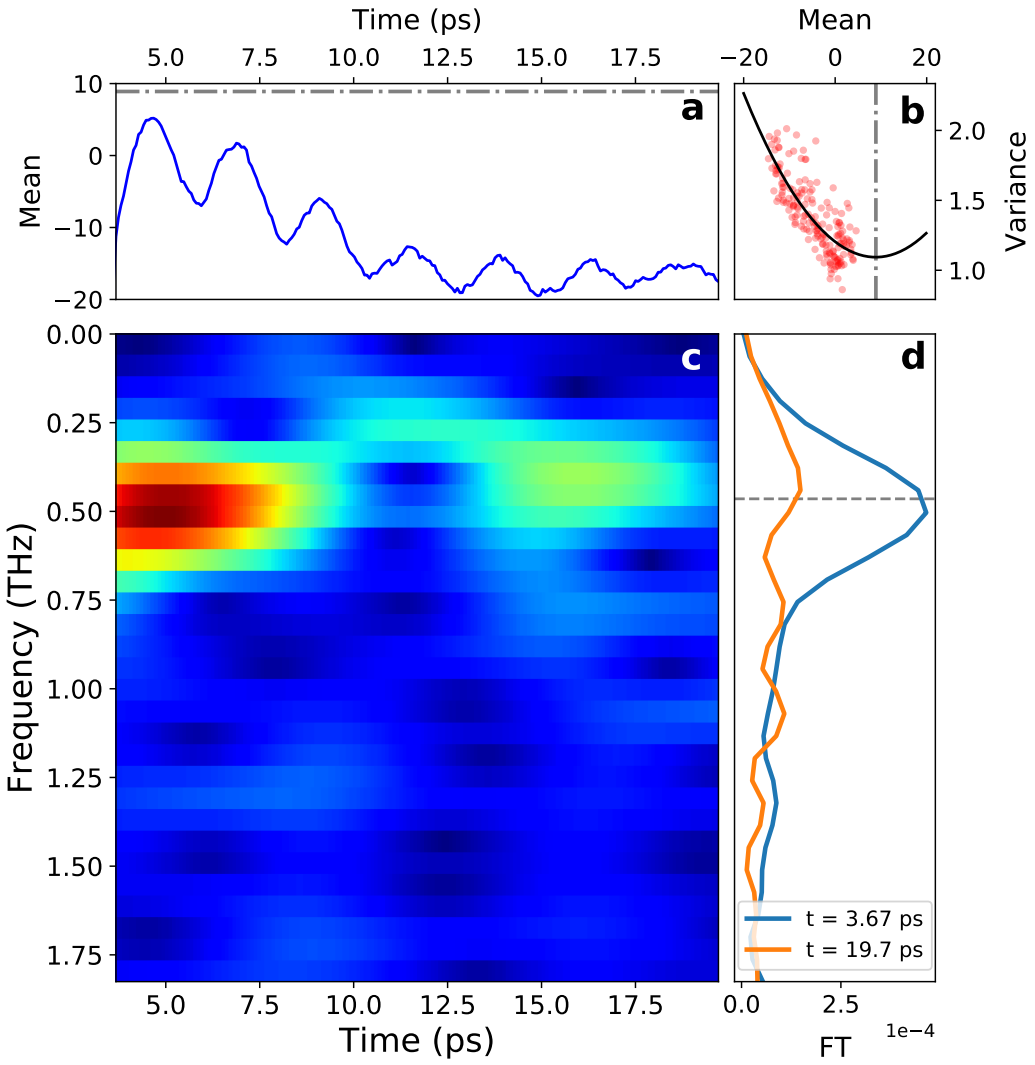

Fig. 7.12.: Absence of 2Ω component: wavelet analysis. Same analysis and plots of Figure 7.11 in absence of crossing between the mean photon number dynamics and the point of minimum variance (**a** and **b**). In this case no frequency component at 2Ω is visible (**c** and **d**), reinforcing the hypothesis of the connection between the mean value oscillation around the minimum of the characterization function and the appearance of the double frequency component in the variance dynamics.

phonon contributions, with interesting results and connections with the Beam Splitter model.

7.4.1 Bismuth: measurement concept

The results on the mean photon number dynamics in a Bismuth measurement are shown in Figure 7.13.

In **a** the results obtained with each of the the two single pumps are shown. The vertical dashed lines marks the phase difference between the two excited phonons:

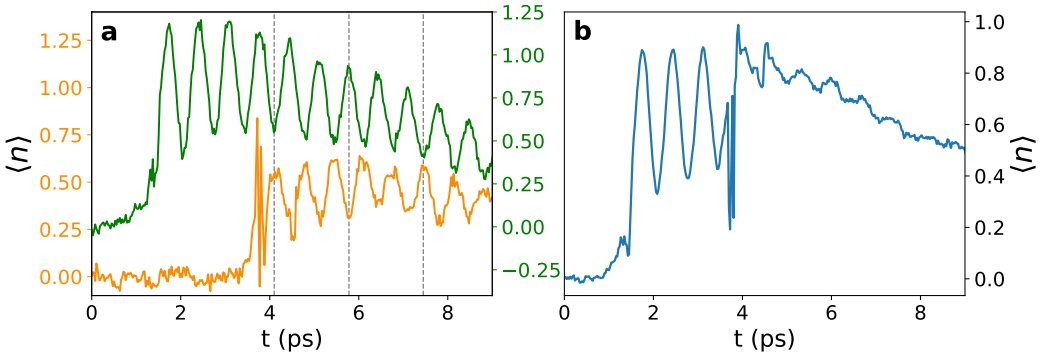

Fig. 7.13.: Two pump measurement on Bismuth. a Mean photon number time resolved signal for the two pumps used in the double pump measurement. The vertical lines are guides to compare the phase difference between the oscillations mapped on the reflected probe. **b** Complete time resolved measurement, in which the phonon mode is excited by the first pump pulse and destroyed by the second one. A small periodic component is still present after the second pulse and its frequency content is analyzed in Figure 7.14.

when the first signal is in its minimum value the second is at the maximum and vice versa. This π-shift in the phonon phase is the first essential condition to make the second pump pulse destructive of the phonon excitation. The second one is related to the pulse intensity: the two pumps must have different intensities since after few signal periods the reflectivity amplitude has already experienced a small de-excitation decay, so, the second pump should be less intense than the previous one. The result of the two pump measurement is plotted in Figure 7.13 **b**: from about 1.8 to 3.5 ps the phonon exitation produces the expected strong oscillations in the transient reflectivity. After the second pump ($t > 4\,\mathrm{ps}$) the oscillation amplitude is strongly suppressed, although small periodic signals are still visible. This can be due to the reflectivity dynamics, which presents two "different" decays for the two single pump measurements, as well as to experimental issues, such as the slight variation of the pumps fluences.

The wavelet analysis of the mean dynamics after the destructive pulse (Figure 7.14 **c**) unveils the presence of two frequency components: the usual one at the phonon frequency ($\Omega = 3\,\mathrm{THz}$) and another one at about $1\,\mathrm{THz}$. Notice that no phonon mode has been observed at this frequency and the E_g mode of Bismuth (at $\Omega_{Eg} = 2\,\mathrm{THz}$) is very hard to measure; usually it is detected just through signals at the frequency sum or difference with the more intense A_g mode. So the a possible explanation for this $1\,\mathrm{THz}$ oscillation is the difference of the A_g ($\Omega \approx 3\,\mathrm{THz}$) and E_g ($\Omega \approx 2\,\mathrm{THz}$)[4].

[4]The symbol "≈" is used since the frequency of both phonons is both fluence and time dependent, as discussed in section 7.2

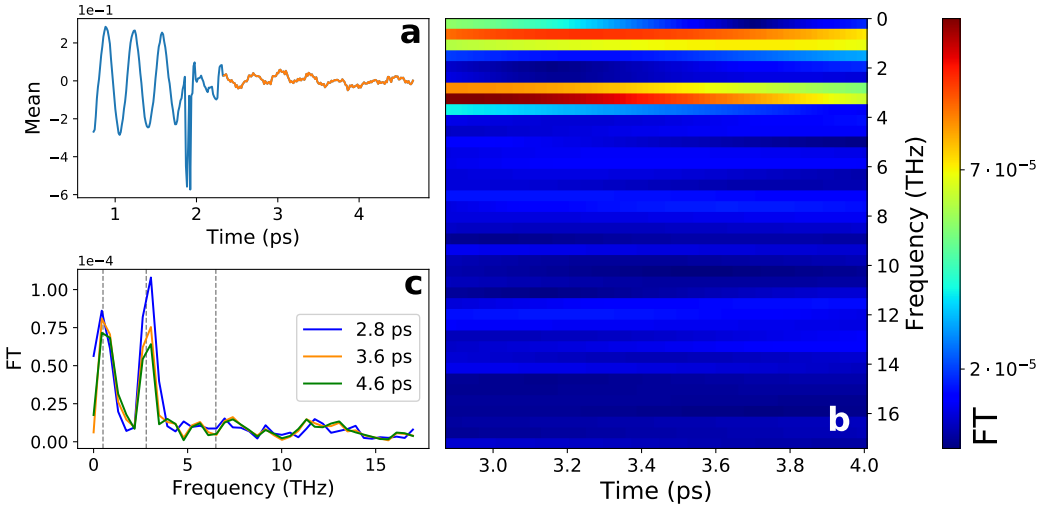

Fig. 7.14.: **Two pumps measurement: wavelet analysis. a** Mean value signal subtracted of the non-coherent de-excitation. The new signal has the advantage of eliminate the 0 frequency component in the Fourier transform, which could overcome weaker low frequency contributions. **b** Wavelet of the mean photon number dynamics after the second pump (orange signal in **a**). In **c** vertical cuts of map **b** at different time delays are plotted.

Concerning the analysis of the noise dynamics, the detected time resolved variance can be obtained once more by applying the Beam Splitter model (and so the characterization function) to the new mean value signal. The result is plotted in Figure 7.15, where the red line represents the acquired noise signal and the black one is the fit obtained by the model. The data can be quite well fitted by the model, a part for the time delays in which the pump impinges on the sample (at about 0.7, $2\,\mathrm{ps}$ and probably with a small delay even at $2.3\,\mathrm{ps}$), since a small portion of the pump pulse is scattered by the sample and reaches the photodiodes, increasing the variance value. This effect is not included in the model and so cannot be fitted.

On the other hand both the big oscillations between 0.7 and $2\,\mathrm{ps}$ and the small ones after the second pump are obtained by the model, as well as the average increase of the noise after the destructive pump (with respect to the equilibrium condition). Moreover, the variance oscillations are characterized by the same periods of the mean value dynamics, as expected from an unbalancing between probe and reference beam far from the point of minimum variance (as highlighted in the inset of Figure 7.15).

7.4.2 Quartz: two phonon contributions

The measurement described in the previous section was useful to characterize the technique (two pump time resolved measurement) and to study the effects on the noise due to the excitation and sudden de-excitation of one phonon mode.

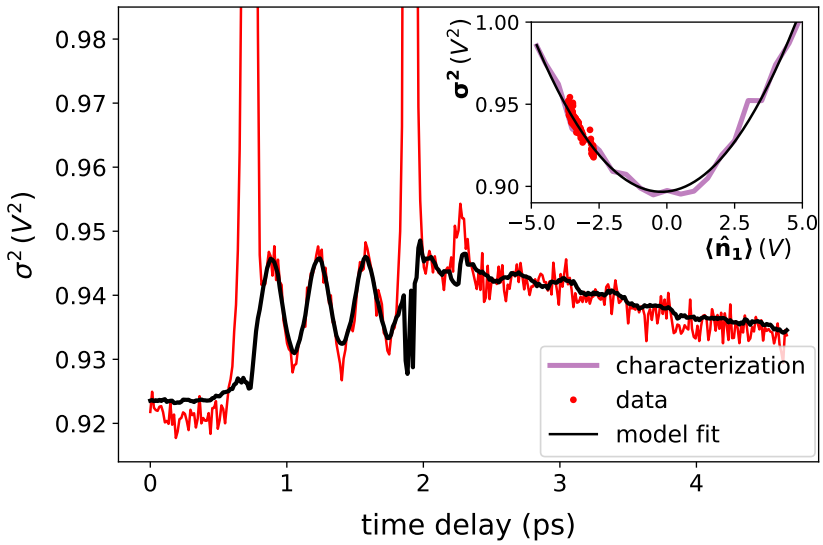

Fig. 7.15.: **Two pumps measurement: variance.** Variance dynamics (red line) associated to the double pump mean value signal plotted in Figure 7.13 **b** and the results of the model calculations

The same measurement, performed on a quartz sample (see Figure 7.16), allowed us to generalize the effect to the case of more excited phonons and suggested a study of the external noise contribution to the variance dynamics.

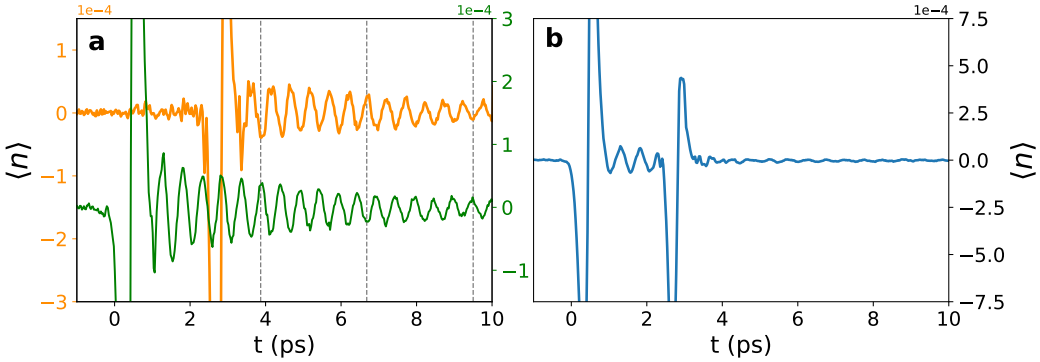

Fig. 7.16.: **Two pump measurement on Quartz.** **a** Mean photon number time resolved signal for the two pumps used in the double pump measurement. The vertical lines are guides to compare the phase difference between the oscillations mapped on the reflected probe. **b** Complete time resolved measurement, in which the E_g phonon mode is excited by the first pump pulse and destroyed by the second one. A small periodic component is still present after the second pulse and its frequency content is analyzed in Figure 7.17.

Multiple Phonon contribution

As in the measurements described in section 7.3.2, the polarization directions of the pumps, the probe and the analyzer after the sample should select a single Raman

mode of quartz, that is the E_g mode with frequency $\Omega = 3.8\,\mathrm{THz}$. On the other hand, the wavelet analysis plotted in Figure 7.17 reveals the presence of a second frequency component at about $6\,\mathrm{THz}$ after the destructive excitation (and eventually a small contribution at about $2\,\mathrm{THz}$, which could represent the difference between the two previous modes). This frequency is associated to the total symmetric A_g mode, which is much more intense than the E_g one and therefore can be detected even in E_g configurations, since a very small misalignment (or imperfection) of the final analyzer is enough not to perfectly select the crossed polarization.

The presence of the second phonon can be even enhanced by a three pulses measurement, since the intensity and time of application of the second pump is chosen to wash out the E_g oscillation, but the A_g one is characterized by a different amplitude and especially a different period. So, an accurate choice of the timing for the second pump could deplete the E_g oscillation and increase the amplitude of the A_g one.

These two defects of the measurement (the non-complete depletion of the E_g mode and the A_g signal passing through the last polarizer) leads to a time resolved mean signal in which at least two frequency components are present and their amplitudes are almost comparable (although the E_g one is still about 10 times the A_g).

External noise contribution

Before going on with the effects of multiple phonon excitation on the variance dynamic, a small digression to discuss the "external noise" contribution must be done. As a matter of fact, up to now we considered the variance as the consequence of the initial beam noise (both quantum and classical, there was no defined assumption) and of the interaction between the optical elements, which, in the model description of Chapter 6, are perfect and lossless Beam Splitters. The aim of this short section is to understand weather an external noise can significantly affect the measurements and, in particular, the variance dynamics. Moreover this aspect must be taken into account in the comparison between the data and the expected results calculated with the Beam Splitter model.

This study becomes important at this stage, since the measurement is quite delicate and the acquired signals are small with respect to the usual mean and variance dynamics (because of the depletion due to the destructive second pump). As a proof, we compare a single measurement and the average of tens of scans in Figure 7.18: notice that the single scan (light blue signal in Figure 7.18 **a**) has very strong fluctuations after $\tau = 3\,\mathrm{ps}$, which completely overcome the small oscillations visible in the average of several scans (dark blue line).

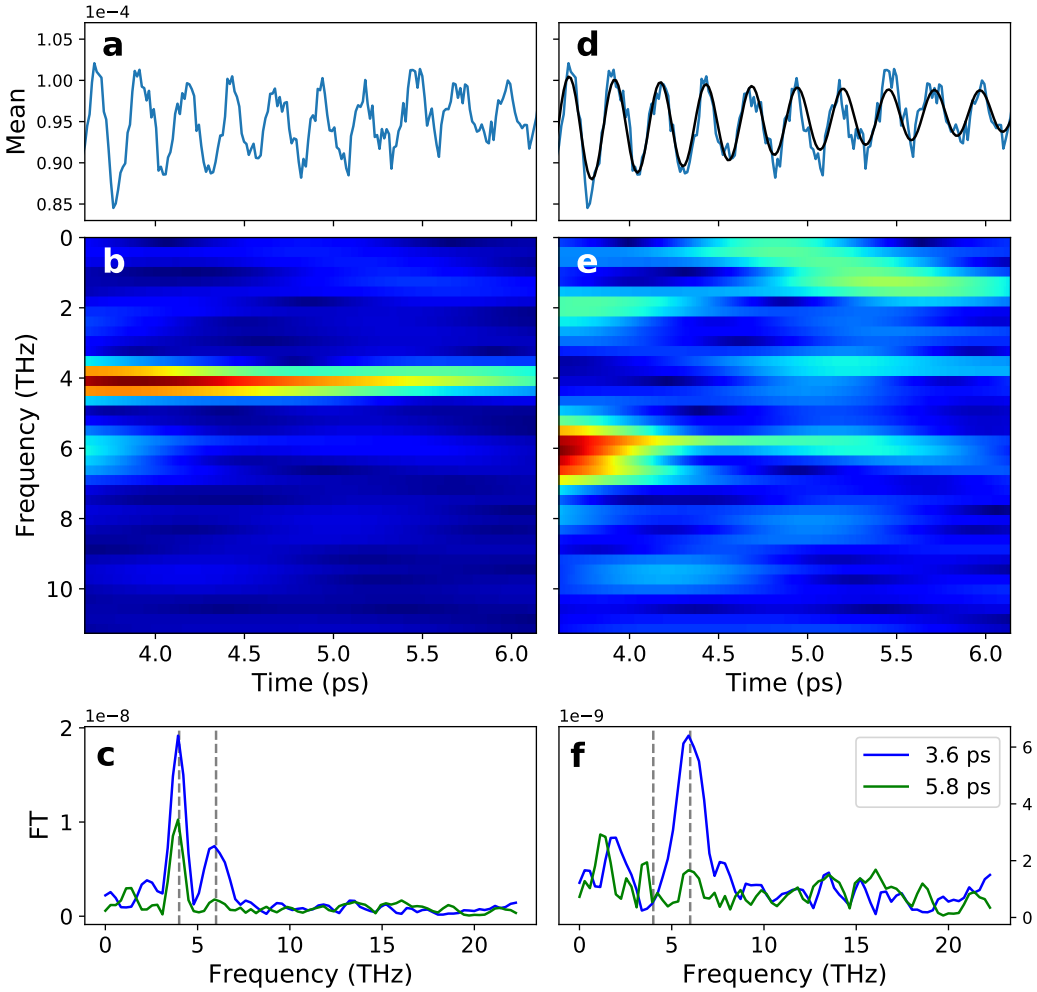

Fig. 7.17.: Multiple phonon contribution: mean value. **a** Mean photon number time resolved signal on quartz after the second pump (zoom of Figure 7.16 **b**): the oscillation due to the phonon excitation is still present. **b** Wavelet analysis of the mean signal plotted in **a**. The most evident component is the E_g one, with frequency $\Omega_{Eg} = 3.8\,\mathrm{THz}$. A small contribution at $6\,\mathrm{THz}$ is visible too. **c** Vertical cuts of the map **b** at 1.6 and 3.8 ps, that is the Fourier transform of the signal for a short time interval around these time delays. The second frequency component is observed at the shorter time delay. **d** Comparison between the mean value dynamics (blue line) and a fit performed with a periodic function with frequency Ω_{Eg} multiplied by an exponential decay (black line). **e** Wavelet analysis of the difference between the two signals plotted in **d**. This operation allows to exclude the most intense Fourier component (E_g), in order to better analyze the remaining one (A_g, with $\Omega_{Ag} = 6\,\mathrm{THz}$). **f** Vertical cuts of the map **e** at 1.6 and 3.8 ps.

The effect of the noise contribution in the model calculations is shown in Figure 7.19. If the measurement is very stable, most of the time the variance dynamics can be calculated from the averaged mean value, using the characterization function of the system. This means that the variance of average signal (on tens of time resolved scans) is almost equal to the average (on the same scan number) of the single scan variances. This is not the case for a noisy system, as highlighted by Figure 7.19,

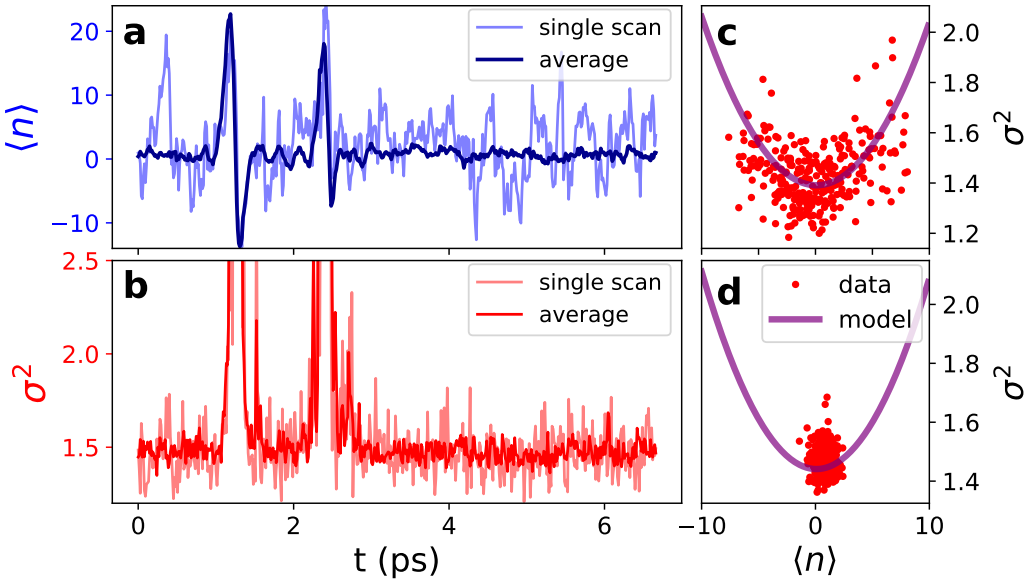

Fig. 7.18.: **External noise contribution.** **a** Comparison between the mean photon number dynamics of a single scan (light blue) and averaged on 30 scans (dark blue line) of a double pump quartz measurement, as the one plotted in Figure 7.16 **b**. Notice that the single scan fluctuations completely overcome the intrinsic signal oscillations due to the phonon excitation. **b** Single scan (light red) and averaged (dark red) variance dynamics. **c** Characterization function fitted with the BS model(purple line) and experimental data (variance *vs* mean photon number, red dots) of a single scan. **d** Characterization function (purple line) and experimental data (***averaged*** variance *vs* ***averaged*** mean photon number).

where the comparison between the acquired variance[5] (red line) and the model one (black curve), calculated from the average mean value (**a**) or as the average of the single scans variances (**b**) is plotted.

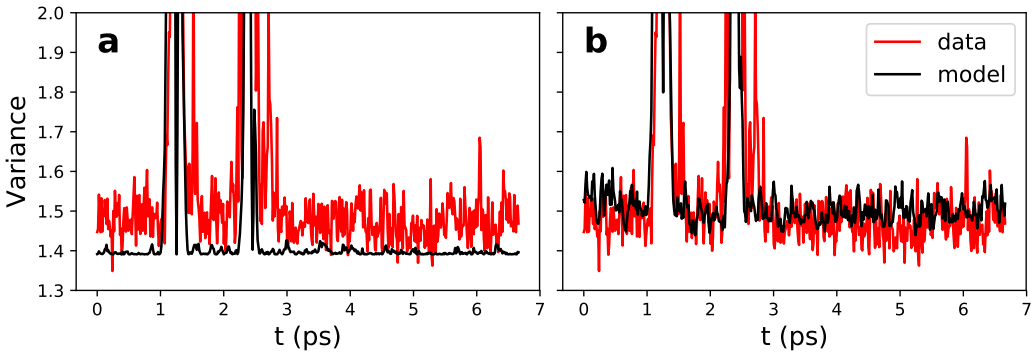

Fig. 7.19.: **External noise contribution: variance estimation.** Comparison between acquired variance, averaged on 30 scans (see Figure 7.18 **b**) and the model one, calculated from the mean photon number dynamics averaged on the same scans **a** or as the average variance computed starting from the single scans mean values.

[5]For all the measurements presented in this thesis, the acquired variance is the average of the single scans variance dynamics.

The comparison shows that the first calculation definitely underestimates the variance level: the main reason for this is that the calculation does not take into account the strong fluctuations of the single scans. The effect is clear if we consider the characterization function of the system: for a single scan high unbalacings can be reached (red points of Figure 7.18 **c**), producing relatively high variance values. On the other hand, if we consider the mean photon number dynamics obtained by averaging several scans, the predicted variance fluctuations will be underestimated, as shown in Figure 7.19 **a**.

Multiple phonon contribution in a noisy measurement

In the present section we are going to observe the effects of both external noise and multiple phonon excitation on the variance dynamics and to compare them with the predictions of the Beam Splitter model.

The results of the measurements are plotted in Figure 7.20 **a**, where the dynamics of the mean photon number for a single scan is displayed; the inset shows the characterization function $\sigma^2(\langle\hat{n}\rangle)$ (purple line) and the acquired variance *vs* mean (red dots). Panel **b** displays the result of the wavelet analysis on the acquired *variance* for three time delays. The use of this analysis is due to the fact that in this case the Fourier transform on the complete (noisy) signal washed out most of the frequency components. The black dashed lines represents the (shifted) average of the three signals: it is not really a significant quantity, it serves mainly as a guide for the eye. The yellow vertical lines highlight the phonon frequencies ($\Omega_{Eg} = 3.8\,\mathrm{THz}$, $\Omega_{Ag} = 6.2\,\mathrm{THz}$ and eventually $\Omega_{Ag2} = 10.9\,\mathrm{THz}$), whereas the green lines represent the sum or difference of the listed phonon frequencies; in particular the dark green line is the $2\Omega_{Eg} = 7.6\,\mathrm{THz}$ component. Notice that the only observable Fourier component of the variance dynamics after the second pump interaction are the ones related to the sum/difference of phonon modes, and in particular $\Omega_{Ag} - \Omega_{Eg} = 2.4\,\mathrm{THz}$ (observed at all time delays), $\Omega_{Ag2} - \Omega_{Ag} = 4.7\,\mathrm{THz}$ (especially visible at 4.1 and 1.6 ps) and the double frequency $2\Omega_{Eg} = 7.6\,\mathrm{THz}$.
This result is completely different from the ones presented in the previous sections, in which the variance dynamics *always* showed a Fourier component at the phonon frequency and then, for particular values of the mean photon number oscillation, a 2Ω component.

In order to understand the reason for these unexpected experimental results we simulated several mean photon number dynamics, different for amplitude of the phonon oscillations, random noise added and balancing between the probe and reference beams and calculated the corresponding variance (through the character-

ization function obtained by the Beam Splitter model) and its Fourier Transform. The aim is to understand which noise, amplitude and unbalancing configuration can give rise to the result plotted in Figure 7.20 **b**.

Figure 7.20 **c** shows the case of weak phonon oscillations, low noise level and unbalancing higher that x_{MIN} (notice that for $\langle\hat{n}\rangle < x_{MIN}$ and $\langle\hat{n}\rangle > x_{MIN}$ the result is similar. A different behavior occurs if the mean oscillation crosses the minimum variance point x_{MIN}). The corresponding variance Fourier Transform (**d**) reveals that in this case the most visible noise contributions have the phonon frequency, although very small peaks are visible even at the sum and differential frequency components. Notice that the addition a higher random noise to the previous simulation (Figure 7.20 **e**) produces the complete disappearance of these weaker Fourier component (Figure 7.20 **f**), suggesting that the considered configuration (and especially the choice of $\langle\hat{n}\rangle > x_{MIN}$ for each time delay) is not descriptive of our experiment.

The scenario completely change if we shift the mean average value around x_{MIN}. A somewhat conunterintuitive result shows that small oscillation amplitudes with low noise (Figure 7.20 **g**) produce variance contributions both at the phonon frequencies and at their sums and differences (Figure 7.20 **h**). A slight increase of the random external noise in the signal makes the weaker Fourier component indistinguishable. It also deplete the Ω_{Eg} peak, which was actually quite high in the low noise case (Figure 7.20 **j**).
The increase of the oscillation amplitude (Figure 7.20 **k** and **l**) reduces the phonon peaks of the variance Fourier Transform, maintaining the additional and differential ones ($\Omega_i \pm \Omega_j$, Figure 7.20 **l**). Finally the enhancement of the random noise (Figure 7.20 **k**) completely overcome the Ω_i variance signals, letting just the sum/difference components (Figure 7.20 **n**.
The following table summarizes the features of the simulations and the obtained results, in terms of frequencies contributions (phonons and sums/differences).

features	a-b	c-d	e-f	g-h	i-j	k-l	m-n
DATA	x						
SIMULATION		x	x	x	x	x	x
NON-CENTERED		x	x				
CENTERED				x	x	x	x
LOW AMPLITUDE		x	x	x	x		
HIGH AMPLITUDE						x	x
LOW EXT. NOISE		x		x		x	
HIGH EXT. NOISE			x		x		x
PHONONS		x	x	x		x	
SUM/DIFFERENCE	x	x		x	x	x	x

The simulation reveals that the essential conditions which prevent detection of the phonon frequencies in the time resolved variance signal are the relatively high added noise level (as expected) and a mean phonon number dynamics, which must oscillates around x_{MIN}. The oscillation amplitude with respect to the added noise can define better (or worse, until they disappear) the peaks of the variance Fourier Transform. Since the experimental data plotted in Figure 7.20 **a** and the Fourier Transform of the related variance are quite noisy, but they show some frequency component at $\Omega = \Omega_i \pm \Omega_j$, the configuration which better describes our measurement is the one with mean oscillations centered on x_{MIN} and a high ratio between the external noise fluctuations and the Ω_i amplitudes in the mean photon number dynamics.

7.5 Summary and conclusions

The aim of the chapter was to verify the validity of the Beam Splitter model introduced in chapter 6 and to analyze the effects related to the noise of a time resolved measurement. In particular we observed the following phenomena:

1. REVERSING OF THE VARIANCE. The variance dynamics is reversed (in the acceptation of *inversion of the slope*, as already defined at the beginning of the Chapter) if the mean photon number shifts from low values (below the point of minimum variance x_{MIN}) to high values (above x_{MIN}). Moreover if the mean is close to the point of minimum variance and its variation is relatively small, the variance has no dynamics after the excitation. Both the effects are predicted by the model and can be calculated through the characterization function of the experimental set-up: in first approximation, the higher is the slope of the characterization function for a certain mean measurement, the bigger is the variance dynamic range. Therefore around the point of minimum variance the amplitude of the variance oscillation is about zero.

2. DOUBLE FREQUENCY COMPONENT. Phononic excitations of the sample produce an oscillating time dependence of the probe intensity, with the same frequency Ω of the excited phonon mode. In some experimental configurations (that is, if $\langle\hat{n}\rangle$ crosses the x_{MIN} value), the acquired variance could present a Fourier component at 2Ω: this effect is due to the almost quadratic behavior of the characterization function $\sigma^2(\langle\hat{n}\rangle)$ around the minimum. In order to exclude any other possible reason for this double frequency component, we checked that both its amplitude and the time decay are strictly related to the mean photon number dynamics and especially to its position with respect to x_{MIN}.

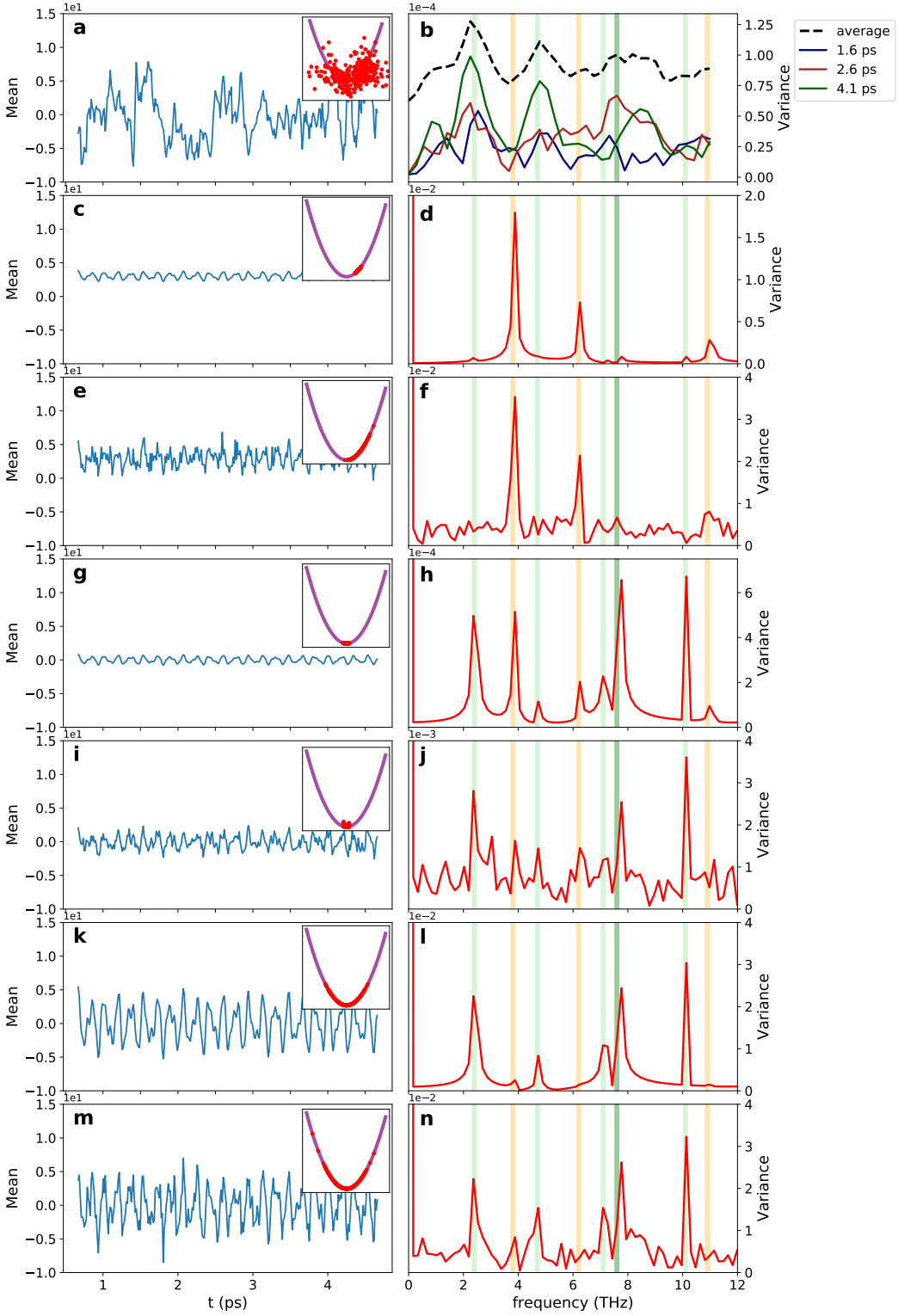

Fig. 7.20.: **Experimental condition: variance simulation. Left column:** Mean photon number dynamics after the second pump excitations. **Inset:** Characterization function (black line) and experimental points (red dots). **Right column:** related variance Fourier Transform.

Finally we performed the measurement on different samples, in order to exclude peculiar material effects.

3. THREE PULSE MEASUREMENT. We performed two-pumps measurements, in which the first pulse excited a phonon mode in the second, whereas the second one destroys the same mode. The measurements and the comparison with the model reveals that in this case the characterization function can describe the variance dynamics.

4. MULTIPLE PHONON EXCITATION. If the pump pulse(s) is able to excite more than one phonon mode, with comparable amplitude, the variance dynamics can oscillates at Ω_i (phonon frequencies) and/or $\Omega_i \pm \Omega_j$, depending on
i. the unbalancing ($\langle \hat{n} \rangle < x_{MIN}$ or $\langle \hat{n} \rangle > x_{MIN}$): it determines the relative amplitude between the phonon components and the sum/difference ones.
ii. the ratio between the external noise and the oscillation amplitude. If the noise is high enough it can eliminate some Fourier components: in the case of oscillations around the point of minimum variance the Ω_i are completely overcome by the experimental noise, while in appropriate condition the difference between the frequencies of the phonon modes can remain visible.

When performing a noise measurement all these aspect must be taken into account.

8

Noise detection in Bi2212 measurements

The measurement of the complete photon number distribution of a light beam (after the interaction with a sample), is expected to provide additive information than a “simple” intensity measurement. The application of this concept to a pump probe measurement could be a way to understand intriguing and still unexplained properties of strongly correlated materials. On the other hand the interpretation of the results is not easy and lots of side effects must be taken into account.

In the previous chapters we tried to find the key for these measurements interpretation and to distinguish the set-up effects from the sample ones. In particular we

1. introduced the measurement concept, the single pulse acquisition (essential to evaluate a photon number distribution), with some technical details on the calculations of the significant quantities;

2. developed a theoretical model (*BS model*) to describe the experimental set-up and to predict the behavior of the variance on the phonon number from the variation of the acquired mean value;

3. verified the validity of the model, comparing its predictions with the experimental data. In particular, we focused on the systematic effects of this kind of measurement, analyzing the acquired signal and noise dynamics on different samples (in order to exclude any material dependence).

Keeping in mind all these results, we are ready now to move to more interesting samples and to check if and how this acquisition system is able to provide new and interesting pieces of information on the sample. Therefore we decided to go back to our initial sample, the high T_c superconductor Yttrium substituted Bi2212 (see chapter 5).

8.1 Measurements and results

Contrarily to the measurements presented in Chapter 7, in this case the sample was excited by a MIR pump ($h\nu \approx 170\,\mathrm{meV}$) and probed with a $1.63\,\mathrm{eV}$ ultrashort pulse (details on the pulse generation are given in section 3.3). The pump and the probe propagation direction are parallel to the sample c-axis, while their polarization directions have always been kept parallel to the copper-copper axis. The same polarization is selected by the final analyzer.

The first goal of the measurement was to compare the variances dynamics after a mid-infrared excitation at room temperature (that is, in metallic phase) and in superconducting state. The preliminary results are plotted in Figure 8.1, where the transient reflectivity (blue curve) and the variance dynamics (red line) are compared for certain experimental conditions.

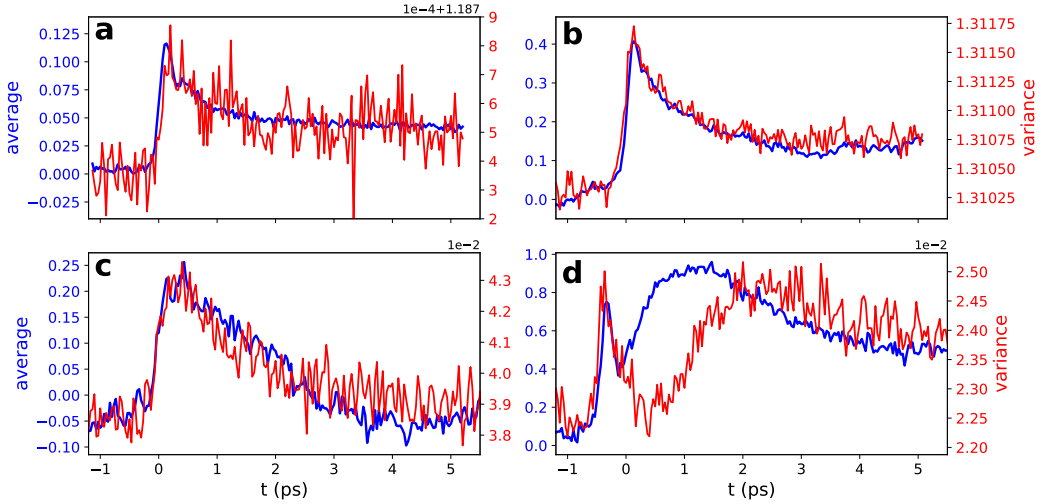

Fig. 8.1.: Mean and variance reflectivity measurements. Mean value (blue) and variance (red) time resolved measurements for different sample phases and pump fluences. In the first row: low fluence measurement ($f = 0.1\,\mathrm{mJ}\cdot\mathrm{cm}^{-2}$) **a** and high fluence measurement ($f = 1\,\mathrm{mJ}\cdot\mathrm{cm}^{-2}$) **b** at room temperature ($T = 300\,\mathrm{K}$). In **c** and **d** measurements the superconducting responses ($T \approx 12\,\mathrm{K}$) for low and high fluence respectively are plotted.

Figure 8.1 **a** and **b** show the results for different pump fluences at room temperature: in both cases the variance shows a dynamics, which seems to be strictly related to the mean value. On the contrary, in superconducting phase mean and variance have different behaviors (Figure 8.1 **c** and **d**), depending on the pump fluence. In particular, while low fluence excitations in superconducting phase produce a qualitatively similar time evolution for intensity and fluctuations, the variance dynamics induced by a high pump fluence in superconducting phase does not follow the mean value one. This evident discrepancy in the de-excitation process can be the clue for a hidden sample features, probably related to the material phase.

8.2 Model comparison

Because of the peculiarity of its results, we will focus at first on the measurement with high pump fluence in the superconducting phase.
The experimental concept is shown in Figure 8.2.

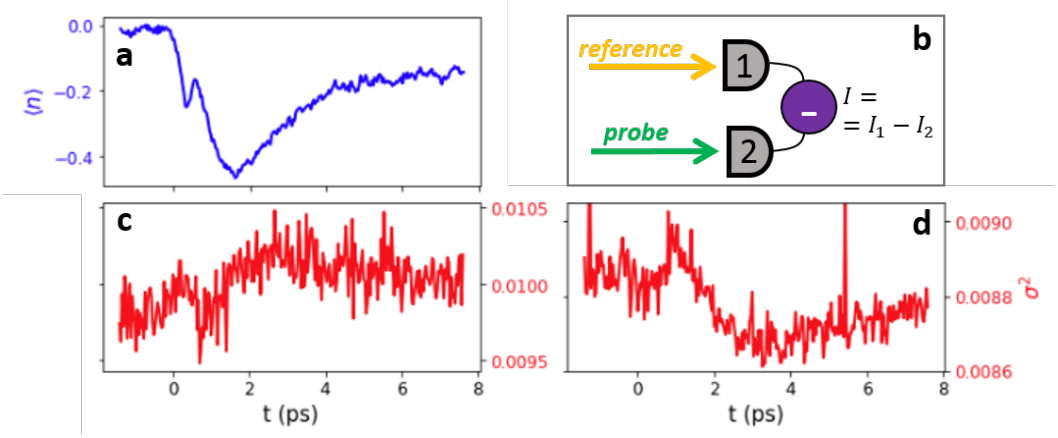

Fig. 8.2.: Variance as a function of the unbalancing. **a** Mean value for initial balanced differential signal. The mean value present a "negative" response, since in our set-up the probe signal is subtracted from the reference one, as shown in **b**. In the measurements plotted in Figure 8.1 the signal has been reversed, in order to show the real time evolution. From now on raw data will be plotted, in order to better explain the results and the developed model. **c** and **d** show the variance dynamics for negative and positive initial unbalancing respectively.

Performing several measurements in various conditions we noticed that the variance dynamics is visible only if the differential signal is far from the point of minimum variance x_{MIN}. Moreover, a change in the initial reflectivity can "reverse" the shape of the variance as shown in Figure 8.2 **c** and **d**, where the variance time dependence for different initial unbalancing is shown. Both the described effects can be explained by the BS model and have been observed on other samples (see Chapter 7)

Anyway, if we try to fit the acquired variance with the BS model (using the related characterization function $\sigma^2(\langle\hat{n}\rangle)$) as for the data of Chapter 7, we cannot end up with satisfactory results (Figure 8.3). As a matter of fact the model does not really fit the variance dynamics, since the modeled noise of the de-excitation is usually much more similar to the mean one. The effect is evident in Figure 8.3 **a** and **c**. It is clear from the simulation that the model (as described up to now) is not enough to fit the data and some other effects must be taken into account.

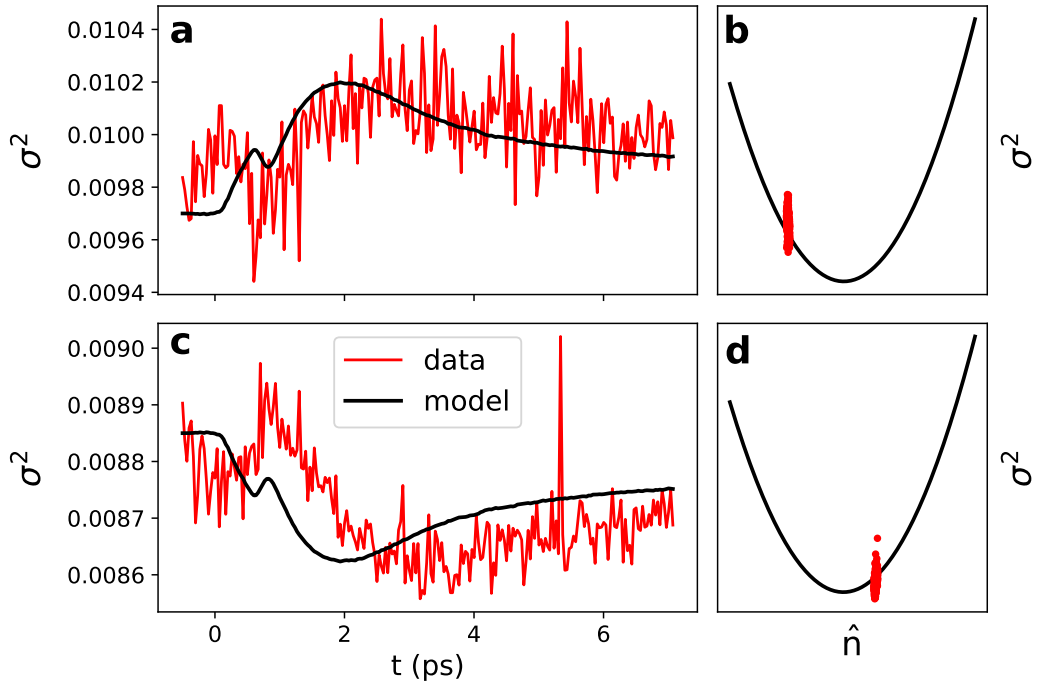

Fig. 8.3.: BS model (1): data and simulation. Comparison between the calculation of the time evolution of the variance obtained through the BS model (black) and the raw variance data (red), for $\langle \hat{n} \rangle < x_{MIN}$ **a** and $\langle \hat{n} \rangle > x_{MIN}$ **c**. The characterization function (black line) and the acquired variance *vs* mean points (red dots) are plotted in **b** and **d** respectively.

8.3 Polarization selection

In the Bi2212 pump-probe measurement a key role is played by the last optical element of the experiment: the final analyzer, whose aim is the selection of the light polarization parallel to the probe initial one. Notice that the signal obtained in crossed polarization is much less intense than the measured one (about $\frac{1}{100}$) and no qualitative modification can be observed in the transient reflectivity at first glance. Like all other dissipators this last polarizer can be described as a beam splitter.

In order to take into account this last optical element, we consider the same model set-up used in section 6.6, but we attribute different meanings to the Beam Splitters. The new interpretation is sketched in Figure 8.4.

In this case BS2 represents the sample, whereas BS3 stands for the last polarizer (analyzer)[1].

[1]Notice that now we are working in the approximation that no other dissipation occurs on the probe beam.

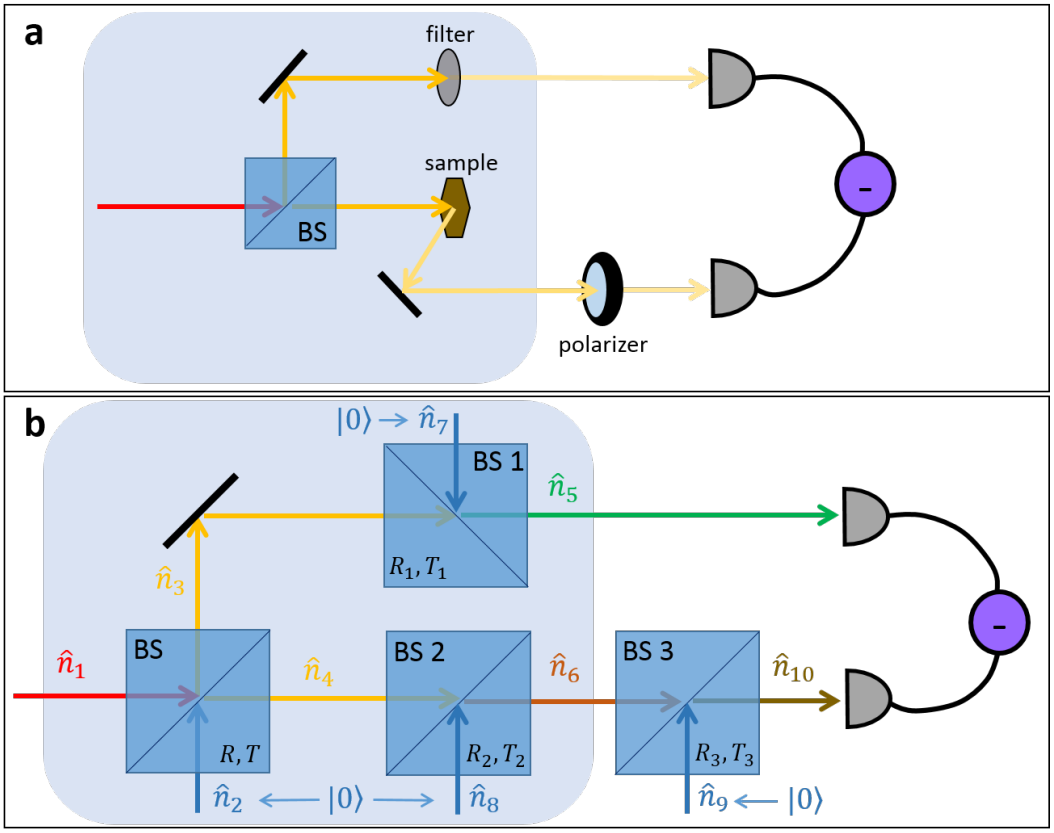

Fig. 8.4.: Bi2212 noise measurement: set-up. a Set-up used for the mean and variance measurement of the Bi2212 sample. The most important difference with respect to the experiments described in chapters 6 and 7 is the presence of the last polarizer on the probe beam. **b** Beam Splitter model for the same set-up. On both representations light blue area indicates the set-up used to calculate the (time dependent) value of $|T_2|^2$.

Let me remind the differential mean photon number (that we often define "unbalancing") and the variance formula for the described set-up:

$$\langle \hat{n}_5 - \hat{n}_{10} \rangle = \left(|T_1|^2 |R|^2 - |T_3|^2 |T_2|^2 |T|^2 \right) \langle \hat{n}_1 \rangle , \tag{8.1}$$

$$\begin{aligned} \sigma^2_{5-10} &= \left\langle (\hat{n}_5 - \hat{n}_{10})^2 \right\rangle - (\langle \hat{n}_5 - \hat{n}_{10} \rangle)^2 \\ &= \left(|T_1|^2 |R|^2 - |T_3|^2 |T_2|^2 |T|^2 \right)^2 \sigma^2_{n1} + \\ &+ \left(|T_3|^4 |T_2|^2 |R|^2 |T|^2 + |T_3|^4 |T_2|^2 |R_2|^2 |T|^2 + \right. \\ &+ |T_3|^4 |R_3|^2 |T_2|^2 |T|^2 + |T_1|^4 |R|^2 |T|^2 + \\ &+ \left. |T_1|^4 |R_1|^2 |T|^2 + 2 |T_3|^2 |T_2|^2 |T_1|^2 |R|^2 |T|^2 \right) \langle \hat{n}_1 \rangle . \end{aligned} \tag{8.2}$$

The characterization function of the system would be $\sigma^2_{5-10}(\langle \hat{n}_5 - \hat{n}_{10} \rangle)$.

The question is then how to describe the measured dynamics due to the pump excitation. Again, we will consider a time-dependent $|T_2|^2$, which represents the fraction of beam reflected by the sample and its time dependence is obtained by a normalized "standard" pump-probe measurement on the same sample, integrated in polarization, that is to say, a measurement obtained by the set-up highlighted by the light blue square in Figure 8.4. Notice that this set-up have already been modeled in section 6.5, therefore the transmittance $|T_2|^2$ can be derived from the relation 6.22 and one gets

$$|T_2|^2 = \frac{|T_1|^2 |R|^2 \langle \hat{n}_1 \rangle}{|T|^2 \langle \hat{n} \rangle}, \tag{8.3}$$

where $\hat{n}_1$ is the initial number of photons, T_i and R_i are the Beam Splitter parameters and $\hat{n}$ is the mean photon number signal measured in absence of the analyzer.

Notice that, in this sample, the pump induces not only an intensity dynamics, but also a polarization one, whose consequence is the detection of different time resolved signals for different (and in particular orthogonal) polarization selections. These signals are the A_g and B_{1g} modes, already discussed in sections 3.1.2, 4.3 and 5.4. To sum up, the measured signal is characterized by:

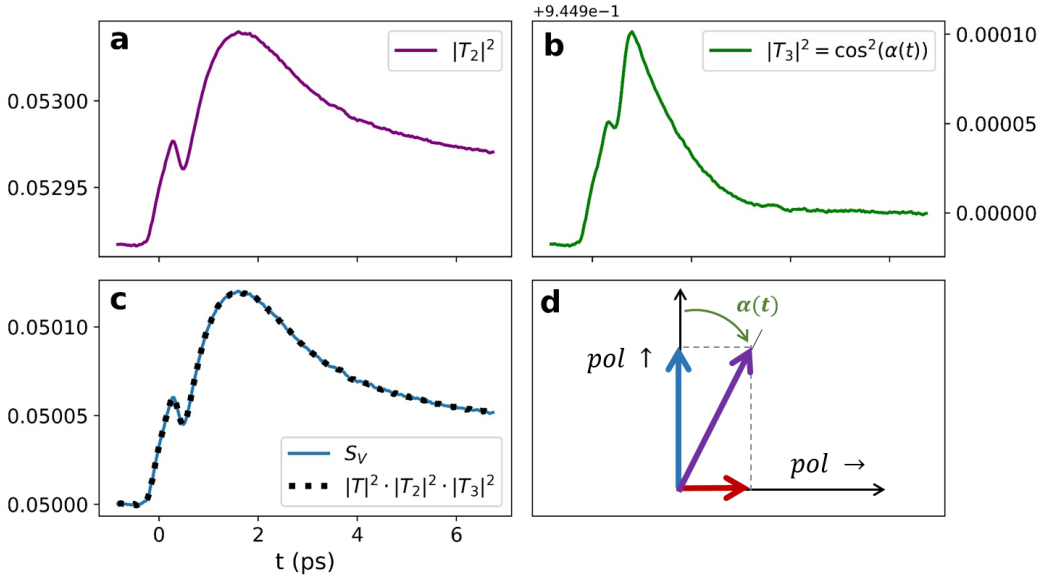

Fig. 8.5.: BS model: parameters dynamics. **a** Dynamics of the transmittance $|T_2|^2$ of the Beam Splitter representing the sample. **b** Dynamics of the transmittance $|T_3|^2$ of the Beam Splitter representing the last polarizer and so the selection of the vertical polarization. **c** Comparison between the signal obtained by selecting the probe vertical polarization and the one obtained by the product of the initial beam times the contributions of **a** and **b**. **d** Sketch of the polarization selection at a fixed time delay: the tangent of the angle $\alpha(\tilde{t})$ is obtained dividing the horizontal component (B_{1g} signal) at $t = \tilde{t}$ from the vertical component (A_g) at the same time delay.

i. a certain intensity $S_{TOT}(t)$ (integrated in polarization and proportional to $|T_2|^2$,

in this model)

ii. a time dependent angle $\alpha(t)$ between the probe polarization before and after the interaction with the sample.

Thus, the last analyzer can be introduced by putting $|T_3|^2 = \cos^2(\alpha(t))$ and so the signal detected by the negative diode will be proportional to $|T_3|^2 |T_2|^2 |T|^2 \langle \hat{n}_1 \rangle$ (see equation 8.1), that is, $S_{TOT} \cdot \cos^2(\alpha(t))$, in agreement with the Malus Law for a polarizer.

The dynamics of $|T_2|^2$ and of $|T_3|^2$ are shown in Figure 8.5 **a** and **b** respectively, whereas the calculation of the angle $\alpha(t)$ between the orthogonal components of the probe is sketched in Figure 8.5 **d**.

Figure 8.6 shows the comparison between experimental data and simulation (starting from equation 8.2), for $\langle \hat{n} \rangle < x_{MIN}$ (**a**) and $\langle \hat{n} \rangle > x_{MIN}$ (**b**). Notice that not only the model variance is reversed depending on the initial value of $|T_1|^2$ (as we observed also in the previous cases), but also the time evolution is similar to the experimental one and not related just to the reflectivity response.

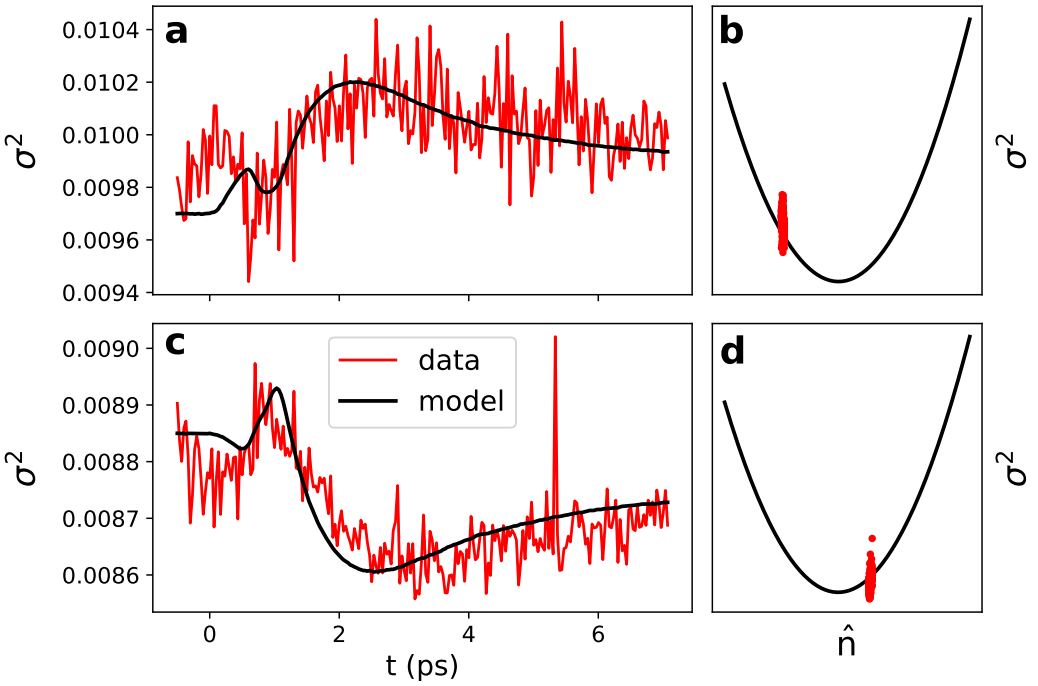

Fig. 8.6.: BS model: data and simulation. The red lines in **a** and **c** represent a pump-probe variance measurements on a optimally doped Bi2212 sample for different mean photon number values with respect to the point of minimum variance x_{MIN}, while the black line is the fit obtained from Equation 8.2. In **b** and **d** the characterization function (black line) and the experimental data (red dots) are plotted, for in **a** and **c** respectively.

This parameter definition (and especially their time dependence) allowed to obtain a better fit of the experimental data, as shown in Figure 8.6. Differently from the simulation of Figure 8.3, here the variance dynamics can be fitted for both mean

values “unbalancings” and, especially, it does not follow any more the mean photon number de-excitation.
According to the model the core of the difference between the two time dependences is that, while the mean value is affected just by T_2 and T_3 (Equation 8.1), the variance keeps also the information coming from R_2 and especially from R_3 (Equation 8.2), which in our case stands for the signal in the orthogonal polarization with respect to the detected one. In this picture the variance actually carries more information than the mean value, since it keeps a signature of every interaction as a product between measured signal and “non-selected signal” (for example the term $|T_3|^4 |R_3|^2 |T_2|^2 |T|^2$ in equation 8.2), as it is clear from the last interaction with the analyzer.

8.4 Temperature and fluence dependence

Up to now we were able to explain the variance dynamics of our Y-Bi2212 sample at low temperatures ($T < T_c$) and in high pump fluence regimes. On the other hand the model does not take into account neither the pump fluence nor the temperature (and so the phase of the sample), while we observed completely different results in the measurements just by tuning these parameters (see Figure 8.1). In particular the time dependence of the noise is qualitatively similar to the mean photon number one both for high temperatures ($T \approx 300\,\mathrm{K}$) and low fluences (even at low temperatures). How can this behavior be explained by the same BS model?

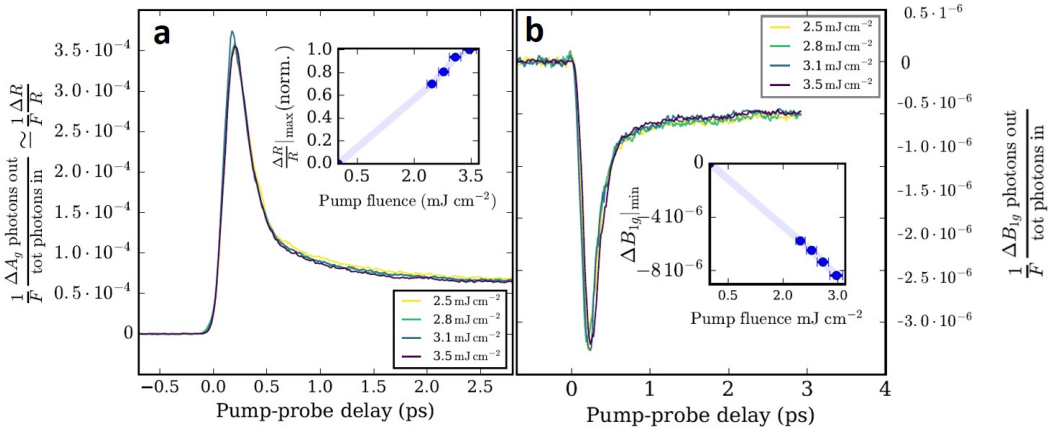

Fig. 8.7.: A_g **and** B_{1g} **signals at room temperature.** A_g (**a**) and B_{1g} (**b**) pump-probe signals at room temperature: the two dynamics are almost proportional for every pump fluence [74]

The difference between the two cases (variance dynamics similar/different from the signal one) is related to the sample response in the orthogonal (that is, non-selected) polarization. Let us consider the room temperature case: in metallic phase the

transient reflectivity measured in the horizontal (B_{1g}) and vertical (A_g) polarization is very similar, almost proportional (Figure 8.7).

Notice that in equation 8.2 the terms which are affected by the orthogonal polarization are the ones containing $|R_3|^2$; in the approximation in which horizontal and vertical signals are proportional ($S_H(t) = k \cdot S_V(t)$, where S_H and S_V are the signals obtained by selecting the horizontal and the vertical polarization respectively) $|R_3|^2$ becomes constant in time and so it does not contribute to the time evolution of the total signal. As a matter of fact

$$\begin{aligned} |R_3(t)|^2 &= 1 - |T_3(t)|^2 = \sin^2(\alpha(t)) \\ &= \left(\frac{S_H(t)}{\sqrt{S_H^2(t) + S_V^2(t)}} \right)^2 \\ &= \frac{k^2 \cdot S_V^2(t)}{k^2 \cdot S_V^2(t) + S_V^2(t)} \\ &= \frac{k^2}{k^2 + 1}. \end{aligned} \tag{8.4}$$

The same linear (or quasi-linear) relation between different polarization signals can be observed for high pump fluences at room temperature and for low fluences in the superconducting state [74], thus explaining the strict connection between mean value and variance in these conditions.

8.5 Conclusions

To sum up, performing time resolved single pulse measurements on Bi2212 we noticed that the time evolution of the variance is strictly connected to the initial balancing of the signal with a reference beam: in particular, the variance seems to "reverse" its dynamics for different initial unbalancings between the pump and the reference signal. This effect can be explained by a model in which all dissipators (BS, sample, filters, polarizers) are described as beam splitters. The pump interaction is introduced by a time evolution of the transmittance of the BS representing the sample and the analyzer, in order to mimic both the intensity and polarization variation induced by the pump excitation. A key role in the model is played by the description of the polarization selection, which makes the variance be affected not only by the mean value signal (mainly A_g symmetry), but also by the orthogonal polarization (B_{1g} symmetry), that are characterized by different de-excitation dynamics.

We observed also that the qualitative similarity of the variance dynamics and the mean photon number one at high temperature or low pump fluences is induced by

the ratio between the vertical (A_g) and horizontal (B_{1g}) signal in these conditions. If the two signals are (almost) proportional, from the BS model the variance is expected to follow the mean photon number dynamics.

9 Conclusion

Time resolved spectroscopy is a powerful tool to study complex materials: the strong correlations between the system degrees of freedom (electrons, spins, lattice etc.) can be studied measuring the relaxation of the different parameters after an external excitation. In pump-probe experiments the excitation is provided by an intense ultrashort light pulse and the de-excitation process is probed by a second laser pulse, whose ***intensity*** (proportional to the mean photon number) is detected after the interaction with the sample.

We used this technique to study the phase transition of an High Temperature Superconductor (optimally doped Y-Bi2212) through a temperature resolved pump-probe measurement across the critical temperature T_c. The results revealed that two excitation parameters are incisive: the pump photon energy and polarization. Concerning the photon energy, the discrimination is related to the characteristic energy of the system, that is, the superconducting gap Δ, while the choice of the polarization is related to the anisotropy of the system in real but especially in the reciprocal space. In particular, we noticed that the combination of low excitation photon energy ($h\nu < 2\Delta$) with a polarization parallel to the Copper-Copper axis of the system produces an enhancement of the superconducting dynamical response both below and above T_c.

The experimental results are supported by an effective theoretical model, based on BCS theory: despite the non conventional superconducting character of cuprates, their dynamical response can be qualitatively described by conventional models (for instance the Rothwarf Taylor equations). The additional terms of the BCS hamiltonian needed to effectively describe our system are the anisotropy of the superconducting gap (characteristic of cuprates) and the description of the pseudogap phase, which is not expected in a conventional superconductor. The interpretation of the pseudogap phase is not unique and we adopted a non-competing order hypothesis, for which paring (typical of the superconducting phase) is predicted even above T_c, but the macroscopic superconducting properties are destroyed by phase fluctuations.

The effective model produced the following results:

1. it predicted the transient enhancement of the superconducting behavior due to a low photon energy excitation polarized along the Cu-Cu direction;

2. it highlighted the importance of phase coherence in order to obtain superconducting macroscopic features: if the pump excitation provokes strong phase fluctuations, the net effect is the reduction of the superconducting properties;

3. it suggested the possibility of inducing phase coherence in a strongly correlated material through a perturbation (with specific characteristics).

The relevance of the superconducting fluctuations, when approaching the critical temperature, encourages a deeper investigation of the probe pulses, in order to understand if and how quantum fluctuations of the material under study can be directly mapped in the quantum ***fluctuations*** of light. In particular, we focused on the fluctuations of the photon number of each pulse after the interaction of the sample, which can be obtained through a single pulse acquisition. Although quite similar to a "standard" pump-probe (intensity) measurement, the noise dynamical results require a completely different (and deeper) interpretation, which goes beyond the simple comparison with the intensity dynamics. For this reason we developed a model based on the quantum description of the Beam Splitter, and we performed several measurements on benchmark samples.

The characterization of the technique allowed to move to our usual sample (Y-Bi2212) and to compare the dynamics of the noise after the pump excitation in metallic and superconducting states. The observed difference can be described by the Beam Splitter model adding a polarization rotation of the probe pulse induced by the interaction with the excited sample. Therefore the experimental results and their interpretation through the Beam Splitter model suggests that:

1. the fluctuation measurement is very delicate and sensitive both to external factors and to set-up configurations, even the ones which are not expected to produce noise (for example the presence of a filter). Consequently the interpretation of the experimental results is much more complicated than the intensity one. It requires a detailed set-up characterization before each measurement, in order to discriminate the sample contribution;

2. footprints of each interaction are kept in the noise;

3. in metallic and superconducting phase the main noise results are induced by intensity and polarization changes, generated by the interaction between the probe pulse and the excited sample. Further investigations could concern the pseudogap phase (especially about the critical temperature), where we

expect larger phase fluctuations. The comparison with the superconducting and metallic phases could give some hints about the interactions at the basis of the sample properties and phase transitions.

The new technique potentially provides a tool to detect an increasing number of (dynamical) phenomena in complex systems.
As a matter of fact the preliminary results presented in this thesis show that, not only the variance on the photon number conveys more information than a "standard" pump probe signal, but also, unexpectedly, its dynamical range can be consciously amplified without reducing the quality of the measurement. The controlled increase of the variance of the time resolved signal allows on one side to reduce (or optimize) the ratio between the external noise and the inner light fluctuations and, on the other hand, to amplify the light-matter interaction footprints contained in the photon number distribution, but completely hidden in an intensity (or mean photon number) "standard" measurement.

This approach opens new perspectives in the study of complex systems, in which quantum fluctuations are expected to be relevant to describe intriguing properties, such as high temperature superconduction, quantum paraelectricity [27] and quantum phase transitions in general [82, 81].

A

Short summary of BCS theory

In this appendix we want to briefly summarize the main quantities and equations introduced by the BCS model[1].
BCS theory is a microscopic model which describes conventional superconductivity: the solution is based on three main intuitions:

1. COOPER INSTABILITY: L. Cooper found that an arbitrarily weak electron-electron attraction induces a two particle bound state that destabilizes the Fermi surface.

2. SCHRIEFFER HYPOTHESIS: J. R. Schrieffer proposed that the ground state of a conventional superconductor can be described as a coherent state of the electron pair (or "Cooper pair") operator $\Lambda = \sum_{\mathbf{k}} \phi_{\mathbf{k}} c_{\downarrow -\mathbf{k}} c_{\uparrow \mathbf{k}}$ (with c is the single particle annihilation operator, the arrown $\uparrow\downarrow$ refer to the z-component of the spin and $\phi_{\mathbf{k}} = \int d\mathbf{x} e^{-i\mathbf{k}\cdot\mathbf{x}} \phi_{\mathbf{r}}$ is a sort of weight of the Cooper pairs contributions: in BCS it is isotropic)

$$|\Psi_{BCS}\rangle = e^{\Lambda^\dagger} |0\rangle . \tag{A.1}$$

3. PHONON MEDIATION: J. Bardeen, L. N. Cooper and J. R. Schrieffer proposed in their paper[2] the interaction between electrons resulting from virtual exchange of phonons is attractive when the energy difference between the electrons states involved is less than the phonon energy. The calculations were then developed by A. B. Migdal[3] and Y. Nambu[4].

[1] The summary follows treatment found in P. Coleman (P. Coleman, *Introduction to Many Body Physics*, Cambridge University Press (2015))
[2] J. Bardeen, L. N. Cooper, and J. R. Schrieffer, *Theory of Superconductivity*, Physical Review, 108, 1175 (1957)
[3] A. B. Migdal, *Interaction between electrons and lattice vibrations in a normal metal*, Soviet Physics jetp 34, 6 (1958)
[4] Y. Nambu, *Quasi-Particles and Gauge Invariance in the Theory of Superconductivity* Physical Review 117, 648 (1960)

From the Schrieffer hypothesis A.1 one can expand the exponential and, keeping in mind that two electrons with the same $\mathbf{k}$ and σ cannot be created (Pauli principle), you end up with the non-normalized BCS wavefunction

$$|\Psi_{BCS}\rangle = \prod_{\mathbf{k}} (1 + \phi_{\mathbf{k}} c_{\uparrow}^{\dagger}(\mathbf{k}) c_{\downarrow}^{\dagger}(-\mathbf{k})) |0\rangle . \tag{A.2}$$

A.1 Hamiltonian

The general quantum Hamiltonian which describes the interaction between two electrons can be written as:

$$H = \sum_{\mathbf{k},\sigma} \varepsilon_{\sigma}(\mathbf{k}) c_{\sigma}^{\dagger}(\mathbf{k}) c_{\sigma}(\mathbf{k}) + + \sum_{\mathbf{k},\mathbf{k}'} V_{\mathbf{k}\mathbf{k}'} c_{\uparrow}^{\dagger}(\mathbf{k}) c_{\downarrow}^{\dagger}(-\mathbf{k}') c_{\downarrow}(-\mathbf{k}') c_{\uparrow}(\mathbf{k}) , \tag{A.3}$$

where $\sigma = \{\uparrow, \downarrow\}$.

In BCS superconductors the scattering between the electrons is produced by the exchange of a virtual phonon, so the interaction can be described by the Fr'olich potential

$$V_{\mathbf{k}\mathbf{k}'}^{EFF} = g_{\mathbf{k}-\mathbf{k}'}^{2} \frac{2\omega_{\mathbf{k}-\mathbf{k}'}}{\varepsilon(\mathbf{k}) - \varepsilon(\mathbf{k}')^{2} - \omega_{\mathbf{k}-\mathbf{k}'}^{2}}, \tag{A.4}$$

where $\mathbf{k}$ refers to the first electron and $\mathbf{k}'$ to the second one, ε is the electronic energy and ω the phoninc one.

Cooper suggested that the interaction is not strongly $\mathbf{k}$ dependent and that it becomes attractive within the Debye energy ω_D from the Fermi surface, so

$$V_{\mathbf{k}\mathbf{k}'} \begin{cases} -\frac{g_0}{V} \text{if } \varepsilon(\mathbf{k}), \varepsilon(\mathbf{k}') < \omega_D \\ 0, \qquad\qquad\qquad \text{otherwise.} \end{cases} \tag{A.5}$$

In this approximation the Hamiltonian expression becomes:

$$H = \sum_{\mathbf{k}\sigma} \varepsilon_{\sigma}(\mathbf{k}) c_{\sigma}^{\dagger}(\mathbf{k}) c_{\sigma}(\mathbf{k}) - \frac{g_0}{V} \hat{A}^{\dagger} \hat{A}, \tag{A.6}$$

where $\hat{A} = \sum_{\varepsilon_{\mathbf{k}} < \omega_D} c_{\downarrow}(-\mathbf{k}) c_{\uparrow}(\mathbf{k})$.

Let us define

$$\Delta = -\frac{g_0}{V} \left\langle \hat{A} \right\rangle \tag{A.7}$$

and move to the *mean field approximation* $\hat{A} = \left\langle \hat{A} \right\rangle + \delta\hat{A}$, with $\left\langle \hat{A} \right\rangle = -\frac{V}{g_0}\Delta$.
In this approximation and neglecting the second order terms in $\delta\hat{A}$ one finally gets the BCS Hamiltonian

$$H = \sum_{\mathbf{k}\sigma} \varepsilon_{\mathbf{k}} c_\sigma^\dagger(\mathbf{k})\, c_\sigma(\mathbf{k}) - \sum_{\mathbf{k}} \Delta c_\downarrow^\dagger(-\mathbf{k})\, c_\uparrow^\dagger(\mathbf{k}) + \Delta^* c_\uparrow(\mathbf{k})\, c_\downarrow(-\mathbf{k}) + \frac{V}{g_0}\Delta^*\Delta. \quad \text{(A.8)}$$

A.2 Eigenvualues

A part from the constant term proportional to $\Delta^*\Delta$, the Hamiltonian A.8 can be written in matrix form as

$$H = \sum_{\mathbf{k}} \begin{bmatrix} c_\uparrow^\dagger(\mathbf{k}) & c_\downarrow(-\mathbf{k}) \end{bmatrix} \begin{bmatrix} \varepsilon_{\mathbf{k}} & \Delta \\ \Delta^* & -\varepsilon_{\mathbf{k}} \end{bmatrix} \begin{bmatrix} c_\uparrow(\mathbf{k}) \\ c_\downarrow^\dagger(-\mathbf{k}) \end{bmatrix} \quad \text{(A.9)}$$

If we diagonalize the matrix we get

$$det \begin{bmatrix} \varepsilon_{\mathbf{k}} - E & \Delta \\ \Delta^* & -\varepsilon_{\mathbf{k}} - E \end{bmatrix} = E^2 - \varepsilon_{\mathbf{k}} - |\Delta|^2 = 0 \Rightarrow E_{1,2} = \pm\sqrt{\varepsilon_{\mathbf{k}} + |\Delta|^2} \quad \text{(A.10)}$$

A.3 Eigenstates

The system

$$\begin{cases} det \begin{bmatrix} \varepsilon_{\mathbf{k}} & \Delta \\ \Delta^* & -\varepsilon_{\mathbf{k}} \end{bmatrix} \begin{bmatrix} \tilde{A}_{\mathbf{k}} \\ \tilde{B}_{\mathbf{k}} \end{bmatrix} = \pm |E| \begin{bmatrix} \tilde{A}_{\mathbf{k}} \\ \tilde{B}_{\mathbf{k}} \end{bmatrix} \\ \tilde{A}_{\mathbf{k}}^2 + \tilde{B}_{\mathbf{k}}^2 = 1 \end{cases} \quad \text{(A.11)}$$

allows to calculate the eigenstates

$$\begin{cases} v_1 = \begin{bmatrix} A_{\mathbf{k}} \\ B_{\mathbf{k}} \end{bmatrix} \\ v_2 = \begin{bmatrix} -B_{\mathbf{k}} \\ A_{\mathbf{k}}, \end{bmatrix} \end{cases} \quad \text{(A.12)}$$

where $A_{\mathbf{k}} = \sqrt{\frac{1}{2}\left(1 + \frac{\varepsilon_{\mathbf{k}}}{\sqrt{\varepsilon_{\mathbf{k}}^2 + |\Delta|^2}}\right)}$ and $B_{\mathbf{k}} = \sqrt{\frac{1}{2}\left(1 - \frac{\varepsilon_{\mathbf{k}}}{\sqrt{\varepsilon_{\mathbf{k}}^2 + |\Delta|^2}}\right)}$.

The unitary matrix which diagonalizes the Hamiltonian is

$$U = \begin{bmatrix} A_{\mathbf{k}} & -B_{\mathbf{k}} \\ B_{\mathbf{k}} & A_{\mathbf{k}} \end{bmatrix} \tag{A.13}$$

and it can be used to move from the single particle operator $c_\sigma(\mathbf{k})$ to quasiparticle creation and annihilation operators though the relation $U \begin{bmatrix} \gamma_\uparrow(\mathbf{k}) \\ \gamma_\downarrow^\dagger(-\mathbf{k}) \end{bmatrix} = \begin{bmatrix} c_\uparrow(\mathbf{k}) \\ c_\downarrow^\dagger(-\mathbf{k}) \end{bmatrix}$ and one gets

$$\begin{cases} \gamma_\uparrow(\mathbf{k}) = A_{\mathbf{k}} c_\uparrow(\mathbf{k}) + B_{\mathbf{k}} c_\downarrow^\dagger(-\mathbf{k}) \\ \gamma_\downarrow^\dagger(\mathbf{k}) = B_{\mathbf{k}} c_\uparrow(\mathbf{k}) - A_{\mathbf{k}} c_\downarrow^\dagger(-\mathbf{k}). \end{cases} \tag{A.14}$$

Notice that the quasi-particles are non-interacting fermions, since they fulfill the Dirac-Fermi distribution

$$\left\langle \gamma_\sigma^\dagger(\mathbf{k}) \gamma_\sigma(\mathbf{k}) \right\rangle = \frac{1}{e^{\frac{\varepsilon_{\mathbf{k}}}{k_B T}} + 1}. \tag{A.15}$$

In this picture an excitation corresponds to break a Cooper pair and create two quasi-particles. The energy needed by this process $E_\uparrow(\mathbf{k}) + E_\uparrow(\mathbf{k}) = 2\sqrt{\varepsilon_{\mathbf{k}}^2 + |\Delta|^2} > 2|\Delta|$[5].

Once we have introduced $A_{\mathbf{k}}$ and $B_{\mathbf{k}}$, we can write the normalized BCS wavefunction as

$$|\Psi_{BCS}\rangle = \prod_{\mathbf{k}} (A_{\mathbf{k}} + B_{\mathbf{k}} c_\uparrow^\dagger(\mathbf{k}) c_\downarrow^\dagger(-\mathbf{k})) |0\rangle. \tag{A.16}$$

A.4 Gap equation

From the definition of the parameter Δ (equation A.7), substituting single particle operators with quasi-particle ones and keeping in mind the Fermi-Dirac distribution A.15, one gets

$$\Delta = \frac{1}{2} g_0 N(0) \int_{|\varepsilon_{\mathbf{k}}| < \omega_D} \frac{|\Delta|}{\sqrt{\varepsilon_{\mathbf{k}}^2 + |\Delta|^2}} \left(1 - 2f\left(\sqrt{\varepsilon_{\mathbf{k}}^2 + |\Delta|^2}, T\right)\right), \tag{A.17}$$

where $N(0)$ is the density of states per spin per unit volume at the Fermi energy.

[5] You cannot have single particle excitations for $E < 2|\Delta|$: there is no dissipation, which is the reason why the resistance drops to zero in a superconductor.

Equation A.17 allows to calculate important parameters of the system, such as:

- **the transition temperature** T_c (you have to impose $|\Delta| = 0$ and invert the equation)

- **the maximum value of the gap** $|\Delta|$ (in the limit for $T \longrightarrow 0$). The result is $\Delta = 2\omega_D e^{-\frac{1}{g_0 N(0)}}$

Irreducible representation

B

The following table summarizes the Mulliken symbols for irreducible representations [95].

SYMBOL	PROPERTY
A	symmetric with respect to rotation around the principal rotational axis
B	anti-symmetric with respect to rotation around the principal rotational axis
E	degenerate (*entartet* in German) - higher order principal axes -
subscript **1**	symmetric with respect to a vertical mirror plane perpendicular to the principal axis
subscript **2**	anti-symmetric with respect to a vertical mirror plane perpendicular to the principal axis
subscript **g**	symmetric with respect to a center of symmetry (*gerade* in German)
subscript **u**	anti-symmetric with respect to a center of symmetry (*ungerade* in German)
prime (')	symmetric with respect to a mirror plane horizontal to the principal rotational axis
double prime (")	anti-symmetric with respect to a mirror plane horizontal to the principal rotational axis

D_{4h} character table [95]:

$\mathbf{D_{4h}}$	$\mathbf{E}$	$\mathbf{2C_4}$	$\mathbf{C_2}$	$\mathbf{2C_2'}$	$\mathbf{2C_2''}$	$\mathbf{i}$	$\mathbf{2S_4}$	$\mathbf{\sigma_h}$	$\mathbf{2\sigma_v}$	$\mathbf{2\sigma_d}$
$\mathbf{A_{1g}}$	1	1	1	1	1	1	1	1	1	1
$\mathbf{A_{2g}}$	1	1	1	-1	-1	1	1	1	-1	-1
$\mathbf{B_{1g}}$	1	-1	1	1	-1	1	-1	1	1	-1
$\mathbf{B_{2g}}$	1	-1	1	-1	1	1	-1	1	-1	1
$\mathbf{E_g}$	2	0	-2	0	0	2	0	-2	0	0
$\mathbf{A_{1u}}$	1	1	1	1	1	-1	-1	-1	-1	-1
$\mathbf{A_{2u}}$	1	1	1	-1	-1	-1	-1	-1	1	1
$\mathbf{B_{1u}}$	1	-1	1	1	-1	-1	1	-1	-1	1
$\mathbf{B_{2u}}$	1	-1	1	-1	1	-1	1	-1	1	-1
$\mathbf{E_g}$	2	0	-2	0	0	-2	0	2	0	0

C

Acquisition system in noise measurements

In this appendix some details about features and requirements for the acquisition system of a fluctuation measurements are given. In particular we will focus on two steps of the acquisition: the *detection*, with particular attention on the electronics features, such as noise and acquisition rate, and the *integration process*, needed to get the final output.

C.1 Detection system

The experimental set-up is the same of the temperature measurement on Bi2212 (see Figure 3.8: the laser optical beam ($\lambda = 760\,\mathrm{nm}$) is split in two by a beam splitter. The first beam, adequately attenuated, is used a reference, while the second is reflected by the sample and then sent to the differential detector. The excitation of the sample is provided by a mid-infrared pulse ($\lambda \approx 8\,\mu m$). The time delay between pump and probe can be tuned by changing the latter optical path through a μm-translation stage. The detector measures the difference between the reference beam and the probe one. The two beams are balanced in order to have zero signal in absence of excitation.

The only difference with respect to a standard pump-probe measurement is related to the acquisition system, which must have the following fundamental features:

1. **Shot-to-electronic noise ratio:** the detection system must be able to work in the shot noise limit, that is, it must be sensitive to instrinsic fluctuation of the photon number, due to the quantum nature of light. A very naif idea of this concept can be given by considering a single light beam split by a perfect 50:50 beam splitter. Classically the initial intensity is separated in two identical final beams. On the other hand, from the quantum point of view, we expect fluctuations on the photon number of the two resulting pulses, because of the particle nature of photons. This example becomes clear if you consider an input pulse of 3 photons: the output pulses can have respectively 0-3, 1-2, 2-1, 3-0 photons. So, in this case, although the mean intensities in time on the output branches are equal, single pulse acquisition shows an intinsic variation,

or noise, in the photon number (for further information see section 6.4). In order to detect this kind of fluctuations the electronic noise must be very low.

2. **Acquisition rate:** the laser system produces $\approx 20\,\mathrm{fs}$ pulses with 50 KHz repetition rate, that is a pulse every $\tau = 20\,\mu\mathrm{s}$. In order to acquire single pulses the detection rate should be bigger than $1/\tau$.

Our system is made up of a custom highly efficient differential detector, based on the work of Hansen [41], and a fast digitizer.

The **detector** consists of two Hamamtsu S3883 Silicon PIN photodiodes with 0.94 quantum efficiency (that is, the ratio between number of electrons produced by the diode and the number of impinging photons) at 800 nm, connected in reverse bias and followed by a low noise charge amplifier. The reverse bias allows to physiscally subtract the photocurrents produced by the diodes, while the amplification takes place only at the final stage, in order not to increase the value of the noise produced by the electronic system. The preamplifier sensitivity is 5.2 mV/fC, i.e. a detector response of 1 mV corresponds to about $1.15 \cdot 10^3$ electrons. Notice that the total efficiency (called *equivalent efficiency*) of the detector is not the same as the diodes one, because of the presence of the electronic noise. The measured efficiency (defined as the ratio between the shot noise value and the total noise for a certain photon number input) of our detector is about $\eta_{eq} \approx 0.86$. All preliminary tests on our detection system can be found in [33].

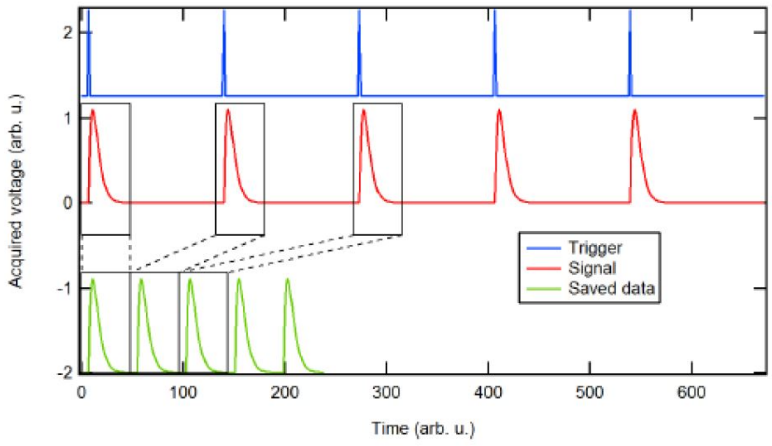

Fig. C.1.: Scheme of the multiple recording acquisition system: only a defined time interval of the signal is saved. The beginning of the acquisition is determined by a trigger

The output voltage is the digitized by a high speed **digitizer** PC plug in card (Spectrum M2i), with 16 bit resolution. The *Multiple Recording* option allows to acquire just the "interesting" portion of the signal (that is the detection response, about $1\,\mu s$, discarding the remaining $19\,\mu s$ time delay between two subsequent pulses), in order

to reduce the amount of acquired data. The Multiple Recording scheme is sketched in Figure C.1.

C.2 Integration process

Once the detector response has been digitized, we need a technique to convert the signal (as the one plotted in Figure C.1) to a single number representing the pulse intensity. Multiple choices are possible:

- **Peak:** one could collect the absolute peak value of the detector response: it is a correct procedure in principle, but it is very sensitive to external noise and, since we are interested in small intensity variations, this could affect the measurement, especially when the differential photocurrent is close to zero.

- **Integration:** a second possibility consists in the integration of the detector response in time. The integral is proportional to the peak value of the previous point, but it is less affected to "random" external noise. The limit of this kind of acquisition is the "weight" associated to the noise: the noise before and after the pulse detection has the same weight as the one related to the maximum of the signal. Again, this could be problematic when the differential signal oscillates around zero.

- **Scalar product:** a good compromise between the two previous options is a sort of scalar product between the measured signal and an expected (normalized) one. The latter is usually measured with just one diode and represent the typical detector response. This option keeps the stability reached in the second point, but applies different weights to different noise contributions.

Once the conversion is done, the probe intensity (actually the difference between the probe and the reference intensity) can be acquired pulse by pulse and then the needed quantities (i.e. mean $\bar{I} = \frac{1}{N}\sum_i I_i$, variance $\sigma^2 = \frac{1}{N-1}\sum_i (I_i - \bar{I})^2$ etc., where I_i is the intensity of the i^{th} pulse and N is the number of pulses) can be computed for hundreds of pulses. In the plots presented here, both mean value and avariance have been average on tens of scans, in order to improve the quality of the measurement.

Bibliography

[1] URL: https://en.wikipedia.org/wiki/High-temperature_superconductivity (cit. on p. 8).

[2] A. Abanov et al. „Fingerprints of spinmediated pairing in cuprates“. In: *J. Electron Spectrosc. Relat. Phenom.* (2001), pp. 117–129 (cit. on p. 19).

[3] N. W. Ashcroft and N. D. Mermin. *Solid State Physics*. Cornell University, 1976 (cit. on p. 10).

[4] R. D. Averitt et al. „Nonequilibrium superconductivity and quasiparticle dynamics in $YBa_2Cu_3O_{7-\delta}$“. In: *Phys. Rev. B* 63.140502 (2001) (cit. on pp. 39, 67).

[5] L. N. Bardeen J. Cooper and J. R. Schrieffer. „Theory of Superconductivity“. In: *Physical Review* 108.5 (1957) (cit. on pp. 7, 11).

[6] D. N. Basov et al. „Electrodynamics of high-T_c superconductors“. In: *Rev. Mod. Phys.* 77.721 (2005) (cit. on p. 67).

[7] J. G. Bernordz and K. A. Müller. „Possible High T_c superconductivity in the Ba-La-Cu-O system“. In: *Zeitschrift für Physik B - Condensed Matter* 64 (1986), pp. 198–193 (cit. on pp. 7, 12).

[8] A. V. Boris et al. „In-Plane Spectral Weight Shift of Charge Carriers in $YBa_2Cu_3O_{6.9}$“. In: *Science* 304.5671 (2004), pp. 708–710 (cit. on p. 67).

[9] F. Boschini et al. „Collapse of superconductivity in cuprates via ultrafast quenching of phase coherence“. In: *Nature Materials* 17 (2018), 416–420 (cit. on pp. 42, 65, 78).

[10] C. Buzea and K. Robbie. „Assembling the puzzle of superconducting elements: a review“. In: *Superconductor Science Technology* 18 (2005), R1–R8 (cit. on p. 9).

[11] C. Buzea and T. Yamashita. „Review of the superconducting properties of MgB2“. In: *Superconductor Science and Technology* 14.11 (2001) (cit. on p. 12).

[12] M. Cardona. „Raman scattering in high T_c superconductors: Phonons, electrons, and electron-phonon interaction“. In: *Physica C* 317–318 (1999), pp. 30–54 (cit. on pp. 24–29).

[13] E. W. Carlson et al. „Concepts om High Temperature Superconductivity“. In: *The Physics of Superconductors*. Ed. by Ketterson J.B. (eds) Bennemann K.H. Springer, Berlin, Heidelberg, 2004, pp. 275–451 (cit. on pp. 15, 16, 18).

[14]E. Casandruc et al. „Wavelength-dependent optical enhancement of superconducting interlayer coupling in $La_{1.885}Ba_{0.115}CuO_4$“. In: *Physical Review B* 91.17 (2015) (cit. on p. 66).

[15]Laboratoire National des Champs Magnetiques Intenses Toulouse. URL: `http://www.toulouse.lncmi.cnrs.fr/spip.php?rubrique149&lang=en` (cit. on p. 13).

[16]U. Chatterjee et al. „Nondispersive Fermi Arcs and the Absence of Charge Ordering in the Pseudogap Phase of $Bi_2Sr_2CaCu_2O_{8+\delta}$“. In: *Phys. Rev. Lett.* 96.107006 (2006) (cit. on p. 65).

[17]Y. Chuntang et al. „Structure Refinement of $Bi_2Sr_{1.855}Ca_{1.145}Cu_2O_8$ from Neutron Data“. In: *Chin. Phys. Lett.* 8 (1991), pp. 521–524 (cit. on p. 20).

[18]F. Cilento. „Non-equilibrium Phase Diagram of Bi2212 Cuprate Superconductors revealed by ultrafast optical spectroscopy“. PhD thesis. Università degli Studi di Trieste, 2012 (cit. on pp. 13, 16, 21, 37).

[19]F. Cilento et al. „Photo-enhanced antinodal conductivity in the pseudogap state of high-T_c cuprates“. In: *Nature Communications* 5.4353 (2014) (cit. on p. 55).

[20]P. Coleman. *Introduction to Many Body Physics*. Cambridge University Press, 2015 (cit. on p. 11).

[21]P. Coleman and A. Schofield. „Quantum Criticality“. In: *Nature* 433 (2005), pp. 226–229 (cit. on p. 91).

[22]J. Corson et al. „Vanishing of phase coherence in underdoped $Bi_2Sr_2Y_{0.08}Ca_{0.92}Cu_2O_{8+\delta}$“. In: *Nature* 398.221 (1999) (cit. on pp. 65, 78).

[23]T Cuk et al. „A review of electron–phonon coupling seen in the high-Tc superconductors by angle-resolved photoemission studies (ARPES)“. In: *Phys. Stat. Sol. b* 242.1 (2005) (cit. on p. 19).

[24]P. Dai et al. „The Magnetic Excitation Spectrum and Thermodynamics of High-Tc Superconductors“. In: *Science* 294 (1999), pp. 1344–1347 (cit. on pp. 15, 17).

[25]S. Dal Conte et al. „Disentangling the electronic and phononic glue in a high-Tc superconductor“. In: *Science* 335.6076 (2012), pp. 1600–1603 (cit. on p. 42).

[26]R. Daou et al. „Broken rotational symmetry in the pseudogap phase of a high-Tc superconductor“. In: *Nature* 463 (2010), 519–522 (cit. on p. 65).

[27]N. Das and S. G. Mishra. „Fluctuations and criticality in quantum paraelectrics“. In: *Journal of Physics: Condensed Matter* 21 (2009) (cit. on pp. 2, 91, 157).

[28]J. Demsar et al. „Pair-breaking and superconducting state recovery dynamics in MgB_2“. In: *Phys. Rev. Lett.* 91.26 (2003) (cit. on pp. 38, 67).

[29]J. Demsar et al. „Quasiparticle dynamics and gap structure in $HgBa_2Ca_2Cu_3O_{8+\delta}$ investigated with femtosecond spectroscopy“. In: *Phys. Rev. B* 63.054519 (2001) (cit. on p. 67).

[30]J. Demsar et al. „Superconducting Gap Δ_c, the Pseudogap Δ_p, and Pair Fluctuations above T_c in Overdoped $Y_{1-x}Ca_xBa_2Cu_3O_{7-\delta}$ from Femtosecond Time-Domain Spectroscopy“. In: *Phys. Rev. Lett.* 82.4918 (1999) (cit. on p. 67).

[31]T. P. Devereaux et al. „Inelastic light scattering from correlated electrons“. In: *Rev.Mod.Phys.* 79 (2007), pp. 175–233 (cit. on pp. 23, 24, 30, 34, 67).

[32]V. J. Emery and S. A. Kivelson. „Importance of phase fluctuation in superconductors with small superfluid density“. In: *Nature* 374 (1995), 434–437 (cit. on p. 18).

[33]M. Esposito et al. „Photon number statistics uncover the fluctuations in non-equilibrium lattice dynamics“. In: *Nature Communications* 6.10249 (2015), pp. 1714–1716 (cit. on p. 168).

[34]D. Fausti et al. „Light-Induced Superconductivity in a Stripe-Ordered Cuprate“. In: *Science* 331.6014 (2011), pp. 189–191 (cit. on pp. 38, 66).

[35]M. Gedik et al. „Abrupt Transition in Quasiparticle Dynamics at Optimal Doping in a Cuprate Superconductor System“. In: *Phys. Rev. Lett.* 95.117005 (2005) (cit. on p. 67).

[36]N. Gedik. „Recombination and Propagation of Quasiparticles in Cuprate Superconductors“. PhD thesis. Department of Physics University of California, Berkeley, 2004 (cit. on p. 18).

[37]C. Giannetti et al. „Discontinuity of the ultrafast electronic response of underdoped superconducting $Bi_2Sr_2CaCu_2O_{8+\delta}$ strongly excited by ultrashort light pulses“. In: *Phys. Rev. B* 79.224502 (2009) (cit. on p. 67).

[38]C. Giannetti et al. „Revealing the high-energy electronic excitations underlying the onset of high-temperature superconductivity in cuprates“. In: *Nature Communications* 2.353 (2011) (cit. on pp. 39, 56).

[39]C. Giannetti et al. „Ultrafast optical spectroscopy of strongly correlated materials and high-temperature superconductors: a non-equilibrium approach“. In: *Advances in Physics* 65 (2016), 58–238 (cit. on pp. 8, 19, 36, 65, 67, 72).

[40]J. Graf et al. „Nodal quasiparticle meltdown in ultrahigh-resolution pump–probe angle-resolved photoemission“. In: *Nature Physics* 7 (2011), pp. 805–809 (cit. on p. 38).

[41]H Hansen. „An ultra-sensitive pulsed balanced homodyne detector : Application to time-domain quantum measurements“. In: *Optics letter* 26 (2001), pp. 1714–1716 (cit. on p. 168).

[42]M. Hase et al. „Dynamics of Coherent Anharmonic Phonons in Bismuth Using High Density Photoexcitation“. In: *Physical Review Letter* 88.6 (2002) (cit. on pp. 122, 123).

[43]S. Hellmann et al. „Ultrafast melting of a charge-density wave in the Mott insulator $1T - TaS_2$“. In: *Phys. Rev. Lett.* 105.187401 (2010) (cit. on p. 38).

[44]W. Hu et al. „Optically enhanced coherent transport in $YBa_2Cu_3O_{6.5}$ by ultrafast redistribution of interlayer coupling“. In: *Nature Materials* 13 (2014), 705–711 (cit. on p. 66).

[45]K. Ishioka et al. „Temperature dependence of coherent A_g and E_g phonons in bismuth“. In: *Journal of Applied Physics* 100.093501 (2006) (cit. on p. 122).

[46]R. A. Kaindl et al. „Dynamics of Cooper pair formation in $Bi_2Sr_2CaCu_2O_{8+\delta}$“. In: *Phys. Rev. B* 72.060510 (2005) (cit. on pp. 39, 67).

[47]S. Kaiser et al. „Optically induced coherent transport far above Tc in underdoped $YBa_2Cu_3O_{6+x}$“. In: *Phys. Rev. B* 89.184516 (2014) (cit. on p. 66).

[48]Y. Kamihara. „Iron based layered superconductor: LaOFeP“. In: *Journal of the American Chemical Society* 128.31 (2006) (cit. on p. 12).

[49]S. A. Kivelson et al. „How to detect fluctuating stripes in the high-temperature superconductors“. In: *Rev. Mod. Phys.* 75 (2003) (cit. on p. 65).

[50]M. Knap et al. „Dynamical Cooper pairing in nonequilibrium electron-phonon systems“. In: *Phys. Rev. B* 94.21 (2016) (cit. on p. 36).

[51]K. Kohmoto et al. „Observation of coherent phonons in strontium titanate: Structural phase transition and ultrafast dynamics of the soft modes“. In: *Physical Review B* 74.064303 (2006) (cit. on p. 122).

[52]T. Kondo et al. „Point nodes persisting far beyond T_c in Bi2212“. In: *Nature Communication* 6.7699 (2015) (cit. on pp. 65, 78).

[53]P. Kusar et al. „Controlled Vaporization of the Superconducting Condensate in Cuprate Superconductors by Femtosecond Photoexcitation“. In: *Phys. Rev. Lett.* 101.227001 (2008) (cit. on pp. 53, 67).

[54]A. Lanzara et al. „Evidence for ubiquitous strong electron-phonon coupling in high-temperature superconductors“. In: *Nature* 412 (2001), 510–514 (cit. on p. 19).

[55]J. Lee and S. A. Kivelson. „Interplay of electron-lattice interactions and superconductivity in $Bi_2Sr_2CaCu_2O_{8+\delta}$“. In: *Nature* 442 (2006), 546–550 (cit. on p. 18).

[56]J. Lee et al. „Spectroscopic Fingerprint of Phase-Incoherent Superconductivity in the Underdoped $Bi_2Sr_2CaCu_2O_{8+\delta}$“. In: *Science* 325.5944 (2009), pp. 1099–1103 (cit. on p. 65).

[57]W. S. Lee et al. „Abrupt onset of a second energy gap at the superconducting transition of underdoped Bi2212“. In: *Nature* 450 (2007), pp. 81–84 (cit. on p. 67).

[58]L. Li et al. „Diamagnetism and Cooper pairing above T_c in cuprates“. In: *Phys. Rev. B* 81.054510 (2010) (cit. on p. 78).

[59]J. W. Loram et al. „Electronic specific heat of $YBa_2Cu_3O_{6+x}$ from 1.8 to 300 K“. In: *Journal of Superconductivity and Novel Magnetism* 7.1 (1994), 243–249 (cit. on pp. 15, 16).

[60]R. Loudon. *The Quantum Theory of Light*. 3rd ed. Oxford Science Publications, 1973 (cit. on pp. 98, 104).

[61]I. Madan et al. „Separating pairing from quantum phase coherence dynamics above the superconducting transition by femtosecond spectroscopy“. In: *Scientific Report* 4.5656 (2014) (cit. on pp. 39, 42, 53, 65, 78).

[62]R. Mankowsky et al. „Nonlinear lattice dynamics as a basis for enhanced superconductivity in $YBa_2Cu_3O_{6.5}$“. In: *Nature* 516 (2014), pp. 71–73 (cit. on p. 38).

[63]W. Meissner and R. Ochsenfeld. „Ein neuer Effekt bei eintritt der Supraleitfaehigkeit“. In: *Naturwissenschaften* 21 (1933), pp. 797–788 (cit. on p. 7).

[64]M. Mitrano et al. „Possible light-induced superconductivity in K_3C_{60} at high temperature“. In: *Nature* 530 (2016), 461–464 (cit. on pp. 38, 66).

[65]H. J. A. Molegraaf et al. „Superconductivity-Induced Transfer of In-Plane Spectral Weight in $Bi_2Sr_2CaCu_2O_{8+\delta}$“. In: *Science* 295.5563 (202), pp. 2239–2241 (cit. on p. 67).

[66]F. Novelli. „In search of selective excitations for studying out-of-equilibrium properties in strongly correlated electron systems and high temperature superconductors“. PhD thesis. Università degli Studi di Trieste, 2012 (cit. on p. 38).

[67]H. K. Onnes. „The Superconductivity of Mercury“. In: *Comm. Phys. Lab. Univ., Leiden* (1911), pp. 122–124 (cit. on p. 7).

[68]D. Pelc et al. „Emergence of superconductivity in the cuprates via a universal percolation process“. In: *arXiv* 1710.10219 (2017) (cit. on p. 78).

[69]D. Pelc et al. „Unusual behavior of cuprates explained by heterogeneous charge localization“. In: *arXiv* 1710.10221 (2017) (cit. on p. 78).

[70]L. Perfetti et al. „Ultrafast dynamics of fluctuations in high-temperature superconductors far from equilibrium“. In: *Phys. Rev. Lett.* 114.067003 (2015) (cit. on pp. 65, 78).

[71]P. Popčević et al. „Percolative nature of the dc paraconductivity in the cuprate superconductors“. In: *arXiv* 1710.10220 (2017) (cit. on p. 78).

[72]M. R. Presland et al. „General Trends in Oxygen Stoichiometry Effects on Tc in Bi and Tl Superconductors“. In: *Physica C: Superconductivity* 176 (1991), pp. 95–105 (cit. on p. 20).

[73]A. V. Puchkov et al. „The pseudogap state in high-Tc superconductors: an infrared study“. In: *J. Phys.: Condens. Matter* 8 (1996), 10049–10082 (cit. on pp. 15, 17).

[74]F. Randi. „Low-energy physics in strongly correlated materials via nonlinear spectroscopies“. PhD thesis. Università degli Studi di Trieste, 2016 (cit. on pp. 42, 84, 152, 153).

[75]T. J. Reber et al. „Prepairing and the ”filling” gap in the cuprates from the tomographic density of states“. In: *Phys. Rev. B* 87.060506 (2013) (cit. on p. 78).

[76]C. Renner et al. „Pseudogap Precursor of the Superconducting Gap in Under- and Overdoped $Bi_2Sr_2CaCu_2O_{8+\delta}$“. In: *Physical Review Letters* 80.1 (1998) (cit. on pp. 15, 16).

[77]J. W. Rohlf. *Modern Physics from alpha to Z0*. Wiley, 1994 (cit. on p. 11).

[78]T. Rohwer et al. „Collapse of long-range charge order tracked by time-resolved photoemission at high momenta“. In: *Nature* 471 (2011), pp. 490–493 (cit. on p. 38).

[79]A. Rothwarf and B. Taylor. „Measurement of Recombination Lifetimes in Superconductors.“ In: *Physical Review Letters* 19 (1967), pp. 27–30 (cit. on p. 39).

[80]A. Rundquist et al. „Polarization-dependent detection of impulsive stimulated Raman scattering in α-quartz“. In: *Journal of Modern Optics* 52:17 (2005), pp. 2501–2510 (cit. on p. 27).

[81]S. Sachdev. „Quantum criticality: competing ground states in low dimensions“. In: *Science* 288 (2000), pp. 475–480 (cit. on pp. 2, 91, 157).

[82]S. Sachdev. *Quantum phase transitions*. Cambridge University Press, 1998 (cit. on pp. 2, 91, 157).

[83]D. J. Scalapino et al. „d-wave pairing near a spin-density-wave instability“. In: *Physical Review B* 34.8190 (1986) (cit. on p. 19).

[84]F. Schmitt et al. „Transient Electronic Structure and Melting of a Charge Density Wave in $TbTe_3$“. In: *Science* 321 (2008), pp. 1649–1652 (cit. on p. 38).

[85]K. M. Shen and J. C. S. Davis. „Cuprate high-T_c superconductors“. In: *Materials Today* 11.9 (2008), pp. 14–21 (cit. on pp. 11, 18).

[86]S. V. Shulga et al. „Electronic states and optical spectra of HTSC with electron-phonon coupling“. In: *Physica C: Superconductivity* 178 (1991), pp. 266–274 (cit. on p. 19).

[87]C. Smallwood et al. „Tracking Cooper Pairs in a Cuprate Superconductor by Ultrafast Angle-Resolved Photoemission“. In: *Science* 336 (2012), pp. 1137–1139 (cit. on p. 38).

[88]C. L. Smallwood et al. „Time- and momentum-resolved gap dynamics in $Bi_2Sr_2Ca_Cu_2O_{8+\delta}$“. In: *Phys. Rev. B* 89.115126 (2014) (cit. on p. 65).

[89]R. Sooryakumar and M. V. Klein. „Direct observation of the coexistence of the pseudogap and superconducting quasiparticles in $Bi_2Sr_2CaCu_2O_{8+y}$ by time-resolved optical spectroscopy.“ In: *Physical Review Letters* 101.137003 (2008) (cit. on p. 39).

[90]R. Sooryakumar and M. V. Klein. „Raman Scattering by superconducting-gap excitations and their coupling to Charge-Density Waves“. In: *Physical Review Letters* 45.8 (1980) (cit. on p. 28).

[91]H. Takagi et al. „Systematic Evolution of Temperature-Dependent Resistivity in $La_{2-x}Sr_xCu0_4$“. In: *Physical Review Letters* 69.20 (1992) (cit. on pp. 14, 15).

[92]L. R. Testardi et al. „Destruction of Superconductivity by Laser Light“. In: *Physical Review B* 4.7 (1971) (cit. on p. 53).

[93]D. K. Thapa and A. Pandey. „Evidence for Superconductivity at Ambient Temperature and Pressure in Nanostructures“. In: *arXiv:1807.08572* (2018) (cit. on p. 12).

[94]C. Thomsen and G. Kaczmarczyk. „Vibrational Raman Spectroscopy of High-temperature Supperconductors“. In: *from Handbook of Vibrational Spectroscopy* (2002) (cit. on pp. 24, 27–29, 33).

[95]T. Timusk et al. „Report on Notation for the Spectra of Polyatomic Molecules“. In: *The Journal of Chemical Physics* 23 (1955) (cit. on pp. 165, 166).

[96]T. Timusk et al. „The pseudogap in high-temperature superconductors: an experimental survey“. In: *Rep. Prog. Phys.* 62.61 (1999) (cit. on p. 65).

[97]Y Toda et al. „Rotational symmetry breaking in $Bi_2Sr_2CaCu_2O_{8+\delta}$ probed by polarized femtosecond spectroscopy“. In: *Physical Review B* 90.094513 (2014) (cit. on pp. 35, 39, 51, 82).

[98]Y. Wang et al. „Onset of the vortexlike Nernst signal above T_c in $La_{2-x}Sr_xCuO_4$ and $Bi_2Sr_{2-y}La_yCuO_6$“. In: *Phys. Rev. B* 64.224519 (2001) (cit. on p. 78).

[99]J. Yang. „Conventional and ultrafast pump-probe time resolved Raman spectroscopy of strongly correlated systems“. PhD thesis. University of Colorado, Boulder, 2017 (cit. on pp. 30, 33).

[100]G. Yu et al. „Universal superconducting precursor in the cuprates“. In: *arXiv* 1710.10957 (2017) (cit. on p. 78).

[101]R. Yusupov et al. „Coherent dynamics of macroscopic electronic order through a symmetry breaking transition“. In: *Nature Physics* 6 (2010), pp. 681–684 (cit. on p. 38).

List of Figures

I1 Timeline of Superconductivity. 8

2.1 Periodic table of Superconductivity. 9
2.2 Cuprate phase diagram. 14
2.3 Resistivity in pseudagap phase. 15
2.4 Gap in pseudogap phase. 16
2.5 Specific Heat in pseudogap phase. 16
2.6 Infrared conductivity in pseudogap phase. 17
2.7 Inelastic neutron scattering in pseudogap phase. 17
2.8 d-wave gap. 19
2.9 Bi2212 crystal structure. 21

3.1 Raman process Feynman diagrams. 25
3.2 Electronic dispersion and optical transitions. 26
3.3 Raman measurements on BCS superconductors. 28
3.4 Raman measurements on High-T_c superconductors. 29
3.5 Sketch of a pump-probe experiment. 37
3.6 Transient reflectivity in a quasi-equilibrium measurement. 38
3.7 Process of time resolved measurements at $\mathbf{T < T_c}$. 40
3.8 Set-up scheme 44

4.1 Photon energies. 47
4.2 Probe linearity. 49
4.3 Reflectivity versus pump-probe polarization angle. 50
4.4 Different modes dynamics in superconducting phase. 52
4.5 Pump photon energy and fluence dependence at 80 K. 53
4.6 Pump photon energy and fluence dependence at 110 K. 53
4.7 Pump photon energy dependence. 54
4.8 Temperature map 55
4.9 Probe photon energy dependence 56
4.10 High photon energy probes comparison 57
4.11 High photon energy probes comparison: non-equilibrium 58
4.12 Transition temperature at $h\nu_{probe} = 1.88\,\mathrm{eV}$ 59
4.13 Transition temperature at $h\nu_{probe} = 1.44\,\mathrm{eV}$ 59
4.14 Temperature maps as a function of pump frequency and fluence 61

4.15 Temperature maps as a function of pump frequency and fluence 62

5.1 MIR pump - optical probe measurements. 66
5.2 Wavelength dependent anisotropy 68
5.3 Complete dataset for wavelength dependent anisotropy 68
5.4 Measurements and fit for high photon energy data 70
5.5 Measurements and fit for $h\nu = 70\mathrm{meV}$ data 70
5.6 Temperature evolution of the fit parameters 71
5.7 High fluence regime 72
5.8 d-wave BCS microscopic model 75
5.9 Photon energy and fluence dependence 76
5.10 Time dependent pair operator representation 77
5.11 Extension of the d-wave BCS model to larger temperatures 78
5.12 Gap amplitude evolution at $T > T_c$ 79
5.13 Coherence length 80
5.14 Birefringence acquisition set-up 81
5.15 Measurement correspondence 83
5.16 Measurement comparison 84
5.17 B_{2g} temperature measurement - low pump fluence 85
5.18 B_{2g} temperature measurement - high pump fluence 86
5.19 B_{1g} temperature measurement - low pump fluence 87
5.20 B_{1g} temperature measurement - high pump fluence 88

II1 Statistical measurements: concept 92
II2 Statistical measurements:data 93

6.1 Description of dissipative effects 96
6.2 Differential acquisition set-up 97
6.3 Variance for a photon poissonian distribution 98
6.4 Lossless Beam Splitter 99
6.5 Classical *vs* Partition noise 100
6.6 One beam Splitter output 101
6.7 Mean and variance measurements as a function of the beam attenuation 102
6.8 Shot Noise set-up 103
6.9 Shot noise test 105
6.10 First approximation of the experimental set-up 107
6.11 Variance as a function of the mean value 108
6.12 Point of minimum of the variance 109
6.13 Characterization function: contributions 109
6.14 Variance for non-50:50 beam splitter 111
6.15 Additional dissipation: model set-up 112
6.16 Additional dissipation: effects of the filtering 113
6.17 Additional dissipation: effects of the splitting 113

6.18 Shot noise test with non-50:50 BS . . . 115
6.19 Signal-to-noise ratio: minimum noise . . . 117
6.20 Systematic effects on the variance . . . 118

7.1 ISRS: frequency difference . . . 121
7.2 Bismuth time-resolved response . . . 123
7.3 Bismuth noise dynamics: positive balancing . . . 125
7.4 Bismuth noise dynamics: negative balancing . . . 125
7.5 Noise dynamics: minimum noise and low signal intensity . . . 127
7.6 Noise dynamics: minimum noise and higher signal intensity . . . 127
7.7 Noise dynamics: double frequency amplitude . . . 128
7.8 Noise dynamics: variance comparison . . . 129
7.9 Noise dynamics: 3Ω component . . . 130
7.10 $\mathbf{SrTiO_3}$ measurement . . . 131
7.11 $\mathbf{2\Omega}$ component: wavelet analysis . . . 132
7.12 Absence of $\mathbf{2\Omega}$ component: wavelet analysis . . . 133
7.13 Two pump measurement on Bismuth . . . 134
7.14 Two pumps measurement: wavelet analysis . . . 135
7.15 Two pumps measurement: variance . . . 136
7.16 Two pump measurement on Quartz . . . 136
7.17 Multiple phonon contribution: mean value . . . 138
7.18 External noise contribution . . . 139
7.19 External noise contribution: variance estimation . . . 139
7.20 Experimental condition: variance simulation . . . 143

8.1 Mean and variance reflectivity measurements . . . 146
8.2 Variance as a function of the unbalancing . . . 147
8.3 BS model (1): data and simulation . . . 148
8.4 Bi2212 noise measurement: set-up . . . 149
8.5 BS model: parameters dynamics . . . 150
8.6 BS model: data and simulation . . . 151
8.7 A_g and B_{1g} signals at room temperature . . . 152

C.1 Multiple recording acquisition system . . . 168

Ringraziamenti

Acknowledgments

Il primo ringraziamento va ai miei compagni di (dis-)avventure degli ultimi tre anni. Primo fra tutti Daniele, già relatore, e ora supervisore delle mie tesi. Lo ringrazio perchè riesce a guardare avanti e a spronarmi anche quando i risultati non sono così convincenti. La sua capacità di stupirsi, che buona parte di noi perde in giovanissima età, e di pensare in grande (che io forse non ho nemmeno mai avuto) è sicuramente il motore del gruppo.

Un grazie ad Alexandre (che capisce perfettamente l'italiano, sebbene lo neghi), per la sua voglia di mettersi in gioco e di migliorare costantemente tutto (dal set-up ai programmi Labview...), che spesso ci hanno portato ad interpretare i nostri risultati in maniera completamente diversa.

A Giorgia, Filippo e Angela, i tre dottorandi che sono stati così pazzi da aggregarsi al gruppo. Con loro non ho ancora avuto l'occasione di condividere il set-up (se non per brevissimi periodi), ma di certo le gioie e i dolori del dottorato. Ognuno, a suo modo, ha portato un po' di colore nel nostro (buio) laboratorio.
Grazie anche a Giacomo, unico studente di cui sia stata correlatrice di tesi e che, nonostante questo, ha deciso di tornare a far parte del gruppo.

I must also acknowledge Jonathan for conveying its approach to research, less anxious and impatient than anyone else, but productive as well (and even more).

A Federico per rispondere prontamente (e gentilmente!) a tutte le domande che iniziano con "Avresti per caso un..." o "Secondo te, come posso fare per...".

Un ringraziamento anche a Martina e Francesco, che hanno lasciato il gruppo da un paio di anni, ma di cui si sente ancora la mancanza.

Ringrazio anche tutti coloro che ho stressato durante questi tre anni e per cui sono diventata (testuali parole) un "incubo".

In senso stretto, le persone che ho nominato mi hanno permesso di portare a termine questo progetto di dottorato. D'altra parte non si può tralasciare un breve ringraziamento al "mondo reale" (come l'ho sentito definire proprio ad una difesa di dottorato), quello a cui probabilmente - e per fortuna - non interessa poi tanto il ruolo delle fluttuazioni del numero di fotoni in un esperimento di pump-probe, ma che, senza dubbio, ha una buona fetta di responsabilità nella riuscita di ciò che faccio.

Di questo mondo fa sicuramente parte la mia famiglia, sprone (a volte involontario, altre perfettamente consapevole) nel lavoro e negli altri aspetti della vita.

Un grazie infine agli altri protagonisti della "vita reale", essenzialmente gli stessi che ho ringraziato quattro anni fa. Ciò non significa che tutto sia come allora, anzi, moltissime cose sono cambiate: alcune avrebbero potuto funzionare meglio, altre invece hanno superato ogni aspettativa.
Non posso che chiedere tempo (e anche una mano, se possibile) per le prime ed essere enormemente grata per le seconde. Come si fa in laboratorio, del resto...

Francesca